CONSTRUCTION MATERIAL CLASSIFICATION USING MULTI-SPECTRAL TERRESTRIAL LASER SCANNING

by

Hywel F.J. Evans

Thesis submitted to the University of Nottingham

for the degree of Doctor of Philosophy

July 2016

Abstract

This research addresses the problem of populating Building Information Model databases with information on building construction materials using a new classification method which uses multi-spectral laser scanning intensity and geometry data. Research in multi-spectral laser scanning will open up a new era in survey and mapping; the 3D surface spectral response sensitive to the transmitted wavelengths could be derived day or night in complex environments using a single sensor. At the start of this research a commercial multi-spectral sensor did not exist, but a few prototype level instruments had been developed; this work wished to get ahead of the hardware development and assess capability and develop applications from multi-spectral laser scanning. These applications could include high density topographic surveying, seamless shallow water bathymetry, environmental modelling, urban surface mapping, or vegetative classification. This was achieved by using from multiple terrestrial laser scanners, each with a different laser wavelength. The fused data provided a spectral and geometric signature of each material which was subsequently classified using a supervised neural network. The multi-spectral data was created by precise co-positioning of the scanner optical centres and sub-centimetre registration using common sphere targets. A common point cloud, with reflected laser intensity values for each laser wavelength, was created from the data. The three intensity values for each point were then used as input to the classifier; ratios of the actual intensities were used to reduce the effect of range and incidence angle differences. Analysis of

five classes of data showed that they were not linearly separable; an artificial neural network classifier was the chosen classifier has been shown to separate this type of data. The classifier training dataset was manually created from a small section of the original scan; five classes of building materials were selected for training. The performance of the classification was tested against a reference point cloud of the complete scene. The classifier was able to distinguish the chosen test classes with a mean rate of 84.9% and maximum for individual classes of 100%. The classes with the highest classification rate were brick, gravel and pavement. The success rate was found to be affected by several factors, among these the most significant, inter-scan registration, limitation on available wavelengths and the number of classes of material chosen. Additionally, a method which included a measure of texture through variations in intensity was tested successfully. This research presents a new method of classifying materials using multi-spectral laser scanning, a novel method for registering dissimilar point clouds from different scanners and an insight into the part played by laser speckle interpretation of reflected intensity.

Declaration

I declare that, except where cited in the text, all work contained within this thesis is my own original work, under the direction of my supervisor. This thesis has not been submitted to any institution other than the University of Nottingham for the degree of Doctor of Philosophy.

Hywel FJ Evans

University of Nottingham

July 2016

Dedication

This thesis is especially dedicated to my family and partner, their never ending love and support was always there and they helped me through some difficult times.

I would also like to thank my supervisor Dr. Martin Smith for his guidance and understanding.

Acknowledgements

The author would like to thank and acknowledge the following:

1. 3D Laser Mapping, Bingham, Notts, for the loan of the Riegl laser scanner.
2. Spectrum Aviation, Stamford, Lincs, for the use of a very powerful computer to process the very large point cloud data sets and classifiers. The recommended specification for a computer to replicate this work is: Dual Xeon 18 core, 128Gb ram, 2 x NVidia Titan graphics (SLI).

Copyrights

MATLAB, © 1994-2013 The MathWorks, Inc.

Cloud Compare V2, http://www.danielgm.net/cc, License: GNU,PL (General Public Licence), Version: 2.4.Qt/MSVC - 09/22/2012

Papers and Conference Proceedings

Presentation to Geo Business conference, 2015, London, Multi-spectral laser scanning.

Table of Contents

Chapter 1. Introduction 1

1.1 Building Information Modelling 2

1.2 Possible methods of data and information collection for BIM ... 6

1.3 Motivation for the Study 7

1.4 Aim of the Study 7

1.5 Research Objectives 7

1.6 Hypothesis 8

1.7 Methodology 8

1.8 Significance of the Research 9

1.9 Layout of Thesis 9

Chapter 2. Multispectral Remote Sensing and Classification Methods 11

2.1 Introduction 11

2.2 Multi-spectral Remote Sensing 12

2.3 Multi-spectral Laser Scanning 12

2.4 Production of 3D Models 14

2.5 Classification Methods 18

2.5.1 Algorithmic Approaches to Feature Classification 22

2.5.2 Knowledge Based Feature Extraction 23

2.5.3 Dealing with missing point data 24

2.5.4 Point Cloud Segmentation 25

2.5.5 Full Waveform Data 26

2.5.6 Correlation as a Basis for Classification..... 27

2.5.7 K-Nearest Neighbour Classification Method 30

2.5.8 Decision Tree..... 31

2.5.9 Discriminant Analysis..... 33

2.5.10 Support Vector Machine 34

2.5.11 Iterative Self-Organising Data Analysis Techniques (ISODATA) 36

2.5.12 Random Sample Consensus Iterative Algorithm (RANSAC) 37

2.5.13 Scale Invariant Feature Transform (SIFT) 38

2.5.14 Classifying LIDAR Waveform Data..... 39

2.5.15 Genetic Algorithms and Feature Classification 40

2.5.16 Biological Feature Recognition 41

2.6 Artificial Neural Networks 44

2.6.1 Design..... 46

2.6.2 Training..... 48

2.6.3 Network Types..... 49

2.6.4 Feed-forward 50

2.6.5 Self-organising Map..... 51

2.6.6 Radial Bias Function 51
2.6.7 Neural Network Classifiers 52
2.7 Summary 55
Chapter 3. Laser Scanners 58
3.1 Introduction 58
3.2 Types of Laser Scanner 59
3.2.1 Time of Flight 59
3.2.2 Phase Comparison 60
3.2.3 Scanner Detectors 61
3.2.4 Multi-spectral Laser Scanners 62
3.3 Reflected Intensity Characteristics 63
3.3.1 Intensity Correction 70
3.3.2 Surface Reflectivity 71
3.3.3 Multipath 72
3.3.4 Corners and Edges 72
3.3.5 Range and Incidence Angle Effect on Reflected Intensity 74
3.3.6 Retro-reflection 76
3.3.7 Laser Speckle 78
3.4 Analysis of Factors Affecting Reflected Intensity 82
3.4.1 Ambient Light 84
3.4.2 Range 85

3.4.3 Angle of Incidence 90

3.4.4 Intensity Normalisation – Idealised Test Case 91

3.4.5 Normalising Intensity for Range and Incidence Angle using Scan Point Density 97

3.4.6 Point Clouds 99

3.4.7 Difficult materials for laser scanning 100

3.4.8 Index Point Cloud 101

3.4.9 Effect of Range Error on Surface Normal Vectors 102

3.4.10 Reflection from Textured Surfaces 107

3.5 Registration methods 108

3.5.1 Rigid registration 111

3.5.2 Registration algorithms 111

3.5.3 Rigid 112

3.5.4 Semi-rigid 116

3.5.5 Non-rigid 116

3.5.6 Iterative closest point 117

3.6 Summary 117

Chapter 4. A New method for Classification of Construction Materials 120

4.1 Introduction 120

4.2 The Laser Scanners 121

4.2.1 FARO 3D 120 Intensity Values 124

4.2.2 Leica HDS3000 Intensity Values 125

4.2.3 Riegl VZ400 Intensity Values 125

4.3 Test Scan Sites 125

4.4 Scan Data Pre-processing 130

4.5 Intensity Ratios to Normalise for Incidence Angle and Range Variations 130

4.6 Registration 133

4.6.1 Multi-scanner point cloud registration 136

4.6.2 Finding a Unique Common Point 137

4.6.3 Scanner and Sphere Alignment 137

4.6.4 Calculating Registration Sphere Centres 138

4.6.5 Least squares fit of a sphere (CloudCompare) 139

4.6.6 Least squares fit of a sphere (unknown radius) 140

4.6.7 Minimalizing function of a sphere (known radius) 142

4.6.8 Artificial sphere point cloud 142

4.6.9 Error assessment of sphere centres 143

4.6.10 Inter-scanner sphere position error 146

4.6.11 Registration Sphere Position Error Correction 148

4.6.12 Pseudo traverse correction method 150

4.6.13 Bowditch compass rule 150

4.6.14 Transit Rule 151
4.6.15 Pseudo traverse correction method selection 151
4.6.16 Registration using the corrected sphere centres 152
4.6.17 Detection of angle and range error 152
4.6.18 Sphere position errors 153
4.7 Classifiers 154
4.7.1 Neural Network Classifier 156
4.7.2 Artificial Neural Network Approach 157
4.7.3 Design 158
4.7.4 Data 158
4.7.5 Training 159
4.7.6 Testing 159
4.8 Summary 160
Chapter 5. Results 163
5.1 Introduction 163
5.2 Intensity Ratio Validation 163
5.3 Class Separation 166
5.4 Site 1 Classification Results 167
5.4.1 Site 1 Classifier Results 169
5.4.2 Site 1 Classifier Results Analysis 173
5.4.3 Class 1 Wood 177

5.4.4 Class 2 Brick 178
5.4.5 Class 3 Steel 178
5.4.6 Class 4 Gravel 179
5.4.7 Class 5 Pavement 180
5.5 Site 2 Classification Results 181
5.5.1 Introduction 181
5.5.2 Site 2 Classification Results Discussion 183
5.6 Pseudo Texture 184
5.7 Summary 188
Chapter 6. Conclusions 191
6.1 Introduction 191
6.2 Objective 1 193
6.3 Objective 2 194
6.4 Objective 3 196
6.5 Objective 3 &4 197
6.6 Comparison with Current Research 199
6.7 Main Research Findings 200
6.8 Research Contributions 202
6.9 Suggestions for Research 202

Table of Tables

Table 1 BIM levels definitions (RIBA Enterprises Ltd (©2016) 3

Table 2 Beam divergence angles (mrad) and footprint (mm) for the FARO 120, Leica HDS3000 and Riegl scanners. 66

Table 3 Typical Reflectivity of Materials at 900nm wavelength (similar wavelength to the FARO scanner)..... 72

Table 4. Offset from base of scanner to optical centre, height from ground to top of tribrach (dHt)..... 127

Table 5 Residual sphere fitting error..... 134

Table 6 Residual registration errors..... 135

Table 7 Published scanner range error. 136

Table 8 Sphere position sources and associated errors (*estimated) 147

Table 9 Scanner laser beam diameter and point spacing with range at maximum resolution (min step angle). 148

Table 10 Comparison of linear precision due to angle and range. 152

Table 11 Classifier results for site 1..... 169

Table 12 Summary of ANN classifier results for site 1..... 171

Table 13 Training function and acronyms used in results table. 173

Table 14 Transfer functions and acronyms used in results table..... 173

Table 15 summary of classification rate by class. Number of neurons in hidden layer (#), ANN score threshold (Thr). 176

Table 16 ANN: classification rate, test data, per true class. 183

Table 17 Site 1ANN: classification rate, validation data, per true class. Pseudo texture trial..... 185

Table 18 Site 1ANN: classification rate, test data, per true class. Pseudo texture trial..... 185

Table 19 Classifier results for site 1. Validation data was an unused sub-set of the complete dataset..... 1

Table 20 ANN classifier results for site 1. Validation data was an unused sub-set of the complete dataset..... 2

Table 21 Complex decision tree: classification rate, site 1 test data..... 3

Table 22 Linear Discriminant: classification rate, site 1 test data. 5

Table 23 Quadratic Discriminant: classification rate, site 1test data..... 7

Table 24 Linear SVM: classification rate, site 1 test data. 9

Table 25 Quadratic SVM: classification rate, site 1 test data..... 11

Table 26 Gaussian SVM: classification rate, site 1 test data. 13

Table 27 KNN: classification rate, site 1 test data. 15

Table 28 Sub-space KNN: classification rate, site 1 test data. 17

Table 29 Weighted KNN: classification rate, site 1 test data. 19

Table 30 Weighted KNN: classification rate, test data, per true class, ratios 1 & 3. 21

Table 31 Weighted KNN: classification rate, test data, per true class, ratios 2 & 3. 23

Table 32 Weighted KNN: classification rate, test data, per true class. 25

Table 33 ANN classifier results 27

Table 34 Summary of classification rate by class. Number of neurons in hidden layer (#), ANN score threshold (Thr). 28

Table 35 Training function and acronyms used in results table. 29

Table 36 Transfer functions and acronyms used in results table. 29

Table 37 Artificial Neural Network classification rate, Scaled Conjugate Gradient, site 1 test data. 30

Table 38 Artificial Neural Network classification rate, Conjugate Gradient Powell/Beale Restarts, site 1 test data. 32

Table 39 Artificial Neural Network classification rate, Resilient backpropagation, 10 hidden layer neurons , site 1 test data. 34

Table 40 Artificial Neural Network classification rate, Resilient backpropagation, 5 hidden layer neurons, site 1 test data. 36

Table 41 Artificial Neural Network classification rate, Resilient backpropagation, 15 hidden layer neurons, site 1 test data. 38

Table 42 Artificial Neural Network classification rate, Resilient backpropagation, 2 hidden layers,10 neurons per hidden layer, site 1 test data. 40

Table 43 Artificial Neural Network classification rate, Resilient backpropagation, 1 hidden layers,10 neurons per hidden layer, Ratios 2 & 3, site 1 test data. 42

Table 44 Artificial Neural Network classification rate, Resilient backpropagation, 1 hidden layers,10 neurons per hidden layer, Ratios 1 & 2, site 1 test data. 44

Table 45 Artificial Neural Network classification rate, Resilient backpropagation, 1 hidden layers,10 neurons per hidden layer, Ratios 1 & 3, site 1 test data. 46

Table 46 Artificial Neural Network, Resilient backpropagation, 1 hidden layers,10 neurons per hidden layer, Ratios all, site 1 test data. 48

Table 47 Artificial Neural Network classification rate, Resilient backpropagation, 1 hidden layers,10 neurons per hidden layer, Ratios 1 & 3, threshold 0.5, site 1 test data. 50

Table of Figures

Figure 1 BIM levels, (BIM Industry Working Group (BIWG) 2011). 3

Figure 2 Correlation of Reflectance Wavelength 27

Figure 3 Result of K-means clustering with five clusters, the lines from the data points in each cluster intersect at the centroids (wikispaces.com). 29

Figure 4 Example of non-linear data. This dataset could be separated in a third dimension by a plane. (MatLab ©) 30

Figure 5 Spherical K-nearest neighbour classification of hyperspectral imagery. Nearest neighbour based on distance along surface of feature space projected onto a sphere rather than Euclidean distance, (Lunga and Ersoy 2011). 31

Figure 6 Fisher's discriminate for two classes; the differences between the class means in directions μ_1 and μ_2 is large in comparison to the variance about the means σ_1 and σ_2, (Bandos and Bruzzone 2009). ... 34

Figure 7 Linear SVM method two class example, hyperplane separates the classes and maximises the distance (gap) to the data points in both classes. The nearest data points to the hyperplane in each class are known as the support vectors (Statnikov et al. 2011). 35

Figure 8 Non-linear SVM classification example; maps the two dimensional input space to three dimensions using a kernel function (Statnikov et al. 2011) 35

Figure 9 Haralick texture features generated from the four co-occurrence matrices using the above directions of adjacency. 36

Figure 10 RANSAC Line Fitting Example 37

Figure 11 Object Recognition using the SIFT Algorithm (Lowe 2004) . 39

Figure 12 False Targets in Random Dot Arrays 44

Figure 13 Neural Network Architecture (MatLab ©)..... 46

Figure 14 Common ANN transfer functions. 48

Figure 15 The laser wavebands used in this research: Leica visible green, FARO near infra-red, Riegl mid infra-red. Chart curtesy of Optech © 2015. 62

Figure 16 Diffuse and Specular Refection 71

Figure 17 Range v Beam Diameter FARO 3D 120..... 73

Figure 18 Corner and Edge Range Errors..... 74

Figure 19 Corner and Edge Range Error..... 74

Figure 20 Plane test target for assessment of the effects of range and incidence angle on reflected intensity. 75

Figure 21 3D Corner Cube Retro-reflection..... 76

Figure 22 Ray traced to target including beam divergence and showing ‘ghost’ points [grey] caused by retro-reflection. 77

Figure 23 2D Retro-reflection 77

Figure 24 Double retro-reflection..... 78

Figure 25 Simulated laser speckle pattern (Welde 2010) 79

Figure 26 Distribution of reflected laser intensity from concrete blocks of different texture. (Vickers 2013)..... 81

Figure 27 Image (A) of concrete block 4mm roughness. 81

Figure 28 FARO^{120} scan of concrete block (A), range 10^{-3} m..... 81

Figure 29 FARO^{120} scanner intensity plot of block (A). Scale in laser scanner intensity DNs..... 82

Figure 30 Variation of reflected laser intensity with change in range and incidence angle on a sphere (FARO^{120}3D scanner, FARO registration sphere target) 83

Figure 31 Variation of laser reflected intensity with range, with ambient light and in darkness (FARO^{120}Focus 3D, white reference target)..... 84

Figure 32 Intensity v Range (FARO^{120} Focus 3D) using a black and a white target, the black target values were only measured to 3m range. 85

Figure 33 Comparison of calculated to actual range, FARO 120 scanner..... 87

Figure 34 Range error from calculated plane, FARO 120 scanner..... 88

Figure 35 Variation in Intensity across a plane. Data from FARO 120 scanner..... 89

Figure 36 Variation of range from scanner and intensity. The intensity values are inverted to visualise the correlation with range and chord. Data from FARO 120 scanner. 89

Figure 37 Variation of laser reflected intensity with incidence angle and target colour (FARO[120]Focus 3D). The intensity is normalised to the white target at zero incidence angle. 91

Figure 38 Normalised intensity for an ideal plane 92

Figure 39 Section of NGI lobby scan 93

Figure 40 Dot product of surface normals with primary axes 94

Figure 41 Histogram equalised IR image of wall 95

Figure 42 Re-scan of section of wall 96

Figure 43 Leica HD 3000 scan of wall 96

Figure 44 Laser reflected intensity (A) point cloud density (number of neighbours) (B) versus incidence angle of a plane. Right hand scale denotes DN values of intensity. 98

Figure 45 Point density / incidence angle. 99

Figure 46 Two buildings with glass which was not detected by the FARO 120 laser scanner. Image of buildings shown with the respective scans shown below. 101

Figure 47 Face Normals (green), Incident laser(red) 103

Figure 48 Artificial Plane Face Normals 103

Figure 49 Normal angle error due to range error 104

Figure 50 Face Normal to Sphere (Green) Incident Rays (Red) 105

Figure 51 CloudCompare (V2) Normals to Sphere 106

Figure 52 Vertex Normals 106

Figure 53 Vertex Normals (green) of Plane 107

Figure 54 Reflection from textured Surfaces 108

Figure 55 ICP registration using point to point matching, image (Bellekens et al. 2014)..... 115

Figure 56 ICP registration using point to surface matching, image (Low 2004). 116

Figure 57 FARO 3D 120, left, FARO © and Leica HDS3000, right, Leica ©. 121

Figure 58 Riegl VZ400, Riegl ©. 122

Figure 59 Workflow diagram of proposed method for materials classification. Based on a Simulink (Mathworks ©) model. This example shows the use of an Artificial Neural Network classifier; trials were also carried out using other classification methods..... 123

Figure 60 Position of scanners (black cross) and location of buildings for site 1 (blue) and 2 (red). 126

Figure 61 Point cloud of full FARO scan showing reference spheres and site positions. Both sites were scanned from the same position..... 128

Figure 62 Site 1 (Three of the five registration spheres are shown in green)..... 129

Figure 63 Site 2. 129

Figure 64 Training (red) and test (blue) data areas. 130

Figure 65 Residual sphere fit error, least squares method with radius unknown. Histogram shows mean [green], 1 std dev red]. Top shows initial fit and bottom shows fit with residuals >0.002m removed. 141

Figure 66 Artificial sphere point cloud [red] of defined radius (0.0725m) aligned to registration sphere point cloud [blue], then fitted with a sphere mesh [grey]. 143

Figure 67 Residual error, in each scan, between each method of calculating sphere centres. 144

Figure 68 FARO scanner sphere radius residual error (m), where the method has estimated the radius. Artificial sphere method residuals <5 x 10^{-7}m 145

Figure 69 Leica scanner sphere radius residual error (m), where the method has estimated the radius. Artificial sphere method residuals <1 x 10^{-6}m 145

Figure 70 Riegl scanner sphere radius residual error (m), where the method has estimated the radius. Artificial sphere method residuals <2 x 10^{-6}m 146

Figure 71 Residual sphere centre position errors (Uncorrected), Faro scanner reference system. 153

Figure 72 Residual sphere centre position errors (Transit rule correction), Faro scanner reference system. 154

Figure 73 Residual sphere centre position errors (Bowditch correction), Faro scanner reference system. 154

Figure 74 MATLAB Neural network design: w=weight, b=bias, activation function denoted by the rectangle and sum. 158

Figure 75 Sphere: Intensity ratios versus incidence angle (degs) @6.2 m: (FARO/Riegl [green], Leica/Riegl [red], FARO/Leica [blue]). Outer axis is incidence angle in degrees. 164

Figure 76 Sphere: Intensity ratios versus range (6.23m, 10.31m, 14.91m, 17.13m) FARO/Riegl [green], Leica/Riegl [red], FARO/Leica [blue]. Outer axis is range in metres. 164

Figure 77 Variation of intensity across the surface of a registration sphere (FARO Flexi), single wavelength NIR, using the FARO scanner. 165

Figure 78 Constant intensity ratio variation across the surface of a registration sphere (FFARO Flexi), two wavelengths NIR and green, FARO and Leica scanners respectively. 166

Figure 79 Ratios of intensity shown from a registration sphere and the mounting pillar. The pillar is polished steel, a specular reflector. 166

Figure 80 A plot of intensity ratios for each class at 1550nm, 905nm and 510nm wavelengths, ... 167

Figure 81 Site 1 reference point cloud. The reference cloud was manually created within CloudCompare ©. 168

Figure 82 Log Sigmoid transfer function definition. 172

Figure 83 ANN classifier result as false colour image. Some areas of the scan are in shadow from vegetation. 177

Figure 84 Classifier 21 classification rate as false colour. 178

Figure 85 Histogram of ANN classifier scores for network 23, score threshold 0.5. 179

Figure 86 Site 2 Reference Cloud. 182

Figure 87 Site 2 ANN classified point cloud 182

Figure 88 Site 1 ANN classified point cloud, pseudo texture trial 186

Figure 89 Site 1 ANN classified point cloud, score histogram, pseudo texture trial. 186

Figure 90 Complex decision tree: classification rate created as a false colour point cloud. 4

Figure 91 Linear Discriminant: classification rate created as a false colour point cloud. 6

Figure 92 Quadratic Discriminant: classification rate created as a false colour point cloud. 8

Figure 93 Linear SVM: classification rate created as a false colour point cloud. 10

Figure 94 Quadratic SVM: classification rate created as a false colour point cloud. 12

Figure 95 Gaussian SVM: classification rate created as a false colour point cloud. 14

Figure 96 KNN: classification rate created as a false colour point cloud. 16

Figure 97 Sub-space KNN: classification rate created as a false colour point cloud. 18

Figure 98 Weighted KNN: classification rate created as a false colour point cloud. 20

Figure 99 Weighted KNN: classification rate created as a false colour point cloud, ratios 1 & 3. 22

Figure 100 Weighted KNN: classification rate created as a false colour point cloud, ratios 2 & 3. 24

Figure 101 Weighted KNN: classification rate created as a false colour point cloud, ... 26

Figure 102 (Network #13) Network classification rate, false colour point cloud. 31

Figure 103 (Network #14) Network classification rate, false colour point cloud. 33

Figure 104 (Network #15) Network classification rate, false colour point cloud. 35

Figure 105 (Network #16) Network classification rate, false colour point cloud. 37

Figure 106 (Network #17) Network classification rate, false colour point cloud. 39

Figure 107 (Network #18) Network classification rate, false colour point cloud. 41

Figure 108 (Network #19) Network classification rate, false colour point cloud 43

Figure 109 (Network #20) Network classification rate, false colour point cloud 45

Figure 110 (Network #21) Network classification rate, false colour point cloud 47

Figure 111 (Network #22) Network classification rate, false colour point cloud 49

Figure 112 (Network #23) Network classification rate, false colour point cloud 51

List of Appendices

A. Full classification results.

B. MatLab programs.

C. Scanner specifications.

D. Neural network definitions.

Chapter 1. Introduction

Building Information Modelling (BIM) is the process of generating and managing project information throughout the whole lifecycle of the infrastructure through the use of a building information model. The UK Government made a commitment in 2012 that required fully collaborative BIM on all centrally funded construction projects by 2016 (Cabinet Office 2012). The proposal relies heavily on the use of digital 3D building models; this government strategy, which was adopted in April 2016, will drive a need for more automated production of these building models. This information management concept has already been a in several major infrastructure and building projects, including High Speed rail link two (Mace Ltd 2013), Royal Arsenal Woolwich (over station development blocks, 345 residential units across three towers, for detailed planning through to construction) (GVA 2014), Manchester city library redevelopment (Royal Institute of Charted Surveyors 2015) and London residential development (PRP Architects LLP 2016). The advent of terrestrial laser scanning introduced a very rapid survey method, especially suited to ‘as built’ requirements. Creation of information models initially used modified computer aided design software; recently software companies have begun to focus on specific tools for data collection, measurement and data-processing aimed at BIM. Current infrastructure and building design software, such

as Revit[1], can extract complex features from a point cloud, the more complex task of classification has been well established in imagery but the use of laser scanner point cloud intensity data has been slow in development. Some early use of laser scanner intensity data was by Abmayr et al. (2005), in the field of cultural heritage and civil engineering. Current industry and research feature extraction tools have developed from tools used in photogrammetry and image processing. BIM has provided the practical application area for the motivation to this research although it has potential for wider areas of interest including agriculture and land use classification.

1.1 Building Information Modelling

The original Government paper on Building Information Modelling (BIM) (HM Government Cabinet Office 2011) stated:

'*A lack of compatible systems, standards and protocols, and the differing requirements of clients and lead designers, have inhibited widespread adoption of a technology which has the capacity to ensure that all team members are working from the same data, and that: the implications of alternative design proposals can be evaluated with comparative ease; projects are modelled in three dimensions'*.

This paper started the process for developing a pathway to implement the BIM concept, the levels are defined in Table 1 and Figure 1.

[1] Autodesk ©2016

Table 1 BIM levels definitions (RIBA Enterprises Ltd (©2016)

Level 0 BIM
In its simplest form, level 0 effectively means no collaboration. 2D CAD drafting only is utilised, mainly for Production Information (RIBA Plan of Work 2013 stage 4). Output and distribution is via paper or electronic prints, or a mixture of both.
Level 1 BIM
This typically comprises a mixture of 3D CAD for concept work, and 2D for drafting of statutory approval documentation and Production Information. CAD standards are managed to BS 1192:2007, and electronic sharing of data is carried out from a common data environment (CDE), often managed by the contractor.
Level 2 BIM
This is distinguished by collaborative working – all parties use their own 3D CAD models, but not necessarily working on a single, shared model. The collaboration comes in the form of how the information is exchanged between different parties – and is the crucial aspect of this level. Design information is shared through a common file format, which enables any organisation to be able to combine that data with their own in order to make a federated BIM model.
Level 3 BIM
Currently seen as the holy grail, this represents full collaboration between all disciplines by means of using a single, shared project model which is held in a centralized repository. All parties can access and modify that same model, and the benefit is that it removes the final layer of risk for conflicting information. This is known as 'Open BIM'.

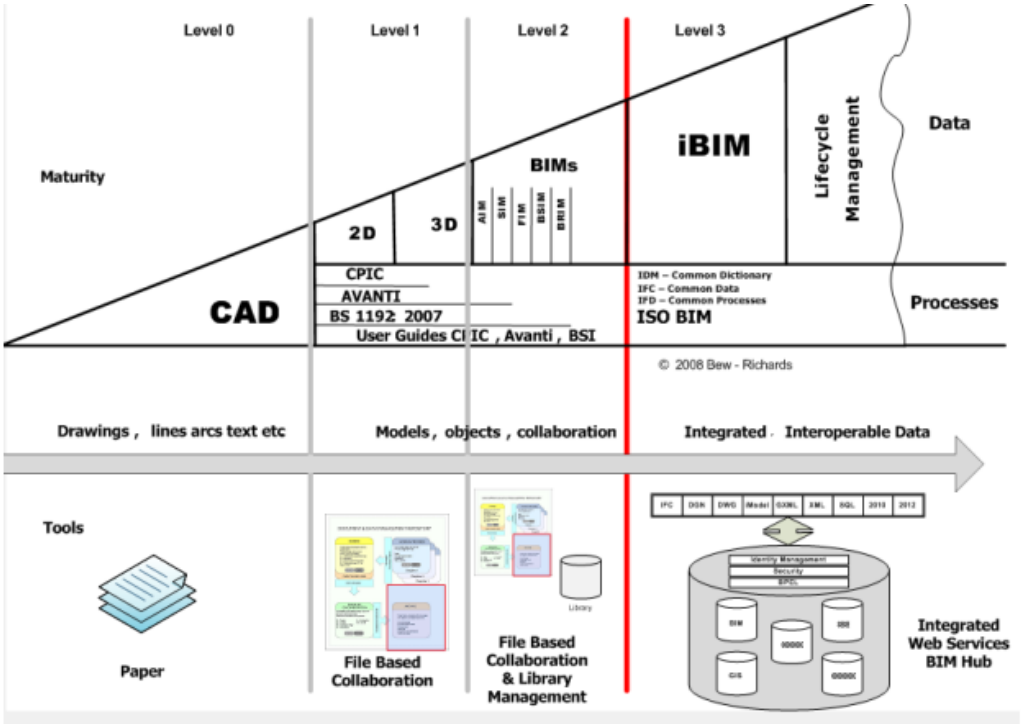


Figure 1 BIM levels, (BIM Industry Working Group (BIWG) 2011).

BIM is the process of generating and managing project information throughout the whole lifecycle of the infrastructure - UK Government BIM construction strategy stated that all public capital projects would be carried out to Level 2 BIM by 2015, level 3 by 2016. Since the white paper the implementation, problems and future of BIM has been studied by serval groups including, (Azhar et al. 2012; Miettinen and Paavola 2014; Becerik-gerber et al. 2010). Future needs for automation of BIM processes, especially for existing buildings where the construction materials are unknown has been studied (Volk et al. 2014).

The government strategy for BIM will require 3D digital drawings which will drive a need for automated production of digital 3D building models. Terrestrial Laser Scanning (TLS) is in widespread use for land and building survey, especially in the post construction and life maintenance phases. TLS is particularly well suited to survey of complex non-rectangular buildings or infra-structure. Creation of a BIM is currently by use of modified Computer Aided Design (CAD) software containing data attribute tables linked to the structure, measurement and data-processing tools. There is a major R&D challenge to create software that supports acquisition and processing of the laser point cloud data for creating BIMs dimensional levels (Lemmens 2011). BIM not only requires the measurements of a building or infra-structure but also information about each component within the construction. BIM databases potentially require very large datasets of a building characteristics including the geometry and the construction materials, very little of this data gathering is currently automated which is not cost

effective. The motivation for automating the process of transferring point cloud data to a 3D model is based on the very time consuming manual alternative.

The main body of previous research into 3D modelling using Laser scanner point cloud data has focused on feature extraction and has depended on techniques that use segmentation of the point cloud into planar surfaces and the application of constraints to classify each segment (Chengyi and Zhongming 2006; Gumhold et al. 2001; Daniels et al. 2007; Zhang et al. 2005). Segmentation methods have had difficulty with features that are defined by only a small number of points such as windows, as only the frame can be used as the glass is transparent to laser light. Knowledge based methods which use constraints in a decision tree structure have been attempted (Xu et al. 2012); unfortunately, these have required a large number of rules to define a feature, especially complex non-linear features. The best image-interpretation system is a combination of our eyes and our brain. Learning (supervised) and self-learning (un-supervised) methods used with artificial neural networks have been shown to be powerful pattern recognition system. Artificial neural networks have been used for classification in remote sensing but they have been restricted to 2D data although some work has been done in 3D (Baligh Jahromi et al. 2011); the aim of this research is to extend this to 3D, more specifically 3D point clouds. The main effort of this research was to develop techniques and workflows that extract and use the spectral information

from laser scanner point cloud data for classification of construction materials.

1.2 Possible methods of data and information collection for BIM

A suitable method for producing data for a BIM database must produce the measurement of spatial and material classification data. This would be most efficient if it was achieved by a technique that provided spatial measurement and spectral data of the structure concurrently; the material type might then be deduced from the data. Classification techniques have used sensors such as:

1. Aerial cameras (Bekkari et al. 2013).
2. Aerial cameras and satellite imagery (Varga et al. 2014).
3. Laser scanner (Yan et al. 2015), (Guo et al. 2015).
4. Imagery and LiDAR (Buján et al. 2012).
5. SAR (Ban and Wu 2005).
6. Sonar (Lucieer 2008).

Stereo photogrammetry, whether by multiple cameras or by motion, have provided the spatial data by an indirect method. SONAR, although not electromagnetic, provides pseudo spectral data related to the absorption and reflection of sound which might be used for classification of the reflecting objects. In order to collect multi-spectral data for BIM classification, existing sensors were considered; some of the capabilities required considered were:

1. Measurement
    a. Speed
    b. Precision
2. Max range
    a. Interior, 50m.
    b. Exterior, 5000m.
    c. Aerial, 3000m.
    d. 1m – 1000m.
3. Spectral characteristics

    a. Multi/hyper spectral in order to automate classification.
    b. Unaffected by lighting conditions.
    c. Repeatability of results.
    d. Control of illumination of target.
4. Processing
    a. Creation of 3D models.
    b. Provide input to BIM database.
    c. Create 3D model of homogeneous scenes (structures often have very similar and homogeneous areas which would confound automatic point tie point matching algorithms in photogrammetry.
    d. Speed of processing (laser scanning outputs the 3D model, photogrammetry requires considerable post processing)
5. Portability
    a. Man portable or suitable for vehicle or aerial use.

1.3 Motivation for the Study

To develop an automatic method of populating BIM databases with both spatial (3D) and related materials data.

1.4 Aim of the Study

The aim of this research is to extend the application of Laser scanners to classify man-made and natural materials by using multi-spectral intensity data, which could automate some BIM processes.

1.5 Research Objectives

The main objectives of this research were:

1. To investigate multispectral remote sensing and classification methods.
2. To investigate laser scanning intensity values and potential use of multi-spectral scanners for material classification.
3. To propose and develop an approach using multi-spectral laser scanner data for material classification.

4. To undertake trials to validate the development and implementation of the proposed method.

1.6 Hypothesis

Laser scanner multi-spectral and spatial data can represent the physical composition of materials. Using suitable classification methods materials can be classified by their spectral and spatial signature. The use of spatial information provides a filtering attribute where materials have similar spectral signatures.

1.7 Methodology

The research followed the following methodology:

1. Undertake a review of multispectral remote sensing, classification methods and laser scanners (objective 1).
2. Practical trials to understand laser scanner intensity data (objective 2).
3. Proposed method (objective 3).
4. Implement method through MatLab and other software tools (objective 3).
5. Undertake trials to assess the capabilities and potential of multi-spectral approach by using a test site (objective 4)
6. Validate transferability of method using a second test site (objective 4).

1.8 Significance of the Research

The work investigates classification of both geometric and spectral aspects of the point cloud data. The novel multi-spectral laser scanning technique presented in this thesis solves and improves on a number of existing applications by offering:

1. Collection of multi-spectral data using multiple laser scanners.
2. Multi-spectral laser scan data classification using a range of classifiers including neural networks.
3. Range and incidence angle normalisation using ratios of intensity.
4. Multi-spectral classification which includes pseudo texture as an attribute with intensity ratios.
5. Investigation into the variation of scanner spectral data due to laser speckle effects generated by surface texture.
6. Investigation of registration methods for dissimilar scanner data.

1.9 Layout of Thesis

The thesis begins with a section that lays out the motivation, aim and objectives of the research. Next a review of multispectral remote sensing and classification methods is presented, (objective 1). This is followed by a background to laser scanners and review and practical trials intended to improve understanding of laser scanning spatial and spectral data, (objective 2). The proposed new method of classification of construction materials is described in Chapter 4, (objective 3). The results of investigating the proposed method on real world data and

analysis of the results is presented in Chapter 5 (objective 4). Finally, Chapter 6 summarises and presents conclusions from the research and suggestions for future research.

Chapter 2. Multispectral Remote Sensing and Classification Methods

2.1 Introduction

The classification of the Earth and its features has used instruments ranging from cameras, radar and sonar to multi-spectral space-based scanners. For successful classification, measureable attributes unique to the material under classification are required; these could be waveform shape (radar), colour (photography) or reflected intensity in the case of laser scanning and optical reflectance. Initially the reflected intensity from commercial laser scanners had no intended use, but it has been shown that intensity could be calibrated (Wagner et al. 2008; Kaasalainen et al. 2009; Kaasalainen et al. 2011; Ahokas et al. 2006) making object classification possible.

This chapter will discuss multispectral remote sensing and classification methods. First, the chapter presents and overview of multispectral remote sensing and laser scanning, leading onto production of 3D models and their requirements. The pros and cons of using remote sensing that uses ambient and active light sources are also discussed. The chapter moves on to review currently available classification methods that may be applicable to multispectral data; including discriminant analysis, support vector machines and artificial neural networks.

2.2 Multi-spectral Remote Sensing

The use of passive illumination introduces variation within a single image and across sets of images to be used in the classification process as the direction and radiometric qualities of the illumination may be unknown. Radiometric correction is therefore required prior to classification (Pozo et al. 2014). Many scanners include a passive sensor (digital camera); a multi-spectral classification method using red, green and blue (RGB) passive sensor data and the laser intensity was implemented by Lichti (2005). The use of passive sensor data introduced classification errors which were attributed to non-uniform solar illumination. Multi- spectral imagery in conjunction with LiDAR intensity data has been used to improve roof outline extraction (Awrangjeb et al. 2013) and solar illuminated data was also gathered for comparison laser illuminated data of the same areas.

2.3 Multi-spectral Laser Scanning

Pfennigbauer and Ullrich (2011) investigated the use of multi-wavelength airborne laser scanning, selecting optimal wavelengths for the scanned topography. They also proposed that using several wavelengths within the same scan could retrieve additional information for crop analysis or tree species detection. A dual wavelength test instrument has been developed by Gaulton et al. (2013) for estimating vegetation moisture content. Near and mid infra-red wavelengths (1063 nm and 1545 nm) were chosen to separate wood from foliage. Three TLS, with three different laser wavelengths, were used by Hartzell et al. (2014) to extract spectral signatures of different rock types. Their

method only corrected intensity value for range, using calibration panels with known reflectance, rather than ratios of intensity used in this work which compensate for range and incidence angle. Using ratios of wavelengths has benefit in that it requires no prior calibration, the incidence angle does not need to be known and the calculated values work for all ranges and do not require interpolation. As their scanners' optical centres were not co-located there would have been some error in the final combined intensity values in the final multi-spectral point cloud.

In addition to multi-spectral dual band TLS, hyper-spectral TLS have been developed for classification tasks (Hakala et al. 2012); this scanner was also able to record the full waveform of the return pulse. Hyper-spectral scanners are able to take advantage of the broadband output of super continuum lasers, providing a spectral range of 480-2200 nm[2]. Classification using multi/hyper-spectral scan data assumes that a material's surface reflectivity has a definable spectral signature; ideally this would be unique but in the real world there will be some degree of overlap. Selection of certain wavelengths, with prior knowledge of the target materials, can optimise classification (Hakala et al. 2012).

[2] NKT Photonics, SuperK

2.4 Production of 3D Models

At the centre of BIM is the production of 3D models, the main method of production of 3D models prior to the advent of automated photogrammetry was stereo imagery. Stereo photogrammetry was used to produce 3D models of urban areas, Digital Terrain Models (DEM) and Digital Surface Models (DSM) and has been shown to be as accurate as laser scanning (Mills and Barber 2004). Automated photogrammetry has become a primary tool for topographic modelling (Remondino and El-Hakim 2006). The main automated method now adopted uses Structure from Motion (SfM), which uses the same concept as stereo photogrammetry that 3D structure can be resolved from overlapping images. SfM uses multiple images from a moving camera as opposed to two cameras in the stereo method (Westoby et al. 2012). Laser scanning though has some advantages over photogrammetry in the production of 3D data:

1. Model can be generated from a single location.
2. Most scanners directly output a 3D point cloud.
3. It can provide a persistent, near real time, rapid measurement of a changing environment using multiple scans.
4. It can provide a near real-time feedback of a structure's 3D position, similar to Radar or Sonar.
5. The point cloud data 3D can be output georeferenced if the scanners position is known.
6. It is independent of ambient light conditions.
7. There are no processing errors due to shadows.

8. It has no dependence on scene surface homogeneity, tie point matching in automated photogrammetry can be impossible in homogeneous areas of a scene.
9. It is less affected than photogrammetry by land cover, especially full waveform or multi-pulse systems, in the production of DTM.
10. With suitable choice of wavelength 3D bathymetric models can be produced and with suitable wavelengths the surface and bottom can be measured enabling measurement of volume.

Some areas of weakness in Laser scanning include:

1. The single wavelength can restrict the detection and measurement of objects which have low or no reflectivity at that wavelength.
2. Highly reflective objects can generate stray and drop out of points.
3. Narrow features may be difficult to detect due to the generally smaller point density than imagery. This can be mitigated by the design of the scan pattern.
4. Range precision can be reduced by highly reflective surfaces.

Laser scanning was chosen as the method most suitable for collecting spatial and spectral data for this work, after considering the foregoing arguments. Most laser scanners can colour the scan points with image data from an on-board or integrate camera, this could also be used to provide the spectral data for the classification of the scan points. However, using the laser reflected intensity could also provide spectral data, especially if the laser scanner was multi-spectral.

Stereo image processing, in photogrammetry, normally refers to the process of extracting 3D information from 2D images. The process involves measuring the disparity between adjacent images of a scene that have an overlapping region; the disparity will be proportional to the depth/height at each point. Wang & Hsiao (1999) suggested that extracting 3D information from moving objects was a better choice than Laser scanning and used this as a reason to implement disparity matching of images for stereo vision. In their implementation of disparity matching they used two neural networks; a Back-propagation network (BP) was used to create a primitive disparity map and a self-organising network was used to cluster pixels with similar characteristics. The clustering process reduced the search space and the number of un-matched or miss-matched pixels. The BP network was trained on one of the stereo image pairs; it had 7x7x3 input neurons, 50 hidden neurons and 1 output neuron. The input was derived from 7x7 regions of pixels within the image, in recognition that intensity values were dependent on illumination, three input values for each pixel were calculated: intensity, variation and orientation. In practice the variation and orientation were calculated by using a Sobel operator (Sobel 1978), which gives good approximations (Gonzalez and Woods 1992). The input to the BP network was the difference of the three features (intensity, variation and orientation) between the stereo pair of images; this created a 7x7x3 (147) input vector. Using these differences, the BP network was image independent; trained on one stereo pair of images it can be used to match any other pair.

After training the BP network classified the pixel within matching clusters in the two images; the clusters were determined by the self-organising neural network prior to this stage. Some constraints were used to even further reduce the search space: epipolar line, geometric, ordering and continuity. Matching pixels should be located on the same epipolar line; however, this only works if the axes of the images are aligned. For parallel stereo images objects at infinity will have zero disparity; this can be used as a geometric constraint. The ordering of the pixels should be the same in both images of the pair. The continuity constraint is related to depth (disparity) constancy theory developed by Marr & Poggio (1976).

The clustering process was carried out by a Vitality Conservation (VC) neural network (Wang and Hsiao 1997), this was a self-designing, self-organising network. It differed from other self-organising networks (Kohonen 1989) in that it that generated new nodes during the training process. The network was trained on one of the stereo pair before being used to cluster both images. During the matching phase by the BP network candidates are only matched between matching clusters in the two images. To visualise the results a 3D mesh was created from the disparity map of a test image and this was then constructed as a 3D model.

The use of vertical (depth) disparity to improve the match between images was employed by Yang et al. (2010) in their work on neural network based stereo robot vision. Their assumption was that correct matched pairs of points would have similar vertical disparity. This

technique must rely on initial estimate of registration between the images to extract depth information; iteration was then used to refine the registration and the vertical disparity. The iteration process using a point cloud should not be required as the vertical information is available directly from the 3D position of each point.

There may be some advantage in using the rotation and scale invariance of the Scale Invariant Feature Transform (SIFT) (Lowe 2004) algorithm in conjunction with neural network stereo image disparity matching.

2.5 Classification Methods

Laser scanning has provided an instrument that can create rapid 3D surveys. The first laser scanners came into commercial use after 1985. Development has progressed quickly and now laser scanners are in common use for tasks including survey, deformation monitoring (Monserrat and Crosetto 2008), change detection (Alba et al. 2009), digital terrain models (DEMs) (Guarnieri et al. 2009) and cultural heritage (Grussenmeyer et al. 2008).

The main categories of laser scanners in production include terrestrial, airborne and mobile; this research uses terrestrial laser scanners (TLS). Most TLS output Cartesian coordinates and a measure of reflected laser intensity; some also provide the full waveform of the reflected pulse.

Automated classification of objects and materials using laser scan data has been a goal since the first laser scanners were commercially

available. Research on classification has been diverse including areas such as urban, land use and forestry. Urban classification methods have included automated extraction of building features using segmentation techniques (Pu and Vosselman 2006) and plane growing and Gaussian sphere surface normal clustering (Loncharich et al. 1992); this was developed further to identify clusters of normals representing shape primitives (Wang et al. 2013). Land use classification has included vegetation mapping (Ducic et al. 2006) and forestry classification measurement of vegetation moisture content (Were: et al. 2013). Choice of specific laser wavelength, in relation to specific materials, may improve classification accuracy. Materials reflect or absorb at certain wavelengths, providing a spectral signature; some may absorb so strongly that the scanner is unable to detect a surface. Ice can appear invisible to scanners that operate from mid to far infra-red wavelengths (Wehr and Lohr 1999). The effect on scanner range accuracy caused by reflection from different colour materials was investigated by Clark and Robson (2004), they were able to improve the range accuracy by applying corrections for the type and colour of the surface material. A common limitation of laser scanners is the poor results from scans of specular reflective surfaces or dark reflectors due to the low energy of the return signal; this seems to especially effect the lower power phase based scanners. Their work demonstrated that range differences of up to 11mm were possible between a neutral grey and a black surface, especially at close range. During this research the reflected intensity from a homogeneous white surface showed a non-

linear relationship to range; further investigation of the scanner design revealed an auto-gain control on the receiving optics to prevent sensor saturation at close range. The effects on measurements caused by different object materials, with a specific focus on common building façade materials was further developed by (Voegtle and Wakaluk 2009). The scanner in their test was the Leica HDS6000 which has a red laser; the results of intensity measurements from different building materials was consistent with relationship between the colour of the material and the laser wavelength. These perceived disadvantages of changes in material colour could be an advantage in classification methods.

Laser scanning provides controlled, active illumination, reducing the need for correction required in passive sensor data. Multi-temporal scene analysis using passive senor reflectivity data requires correction for variations in illumination, primarily the solar zenith angle (Conghe Song and Woodcock 2003). Nitzan et al. (1977) proposed the use of registered reflectance and range data for scene analysis, using an experimental laser scanner. Classification methods were also developed for laser altimetry data, a fusion of object geometry and surface reflectivity was exploited by Hug and Wehr (1997). Land use classification has been carried out using laser scanner reflectance data, often in conjunction with imagery (Tymkow and Borkowski 2002); forested areas have provided significant challenges to this method (Hofle and Pfeifer 2007). Single wavelength laser reflectance data has been used for surface material type classification of wood, concrete and

other building materials (Kirchner et al. 2007). A combination of height and reflectance in LiDAR data was implemented by Li et al. (2008) and Antonarakis et al. (2008) to improve classification accuracy.

The use of passive illumination introduces many complications in the classification process as the source and direction of the illumination may be unknown or difficult to calculate. Many scanners include a passive sensor (digital camera); a multi-spectral classification method using red, green and blue (RGB) passive sensor data and the laser intensity was implemented by Lichti (2005). The use of passive sensor data introduced classification errors which were attributed to non-uniform solar illumination. Multi- spectral imagery in conjunction with LiDAR intensity data has been used to improve roof outline extraction (Awrangjeb et al. 2013). Solar illuminated data was also gathered for comparison laser illuminated data of the same areas.

Many different classification methods have been used with multi-spectral data, both statistical and others including artificial neural networks (Zhou and Yang 2004; Kavzoglu and Mather 2003; Bischof et al. 1992). There are similarities between classification of laser scanner intensity data and remotely sensed image data and some use a fusion of passive and actively sensed data (Lichti 2005). Often a novel classifier is used which combines existing techniques such as the Spectral Correlation Mapper (SCM) and a region growing algorithm (Suomalainen et al. 2011); the SCM compares the similarity of two spectra. Of the many classification methods, the Maximum Likelihood Classifier (MLC) is possibly the most established approach. MLC

assumes a normal Gaussian data distribution of multivariate data (Mather 2004). Artificial neural networks (ANN) are a non-parametric classification technique which does not depend on normally distributed data, unlike MLC, ANNs can classify data often found in land use and urban remotely sensed data that are multi-mode or not linearly separable in the original spectral space (Szuster et al. 2011). A detailed comparison between MLC and ANN classification methods was carried out by Paola and Schowengerdt (1995) and Erbek et al. (2004).

Application of laser reflected intensity has been used mainly for land use and forest classification (Song et al. 2002; Puttonen et al. 2010; Li et al. 2008; Shaker and Nagwa 2012) and fusing imagery and intensity (Guan et al. 2013; Buján et al. 2012; Liu et al. 2011).

2.5.1 Algorithmic Approaches to Feature Classification

Much research has been done in extracting building features from laser point clouds using both airborne and terrestrial scanners. It has been found that extracting features that are part of a building's façade is difficult using airborne point cloud data because of the oblique aspect of acquisition; as a result researchers have turned to terrestrial scanned data to provide the required level of detail (Pu & Vosselman 2007). Research into feature extraction techniques dates back to the introduction of the first laser scanners, airborne laser scan data was in the forefront as it followed easily in the footsteps of analysis of airborne imagery; which dates back to balloon photographic reconnaissance during the First World War.

It is not surprising that the initial feature extraction techniques that were investigated used methods that had been tried and tested in imagery. Edge based approaches (Gross and Thoennessen 2006), (Wani and Arabnia 2003) and (Sotoodeh 2006) were used to fit lines to boundary points. A step on from edge based methods was local surface properties which cluster points that are spatially similar. The surfaces were either planar (Dold and Brenner 2006), (Biosca and Lerma 2008) and (Schmitt and Vögtle 2009) or solids such as spheres, cylinders or cones (Wahl and Klein 2006) and (Ogundana et al. 2007); Ogundana et al. (2007) used a novel 3D extension of the Hough transform. Once geometric shapes can be extracted higher level features can be derived by segmentation of the data so that points belonging to the planes are grouped together; Segmentation was defined by (Wani and Arabnia 2003) to be 'a process of dividing an image into a number of meaningful regions'. Each segment is compared with different building feature constraints to determine to which feature the segment belongs.

2.5.2 Knowledge Based Feature Extraction

Humans identify building features by knowledge of the characteristics and context of the features. Attempts to mimic this knowledge based method of feature extraction have often depended on the use of constraints and a set of logic functions to filter individual features (Pu and Vosselman 2006). This method requires prior knowledge to be programmed into the software; this is not a self-learning method. Constraints such as: size, position, direction, topology and point density; point density can be thought of as the area of the features in

points. The method firstly segments the point cloud into planar surfaces and lines, this is followed by a recognition phase which filters each segment by the defined constraints. A convex hull was created for each segment and the constraints derived from the convex hull geometry; size from its area, position from its geometric centre and direction by its normal. This method relied on using a region growing algorithm to create the planar surfaces; the accuracy of the definition of the surface was directly proportional to the size i.e. number of points.
Unfortunately, window frames are small in comparison to other planar features such as walls and doors; this resulted in partially segmented areas which contained windows. As the laser penetrates though glass a window can only be detected by the lack of points (hole) or by its frame. Higher resolution scans may provide a path to overcome the difficulties found with window frames.

2.5.3 Dealing with missing point data

Holes in the point cloud have been used to assist in the extraction of windows (Pu and Vosselman 2007), this was achieved by discarding the holes created by doors or extrusions. Window frames, due to their dimensions, may only be represented by a few points in a laser point cloud of a building façade. Also if the window is not covered the laser penetrates through the glass recording no points on the glass surface; some data points may exist at a greater range due to reflection from objects within the room. The frame may only be set back from the wall by a few centimetres causing difficulty in discrimination of the frame depending on the scanner’s range resolution. Pu & Vosselman's (2007)

method of window extraction by hole detection required the point cloud to be converted to a Triangulated Irregular Network (TIN); both interior and exterior boundary points are extracted from the end points of long edges within the TIN (this is achieved by noting the number of neighbouring triangles, three represents an interior boundary). Although this method did produce results, it sometimes extracted windows that did not exist in reality often caused by the lack of discrimination between building extrusions and window frame recesses. This method did not address the issues of accuracy; edges and thence lines are difficult to measure accurately in point clouds because of the orientation of the edge and the scan path. Another issue with this method was that it could not discriminate between real holes in the building and windows. The authors proposed to resolve some of these issues by incorporating imagery of building in the analysis of the point cloud data.

2.5.4 Point Cloud Segmentation

The geometry of man-made objects is often assumed incorrectly as consisting of planar surfaces; certainly most of the classification methods so far implemented commercially and in research have adopted this premise. The world of modern architecture is rapidly changing the planar world that existed previously. Extraction of planar surfaces still has its place though in surveying the more conventional and historic buildings, this assumption had also been used in the past to discriminate between buildings and the underlying terrain. The assumption was that terrain was smooth and buildings were planar in

nature (Vosselman et al. 2004). The algorithms used were based on those used for image segmentation; the method would start with a finding neighbouring points that had the same surface characteristics and proceeding until no further matches were found. This method was used as a region growing algorithm by Ballard & Brown (1982) and later Vosselman & Maas (2010). The 3D Hough transform and the RANSAC processes have been used in images and point cloud plane segmentation. In reconstructing building outlines large scale map data is often used to complete the process. Mobile laser scanning data has also been used to extract building features, especially facades (Rutzinger et al. 2009), again they use segmentation as a method of extraction of the planar features in the point cloud.

Window frames, blinds and curtains are usually only a few centimetres behind the plane of the wall but they have been successfully differentiated by segmentation of the individual planes (Pu and Vosselman 2009). Fine segmentation can also be useful in differentiating objects that are in the room behind a window that have been recorded in the point cloud due to the glass being transparent to some laser wavelengths. If the beam encounters a reflective glass surface within the room the objects will appear rotated or inverted in the final data.

2.5.5 Full Waveform Data

Segmentation techniques have been used for both airborne and terrestrial laser scanned data; airborne systems use predominantly

pulse (time of flight) laser scanners due to the large range requirement; some of these systems can record the full waveform of the return and this extra information can enhance the discrimination of a segmentation process (Rutzinger et al. 2008).

2.5.6 Correlation as a Basis for Classification

One of the simplest methods of separating classes of features is geometrical; in 2D this requires two measurable attributes within the plotted on the two axis of a chart. If there is any correlation between these attributes distinctive clusters will form, an example is shown in Figure 2.

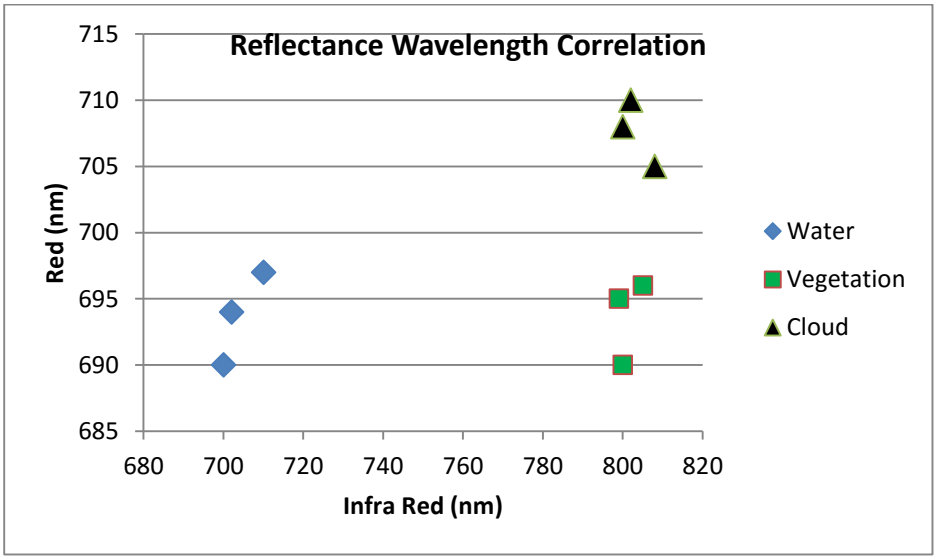


Figure 2 Correlation of Reflectance Wavelength

This method can be extended to n-dimensions. A cluster can be defined by measurements of the geometry which may include distance between points or shape of the cluster. The distance between points a and b is the Euclidean distance (d_{ab}), in (n) dimensions:

$$d_{\mathrm{ab}} = \sqrt{\sum_{i=1}^{n} (p_{ia} - p_{ib})^2} \qquad 1$$

The distance of a point from a cluster centre can be used to classify the point; each point in the image can be labelled with its cluster label and this is then often displayed as a false colour image. A method is required to find the centre of each cluster (centroid); one method is the K-means algorithm, (MacQueen 1967). The K-means algorithm is an iterative method that starts with a random initial seed point and calculates the shortest distance to the centre. This is one of the simplest unsupervised classification methods which attempts to minimise J:

$$J(V) = \sum_{i=1}^{C} \sum_{j}^{C_i} \left(\|x_i - v_j\| \right)^2 \qquad 2$$

Where: C_i is the number of points in i^{th} cluster.

C is the number of clusters.

An example result of this method is shown in Figure 3, where sixty data points are formed into five clusters.

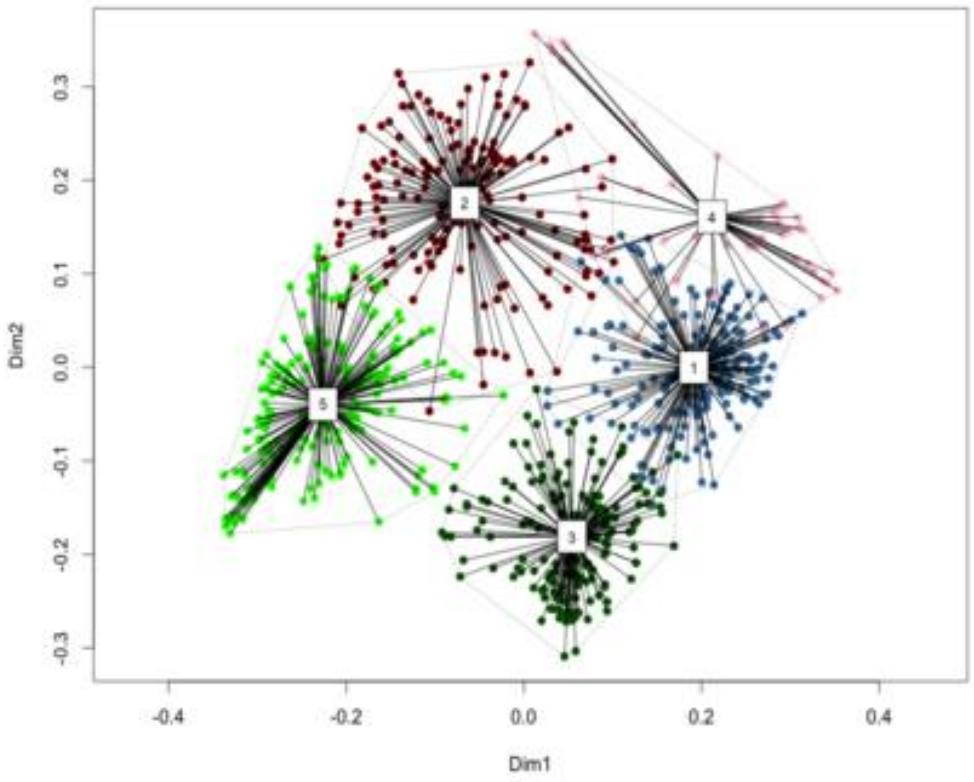


Figure 3 Result of K-means clustering with five clusters, the lines from the data points in each cluster intersect at the centroids (wikispaces.com).

The K-means method fails with non- linear data (Figure 4) and performs poorly with noisy data.

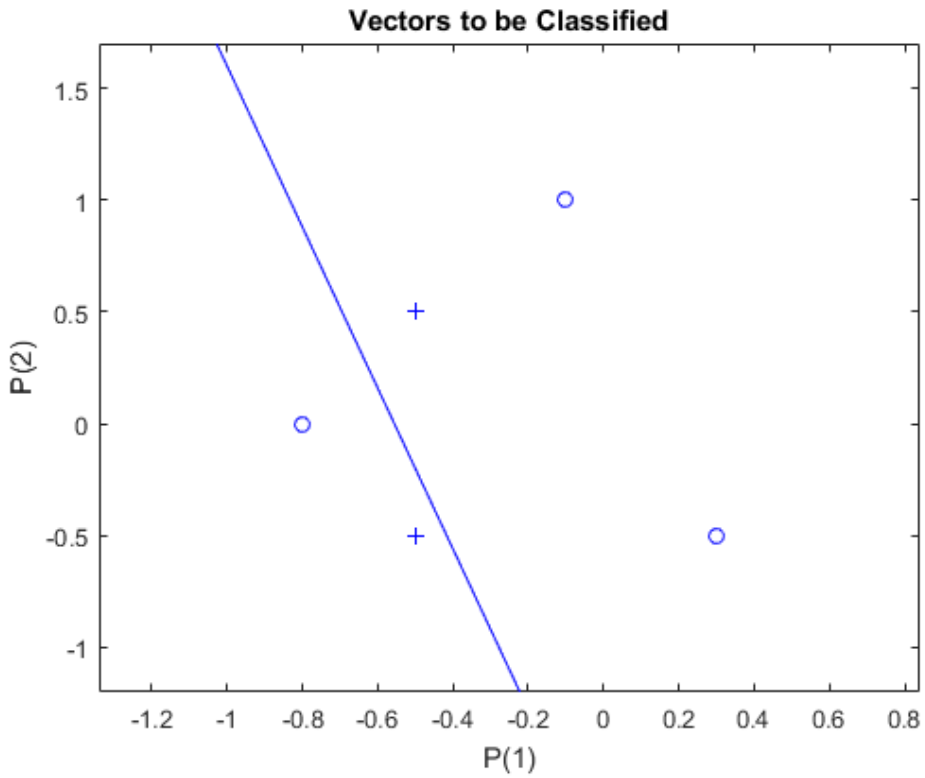


Figure 4 Example of non-linear data. This dataset could be separated in a third dimension by a plane. (MatLab ©)

2.5.7 K-Nearest Neighbour Classification Method

A supervised classification method that uses a similar concept to K-means is K-nearest neighbour (KNN), which is suitable for non-linear datasets. The method finds the nearest neighbours of x_0 in the training data and predicts the class label of x_0 based on a majority vote. This creates continuous and overlapping neighbourhoods, each test vector using a different neighbourhood. The distance measure for the nearest neighbour is usually Euclidean, but other metrics have been used such as manifolds, spherical manifolds were used by Lunga & Ersoy (2011) to classify hyperspectral data.

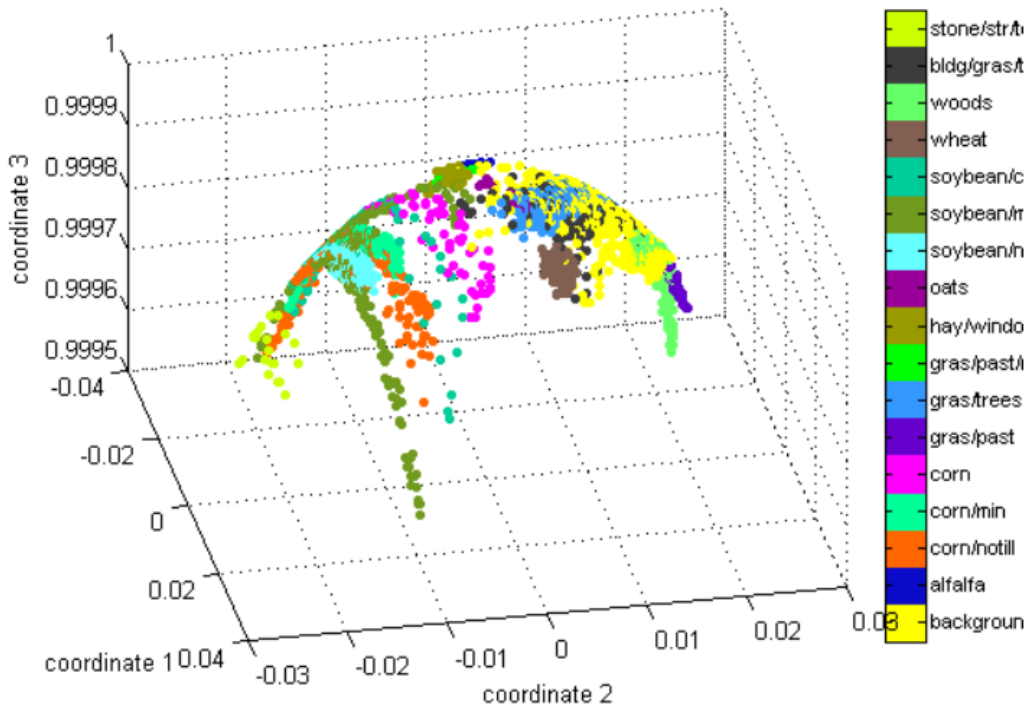


Figure 5 Spherical K-nearest neighbour classification of hyperspectral imagery. Nearest neighbour based on distance along surface of feature space projected onto a sphere rather than Euclidean distance, (Lunga and Ersoy 2011).

This technique is similar to a spatial classification method which projects the normal to a surface on a unit Gaussian sphere (Vosselman et al. 2004). Here the nearest neighbour on the surface of the sphere is used instead of the Euclidean distance in the original feature space. If the training data set is large then a special sub-space version of the KNN classifier can be used to sub-divide the data usually using a random allocation to the sub-KNNs.

2.5.8 Decision Tree

A decision tree classifier is a recursive method that divides the training data into successively purer subsets. One example of this method was develop by Hunt (1962) which follows the following steps:

1. If all of the training data is in the same class, then it is a leaf node and processing stops down this branch.
2. If the data belongs to more than one class, then an attribute is used to sub-divide it forming two child nodes.
3. The process is carried out recursively until all nodes terminate in leaves.

MatLab[3] implementation of decision tree classifiers has three variants: simple, medium and complex. Simple trees are limited to a maximum number of splits of 4, medium to 20 and complex to 100. Using the classifiers directly in MatLab code it is possible to prune the trees to prevent over training. Common pruning methods are Reduced Error Pruning (REP), Pessimistic Error Pruning (PEP), Critical Value Pruning (CVP and Cost Complexity Pruning (CCP).

Decision tree classification methods have been suggested to be more suitable to remotely sensed data because there is no requirement for the Gaussian distribution. Remotely sensed data often exhibits overlapping classes causing classifiers that require Gaussian distribution to fail or produce poor results (Pooja et al. 2011), their work used satellite RGB data and minimum entropy or minimum error to set the decision thresholds. To prevent over training, they implemented a pruning algorithm based on error. Their conclusions were that the Decision Tree Classifier (DTC) performed better than a Maximum Likelihood Classifier (MLC), the DTC was unstable when the training

[3] MatLab® R2015a, Mathworks, Natick, MA

data was changed and the larger the training set the greater the accuracy achieved. A comparison between DTC and backpropagation ANN classifiers was carried out by Pal & Mather (2002) which concluded that the performance of each classifier was similar on the InSAR data set tested. They noted that for the DTC pruning method and size of the training data were the dominant influences on the classification accuracy, while the accuracy of the ANN depended on many factors.

2.5.9 Discriminant Analysis

Discriminant Analysis (DA) was originally developed by Fisher (1936) for a two class problem and modern adaptions of this technique have proven sometimes to be as accurate as other more complex classification techniques. High dimensional data can be used with discriminant analysis classification methods and can provide input data for other techniques that can only work with low dimensional datasets. The high dimensional data often found in hyperspectral images was found to be well suited to Linear Discriminate Analysis (LDA) methods (Bandos and Bruzzone 2009). A LDA finds a linear transformation matrix which reduces the original dimensions of the data to a lower dimension. The Fisher method then maximises the distance among the means of the classes, at the same time minimising the intra-class variance Figure 6.

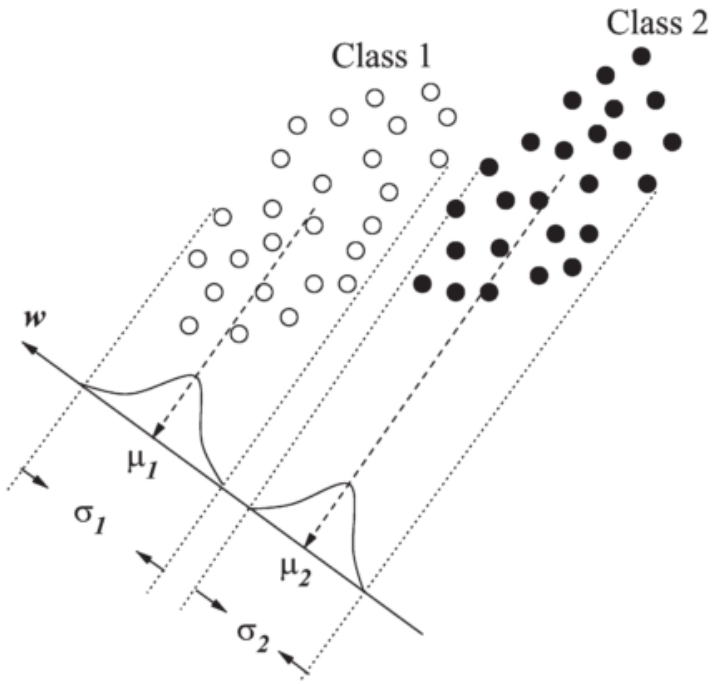


Figure 6 Fisher's discriminate for two classes; the differences between the class means in directions μ_1 and μ_2 is large in comparison to the variance about the means σ_1 and σ_2, (Bandos and Bruzzone 2009).

The MatLab implementation of DA classifiers includes linear, which creates linear boundaries between classes and non-linear quadratic models, which create elliptical, parabolic and hyperbolic boundaries.

2.5.10 Support Vector Machine

Support Vector Machine (SVM) classification methods attempts to separate the classes in a training dataset by maximising the distance that a hyperplane(s) can be positioned from each class Figure 7 (Chao and Horng 2015).

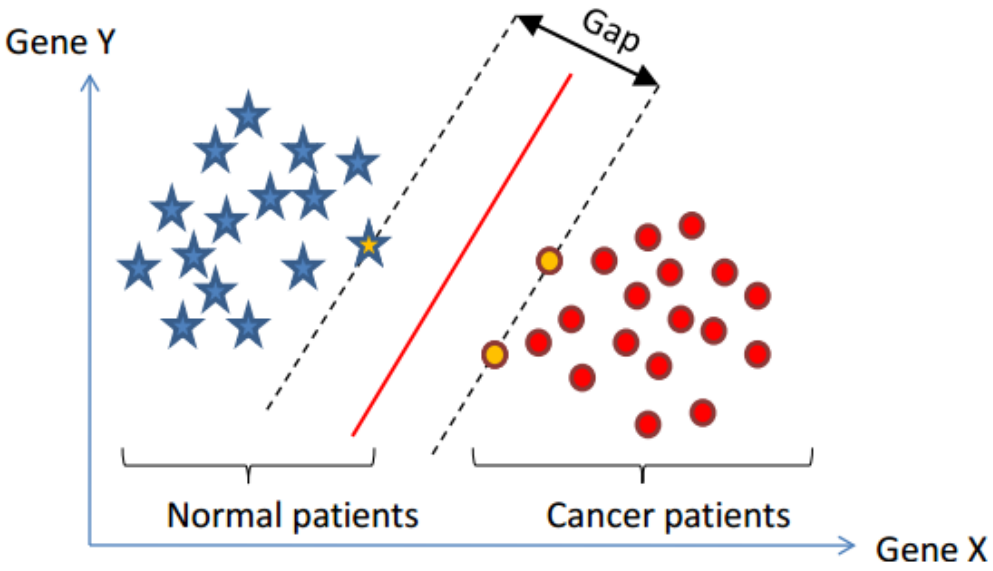


Figure 7 Linear SVM method two class example, hyperplane separates the classes and maximises the distance (gap) to the data points in both classes. The nearest data points to the hyperplane in each class are known as the support vectors (Statnikov et al. 2011).

The linear case of SVM classification can be extended to non-linear by several methods, one popular method, and the Kernel method maps the input space to a feature space using a kernel function Figure 8.

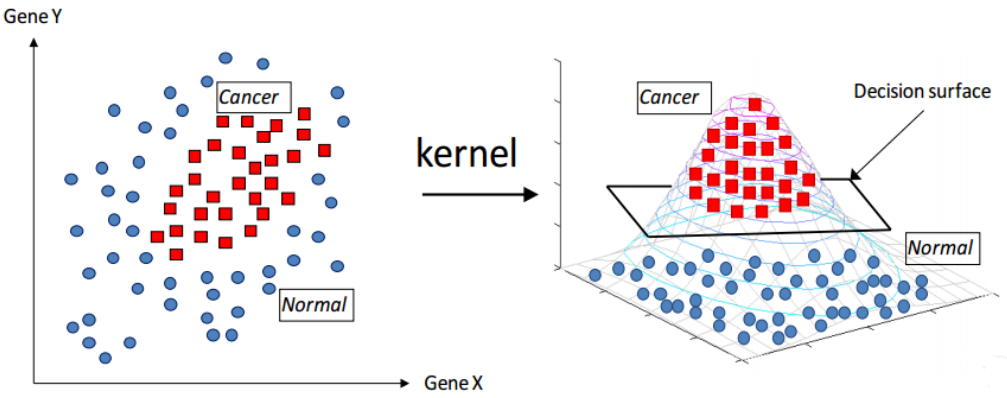


Figure 8 Non-linear SVM classification example; maps the two dimensional input space to three dimensions using a kernel function (Statnikov et al. 2011).

The two most common kernels are the polynomial and Gaussian radial bias functions. Multi-class SVMs were developed to make them more

suitable to remote sensing classification tasks, they include stacked feature and direct summation (Bekkari et al. 2013), their work applied composite kernels to high resolution urban imagery classification. The datasets they used composed of both spectral and spatial data, which they concluded improved the classification rate from 87% (spectral only) to 94% (spectral and spatial). The spatial features were extracted from the imagery by computing the Grey Level Co-occurrence Matrix (GLCM) to extract texture, Figure 9 (Haralick et al. 1973).

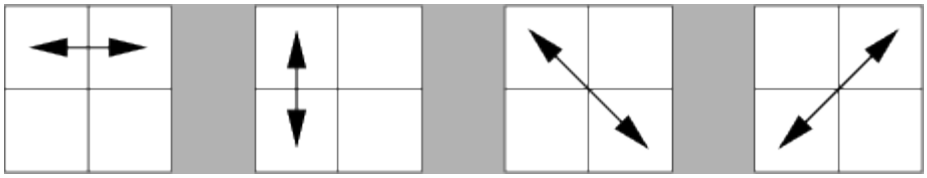


Figure 9 Haralick texture features generated from the four co-occurrence matrices using the above directions of adjacency.

Haralick texture extraction method can be applied to multi-spectral imagery by using the individual spectral layers or one particular layer of interest. Horlick's method could be seen as an adaption of Roberts cross-gradient filter for edge extraction (Roberts 1961).

2.5.11 Iterative Self-Organising Data Analysis Techniques (ISODATA)

A more elaborate version of the K-means classifier was created by Ball & Hall (1965), this endeavoured to overcome the problems associated with the assumptions in the K-means method. The assumptions were that the clusters were compact and well separated; this is generally not the case with real world data. ISODATA method calculates the standard deviation for each feature axis for each non-null cluster; any cluster that

has one or more ‘large’ deviations is split perpendicular to the feature axis and any clusters that are closer together than a user defined distance are amalgamated to form a single cluster. This split and merge technique firms the basis of the ISODATA algorithm. ISODATA can use a very large amount of processing time and can iterate eternally if some precautions in programming are not taken.

2.5.12 Random Sample Consensus Iterative Algorithm (RANSAC)

RANSAC is a type of classifier that creates a model (pattern) of the provided data; the special characteristic of RANSAC is that it is tolerant to noise, referred to as ‘Outliers’. Figure 10 shows an example of the algorithm fitting a line to ‘Inlier’ points and ignoring the ‘Outliers’. The input to RANSAC is the raw data, parameterized model which can match or be fitted to the data and confidence parameters.

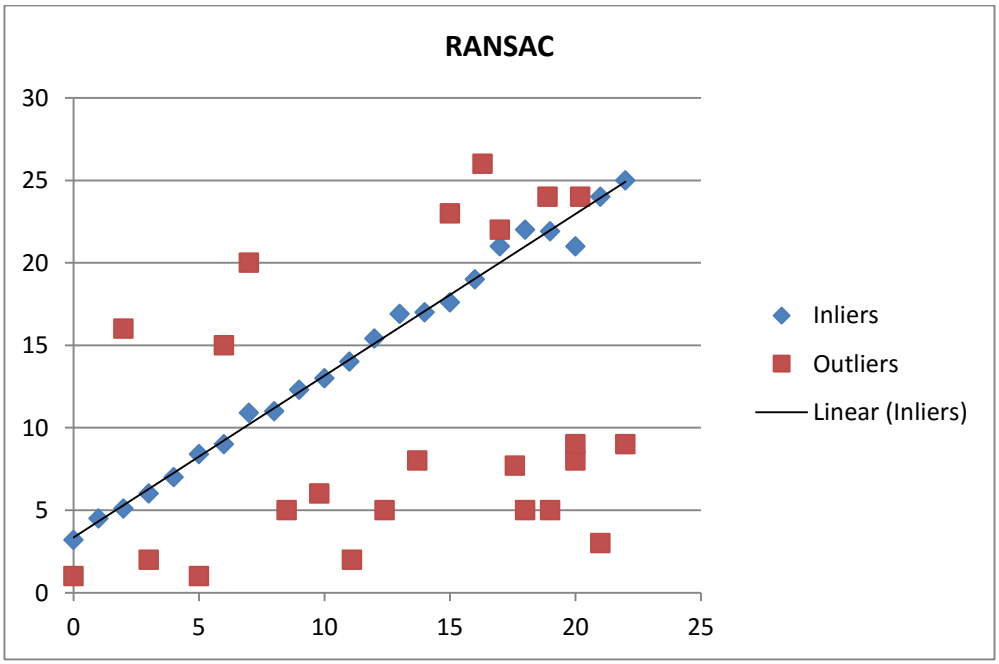


Figure 10 RANSAC Line Fitting Example

This is an iterative process that gradually increases the number of Inliers that fit the model (in the example an equation of a straight line) and reduces the error between the Inliers and the model.

2.5.13 Scale Invariant Feature Transform (SIFT)

SIFT was developed by Lowe (2004) as a method of extracting features from images that can be used to perform reliable matching between different views of an object. It was named Scale Invariant Feature Transform (SIFT), because it transformed image data into scale-invariant coordinates relative to local features. The features are invariant to scale and rotation. The process is not affected by a affine distortion, change in 3D viewpoint, addition of noise or small changes in illumination. The process matches individual features to a database of features from known objects using a nearest-neighbour algorithm, followed by a Hough transform to identify clusters belonging to a single object and then verification using least-squares. The advantage of this technique is its tolerance of clutter and occlusion. Figure 11 shows SIFT process results from Lowe's original paper (the training images are the small images), rectangles enclose the recognised feature and smaller rectangles the key points used for recognition; this shows very clearly the rotational tolerance of the method.



Figure 11 Object Recognition using the SIFT Algorithm (Lowe 2004)

A disadvantage of this method is that it must search a database of object parameters to find a match; as the number of objects required to be recognised increases the database size increases and in turn the computational time increases. Although the training phase of a Neural Network approach increases with the number of objects to be matched the recognition phase remains the same. The scale invariance of the SIFT method would be very useful if it could be adapted for use with a neural network.

2.5.14 Classifying LIDAR Waveform Data

Advanced LIDAR systems are able to record the entire laser return pulse. The shape, polarisation and phase of the full waveform can be used to analyse the properties of the reflecting surface; this information could be used to classify objects in the point cloud based on the material properties. Toth et al. (2010) proposed a method of

classification which used wavelet coefficients as input to a Kohonen Self Organising Map (SOM).

Since the introduction of full-waveform LIDAR systems there have been numerous methods of feature and material classification based on decomposing the waveform into various components. The waveforms have been decomposed by Gaussian (Wagner et al. 2006), generalised Gaussian or Lognormal function (Chauve et al. 2007). Wagner et al. (2006) used Gaussian decomposition, amplitude and standard deviation (pulse width) to discriminate between vegetation and no-vegetation. Mallet et al. (2008) used generalised Gaussian decomposition with a shape parameter to classify urban areas.

Unsupervised robust planar segmentation of terrestrial laser scanner point clouds based on fuzzy clustering methods (Biosca and Lerma 2008).

2.5.15 Genetic Algorithms and Feature Classification

G Turhan-Sayan et al. (1998) approach to the use of genetic algorithms (GAs) was based on a signal shaping method. A GA manipulates a fixed-size population of structures called ‘chromosomes’, through the application of genetic operators, selection, crossover and mutation, the *chromosome* with the highest fitness wins through to the next round of selection. This method acts as a gradient descent algorithm which attempts to find a global minimum. The use of input signal shaping in electromagnetic target classification was suggested by Kennaugh (1981), where he introduced the K-pulse concept. The K-pulse was

defined as a time-limited signal which represented all aspects of the target response and polarisation. A Laplace transform of the K-pulse produce the entire function for a complex frequency with no poles. The K-pulse method becomes a minimisation problem and this is why G Turhan-Sayan et al. (1998) used a GA. Sometimes complicated optimisation problems which cannot be solved by traditional optimisation techniques can be successfully handled by GAs. This technique requires wide band data for only a few target aspects and polarisations. Genetic algorithms make the synthesis of K-pulses possible especially when the K-pulse duration is unknown. This method also achieved a classification rate of over 90%.

2.5.16 Biological Feature Recognition

The main body of previous research into features extraction has depended on techniques that use segmentation of the point cloud into planar surfaces and the application of constraints to classify each segment (Nurunnabi et al. 2015). Segmentation methods have had difficulty with features that are defined by only a small number of points such as windows (Pu and Vosselman 2007), as only the frame can be used as the glass is transparent to laser light. Knowledge based methods which use constraints in a decision tree structure have been attempted; unfortunately, these can require a large numbers of rules to define a feature, especially complex non-linear features (Xu et al. 2012). The best image-interpretation system is a combination of our eyes and our brain. Our brains are thought to be a large scale network of simple processors (neurons), the network being learning (supervised)

and self-learning (un-supervised) methods used with artificial neural networks have been shown to be powerful pattern recognition systems. Artificial neural networks have been used for classification in remote sensing but they have been restricted to 2D data (Castelluccio et al. 2015; Ahmadizadeh et al. 2014); the aim of this research is to extend this to 3D, more specifically 3D point clouds.

In order to understand biological feature recognition, the first stage is to understand how stereo vision provides 3D information. Stereo images have been used in photogrammetry to extract terrain elevation and then use this to create maps with contour information or digital elevation models. Edelman et al. (1997) proposed a model of biological vision related to complex neurons in primary visual cortex. These neurons were seen to respond to gradient at a particular orientation and spatial frequency; additionally, it was observed that the location on the retina could shift over a small area. They hypothesised that the function of these complex neurons was to provide an ability to match and recognise 3D objects from a several viewpoints. The SIFT feature matching algorithm (Lowe 2004) was tolerant to feature size, orientation and affine transformation; these were aspects found in biological vision. Orientation has been thought of as a problem in biological vision, as humans have difficulty recognising complex features, such as characters, if they are rotated more than a few degrees. However, it is possible to learn to read characters in any orientation, but of course we usually learn to read in a single orientation. The extraction of stereo-disparity, and hence range, information from images depends upon

establishing a correspondence between them (Marr and Poggio 1976). They analysed the nature of the correspondence computation and derived an algorithm that extracted information from random-dot stereograms (magic eye pictures) and commented on the implications for psychophysics and neurophysiology of the visual system. The algorithm could provide a method for automatic feature matching where the technique provides recognition by matching features from an image with a database of object images. Marr & T Poggio (1976) saw the recognition process as three steps, select a region in an image, locate the same region in the stereo pair and measure the disparity between the two. The second step, correspondence, was seen as the crux of the problem to be solved and has continued to be the focus of research to this day. Julesz (1971) discovered that humans could recognise patterns in random dot stereograms, which consist of random patterns of dots when viewed in mono, but reveal patterns with depth when viewed stereoscopically. This was a surprising find as correspondence between arrays of random dots should produce many false targets (Figure 12), but the biological vision system was able to delineate the correct correspondence.

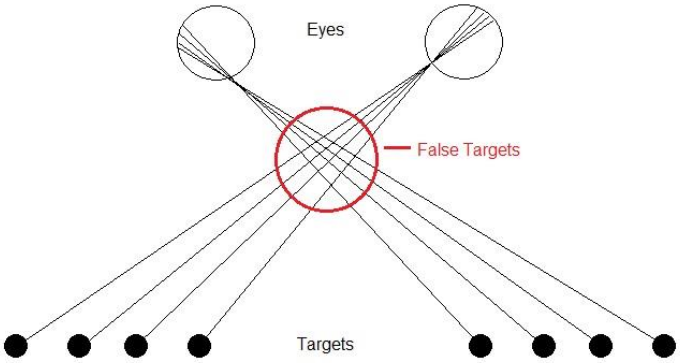


Figure 12 False Targets in Random Dot Arrays

2.6 Artificial Neural Networks

Real world recognition and classification tasks have such great diversity that rule-based methods are unable to cover all possible permutations (Beard 1990). As a result, the main fields of research that have benefitted from artificial neural networks, models of the human brain, are image classification and speech recognition. The best image-interpretation system is a combination of our eyes and our brain. Our brains are thought to be a large scale network of simple processors (neurons), estimates of the number of neurons is 10^{11}; each neuron being connected to around 10^4 other neurons. Although Freud worked on models of the human brain as early as the late nineteenth century, the first modern concepts of a neural network model of the human brain were created by (McCulloch and Pitts 1943) but they were unable to make progress with a viable learning method. Later Hebb (1949) was able to further their research by proposing a relationship between the weights assigned to a neuron and the activation level of the neuron. This network design was named the Perceptron. The networks

designed by Hebb were further developed by (Rosenblatt 1957); he created a network that adjusted the weights in proportion to the error between layers. Research continued to develop a more realistic representation of the brain in the form of multi-layer networks, but a suitable learning rule proved impossible in the late 1960's. Minsky & Papert (1969) stated in their book that two-layer networks had limited use and multi-layer networks were not worth further investigation due to the lack of a suitable learning rule; this prompted Aleksander (1966) to focus his research on single layer networks. Aleksander developed a hardware based network designed to learn and recall human faces (Aleksander et al. 1984). While Aleksander was working on single layer networks Werbos (1974) and Parker (1982) independently developed multi-layer networks which used an iterative method which back-propagated error to improve learning. Back-propagation networks used supervised learning, examples of classification classes were presented to the network in the training phase; un-supervised learning methods were being developed by Kohonen (1984). Un-supervised networks were especially useful for problems where the number or separation of classes within the data were unknown. Back-propagation networks were further developed by Rumelhart & McClelland (1986) and in the next ten years research using these networks progressed and their use became most evident in classification tasks, handwritten ZIP code recognition (LeCun et al. 1989), classification of genetic sequences (Lende et al. 1994), land use classification (Paola and Schowengerdt 1995), signal processing (Mahalingam and Kumar 1997) and

chromosome classification (Cho 2000). Further research has developed new methods using a variety of network designs including classification of multi-spectral images (Paola and Schowengerdt R. A. 1995), urban land use classification (Iyer and Mohan 2002), 3D mesh reconstruction form unorganised points (Yuan and Zeng 2004) and self-organizing surface map: learning surface topology from a laser point cloud.(Mole and Araujo 2010). Two areas of research using neural networks that may be relevant to laser point cloud data analysis are classification and self-organising maps.

2.6.1 Design

A neural network is a series of layers of neurons and synapses. Each neuron is interconnected to the next by a synapse, the synapse stores a value know as a weight and the output value of the neuron is produced by a transfer and activation function (Figure 13).

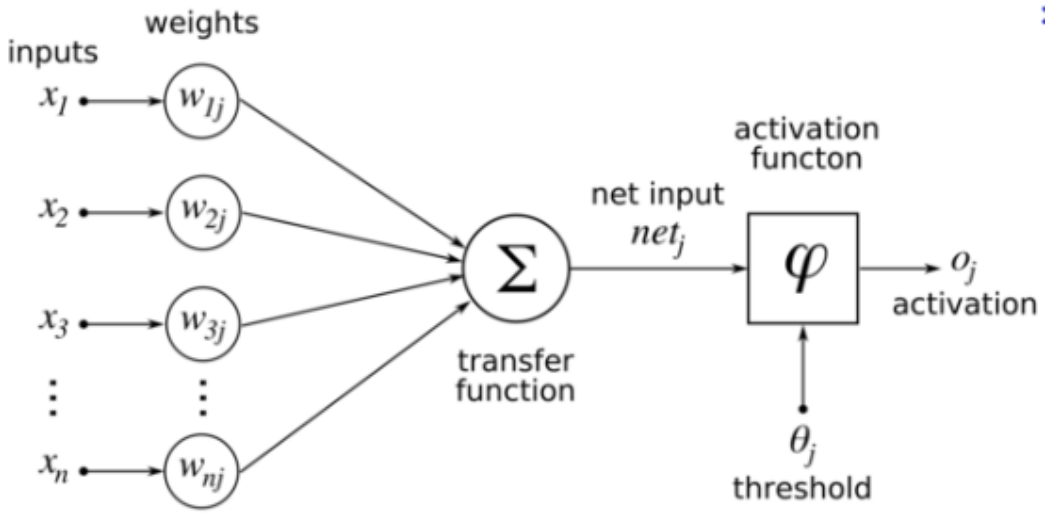


Figure 13 Neural Network Architecture (MatLab ©)

There are many network architectures, from fully connected where every neuron is connected to every other neuron and variations which reduce the interconnections. Neural networks have been created in hardware (Aleksander 1966), (Aleksander et al. 1984), but most research has been carried out using software simulations. The brain uses three dimensions to interconnect neurons and this can be simulated in software; this has been more challenging in hardware networks. The synapses store a weight (W) and the neurons sum the weights with the output values of each connected neuron (A):

$$x_j = \sum_{i=0}^{n} A_i W_i \qquad 3$$

The sum is the input to an activation function (φ) to provide output to connected neurons in the next layer. This function is normally non-linear in order to give the network the capability to separate classes greater than two dimensions. The most widely used non-linear transfer functions are shown in Figure 14.

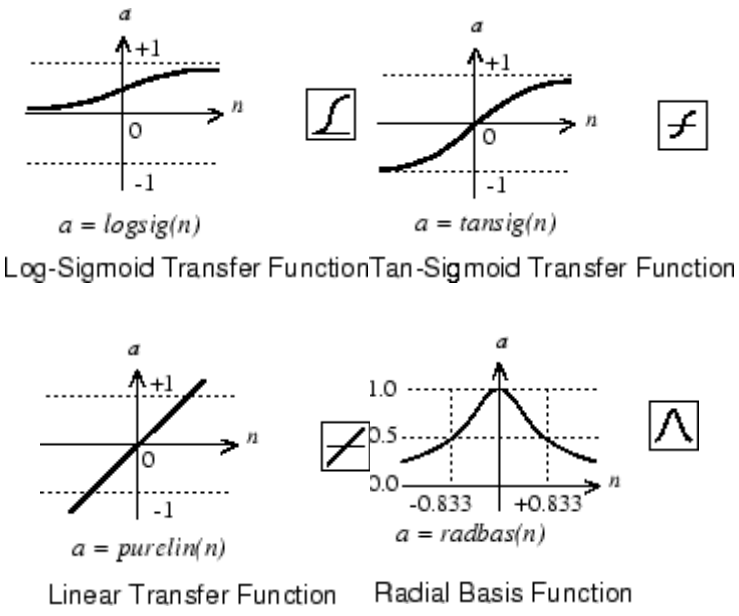


Figure 14 Common ANN transfer functions.

2.6.2 Training

The training process is iterative and consists of a forward calculation of neuron activation followed by a backward adjustment of weights derived from the error between the required outputs to a given input. One training method is correlation using a learning rate factor (α) and activation values (a & b) in layers (A & B) (Hebb 1949).

$$\Delta w_{ij} = \propto a_{ij} b_{ij} \qquad 4$$

Hebb modified this method to use the sigmoid hyperbolic function (S(x)) which produced the 'Sigmoid Hebbian Law':

$$\Delta w_{ij} = -w_{ij} + S(a_i) S(b_j) \qquad 5$$

This method can be applied to multiple layers and feedback can be between any layers.

Neural networks have the ability to accept a large variety of data which do not need to conform to any multivariate normal distribution or multi-

modality. The freedom of input data type is useful in classification tasks as image, point cloud and non-spatial types can be used to improve performance. Neural networks are able to generalise; this is especially useful in applications where the input data is noisy or contains errors.

The design of individual networks requires the choice of the number of layers, the learning mechanism and the activation function, along with several other minor factors. The network size and the ability to generalise appear to be inversely proportional (Paola and Schowengerdt 1995); pruning some of the interconnections can help reinvigorate generalisation in large networks. Training times vary with the size of the dataset, but will also depend on class separation. Fortunately, recall is usually a single pass process, so that once trained a network can produce vary fast results. As these networks are designed using some of the features in our own brains, they are also able to make similar mistakes to us! Recall from a trained network is achieved by presenting the unknown values to the input and then calculating the output values from each layer using the same method as training in a single pass.

2.6.3 Network Types

Many network architectures have been developed starting with the single layer Perceptron, (Rosenblatt, 1957); single layer networks were only able to separate classes linearly. To classify non-linearly separable classes required the development of multi-layer networks (Atkinson and Tatnall 1997); these network types included, feed-

forward, self-organising map (SOM), radial bias function (RBF), learning vector quantisation (LVQ), recurrent neural network (RNN), Hopfield network, Boltzmann, associative and variations on these networks. Networks types can be defined by their topology, learning method, activation and transfer function. A few of the more popular designs are described.

2.6.4 Feed-forward

The most common type of feed-forward network uses back-propagation learning (Benvenuto and Piazza 1992); the output vector (**a**) differs from the expected output vector (**o**) by an error (**e**):

$$e = \frac{1}{2}\sum_{j=1}^{k}\left(o_j - a_j\right)^2 \qquad 6$$

The synaptic weights are adjusted *steepest descent* using a fixed step size which is called the *learning rate*. The steepest descent method may not find the global minima but local minima; various techniques have been used to overcome this limitation which includes allowing a jump restart the descent if oscillation is detected. The network gets its name from the method of propagating the error backwards through the network starting at the output layer. At the start of the learning process the weight values are set to random values. The main activations functions used with this network are step and sigmoid. Feed-forward networks can have any number of hidden layers but most commonly have less than three. The output vector is usually designed to have the same number of neurons as classes; each class being denoted by a

neuron with the value of one the remainder zero. The winning class, on recall, can be derived from the output neuron with the highest value; a threshold or statistical method may be used to determine the result.

2.6.5 Self-organising Map

A Self-organising Map (SOM) creates a two dimensional map of the input data (Kohonen 1984). High dimensional data is reduced to two dimensions displaying clusters of points representing input that may belong to the same class. The network learning is un-supervised, there is no prior knowledge of the class structure of the data; this can be very useful for initial data analysis and data mining applications. The ability to use high dimensional data input assists pattern recognition that cannot normally be visualise. SOMs can be used to provide class identification for a feed-forward network. Training uses a process of vector quantisation, the input vector is divided into groups having similar number of points closest to them. The groups are designated by their centroid; this is similar to the *K-means* method. The learning process iteratively moves the centroids by a fraction of the distance to the nearest randomly picked point.

2.6.6 Radial Bias Function

Radial Bias Function networks (RBF) use a Gaussian radial bias function; this overcomes the local minima problem of the steepest descent method as this generates a quadratic error surface which has a singular minimum. This radial bias function is non-linear. RBF networks have three layers, input, hidden and output, the input is

mapped to each radial bias function in the hidden layer and the output is a sum of hidden layer outputs with linear output layer weights, modified by a sigmoid function. The activation function h(x) where w_n is a linear combination of bias functions, θ is the bias function which is defined as the distance between the input vector x and the training vector x^n.

$$h(x) = \sum_n w_n \theta(\|x - x^n\|) \quad 7$$

The Gaussian radial bias function θ(x) and σ is a smoothing parameter.

$$\theta(x) = exp\left(-\frac{x^2}{2\sigma^2}\right) \quad 8$$

The error in the output vector is normally calculated using least squares, where n is the number of input patterns, k is the sum of the values for each output node, $y_k(x^n)$ is the achieved output for node k and t^n_k is the desired output.

$$e = \frac{1}{2}\sum_n \sum_k y_k(x^n) - t_k^{n^2} \quad 9$$

2.6.7 Neural Network Classifiers

Artificial Neural network (ANN) classifiers is a non-parametric method, which means that it is independent of data distribution and can classify datasets with varying precision and different levels of measurement (Pal and Mather 2002). The classification of military objects such as aircraft, ships and tanks using the characteristics of scattered radar energy has been researched almost since radar was invented, Turhan-Sayan et al.

(1998), approached the problem using a method that used artificial neural networks (ANN) and genetic algorithms (GA). Although this research was with radar as the source data the method may be applicable to laser scan data. Their assumption was that the radar returns would implicitly contain the characteristic data about the shape, size and electrical properties of the target. Such data are strongly dependent on frequency, phase, polarisation of the returns and aspect angle of the target. To accurately classify each candidate target or target class the database of the scattered signatures would be considerable in size and difficult to interrogate in real time. The basic polarization, frequency and phase data was not found to be sufficient to provide acceptable classifier performance; pre-processing the basic data to provide higher, second or third order features was required. This was also found to be required when using monochromatic aerial image data (Evans 1996). Several different order features extracted from the original data helped the ANN to eliminate similarities and emphasise differences between classes.

A typical radar target classification system involves a large database of signal data which is pre-processed prior to the active recognition phase. Turhan-Sayan et al. (1998) found that by using an ANN the comparison and information filtering stage of preparing the data prior to the classification stage could be eliminated. To achieve this they used a self-learning / organising (SOM) ANN, first introduced by Kohonen (1989). (Turhan-Sayan et al. 1999) improved the classifier performance by extracting features from the input database using the Wigner

Distribution (WD). The WD produces an energy distribution map with respect to time and frequency (simultaneously) of the signal waveform for a particular time slot; an energy distribution type feature matrix is produced for each signal in the database. For each waveform example a vector from the WD process is produced and this is used as the input into a SOM. If there is pattern in the vector information for each class then these data points should become clusters in the SOM 2D map output. For a limited 5 class example their results showed good clustering of classes; with approximately a 93% success rate. They concluded that a wide frequency range of input data was not required to provide this result and the ANN method would be applicable to narrow band data.

Neural network classifiers have been used in remotely sensed imagery classification by many practitioners including Paola and Schowengerdt (1994); Roli et al. (1996); Iyer and Mohan (2002); Kavzoglu and Mather (2003); Zhou and Yang (2004); Bischof et al. (1992); Serpico et al. (1996); Tso and Mather (2001). Artificial neural networks are based on the biological model of the brain. McCulloch and Pitts (1943) proposed a mathematical model of neural networks and Hebb (1949) showed how learning might be possible. The first networks designed for pattern recognition were developed by Rosenblatt (1957); non-linear datasets, commonly found in land use and urban remotely sensed data, were successfully classified by the creation of back-propagation networks (Werbos 1974). Some research has concluded that neural network classifiers are more accurate for land cover classification than statistical

methods (Szuster et al. 2011; Bischof et al. 1992; Serpico et al. 1996; Chen et al. 1997). A possible drawback of neural networks is the complexity of design and operating parameters; studies of the effects of the number of layers, activation function, threshold and momentum values have been investigated by (Foody and Arora 1997; Kavzoglu and Mather 2003; Shupe and Marsh 2004). The effect of network parameters on the accuracy of classification of remotely sensed imagery was investigated by Zhou and Yang (2004); they concluded that using a large number of hidden layers did not increase accuracy and that the log-sigmoid performed better than the tan-sigmoid function. They also concluded that neural networks were sensitive to training parameter settings such as learning rate, momentum and threshold values.

2.7 Summary

Chapter two reviewed past and current areas of multispectral remote sensing and associated classification techniques for spatial and spectral data. First, the chapter reviewed multispectral remote sensing and laser scanning, leading onto production of 3D models and their requirements. Passive and active sensors were then discussed, highlighting aspects of each sensors illumination source that may need consideration if the data is to be used for classification. The chapter moved on to review currently available classification methods that may be applicable to multispectral data; including discriminant analysis, support vector machines and finally artificial neural networks.

The literature reviewed in this chapter produced the following outcomes:

1. Passive sensor spectral data requires pre-processing to counter the solar variation especially airborne or long range application.
2. Advantages have been seen in using a combination of passive and active sensors, such as LiDAR and imagery.
3. Multispectral LiDAR and a dual wavelength TLS have been successfully used for classification of vegetation and a three waveband system for rock strata analysis. This three waveband setup used three TLS.
4. Some progress has been made with hyperspectral super continuum laser sources, but these are experimental lab based systems to date.
5. Prior knowledge of a materials spectral response and choosing matching wavelengths can increase classification rates.
6. There are other novel approaches to using imagery to produce 3D models, one example is using a neural network to recover depth.
7. Some image classification methods have been applied successfully to laser scan data.

It was apparent that the main focus of classification of laser point clouds had been classification of spatial data rather than spectral and the review focussed on these works to look for cross-over to the spectral feature extraction tasks. The more traditional segmentation and algorithmic approaches to feature classification have assumed that all walls are vertical and large planar surfaces. Assumptions that roofs are

non-vertical large planar surfaces, windows are small parts of walls (not true of a glass building). Windows seem to have been the biggest challenge as glass is transparent to laser light. After segmentation, rule-based methods have been employed to classify each plane or line set; complex buildings would require very large rule sets. AI languages such as Prolog or Lisp might have been more suitable than the languages that have been used in current algorithmic approaches to feature classification. Classification methods covering a wide variety of disciplines were reviewed to search for methods that would be suitable for material classification using spectral data.

Laser point cloud data has a unique aspect in that the light source is controlled and known, unlike photographic images, but it still has the limitation requiring the normalisation for varying range and incidence angle. If the intensity values are normalised for range and angle of incidence, only the reflecting surface remains as a variable; this was a key aspect developing an approach which can normalise the intensity values to enable classification building materials in real world environments. In future research it might be possible to use lasers with different transmission frequencies, super-continuum laser, to further enhance material classification techniques. This would be analogous to hyper-spectral classification techniques using photographic imagery. As the intention of this research was to employ multiple laser scanners, registering point cloud data was also reviewed. This review has shown that there has been very limited research into material classification using laser point cloud data.

Chapter 3. Laser Scanners

3.1 Introduction

This chapter discusses the investigations into the characteristics of laser scanner point cloud data. This work was undertaken to gain a fuller understanding of the nature of laser scan data and aspects which could provide an advantage or limitation to multispectral classification methods. The scanners used in this research were dictated by availability as there funding was not available to acquire scanners of choice; these were the FARO^{3D}, Leica HDS3000 and Riegl VZ400. The experiments discussed in this chapter were based on these instruments.

The first part of the chapter gives a description of laser scanners and their different designs and then a short introduction to multispectral laser scanners. Classification in this research primarily uses laser reflected intensity from the material to be classified; the second section of this chapter discusses reflected intensity and is followed by discussion of factors that may affect the intensity values. To generate multispectral data for this research three scanners of differing wavelength were used; the final section covers different registration methods for aligning data from multiple scanners. This is followed by a summary of the main outcomes.

3.2 Types of Laser Scanner

Current laser scanners use two methods of measuring range are time of flight (TOF) and multi-frequency phase comparison, an additional method can use triangulation. Airborne (LiDAR) scanners which are required to operate at long ranges generally use TOF. Terrestrial scanners, which require high speed scanning in the main use phase comparison.

Laser scanning has provided an instrument that can create rapid 3D surveys. The first laser scanners came into commercial use after 1985. Development has progressed quickly and laser scanners are in common use for tasks including change detection (Alba et al. 2009), digital terrain models (DEMs) (Guarnieri et al. 2009), building façade reconstruction (Pu and Vosselman 2010), detection of fire damaged concrete (Vickers 2013), monitoring rock slope instabilities (Abellan et al. 2014), urban land cover classification (Yan et al. 2015) and forest mapping (Liang et al. 2013; Ryding et al. 2015). The main categories of laser scanners in production include terrestrial, airborne and mobile; this research uses terrestrial laser scanners (TLS). Most TLS output Cartesian coordinates and a measure of reflected laser intensity; some also provide the full waveform of the reflected pulse.

3.2.1 Time of Flight

Time of Flight (TOF) ranging uses accurate time measurement to calculate the distance to the target object (Shan and Toth 2009). The laser pulse triggers a photodiode which triggers the timing device,

usually a very stable oscillator; the return pulse also triggers a separate photodiode which completes the sequence. To measure to an accuracy of 1 cm requires the oscillator to have a frequency of 15 GHz. The photodiode has a threshold to prevent being triggered by reflections from the atmosphere, both on the outward a return path. If a series of pulses is returned then the leading or the last pulse may be used to measure range, alternatively all pulses will be measured and stored. In some designs the complete waveform of the return pulse is stored for later analysis. The pulse width (length) has a major influence on multi-return resolution, 10 ns pulse width will be 3m long. The measuring resolution will be restricted by the accuracy of detection of the leading edge of the return pulse; this is complicated by the distortion of the return by the target material. Pulse repetition frequency will limit the maximum range, the timing accuracy the minimum range. The maximum range limitation can be improved by the use of multiple pulse systems similar to those used in radar

3.2.2 Phase Comparison

Phase comparison to measure distance is used in continuous wave (CW) lasers (Shan and Toth 2009). This type of laser usually has a lower power output than pulsed systems and is therefore used in terrestrial laser scanning and other short range applications. The majority CW laser systems use amplitude modulation. The reflected signal is demodulated and compared with the original transmitted (or reference) signal. The difference in phase angle (φ) represents a fractional part ($\Delta\lambda$) of the total range. To resolve the ambiguity, of the

integer number (M) of wavelengths in the total range, multiple modulation frequencies and hence wavelengths are used. Range (R) can be calculated by the solution of simultaneous equations.

$$R = M_1.\lambda_1/2 + (\varphi_1/2\pi).(\lambda_1/2)$$

$$R = M_2.\lambda_2/2 + (\varphi_2/2\pi).(\lambda_2/2) \quad (10)$$

$$R = M_{\mathrm{n}}.\lambda_n/2 + (\varphi_n/2\pi).(\lambda_n/2)$$

The lowest frequency associated with the longest wavelength will determine the maximum range. The highest frequency with the shortest wavelength will determine the range resolution. A 10 MHz modulation with a wavelength of 30m, with 1° phase resolution results in a range resolution of approximately 8 cm.

3.2.3 Scanner Detectors

Intensity is defined as the ratio of the power of the reflected to emitted Laser light from the scanner. The reflected laser intensity recorded by scanners adds a fourth dimension of data and the reflectance varies between different surface types and materials. The reflected beam is most commonly detected by an Avalanche Photo Diode (APD) or PIN photo diode. Scanners that use near IR lasers may benefit from the spectral response of a silicon PIN diode sensor as they are particularly sensitive at near IR wavelengths, the FARO[120] 3D scanner uses a 905nm laser. The scanners with lasers in the mid IR region would require Indium Gallium Arsenide (InGaAs) Pin diode photo detectors, which are most sensitive around 1500nm.

3.2.4 Multi-spectral Laser Scanners

At the start of this research commercial multi/hyper spectral laser scanners were not in existence, although some dual wavelength instruments existed for specific use in bathymetric surveys, manufacturers included LADS Corp., Terra Systems and SAAB Dynamics. These instruments were solely designed as measurement instruments; the reflected laser intensity was not recorded. The first commercial instrument to be designed to record the laser intensity values was introduced at the European LiDAR mapping forum in Amsterdam on 8 Dec 2014 by Optech; an airborne multi-spectral LiDAR sensor. This sensor had three individual lasers with three different wavelengths, Figure 15 shows that these were the wavelengths of the tree TLS instruments used in this research CRC Press/Taylor & Francis Group. The literature associated with the release of this instrument suggest the main use was aimed at land use classification.

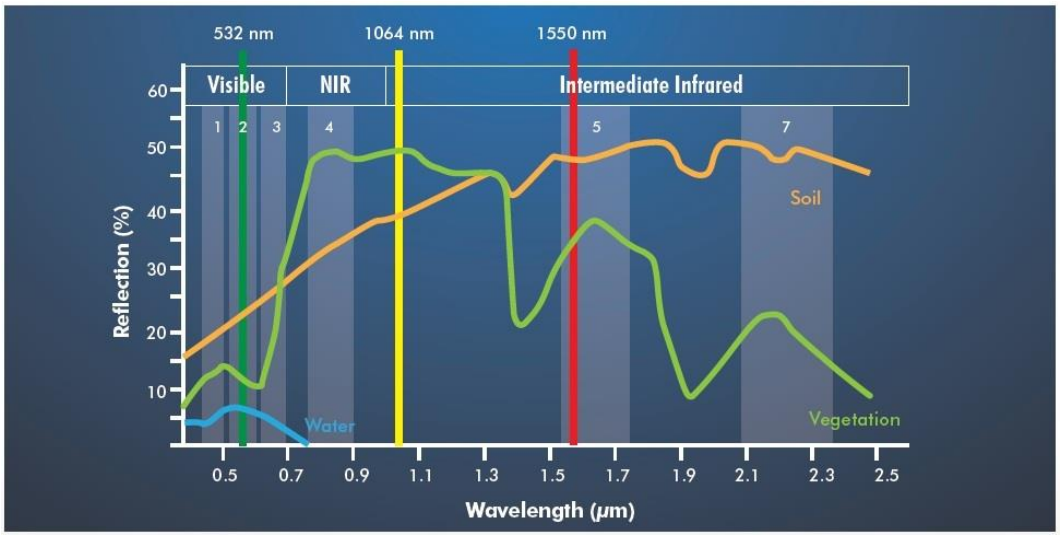


Figure 15 The laser wavebands used in this research: Leica visible green, FARO near infra-red, Riegl mid infra-red. Chart curtesy of Optech © 2015.

In the same year Riegl also introduced a multi-wavelength scanner into their range, aimed at bathymetric survey rather than land use classification. This scanner has two lasers, one using 530nm wavelength and the other NIR wavelength. The research done by Gaulton et al. (2013) assisted by Selex Galileo in developing a ‘breadboard’ instrument using a tuneable laser, but has not developed into a commercial product as yet. Selex Galileo was previously Ferranti, who had a long history of research and development in laser technologies, notably the first military laser target designator which first saw active service within weeks of delivery to the UK armed forces, in the Falklands war (Flight International 1982).

3.3 Reflected Intensity Characteristics

(Kaasalainen and Kukko 2009), carried out calibration experiments on a FARO LSHE80 and a Leica HDS6000 scanner, they discovered that intensity increased with range to about 5 m, after which it reduced with further increase in range. The increase in intensity between 1 m and 5 m for the FARO scanner was attributed to the in-built near distance brightness reducer. According to the manufacturer, the Leica detector should not have any reducing effects, but they were observed to be similar to that of FARO at distances of less than 5 m. As the scanners used in their tests were similar in design to those in this experiment, it was vital to repeat their calibration tests. The experiments in this research confirmed their results.

The intensity of the laser light decreases as a function of beam diameter, which is dependent on beam divergence angle and range. However, most scanner optics have a lens which focuses the beam at specific range, this causes a waist in the beam at that range, beyond that range the beam starts to diverge (Wujanz and Daniel 2009). If the distance between scan points is less than the beam diameter, the coordinates of points within the beam diameter may cause oversampling. With a step-angle of 0.16 mrads (0.009º) the FARO scanner will receive returns 1.6mm apart @ 10m. This suggests that high resolution scans may have oversampling and hence position errors due to the point being assigned an incorrect range. This would be exaggerated at high angles of incidence and on textured surfaces where the incidence angle to the main surface is modified by the surface texture. Beam diameter (D) versus range (R_r) was calculated using (11). The FARO^{3D} 120 scanner has a beam diameter on exit (D_0) of 3.8mm and divergence (θ) of 0.19mrad.

$$D_r = R\theta + D_0 \quad 11$$

The beam intensity is inversely proportional to the area of the beam footprint. The area of the beam footprint is defined by the area of the ellipse (A) with semi-major (A) and semi-minor (B) axes projected onto the reflecting surface (12).

$$A = \pi AB \quad 12$$

The return intensity is also a function of angle of incidence, reflecting surface properties and atmospheric absorption. Atmospheric

absorption increases with range. If the surface absorption and reflectance was a characteristic of the surface material then normalizing the intensity value for angle of incidence, range and other effects might allow classification of the material on a surface that was at any range or orientation.

The amplitude of the return laser energy from a surface is mainly affected by four factors: instrument, atmospheric conditions, incidence angle and range. Wagner et al. (2006) and Kaasalainen, Jaakkola, et al. (2011) proposed that the intensity of the surface reflectance (ρ) measured by a scanner can be expressed as the ratio of the received (P_r) and transmitted (P_t) power (Hug and Wehr 1997).

$$\rho = P_r / P_t \qquad 13$$

Intensity can be expressed as:

$$\rho = P_r / P_t = \mu_\lambda \frac{D_r^2}{4\pi R^4 \beta_t^2} \sigma \cos\theta \qquad 14$$

Where: P_r = reflected power

P_t=power transmitted
D_r=receiver aperture
R=range (distance to the target)
β_t=laser beam width
σ=backscatter cross-section
θ=incidence angle
μ_λ=surface reflectance at wavelength (λ)

The backscatter cross-section is related to the illuminated area (beam footprint) on a target surface, determined by the laser beam divergence.

The beam divergence angles of the three scanners is shown in Table 2. As range increases the beam footprint increases with R^2; this means P_r is inversely proportional to R^2 (assuming the surface illuminated is homogeneous and larger than the backscatter cross-section). For instances where the beam footprint is larger than the individual object scanned P_r is proportional to R^3 or R^4 depending on the objects shape. Due to the small beam divergence and therefore small footprint of the laser for all scanners in this study, P_r inversely proportional to R^2, was assumed. It was also assumed that the atmospheric and instrument factors are very small, especially in short range laser scanning.

Table 2 Beam divergence angles (mrad) and footprint (mm) for the FARO 120, Leica HDS3000 and Riegl scanners.

Scanner	FARO 120	Leica HDS3000	Riegl VZ-400
Beam Divergence (mrad)	0.19	0.12	0.5
Footprint (mm) @ 100m	19	12	50

The reflected power is affected by incidence angle, proportional to Lamberts cosine rule, (Lambert 1760), for non-specular reflectors, and also the footprint increasing in area (becoming elliptical) as the incidence angle increases. The effect of incidence angle can be due to the angle of the whole surface or the texture of the surface. Specular reflectors tend to result in very low reflected power as the majority of the energy is directed away from the receiver.

Due to distortion of the transmitted pulse by the reflection surface the average power rather than the peak power is normally used in time-of-flight scanners. Continuous wave (phase shift) scanners are insensitive to effects of surface distortion as they use peak-to-peak or RMS power, (Hug and Wehr 1997). The power may also be biased by background radiation; this is usually reduced by the use of a band pass filter in the receiver optical path.

Reflected laser intensity from a target surface is controlled by four main factors; instrument, atmospheric, target scattering characteristics and geometry (Kaasalainen et al. 2011). A patent for one of the first laser scanning systems acknowledged that incidence angle and range would affect accuracy (Berg and Gerhard 1998). The quality of the scanner's range data is also affected by these factors (Soudarissanane et al. 2009). The two dominant geometric factors affecting reflected laser intensity are range and incidence angle; these can be calculated from the scan data. However, the accuracy of incidence angle calculation is dependent on the quality of the range data. The accuracy of the range data has been observed to be reduced at high incidence angles (Soudarissanane et al. 2009). Improving the accuracy of incidence angle measurement in full waveform (FW) airborne laser scanning was used by (Abed 2012) creating a new Robust Surface Normal (RSN) estimation method. This method uses a minimum number of nearest neighbour points, using only the three nearest points (Euclidean). The method aims to produce the exact normal by checking for planarity, for planar surfaces and the best estimate for non-planar surfaces. The FW

echo amplitude is used as a weight function in the 3D moment invariant method implemented in this method.

To maximise classification accuracy some form of intensity normalisation is required. For single wavelength scanners, intensity normalisation has proved difficult partly due to the inter-dependence of range and incidence angle (Jutzi and Gross 2009; Hofle and Pfeifer 2007 Proceedings of RSPSoc and Irish Earth Observation Symposium). Ratios of intensity of adjacent points provides a reflectance data, using a single wavelength scanner, which is independent of range and incidence angle (Kirchner et al. 2007). Discontinuities will exist where the two points are on different surfaces or at different ranges and incidence angle for the same surface.

Nitzan et al. (1977) proposed the use of registered reflectance and range data for scene analysis, using an experimental laser scanner. More importantly they suggested that several wavelengths might be used from which ratios of reflected laser intensity could be calculated; the ratios would result in a spectral signature of the target that was independent of range and incidence angle. Lichti (2005) exploits multi-spectral scanner data, using ratios of passive sensor RGB and laser intensity to create incidence angle and range independent data. The use of intensity ratio was also used in a dual wavelength scanner developed for measuring moisture content in vegetation (Were: et al. 2013).

Passive sensor intensity ratios have been used for land-cover classification in order to overcome the requirement for a sun

synchronous orbit in satellite remote sensing. Rouse et al. (1974) found that quantifying the biophysical characteristics of the rangeland vegetation, using satellite spectral signals, was confounded by differences in solar zenith angle creating different spectral signatures on subsequent satellite revisits. Their solution to this problem was to calculate the ratio of red wavelength (μ_{670}) and infrared wavelength (μ_{800}); the ratio was known as the Normalised Difference Vegetation Index (NDVI).

$$NDVI = \frac{(\mu_{800} - \mu_{670})}{(\mu_{800} + \mu_{670})} \tag{15}$$

The NDVI was normally formulated as above to restrict the values to a range between -1 and +1; this formulation also prevented large outliers.

Since then more indices have been developed to characterise specific land use applications (Haboudane et al. 2004). The indices have been extended beyond use for vegetation to correction for range and incidence angle in laser scans of glaciers (Höfle 2007). Ratios have also been employed in hyper-spectral LiDAR to differentiate between vegetation and inorganic material (Chen et al. 2010). In addition to NDVI many indices have been implemented to limit the effects of variable lighting conditions due to changing solar zenith angle and atmospheric absorption. Haboudane et al. (2004) reviewed the majority of vegetation indices in common use. Those of most interest to this research used combinations of three different wavelengths, Triangular Vegetation Index (TVI):

$$TVI = 0.5[120(\mu_{750} - \mu_{550}) - 200(\mu_{670} - \mu_{550})] \quad 16$$

Modified Chlorophyll Absorption Ratio Index (MCARI):

$$MCARI = [(\mu_{700} - \mu_{670}) - 0.2(\mu_{700} - \mu_{550})]\left(\frac{\mu_{700}}{\mu_{670}}\right) \quad 17$$

and the Soil and Atmospherically Resistant Vegetation Index (SARVI):

$$SARVI = (1 + L)(\mu_{800} - \mu_{rb})/(\mu_{800} + \mu_{rb} + L) \quad 18$$

Where: $\mu_{rb} = \mu_{red} - C(\mu_{blue} - \mu_{red})$

L=0.5, to optimise the classification of vegetation.

C=0.1 to control the effect of the blues wavelengths

As the original use of the ratios was for vegetation classification tasks the wavelengths chosen were specific to water and chlorophyll absorption and transmission bands. A pseudo NDVI was proposed by Rottensteiner et al. (2005); created between the red band of an image and the IR laser intensity. Ratios of the laser scanner intensity values at different wavelengths are implemented in this research to normalise the effects of range and incidence angle variations within the scan data. This concept is further developed in materials and methods section.

3.3.1 Intensity Correction

Laser scanners usually measure the intensity of the return in addition to range or waveform. Intensity can be used, much in the same way as in image processing, in feature classification. However, the intensity is dependent on range and any process using intensity values must be related to range. In airborne laser scanning the distances are large and

the intensities must be normalised (Hofle and Pfeifer 2007). Incidence angle and type of reflection, specular or diffuse (Lambertian), are also major factors affecting the intensity of the returned pulse.

3.3.2 Surface Reflectivity

The reflectivity of a target surface or object affects the performance of ranging and scanning systems that use electromagnetic energy. The reflectance will be dependent on the wavelength of the radiation and the material and surface nature of the surface. For diffusively reflecting surfaces the reflected radiation can be idealised as a hemisphere with the maximum perpendicular to the surface (Figure 16). The coherent nature of the radiation can also influence the reflectivity. In most cases the radiation is incoherent except for laser radiation. An example of reflectivity of various diffuse materials for laser radiation at 900 nm is shown in Table 3 (Wehr and Lohr 1990).

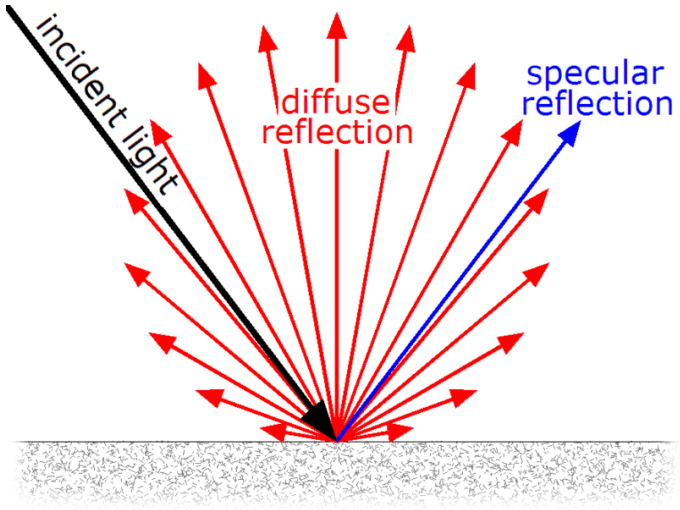


Figure 16 Diffuse and Specular Refection

Table 3 Typical Reflectivity of Materials at 900nm wavelength (similar wavelength to the FARO scanner).

Material	Reflectivity (%)
Wood	94
Snow	80-90
White masonry	85
Limestone	Up to 75
Carbonate sand dry	57
Carbonate sand wet	41
Concrete smooth	24
Asphalt with pebbles	17
Rubber black	5

3.3.3 Multipath

Multipath effects have been well documented in GPS but are also present in laser scanning were there are highly reflective surfaces (Schultz 2007). The observed multipath was characterised as the laser beam being reflected two or more times. The probability of multipath was found to be prevalent in scanning high reflective materials, scanning at close ranges and scanning corners (Runne et al. 2001). They found errors produced by multipath were found to be of any magnitude. Multipath was also seen to result in isolated pixels since the distance was highly different to the pixels in the neighbourhood. Multipath returns were mirror-inverted, which was seen especially when scanning windows.

3.3.4 Corners and Edges

A corner or an outside edge can induce scan range errors proportional to the beam diameter (Runne et al. 2001). Beam diameter (D) versus

range (R_r) of the FARO 3D 120 scanner are shown in Figure 17 the beam diameter on exit (D_0) 3.8mm and divergence (θ) 0.19mrad.

$$D_r = R\theta + D_0 \quad (19)$$

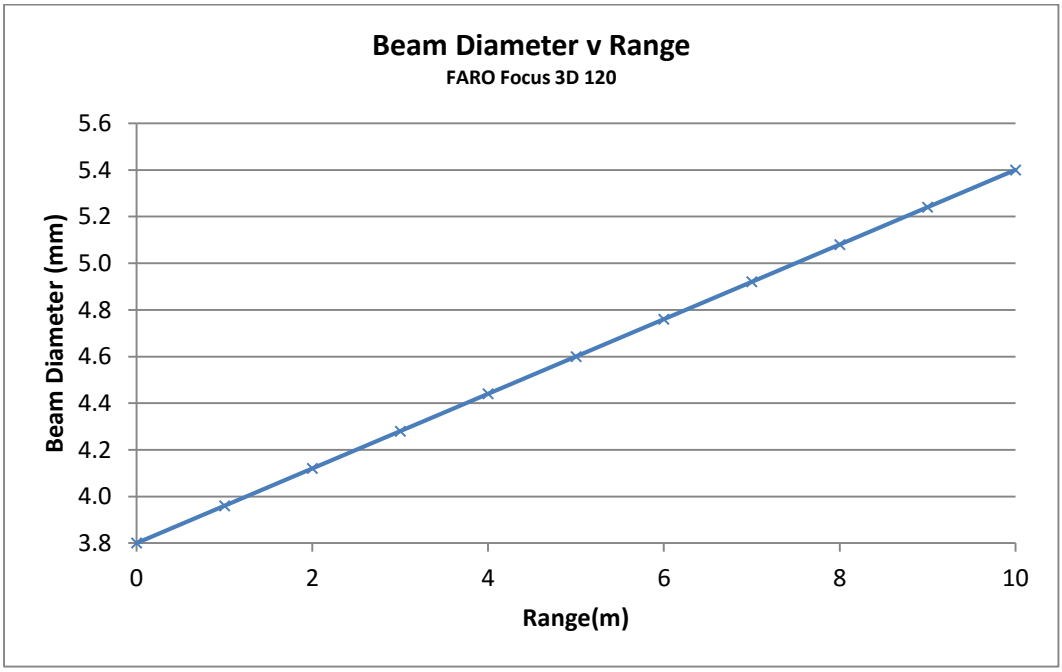


Figure 17 Range v Beam Diameter FARO 3D 120

Corners produce errors in range that are shorter than the actual range and edges longer (Figure 18). The error is proportional to range and inversely proportional to the angle of incidence (φ), Figure 19, range error (R').

$$R' = \mathrm{R} + \mathrm{R}.\frac{\theta}{2} + D_0 \quad (20)$$

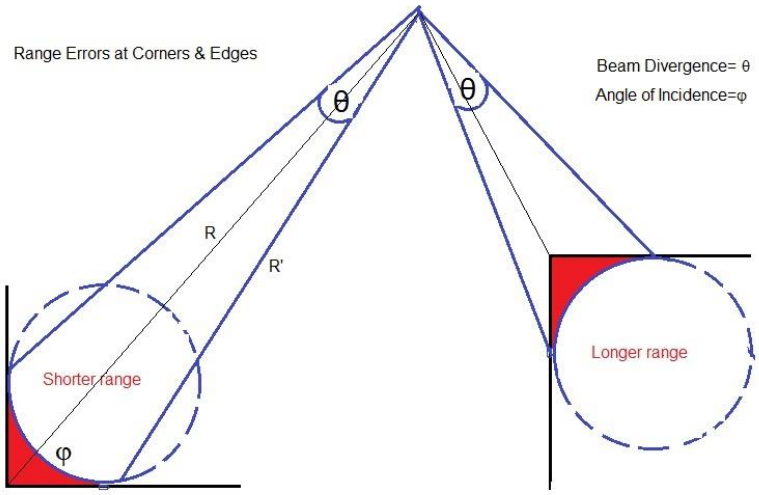


Figure 18 Corner and Edge Range Errors

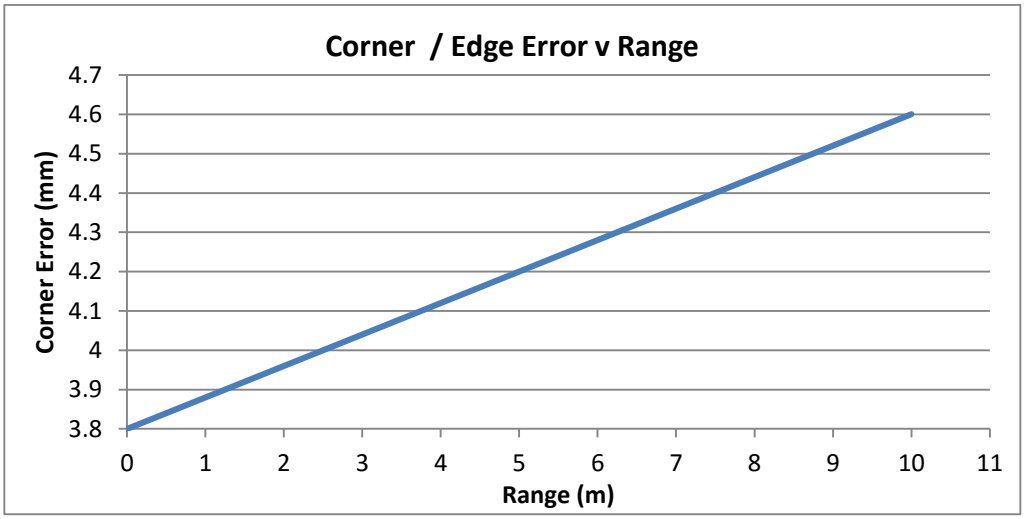


Figure 19 Corner and Edge Range Error

3.3.5 Range and Incidence Angle Effect on Reflected Intensity

The target, shown as a scanned image in Figure 20, was attached to a mount which could be precisely positioned both in angle and range. The target was matt finish white cardboard mounted to a hardboard base.

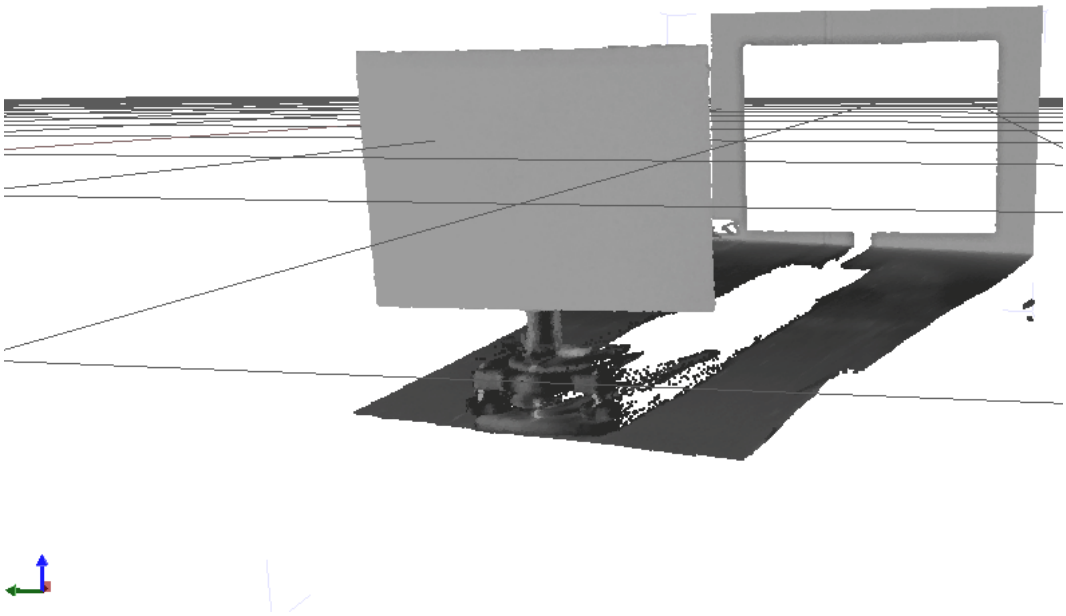


Figure 20 Plane test target for assessment of the effects of range and incidence angle on reflected intensity.

The scan of the target in Figure 20 clearly shows the shadow created by both the mount and the target. The scanner was place in a fixed position on a work bench and the target moved relative to the scanners X axis to vary the range. In this way both range and angle of the target could be varied. Initial scans were made with the target fixed at 2m and rotated in intervals of 10deg. Further scans were made with the target at intervals of 10cm from 1m to 2.5m from the scanner. To check possible effects of ambient light, the scans were carried out under ambient light and in complete darkness. Further scans were made with a target half white half black to check whether the intensity values are modified by the scanner software to stretch the intensity range (histogram stretch). Each set of scan data was processed to remove extraneous points outside the target area.

3.3.6 Retro-reflection

The range errors (increased range) can be the result of retro-reflection (Figure 21); retro-reflection returns a parallel ray back to the scanner regardless of the angle of incidence.

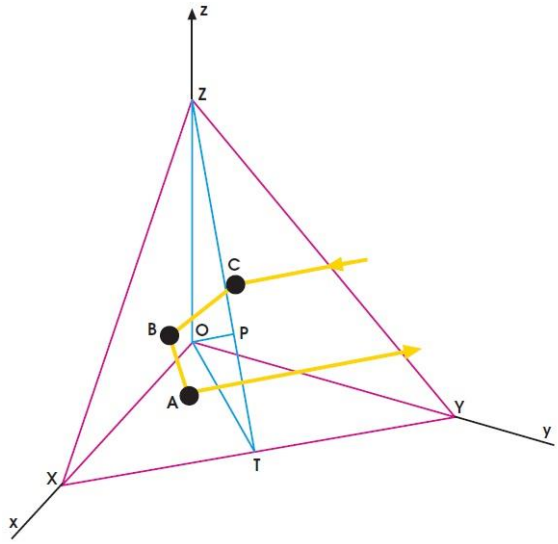


Figure 21 3D Corner Cube Retro-reflection

Retro-reflection increases the path length (Figure 23 shown in red) and it may also cause range errors due to saturation of the detector (Pesci and Teza 2008). Retro-reflected points appear on the same spherical angle as the incident ray but at an increased range, this creates the cloud of ‘ghost’ points.

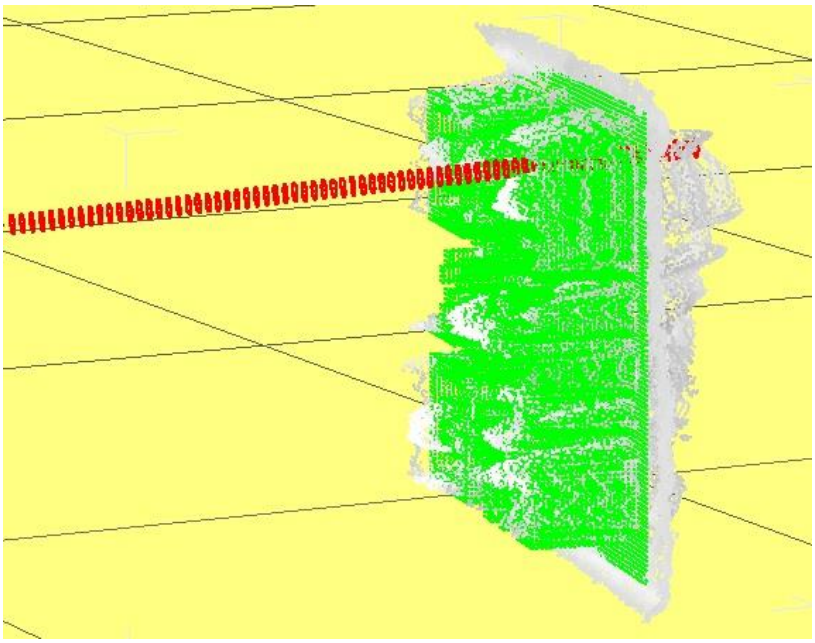


Figure 22 Ray traced to target including beam divergence and showing ‘ghost’ points [grey] caused by retro-reflection.

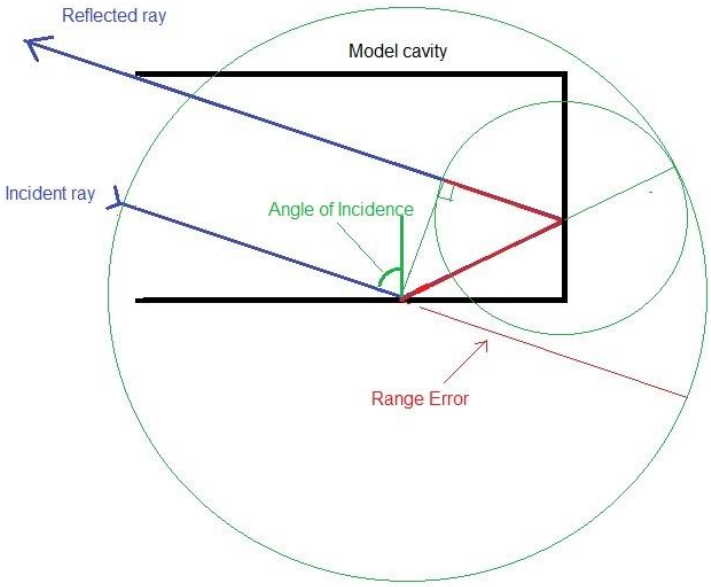


Figure 23 2D Retro-reflection

If the retro-reflection occurs twice, as shown in Figure 24, the ray is reflected at 90° to the incident ray and would not be detected by the

scanner. So we would expect that some points that should exist in the point cloud are missing. The number of reflections is dependent on the angle of incidence of the incident ray, the geometry of the reflecting surface and the position of the first reflection.

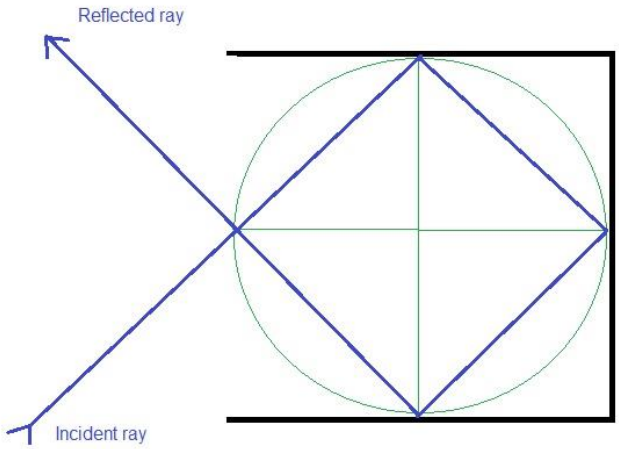


Figure 24 Double retro-reflection

3.3.7 Laser Speckle

Once considered a severe drawback to illuminating objects with laser light was the grainy image that was produced, this would be still apparent today if laser projectors were not modified to remove this ‘Speckle’. The speckle could in fact be put to good use as discovered by Butters & Leendertz (1971), they noticed that if the illuminated object was displaced by a small amount interference fringes were produced. They demonstrated that two speckle superimposed patterns produced a third pattern, this speckle pattern interferometry. Later this effect was modified to create holographic images which had apparent depth. Later in this work laser speckle pattern will be discussed concerning its possible influence on laser scanner reflected intensity measurement

Most natural and manmade materials are extremely rough when compared with the wavelength of visible (400-700 nm) or IR (700-1400 nm) light. The coherent nature of laser light causes constructive and destructive interference on reflection from a textured surface. Laser speckle, as this phenomenon was called, was recognised to be a special case of a well-known property light scattering known as Fraunhofer rings or ‘Coronas’.

The interference may reduce or increase the intensity of the reflected light, speckle has not been considered in any model of laser reflected intensity to date. The theory of speckle is described in a dissertation by Welde (2010) which investigates speckle reduction methods for laser projection systems and models speckle patterns in MatLab, an example is shown in Figure 25.

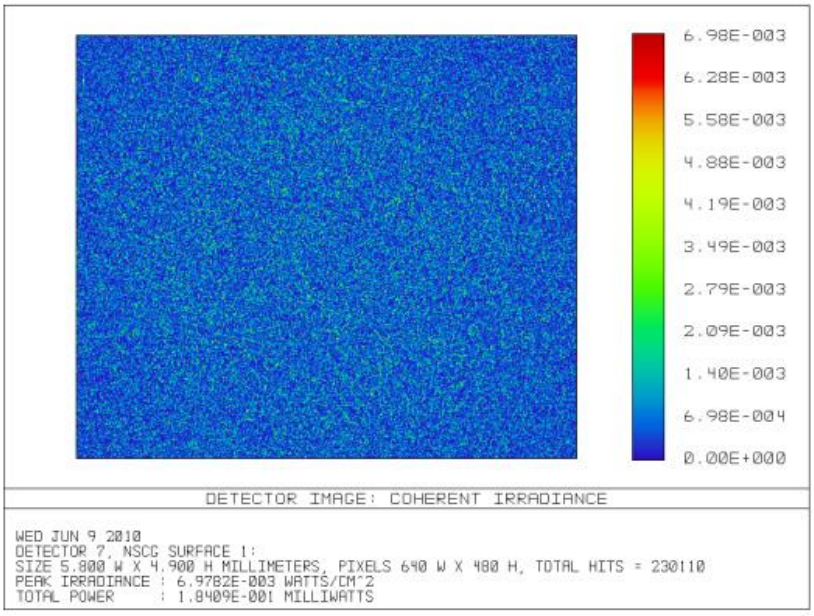


Figure 25 Simulated laser speckle pattern (Welde 2010)

In an attempt to quantify the speckle Duncan & Kirkpatrick (2008) produced an expression for the smallest speckle σ as:

$$\sigma = \lambda R/S \qquad 21$$

Where: R is observation range, λ wavelength and S cross-section of beam.

A method of speckle pattern reduction was proposed by Akram (2011) which uses a rotating sinusoidal grating. If multiple wavelengths of Laser are used then a surface texture will have different but consistent speckle patterns related to the scale of the texture, in assisting an MSc student in laser scanning of concrete blocks damaged by fire (Vickers 2013), it was noted that there was direct relationship between reflected intensity and the texture of the concrete blocks. The intensity gave better clues to the surface texture than the range measurements as the texture scale was less than the range error of the scanner. An example of the distribution of reflected intensity in relation to different surface texture scale is shown in Figure 26, it was not proven that this effect was due to speckle. An image of the block is shown in Figure 27, range in Figure 28 and laser intensity variation in Figure 29.

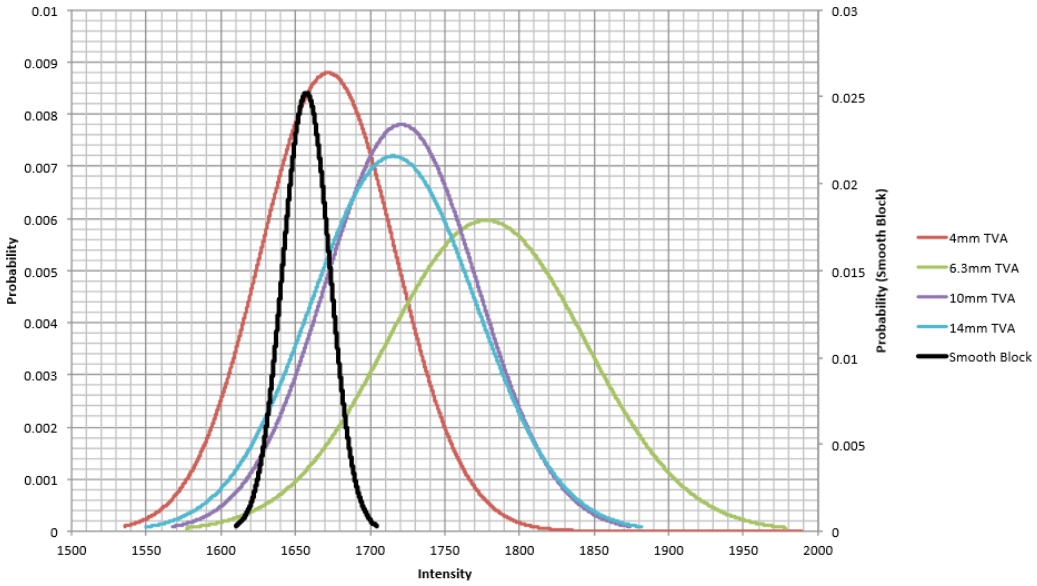


Figure 26 Distribution of reflected laser intensity from concrete blocks of different texture. (Vickers 2013)



Figure 27 Image (A) of concrete block 4mm roughness.

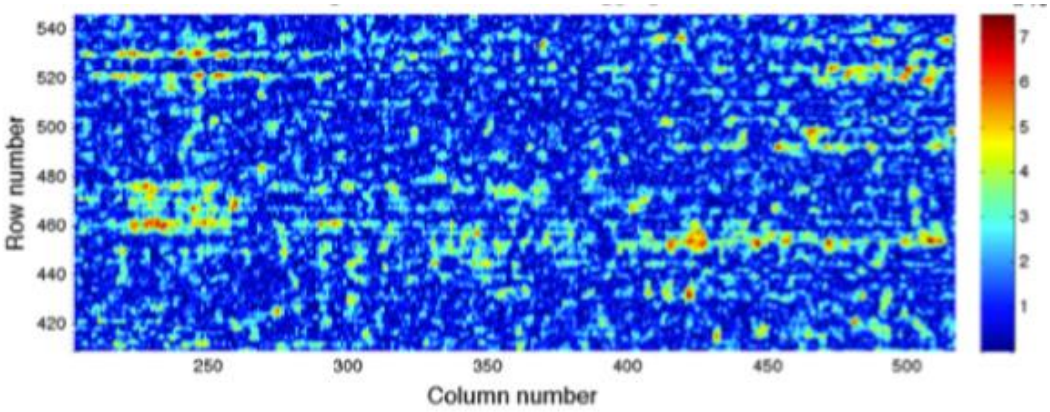


Figure 28 FARO[120] scan of concrete block (A), range 10^{-3} m

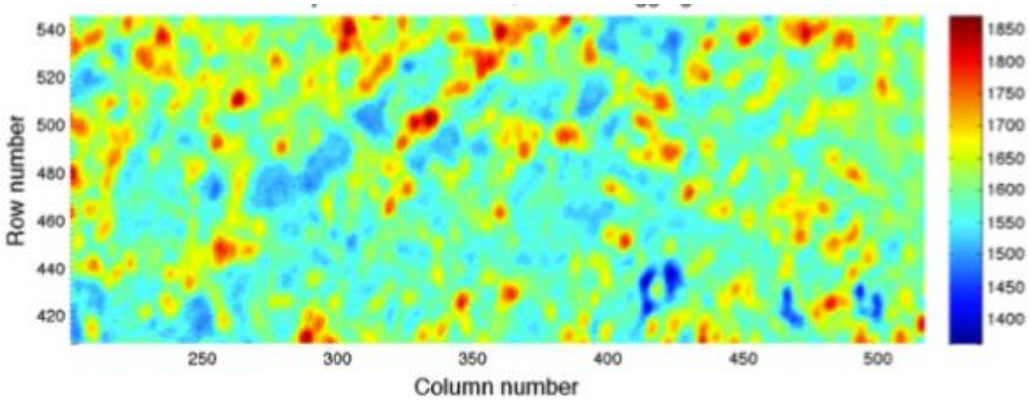


Figure 29 FARO[120] scanner intensity plot of block (A). Scale in laser scanner intensity DNs.

The possible relationship between intensity and surface texture, if related to speckle, should be with respect to the micro not macro texture. The concrete block had both macro (±2mm) and micro (±50µm) texture. The range data showed no relationship to the texture, most likely due to the texture size being of a similar order or less as the range precision, which for the FARO scanner was 2mm. The conclusion was that the speckle would change the reflected intensity of a laser scanner dynamically with time and would be dependent on the surface texture. Continuous wave scanners usually record reflected intensity as the RMS value for each point and time-of-flight scanners often sample the target surface many times for each resultant measurement of range and intensity. These measurement methods act as a low pass filter and therefore would probably disguise any affect that speckle would have on the final recorded intensity value.

3.4 Analysis of Factors Affecting Reflected Intensity

Six factors were identified that were thought to influence reflected intensity values recorded by the laser scanners; surface type, colour,

range, angle of incidence, ambient light and surface contrast. The influence of surface type was sub-divided into texture and material. From the data collected as stated in the previous section analysis was carried out to attempt to identify how each of the six factors influenced intensity values. As the aim of the research was to classify surface types using intensity values, the intensity values would need to be normalised for the influence of the four remaining factors: range, angle of incidence, ambient lighting and surface contrast. The effects of range and incidence angle are demonstrated as an example in Figure 30. A FARO reference sphere, 0.75m radius, was used in this investigation as this provided both variation in range and incidence angle concurrently using the same surface and therefore could be correlated with more confidence.

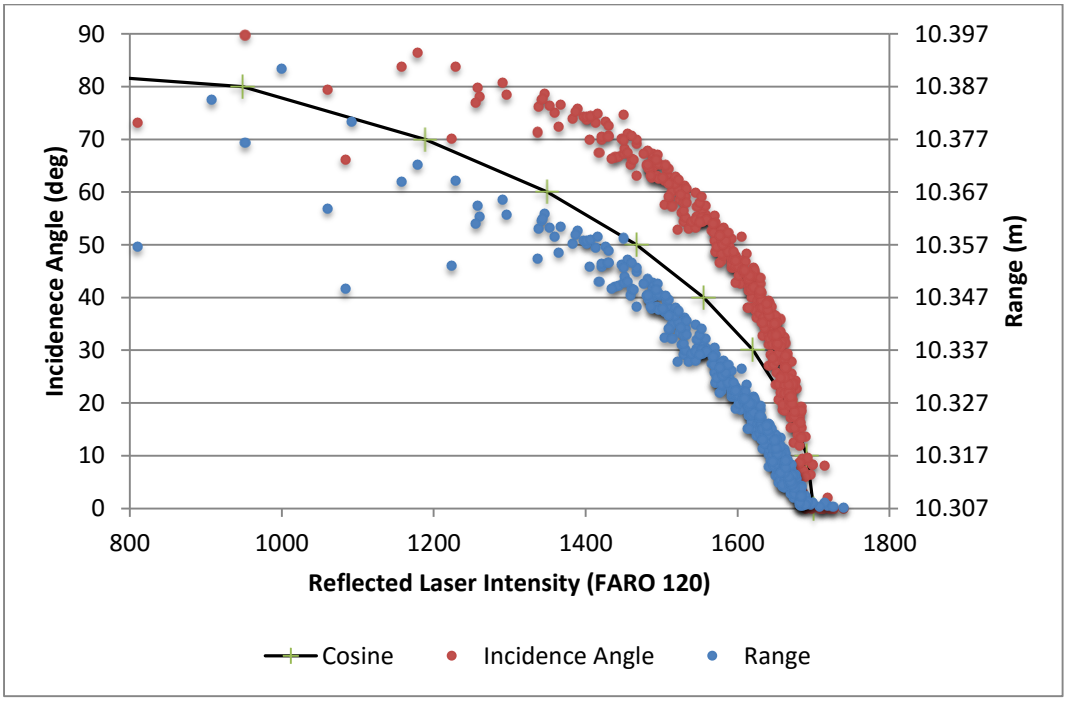


Figure 30 Variation of reflected laser intensity with change in range and incidence angle on a sphere (FARO[120]3D scanner, FARO registration sphere target)

3.4.1 Ambient Light

Some research (S. Lemeš 2009) (Voegtle and Wakaluk 2009) has indicated that the measured reflected intensity from a surface is affected by the ambient light, due to the scanner receiver being able to measure light intensity within the wavelength of the ambient light source. Others found that the difference between the intensity values in darkness and in ambient light were within the normal variation (noise) (Pfeifer et al. 2007). For a technique of classification that relies on intensity values it was important to confirm the effect of ambient light.

Initial testing considered artificial lighting, fluorescent light. The same target was used in the previous trial was scanned with the lights on and off, Figure 31, to investigate if ambient light affected the reflected values. The target was scanned in complete darkness and in fluorescent light at various ranges and angles of incidence.

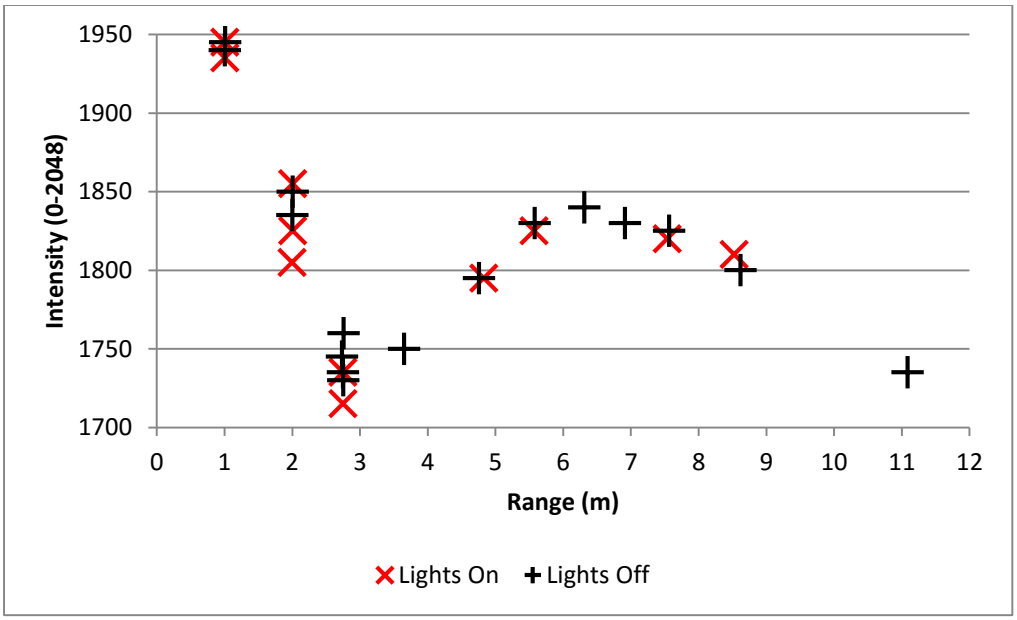


Figure 31 Variation of laser reflected intensity with range, with ambient light and in darkness (FARO[120]Focus 3D, white reference target).

3.4.2 Range

The FARO ^{3D} 120 was used to scan a planar, white A4 size target at ranges from 1m to 11m and a similar sized black target was scanned from 1m to 3m. The scan was in a sector which just encompassed the target to reduce the data size. After scanning, the data was post-processed to extract only the target scan points. The results of intensity versus range are shown in Figure 32. The intensity values are an average of the centre scan points on the target; this was hoped to reduce the influence of incidence angle at ranges of the same order as the width of the target.

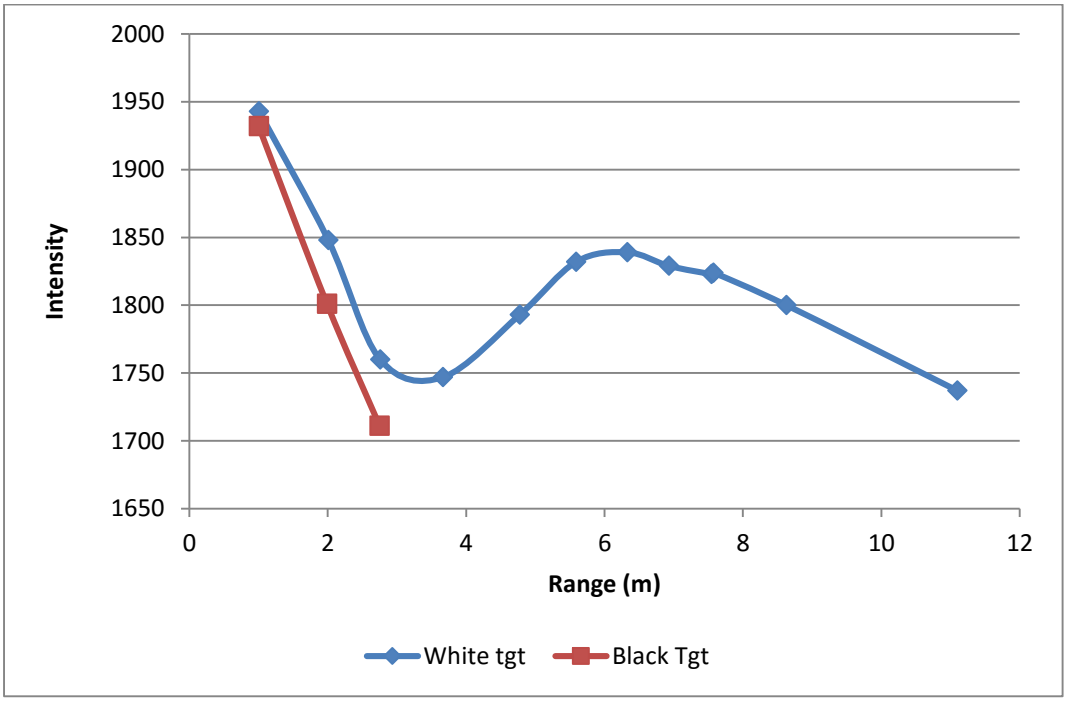


Figure 32 Intensity v Range (FARO^{120} Focus 3D) using a black and a white target, the black target values were only measured to 3m range.

These initial results clearly show that for this scanner the intensity values were not a simple function of range. The previous section on scanner characteristics was reflected in the results; the intensity values

were attenuated at close range. It is understood that for the receiver to remain sensitive over the design range envelope, close range reflectivity would need to be attenuated to prevent receiver saturation. If the receiver saturated below a certain range the intensity values below this range would be identical. The intensity values for the white target were similar at close range, but the black target reflectivity was increasingly lower than the white target as the range increased.

The ranges recorded by the scanner were subject to error, this is shown by the distribution of scan points in range either side of the planar surface. A measure of the error can be calculated by the volume of the generated surface which if planar should have no volume; the standard test for co-planarity. The FARO scanner measures range by phase difference, the Leica by time of flight. Range measured by phase would be expected to have errors related to the wavelength, time of flight to oscillator frequency.

3.4.2.1 Range error using a Planar Surface

To measure the scanner's range error to a surface often a geometric primitive is fitted to the data points using a least squares fit; this shows the error from the mean but not the absolute error. The plane was a white card placed approximately central to the –y axis of the scanner. Row and column data was exported with the x,y,z, and intensity values of the scan. A single row of data points was used to plot the range; this shows a close correlation between the predicted and scanner range. From previous results, Figure 32, it was found that the intensity at

ranges less than 2m increases with decreasing range. A plane surface was scanned with the FARO 120 scanner, the theoretical range r' to the surface was calculated.

$$r' = \sqrt{\left(r_{ref}^2 + c^2 - c'C\right)}$$

Where:

r_{ref} reference range to the plane.

c distance between neighbouring points.

c' distance to point from reference.

C width of scan line.

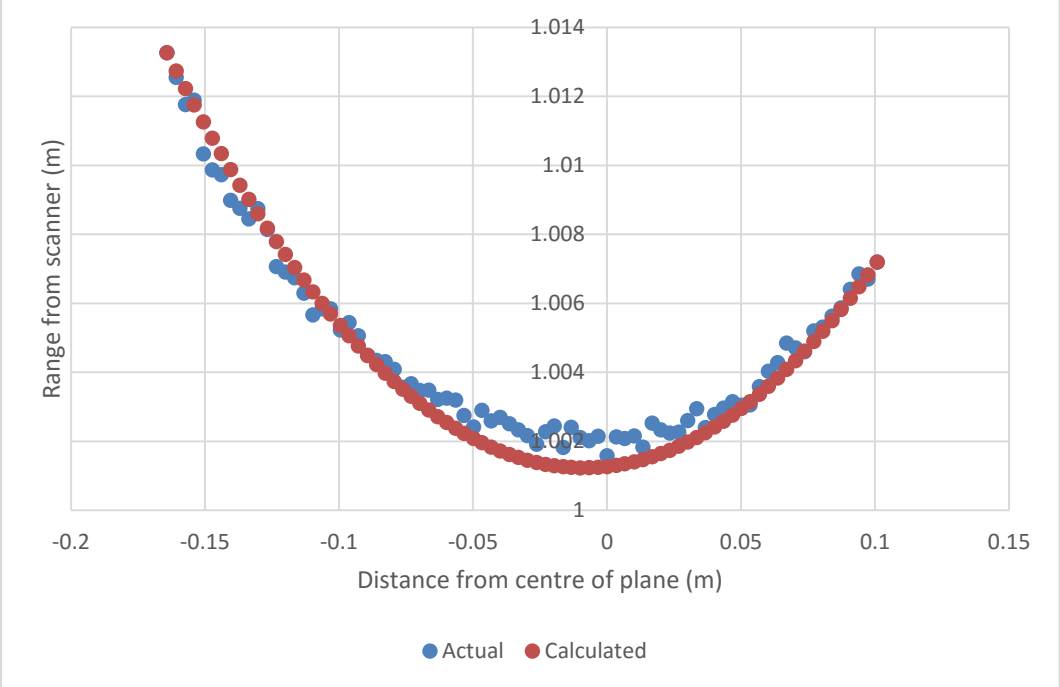


Figure 33 Comparison of calculated to actual range, FARO 120 scanner.

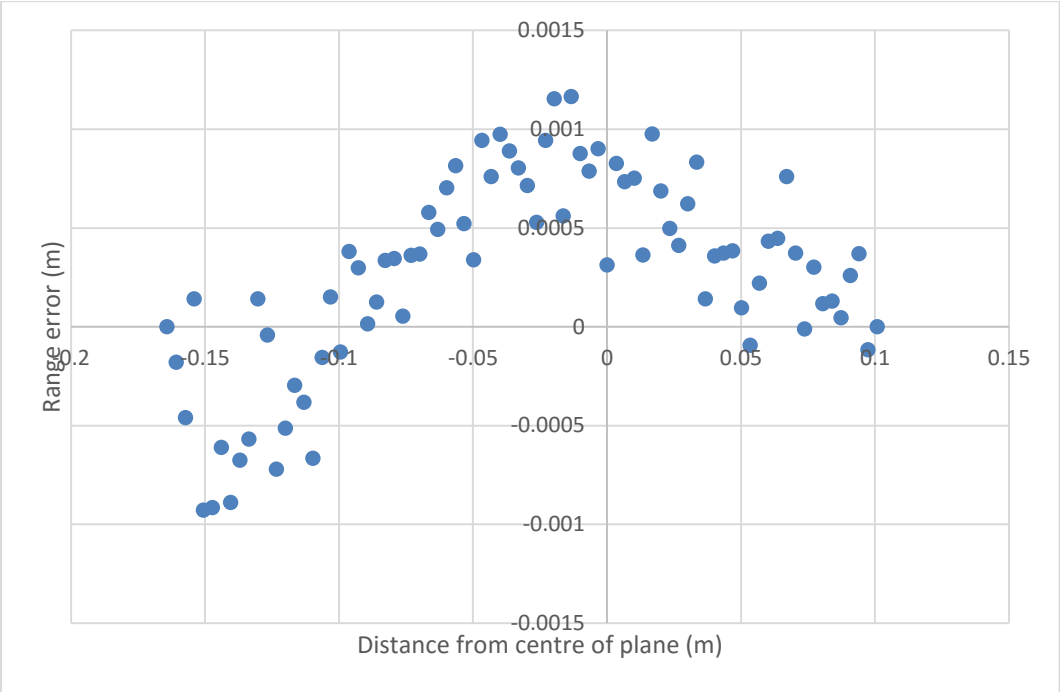


Figure 34 Range error from calculated plane, FARO 120 scanner.

This comparison made it possible to analyse the scanner range measurements. The resulting analysis showed a very good match between the calculated and actual scan ranges, 95% being ±1mm, with a maximum deviation of 1.5mm

The scanner was a FARO 3D 120. Figure 35 shows the intensity variation across the plane, used in the previous range prediction experiment; the results show the intensity variation correlates with the range variation. Figure 36 shows the previous results with intensity overlaid to the same scale (the values have been inverted so correlation with the range profile can be seen).

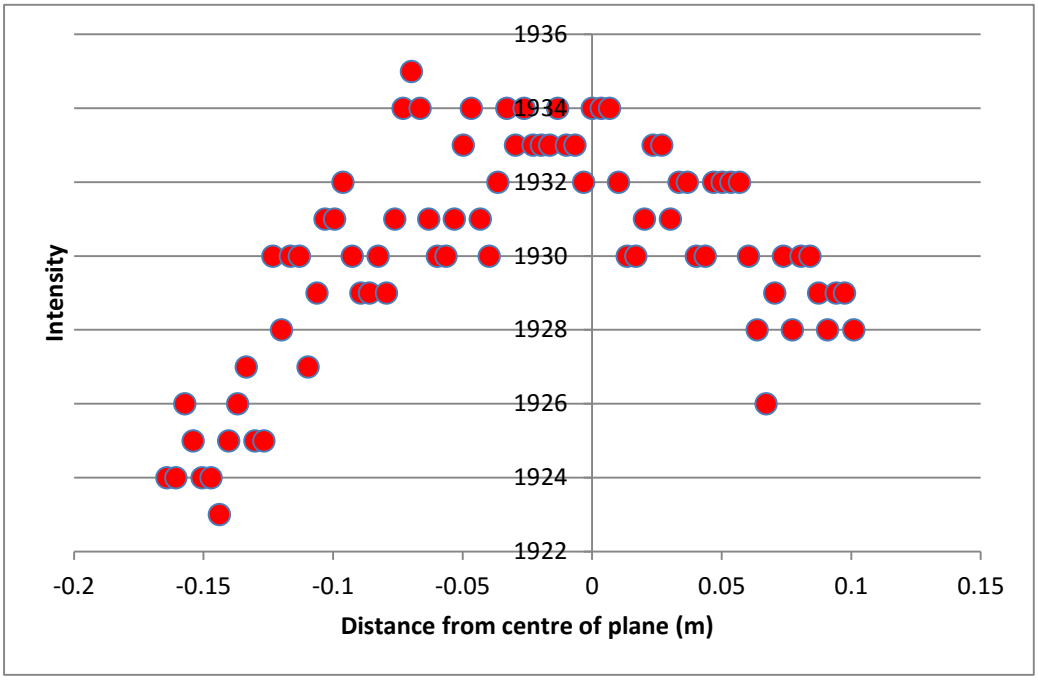


Figure 35 Variation in Intensity across a plane. Data from FARO 120 scanner.

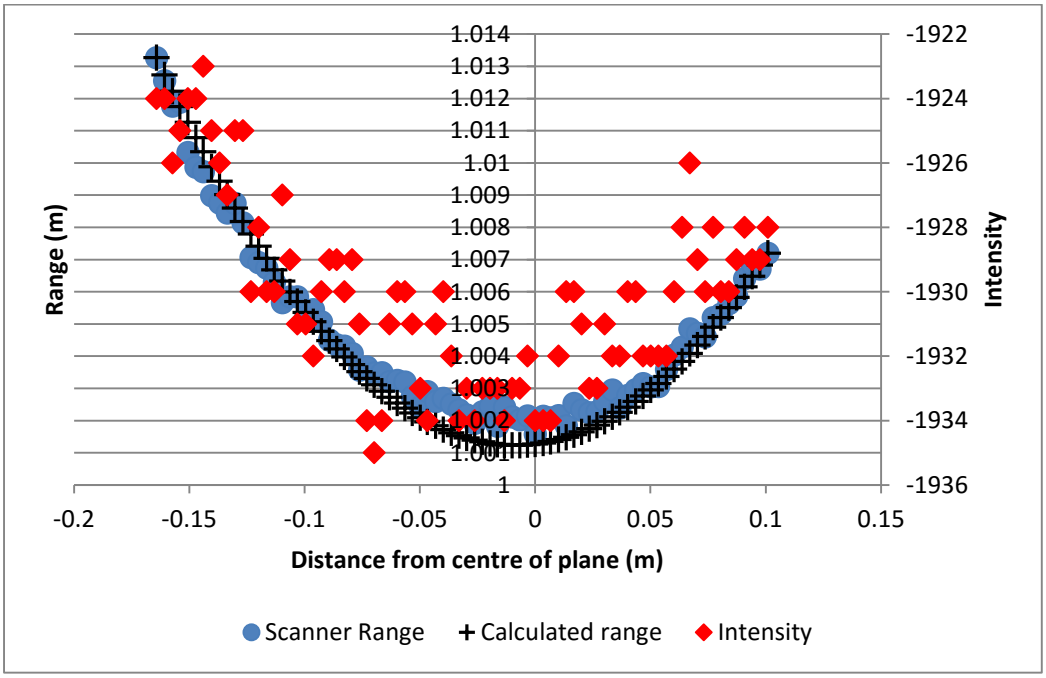


Figure 36 Variation of range from scanner and intensity. The intensity values are inverted to visualise the correlation with range and chord. Data from FARO 120 scanner.

3.4.3 Angle of Incidence

To calculate the angle of incidence the angle between the incident ray and the normal to the surface must be known. The normal were calculated as vertex normal using three neighbouring points. To investigate the variation of angle of incidence a plane surface was scanned at different angles, varying from 0° – 85°. The relationship between the angle of incidence and intensity for the FARO ^{3D} 120 scanner at 2m is shown in Figure 37. These scans were carried out with no ambient light so that there would be no influence from any light source other than the laser itself. Two targets were used, one white and the other black, made from A4 card stock. The black target returns were lower in intensity than the white; this was the expected result, but not as much as expected. The small difference in intensity between the different colour targets was thought to possibly be due to surface texture; this was investigated later in the research.

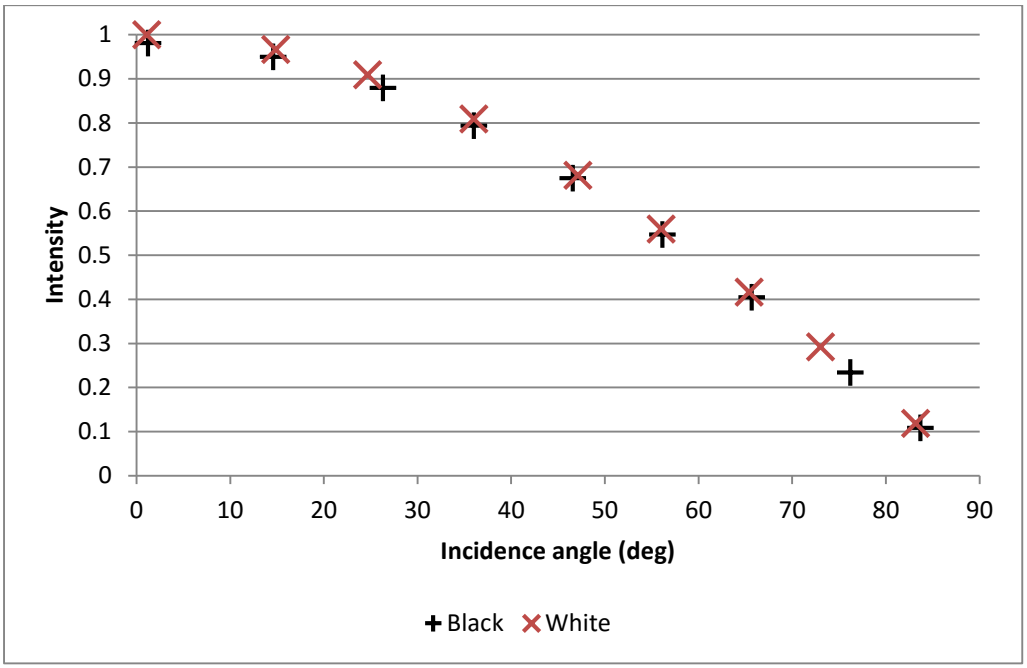


Figure 37 Variation of laser reflected intensity with incidence angle and target colour (FARO[120]Focus 3D). The intensity is normalised to the white target at zero incidence angle.

3.4.4 Intensity Normalisation – Idealised Test Case

(Nitzan et al. 1977) used the basic model of intensity variation with angle of incidence and range; this proposed that intensity was inversely proportional to the square of the range and directly proportional to the cosine of the angle of incidence. To test this case an idealised plane surface was created as a point cloud. The plane's intensity values were calculated using equation 22, where intensity (ρ), angel of incidence (θ) and range (R).

$$\rho = \frac{\cos\theta}{R^2}$$

22

The angle of incidence was calculated from the dot product of the unit normal and unit vector at each point. The results of applying the normalisation function to the ideal plane are shown in Figure 38.

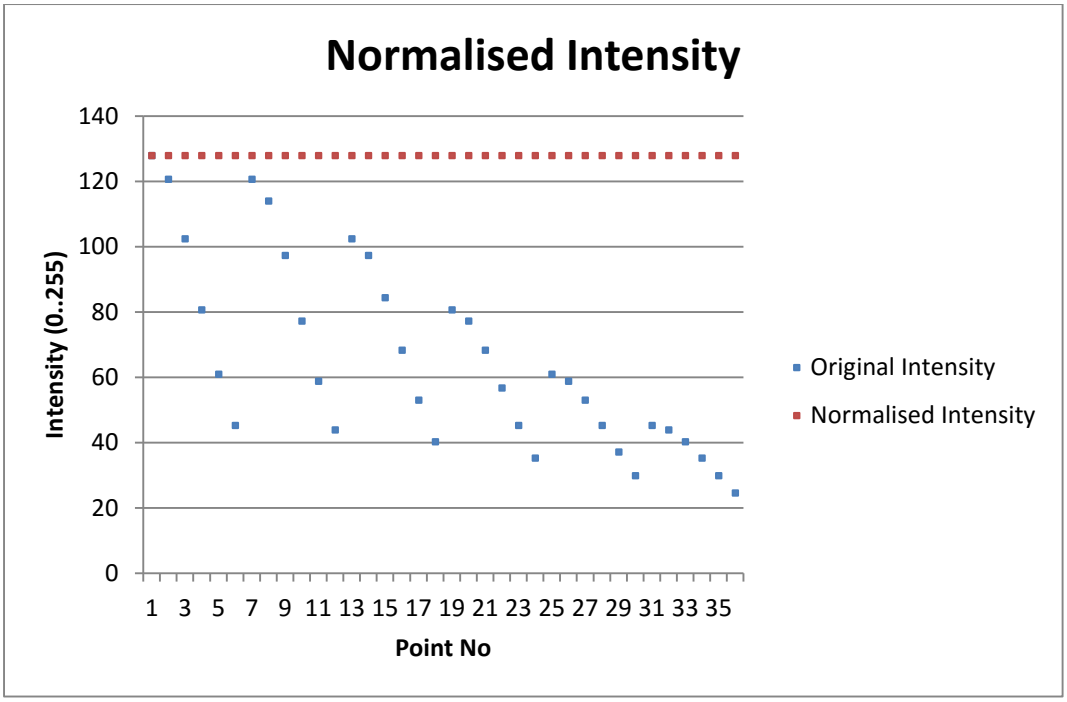


Figure 38 Normalised intensity for an ideal plane

Some initial results have shown a slight difference between the intensity values at the same range and angle of incidence with and without ambient light.

3.4.4.1 Surface Material Absorption and Reflection

A full scan of the interior of the NGI building lobby was made using a FARO^{3D} 120 scanner. A section of this scan was displayed in 3D with the intensity values scaled to a colour map; initial investigation of a wall in this section discovered that the intensity values showed a variation which correlated with the position of the studs. Figure 39 shows the

section of the scan and the intensity values mapped to a contrast stretched colour map.

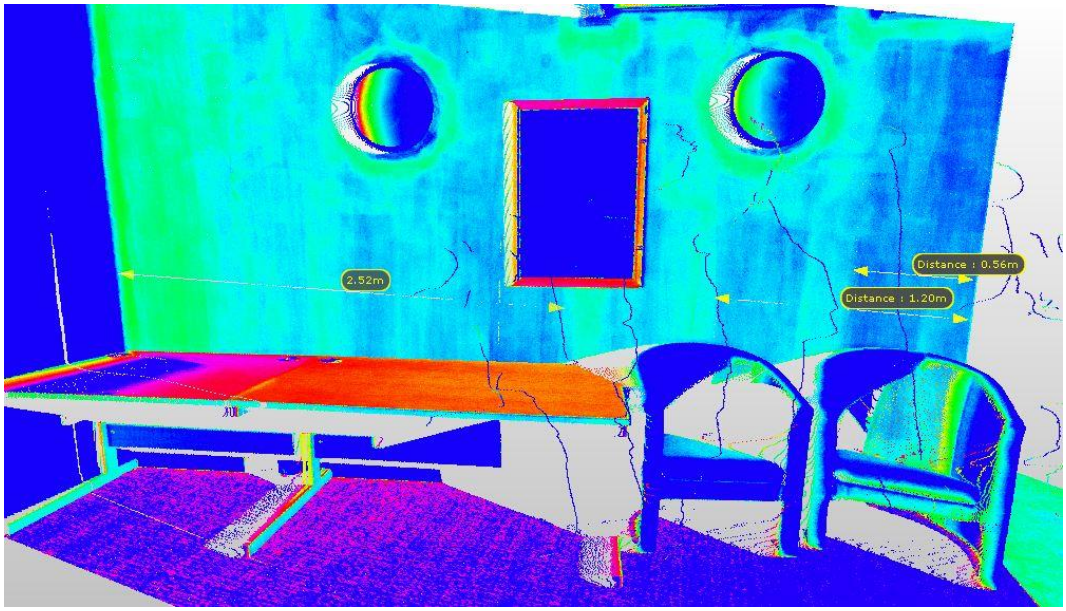


Figure 39 Section of NGI lobby scan

The stud spacing was measured for 2 studs, the distance from the right end of the wall to the 2 nearest edges of each stud were: 0.53m, 1.22m. Figure 39 shows the measurements that were made to the marked change of intensity in the scan: 0.56m and 1.20m. Initially it was assumed that the variation in intensity was due to a surface texture in the region of each stud causing a change in angle of incidence and hence intensity. The top left image in Figure 40 shows the dot product of the surface normals with the primary axes; this image would show the same pattern as Figure 39 if the intensity changes were due to surface texture. [need to reproduce image with same colour map and view angle]

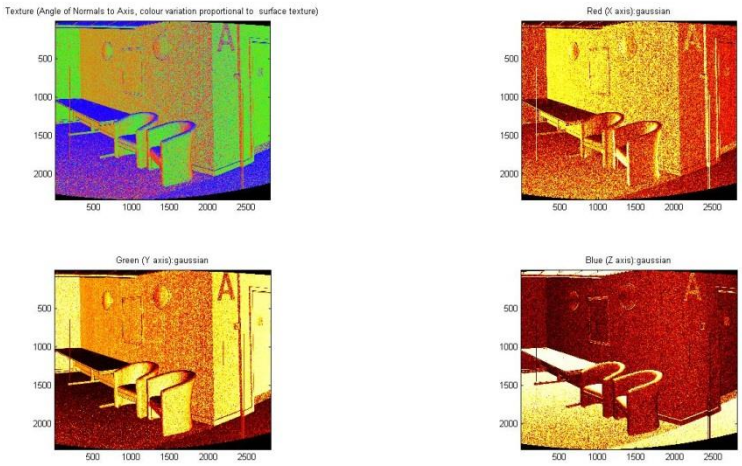


Figure 40 Dot product of surface normals with primary axes

The FARO scanner that was used has an infra-red laser (800nm wavelength) and a detector which is optimised for infra-red wavelengths; the variation across the surface was consistent with the variation in the painted surface.

To investigate further in to these phenomena an IR digital camera was used to record the IR signature of the scan section. The variation in intensity was so low that the image was histogram equalised (Figure 41).

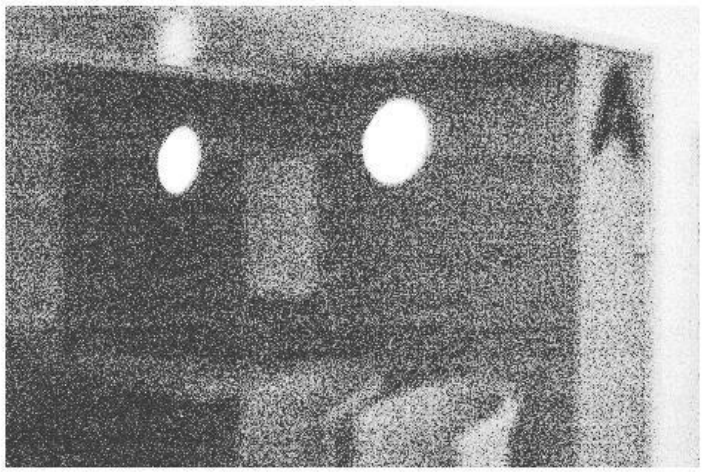


Figure 41 Histogram equalised IR image of wall

The wall section was re-scanned and the result is shown in Figure 42, this scan was made at a higher resolution and clearly shows the brush/roller strokes of the paint on the wall. The texture of the paint is well below the resolution of the scanner; therefore, one theory was that the paint was absorbing the laser proportional to the paint thickness. Another theory was that the micro-texture (due to the type of brush or roller) changes the reflectivity of the paint. The effect may have been more noticeable on this particular wall as it is painted red, unlike the white of the remaining walls, especially as the laser was IR.



Figure 42 Re-scan of section of wall

The wall was also scanned with a Leica HD300 scanner, the results of this scan did not show any of the characteristic effects of the FARO scan (Figure 43).

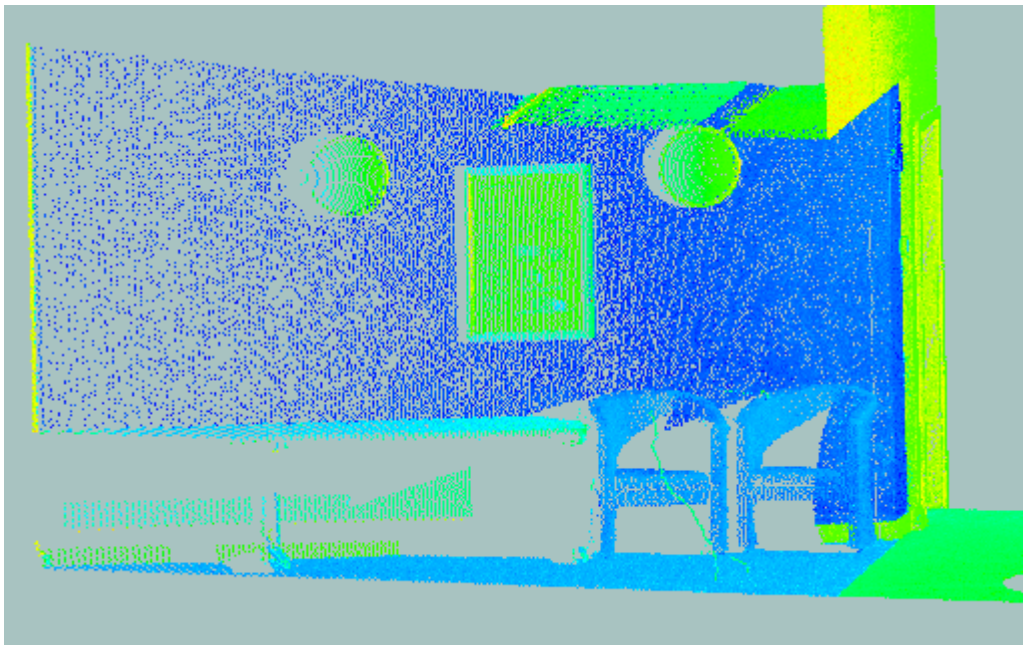


Figure 43 Leica HD 3000 scan of wall

The resolution (point spacing) of the scans were: FARO ^{3D} 120 6mm @ 10m, Leica HDS3000 scan 25mm @ 10m.

3.4.5 Normalising Intensity for Range and Incidence Angle using Scan Point Density

Point cloud density depends on the angular resolution, but also on the scanning geometry: the incidence angle and range to the reflecting surface. Point density decreases with increasing range and increasing incidence angle (Lindenbergh et al. 2005). Point cloud density was based on the number of nearest neighbours to each individual point; the radius of nearest neighbours was set by experimentation dependent on range variation and scanner angular set interval size. Many attempts have been made to normalise reflected intensity using the known incidence angle and range of the laser pulse. Laser scanner point clouds have a defined structure dependent on the angular interval between pulses and the surface geometry the beam is reflected from; this attribute can be used to correct (normalise) the reflected intensity for varying ranges and angles of incidence. To demonstrate this effect planar and curve surfaces were scanned and the density of nearest neighbour points was calculated. The strength of the reflected intensity was then compared with range, incidence angle and point density. The results showed an inverse relationship between point density and range and incidence angle (Figure 44 Laser reflected intensity (A) point cloud density (number of neighbours) (B) versus incidence angle of a plane).

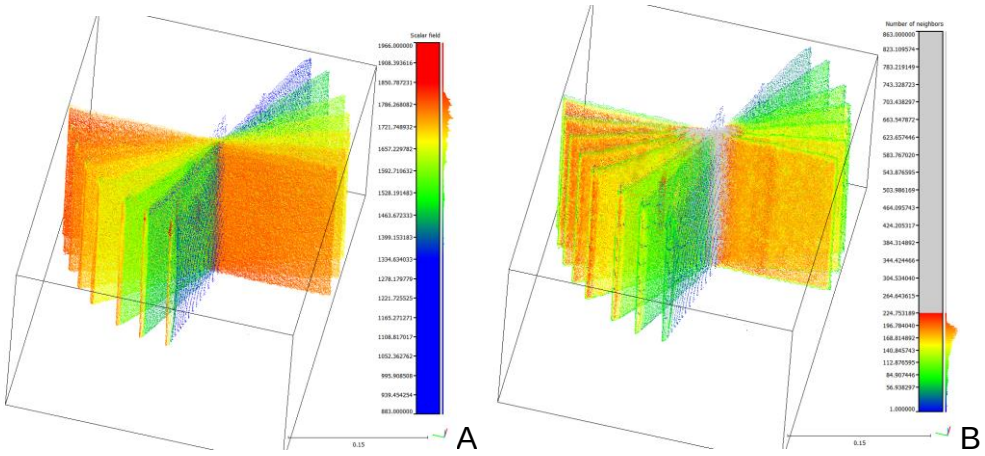


Figure 44 Laser reflected intensity (A) point cloud density (number of neighbours) (B) versus incidence angle of a plane. Right hand scale denotes DN values of intensity.

To show the relationship between reflected intensity, incidence angle and point density the ratio (normalised to a range of -1 to +1, similar method as NDVI) was calculate between intensity and point density. The point density was calculated by counting the number of nearest neighbours within 5mm of each point. The plane target was A4 in size and white in colour at a range of 2m.

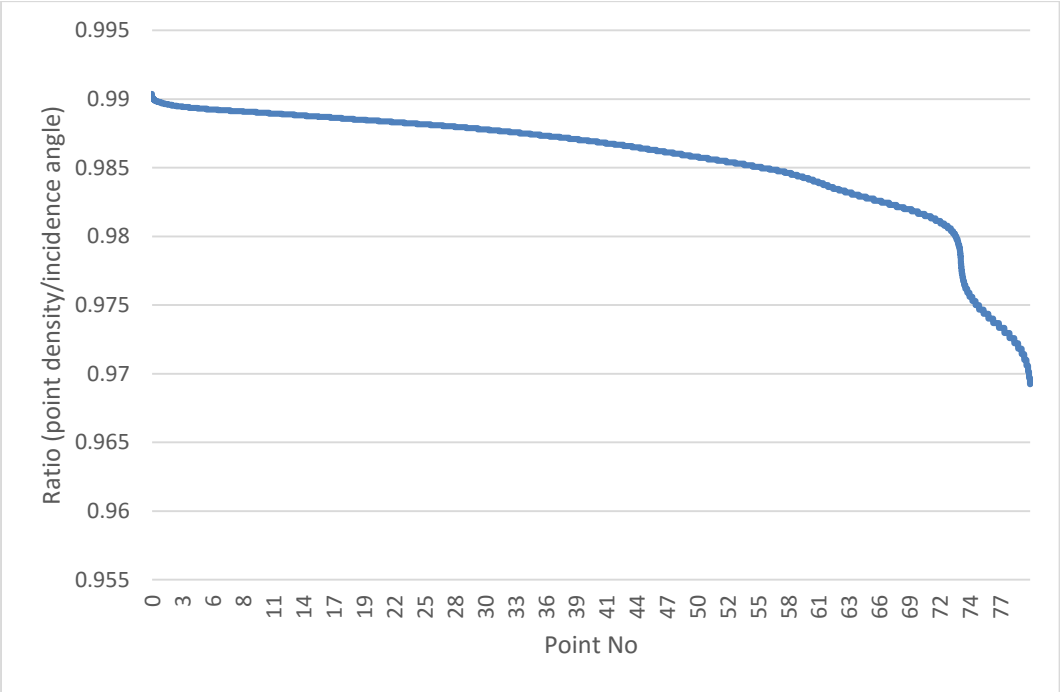


Figure 45 Point density / incidence angle.

The ratio of point density and incidence angle remained almost constant up to an incidence angle of 70° (variation of <0.01%). The close correlation between point density was expected because of the geometry of the laser scan; the repeatability of this geometry suggested that point density could normalise the reflected intensity for variations in surface incidence angle. When this concept was applied to a scan of a building with materials of varying reflectivity the incidence angle and range variations were corrected in such a way that common materials gave a constant reflectance value.

3.4.6 Point Clouds

In order to provide the required inputs for a classifier, the raw scan data was processed using several custom designed software tools. The input values identified for the surface shape and orientation experiment

were the surface normals. The tools were created using MatLab. In the process of creating these tools aspects of the characteristics of the scan data became apparent that affected the design of the tools.

The majority of tools created would require the knowledge of coordinates of each point's nearest neighbours; a face normal calculation requires at least 2 neighbouring points. To provide fast access to the nearest *k*-neighbours a tool to index the point cloud was created. The most common method of indexing scan data is a data structure called an Octree, which is the recursive subdivision of space into octants (each node has 8 child nodes). With an Octree approach the size of the smallest octant will control the number of neighbours returned, whereas a kD-tree will return *k* nearest neighbours regardless of the Euclidean distance to the neighbours; a threshold can be introduced to control the distance.

As the test targets were simple planes a *k* nearest neighbour index routine was sufficient to provide an index which could be used to calculate the face and vertex normals. Scan data of more complex surfaces benefit from the Octree approach as the Euclidean distance between neighbouring points is less than the size of the child octant selected.

3.4.7 Difficult materials for laser scanning

Certain types of glass do not reflect near IR light, which presented a problem for the FARO scanner, which transmit at 900nm wavelength.

The glass in the buildings shown in Figure 46, was not detected by the FARO scanner.



Figure 46 Two buildings with glass which was not detected by the FARO 120 laser scanner. Image of buildings shown with the respective scans shown below.

The highly reflective cladding on both buildings was also not detected by the FARO scanner at high incidence angles.

3.4.8 Index Point Cloud

A function was created which indexed a scan data file and created a new file with the original point position plus the index of the *k*th nearest neighbours. Both FARO and Leica scan points are stored row then

column; the index was created by scanning *n* points behind and ahead, calculating the Euclidian distance to each point. The index of the points and the corresponding distances were stored in an array, this array was then sorted by distance and the *k*th smallest distances indexes were save to the output file. This file could then be used by other functions to rapidly access neighbouring points. An additional threshold could be applied to remove outlier points. Pseudo-code of the function is in Appendix B.

3.4.9 Effect of Range Error on Surface Normal Vectors

A function was created to calculate the face normals of a point cloud. A face normal was calculated from the cross product of two vectors from a point to two neighbouring points, a chosen point and its two nearest neighbours, the only exception was three points which were collinear, in which case the normal direction was indeterminate. The sign of the dot product between the normal and the point vector was used to ensure the normals pointed toward the laser scanner; the dot product between two vectors is positive for angles less than 90°. The normal vector was converted to a unit normal by division of its length; this allowed the same file to be used to calculate the angle of incidence of a laser to a surface in the material classification task. Figure 47 shows the face normals of scan (D3), shown in green, incident laser shown in red.

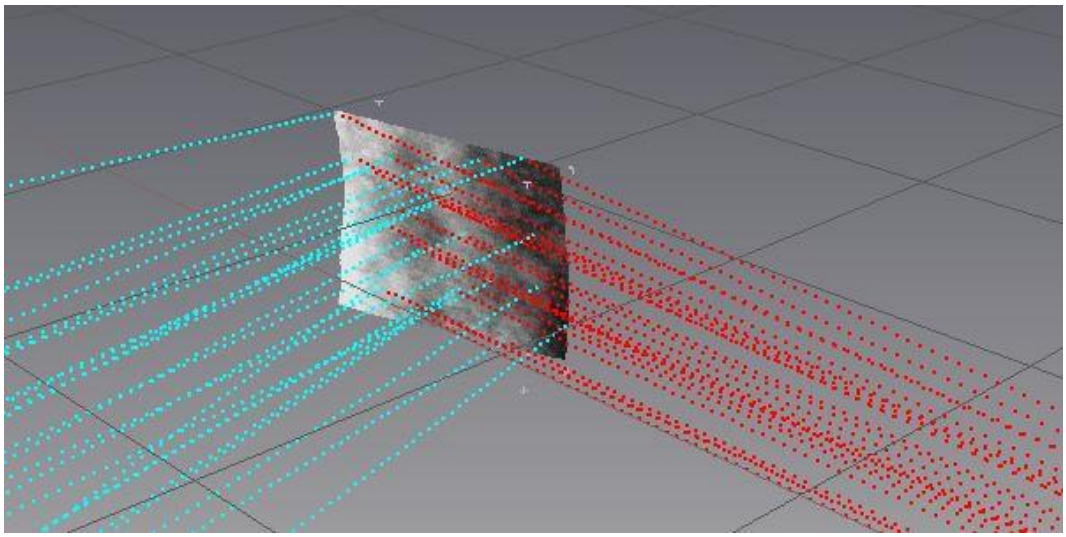


Figure 47 Face Normals (green), Incident laser(red)

The target was a smooth plane and therefore the normals should have been 90° to the surface; the results show that the calculated face normals had a high degree of divergence from 90°. To verify the face normal algorithm an artificial perfectly flat plane was used as input, the results (Figure 48) verified that the algorithm was correctly computing the normals.

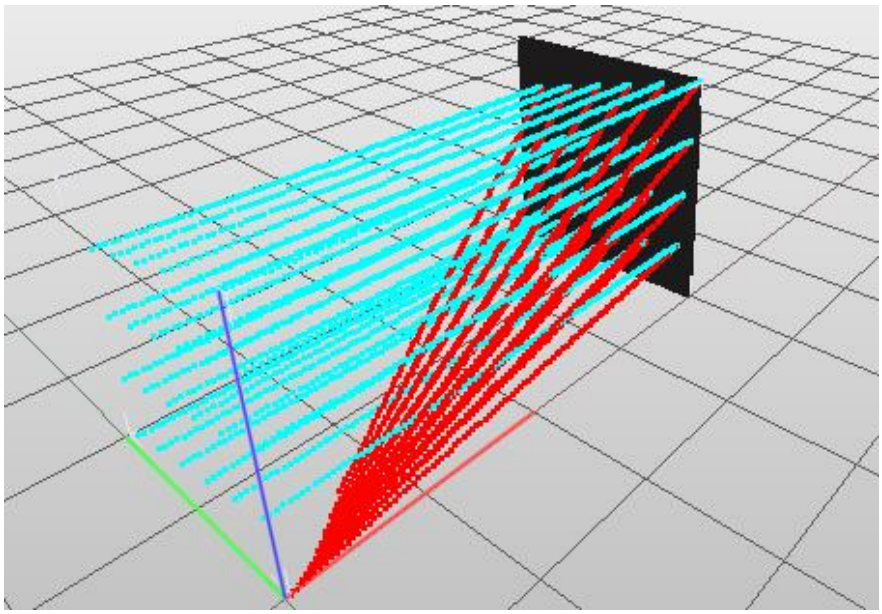


Figure 48 Artificial Plane Face Normals

The range error is approximately ±2.5mm, Figure 49 shows the error in the normal as a function of the inter-point distance and range error.

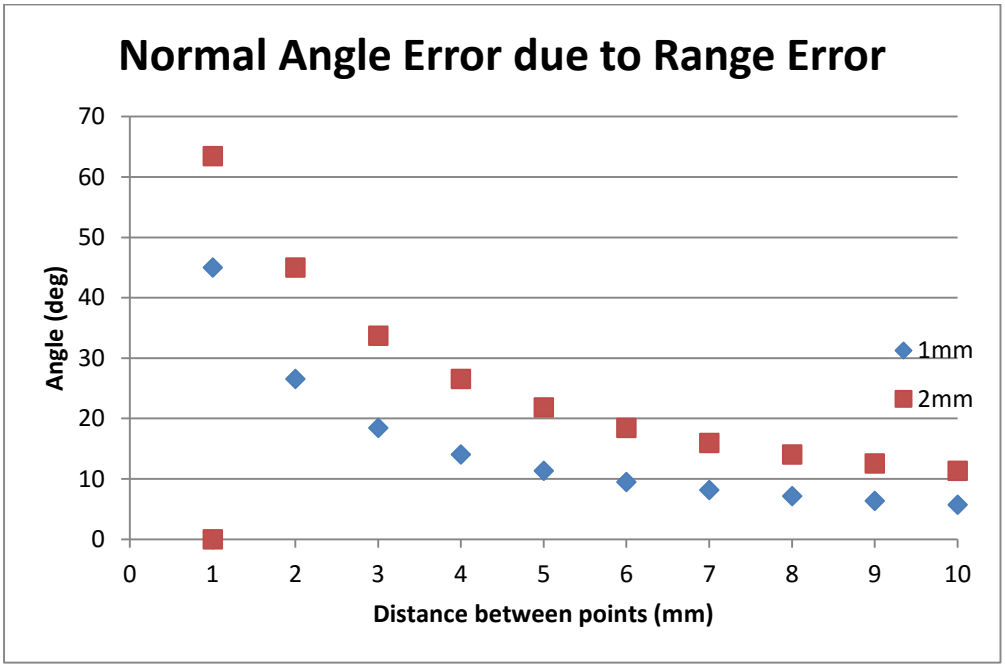


Figure 49 Normal angle error due to range error

As range errors will always be present in real point cloud data it was decided that a minimum inter-point distance was required when calculating normals. By using a large inter-point distance in relation to the range error this would give a better representation of the true normal to the surface at points within the chosen distance. This method would also create more accurate normals for the material classification task; as the reflected intensity is a function of the angle of incidence of the laser at each scan point. A disadvantage of using an inter-point distance greater than the actual inter-point distance is a reduction in resolution of the surface curvature. Determining a suitable inter-point distance may affect a classifier's ability to discriminate between different objects. An object with distinctive face normal orientations is a sphere,

shown in Figure 50. In this case the original sphere data which had an inter-point distance of ≈2mm, was thinned to 1 cm. Face normals, from a sphere, will be used in a neural classifier to identify spherical objects in a point cloud.

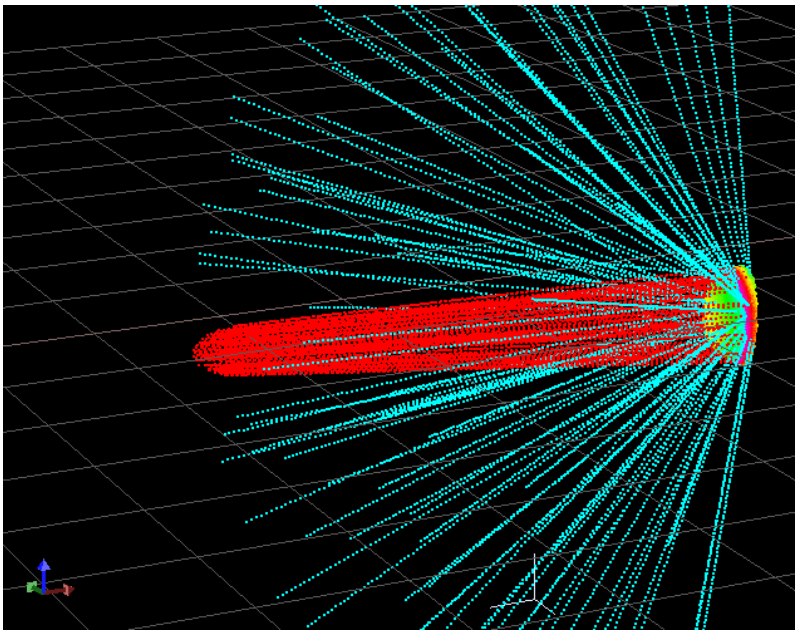


Figure 50 Face Normal to Sphere (Green) Incident Rays (Red)

The face normals in Figure 50 were computed using the Matlab routine shown in Appendix I. A commercial software package CloudCompare was also used to create normals and the poor result is shown in Figure 51.

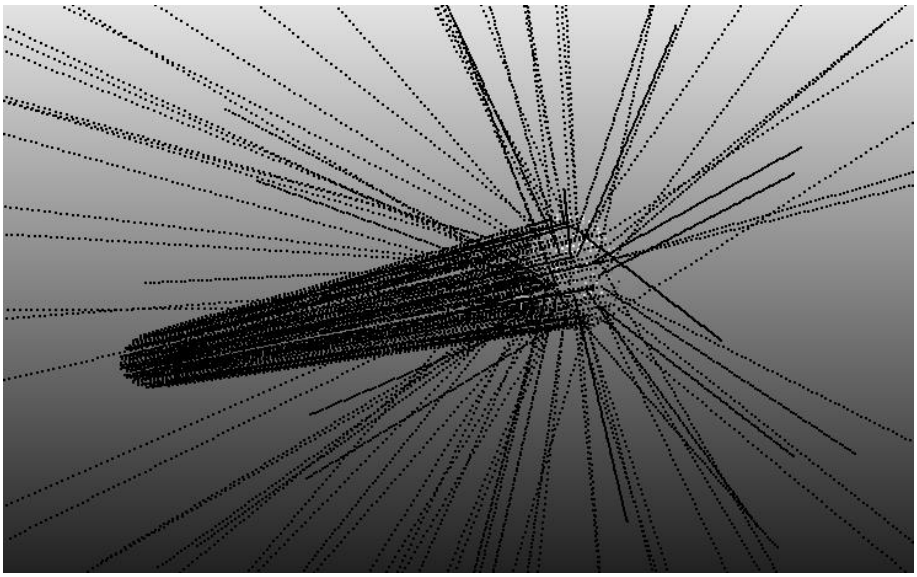


Figure 51 CloudCompare (V2) Normals to Sphere

The ‘CloudCompare’ software makes several errors in calculating the normals as can be seen by rays in Figure 51 which are pointing in odd directions.

An alternative method of improving the face normal angle calculation is to use a set of face normals to calculate the vertex normal (the normal at a point). The face normals surrounding a point are first computed then they are averaged to produce the vertex normal, Figure 52.

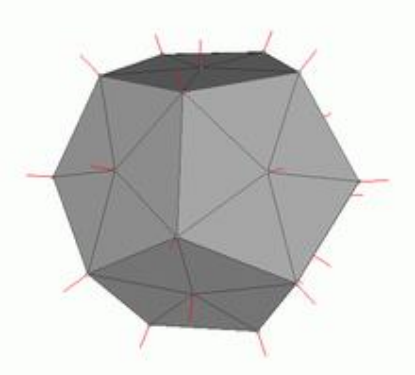


Figure 52 Vertex Normals

The vertex normals of the surface in Figure 47 were calculated and a sample are shown in Figure 53; the vertex normals originate from points.

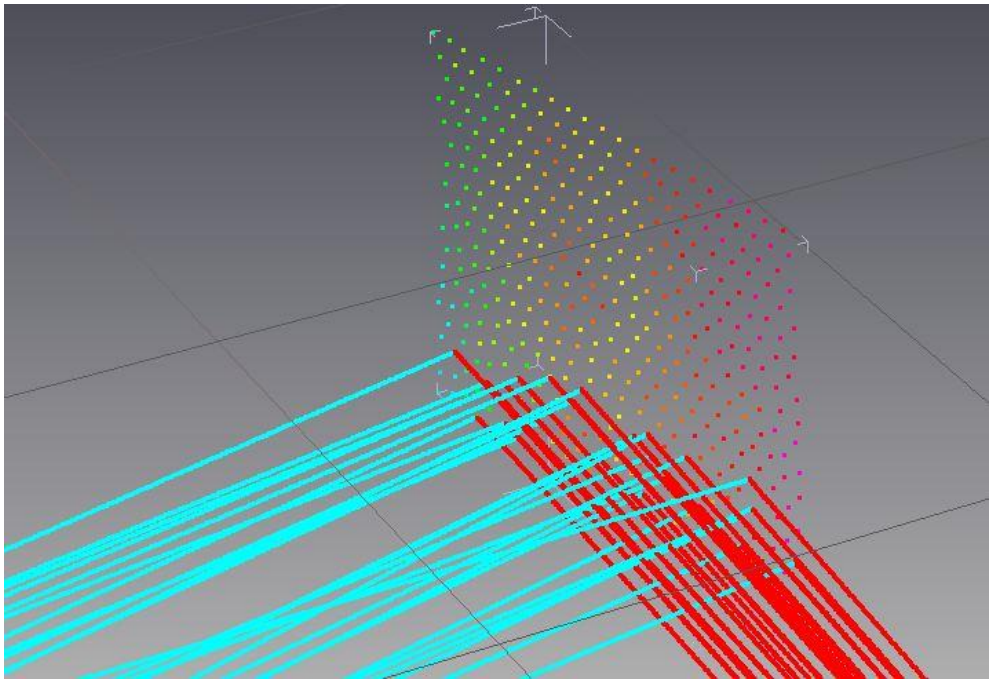


Figure 53 Vertex Normals (green) of Plane

The calculated vertex normals were used as training data for a neural classifier, discussed in the next section.

3.4.10 Reflection from Textured Surfaces

If the surface is textured, then the global (surface) and local normals will not be the same (Figure 54); in which case the actual angle of incidence will not be that of the surface as a whole.

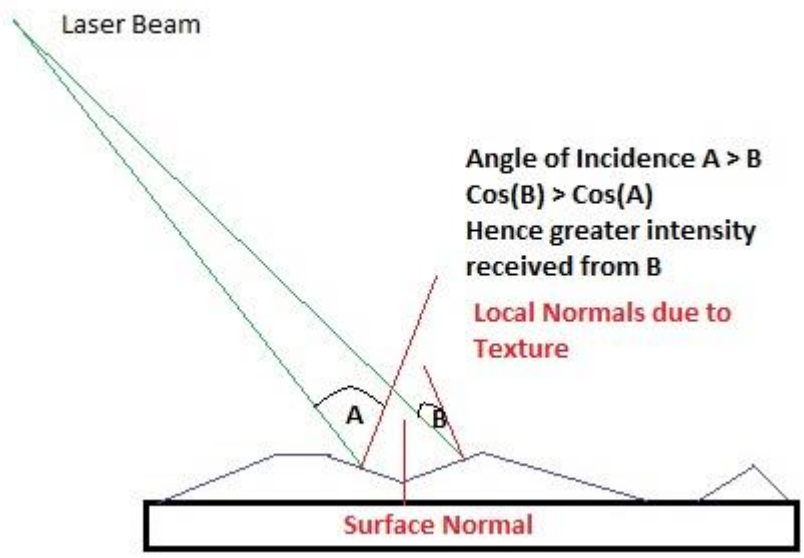


Figure 54 Reflection from textured Surfaces

3.5 Registration methods

The aim of registration of point clouds is to transform a point cloud so that it is aligned with a chosen reference cloud, they will then also have the same coordinate system as a result. The reference coordinate system may be a real world or local. Typically, the transformation is applied to sequences of scans using the same laser scanner to construct a unified point cloud that can be used to generate a 3D model of the area surveyed. A rigid transform has six degrees of freedom, three rotation and three translation (Bellekens et al. 2015). A non-rigid transform has the same six degrees of freedom plus scaling. To create a model without discontinuities there must by design be a degree of overlap between the scans. Each scan will usually have a differing number of scan points and the number of points from individual scans of an overlapping region will have differing point densities due to the

variation in the view point of the scanner. The variation in point density and distribution can affect the implementation of stereo image registration techniques for point clouds. The usual measure of registration accuracy would be to minimise the distance (d) between corresponding points in the transformed cloud T(A) and reference cloud (R); a least squares approach (Besl and McKay 1992). This method, which attempts to find a global minimum is sensitive to outliers which there may be many in the typical noisy laser point cloud, leading to an inaccurate solution.

$$d(T(A), R) = \sum_{a \in T(A)} \sum_{r \in R} (r - a)^2 \qquad 23$$

Where: r= reference points.

A= transformed points.

To solve this problem a robust function (f), which ignores distant points, can be introduced to the least squares formula; a statistical technique known as an m-estimator. This technique to reduce outliers has been used by many in least squares solutions including (Zhang 1995; Tsin and Kanade 2004; Shijiana et al. 2008)

$$d(T(A), R) = \sum_{a \in T(A)} \sum_{r \in R} f(r - a)^2 \qquad 24$$

The least-squares method that transforms a matrix A into matrix B by matrix T that gives the residual E, is known as an orthogonal Procrustes problem and defined:

$$AT = B + E \quad (25)$$

$$TT' = T'T = I \quad (26)$$

$$trace(E'E) = minimum \quad (27)$$

This problem has been researched by many most notably (Green 1952) and later (Schönemann 1966). Many approaches to registration have been developed including those based on finding areas in each point cloud with common intensity, surfaces or points. An intensity based approach has been used to medical tomography to register images from multiple sensors, such as CT and MRI, (Hill 1994) and then refined later by restricting the region used for registration (Studholme et al. 1996). Surface based registration often use an iterative method to find a minimum, but may not be a global minimum. Some surface based methods can use sets of polylines, parametric curves or a point set defining a surface (Besl and McKay 1992). Point based methods can use existing reference objects in scene or reference targets placed before scanning, this method is common in medical imaging as well as terrestrial laser scan registration. This method has inherent errors in the measurement of the reference target position. Reduction of the error can be achieved by minimising the sum of squares of the residual distance between neighbouring points. A method used in this work to reduce reference target position errors adapts that used by surveyors in a traverse (Bowditch 1807).

If the scenes are non-overlapping, then known reference points in a common reference system will be required. In this work the scenes are

overlapping by up to 100%, so only the overlapping methods will be discussed. In some scenes it may be difficult to find suitable matching natural features and therefore artificial features are introduced to the common portion of the scans; these are usually commonly used surveying targets such as chequer board, circles patterns or spheres. Spheres are most useful as they are invariant to orientation. These targets can be manually or automatically detected in the scene.

3.5.1 Rigid registration

Rigid registration aligns the point clouds maintaining the point spacing in each cloud; the transformation may consist of rotations and translations in each axis. Rigid registration is therefore suitable for point clouds where the point spacing's are known to be consistent between both point sets; this rarely is the case with laser scanner point clouds due to angular and range errors. Therefore, non-rigid registration methods should theoretically produce the point cloud best alignment.

3.5.2 Registration algorithms

Point cloud registration algorithms existed before laser scanners. Point clouds were produced during stereo and multi-image processing. More recently, point cloud registration algorithms have been created to support the advent of digital photogrammetry processing data from sensors such as Microsoft Kinect and Asus Xtion, to produce 3D models or provide input into machine vision systems. This section will review some old and some new registration algorithms, both ridged and non-rigid.

3.5.3 Rigid

The most common rigid algorithms use variations on Singular Value Decomposition (SVD) or Principle Component Analysis (PCA) and rigid versions of Iterative Closest Point (ICP). Which algorithm to use for a specific point cloud may depend on the accuracy required, computational complexity or the application to which the point cloud was to be used (Bellekens et al. 2014). Rigid registration algorithms are by definition restricted to six degrees of freedom and have been solved by either a least squares error minimisation or by a homogeneous transformation or a combination of both (Arun et al. 1987). The simplest rigid registration method only requires three matching points (p_1, p_2, p_3) in each point cloud (a and b), this method assumes that there is a match for all three points in each dataset (Allen 2007). Once the transformation is found for the three points it is applied to the entire point cloud.

The transformation is carried in two stages, derivation of a rotation matrix R and a translation vector T, where point sets are a and b. The first part of the process is to construct the 3 axis, x,y,z. Then build the rotation matrices R_a R_b , then solving for R the rotation between the a and b. The translation between a and b is given by t.

$$x = \frac{(p_2 - p_1)}{|p_2 - p_1|} \quad 28$$

$$y = (p_3 - p_1) - [(p_3 - p_1) \cdot x]x \quad 29$$

$$y = \frac{y}{|y|} \quad 30$$

$$z = x \times y \quad (31)$$

$$R_a = |x_a, y_a, z_a| \quad (32)$$

$$R_a = |x_b, y_b, z_b| \quad (33)$$

$$RR_a = R_b \quad (34)$$

$$R = R_b R_a^T \quad (35)$$

$$t = p_{a1} - Rp_{b1} \quad (36)$$

This can be expressed as an affine transformation T:

$$T = \begin{pmatrix} r_{1,1}\, r_{1,2}\, r_{1,3}\, t_{1,4} \\ r_{2,1}\, r_{2,2}\, r_{2,3}\, t_{2,4} \\ r_{3,1}\, r_{3,2}\, r_{3,3}\, t_{3,4} \\ a_{4,1} a_{4,2} a_{4,3} a_{4,4} \end{pmatrix} \quad (37)$$

If $a_{4,1} = a_{4,2} = a_{4,3} = 0 \; and \; a_{4,4} \neq 0$

The affine transformation would cause changes in scale, not normally associated with point cloud registration if no measurement error by the scanner is assumed. In reality there will be range errors and different deviation of range error between different scanners. There are two main sources of error in this simple method, range error in the measurement of the three corresponding points may vary between points within each point cloud and between the two point clouds and the almost certain likelihood that the two scans will not generate points at the same positon on objects within the scans. In addition, the two point clouds may not cover exactly the same area of the scene and therefore there will be outliers. So a method where the two point clouds are not an exact match was required, a direct method to calculate R and T was developed by Arun et al. (1987) which decouples rotation from

translation finding the best transformation by minimising the Euclidean distance error E between each point and the transformed counterpart.

$$E = \sum_{i=1}^{n} \left\| p_i' - \left(R_{p_i} + T \right) \right\|^2 \qquad 38$$

The rotation and translation are decoupled by finding the centroid p of each point cloud and subtracting it from each point in the cloud. This method finds the rotation matrix R by calculating the covariance matrix H, where its eigenvector defines the rotation axis. The direct solution to H can be found by using Singular Value Decomposition (SVD). In a case where there is a large amount of noise or outliers it was suggested that this method would fail to find a solution and a method such using RANSAC was recommended (Fischler and Bolles 1981). Another non-direct approach to solving a least squares problem uses iteration or feedback to attempt to minimise the registration error. This method has been applied to problems where the point clouds do not have a perfect registration solution, which is normally the case with real world laser scanner data. Rigid registration methods attempt to exactly solve least squares, methods have been devised which iteratively remove noise and outliers to reach a ‘best’ solution using a method known as Iterative Closest Point (ICP) (Besl and McKay 1992). Two main registration methods that use ICP are point-to-point (Rusu 2010) and point-to-surface (Low 2004). Both of these methods require the point clouds to be roughly aligned initially so that the distance between related points is small to prevent associating a point in the reference cloud with the incorrect point in the target cloud. They will generally fail if this initial

alignment is not carried out. The point-to point method, Figure 55, attempts to reduce the effect of noise and outliers by assuming that the point clouds are locally coplanar where they align. Other parameters have been used to improve the success of correct point matching by basing the match on: surface normal, colour or curvature. The main difference between the two methods is the premise by which the neighbouring point is determined; point-to-point searches for the nearest neighbour, point-to-surface searches for the nearest neighbour along a line projected from the destination cloud local normal vector, Figure 56.

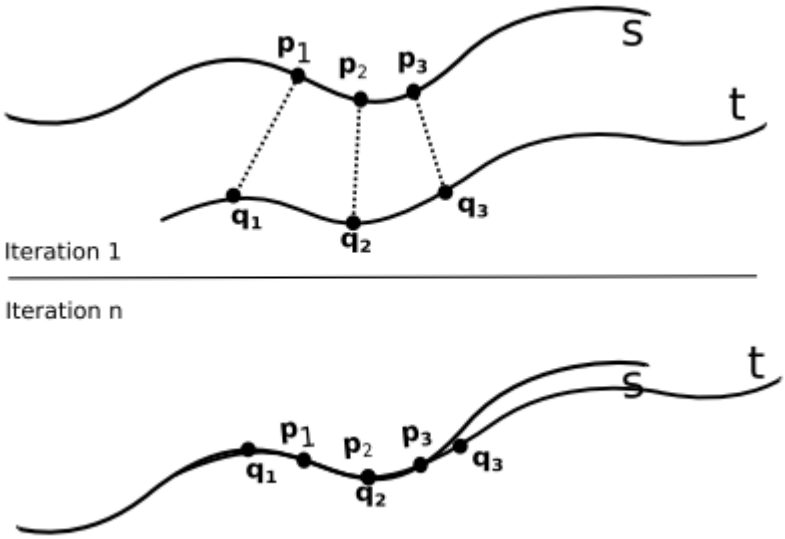


Figure 55 ICP registration using point to point matching, image (Bellekens et al. 2014)

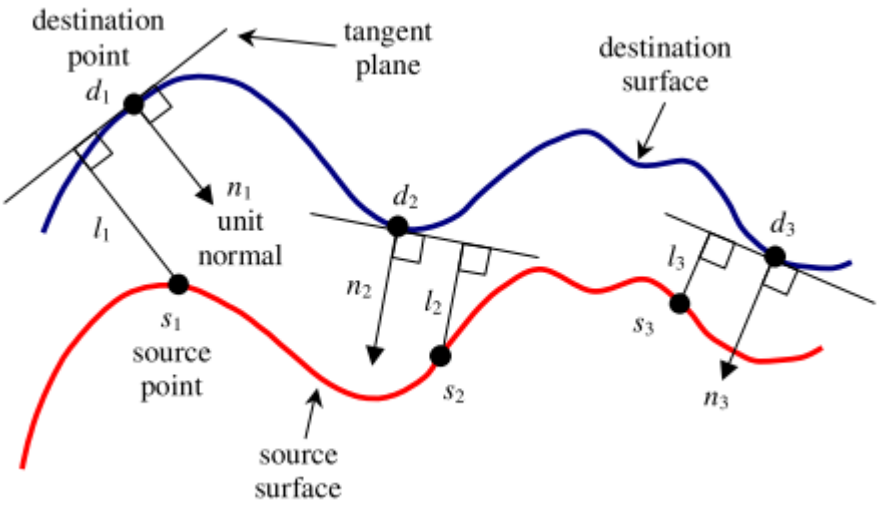


Figure 56 ICP registration using point to surface matching, image (Low 2004).

3.5.4 Semi-rigid

A semi-rigid registration technique (Lin et al. 2013) segments the point cloud prior to registration in order to prevent areas of the scan which are outliers or not present in both scans preventing error minimisation. This method would be very applicable to registration using targets such as spheres, where one or more of the targets may have moved slightly or not been replaced accurately between scans. This was the situation during the data collection phase for this research, which resulted in the development of a semi-rigid registration technique which corrects the sphere target positons prior to calculating the transformation matrices.

3.5.5 Non-rigid

Non-rigid transforms are suitable for registration of point clouds from different sources or the scanned object undergoes deformation between or during a scan. Non-rigid registration methods are often used in medical tomography where the object scanned is tissue that deforms

and point data is derived from different scanners such as MRI and CT. A method of non-rigid registration was developed by Rueckert et al. (1999) which used rigid affine transformation for the global movement of the scanned object and a derivation of free form deformation based on B-splines (Lee et al. 1997) to model the local deformation of the object. This type of non-rigid transformation technique may be applicable, in the context of this research, to scans of buildings which are deformable, such as large areas of glass or metal sheet.

3.5.6 Iterative closest point

ICP can be split into two solution methods; linear (L2), a differentiable squared cost function with a discrete solution and non-linear (L1), where the solution is found by minimising the absolute value of the residuals. The L1 method minimises the effect of outliers; various methods for finding the minima in this non-linear function include gradient decent, Levenberg-Marquart (LMA) (Marquardt 1963) and Gauss-Newton algorithms. A special case of the point-to-point and point-to-plane ICP methods was proposed by Segal et al. (2009) which removed the assumption that the point clouds were geometric surfaces.

3.6 Summary

The objective of this chapter was to investigate the influences on laser scanning intensity values including the potential benefit of multi-spectral scanners to material classification. The basics of laser scanner technology were reviewed, including methods of range measurement, intensity correction and anomalous effects created in laser point clouds.

As this research proposed the use of multiple scanners it was important to review registration methods to combine the resultant point clouds. The geometry of a laser point cloud leads to an assumption that a rigid or semi-rigid method would be appropriate. The following outcomes can be highlighted from this chapter:

1. The increase in intensity with range below 5m for the FARO 120 and the Leica HDS3000 scanners was unexpected and influenced the selection of test data for this research.
2. Laser light is coherent which introduces an extra characteristic to that of non-coherent light, the speckle pattern created by constructive and destructive interference; this should be taken into account when measuring the reflected intensity from a surface. It may also hold a key to measuring texture that is below the range precision of laser scanners.
3. In order to make use of the scanners intensity data, an understanding of each individual scanners method of recording the values was documented. The most significant was the influence of variations in range and incidence angle on the reflected intensity.
4. Direct measurement of incidence angle is considered and the problems that result from range error when the point spacing is of a similar magnitude were discussed.
5. Point clouds cannot be simply index like image data as they are not arranged in rows and columns but a set of points spaced dependent on the geometry of the object scanned; in order not to

lose the raw resolution nearest neighbour indexing must be used to relate the position of one point to another.

6. Registration methods used to align multiple scans from a single instrument may not produce the most accurate results if adopted for aligning point cloud data from different types (makes) of scanners, which may have different range and angle precision, scan patterns and point densities.

Chapter 4. A New method for Classification of Construction Materials

4.1 Introduction

Based on experimental work and the literature review a methodology was developed to classify materials using multispectral laser scanner intensity data. The following Simulink Mathworks © diagram, Figure 59 shows the process that was developed and the following sections explain the detail of this methodology, a neural network classifier is shown in the diagram; other classifiers were also used. To introduce the method this chapter introduces the three laser scanners that were used to create the multispectral data. This includes a discussion of the different formats of intensity data recorded by each scanner. Next the test sites are defined and the reasons for choosing them. This is followed by the method used to normalise the intensity values for variations in incidence angle and range; this is based on ratios of values of different wavelength. Next, to create the multispectral dataset the point clouds of the three scanners were combined, the method adopted for this process is defined. The final section of the chapter presents the chosen classification methods, which included a neural network classifier. The MatLab programs that were developed for the classification tasks are provided in Appendix B. The chapter concludes with a summary of the methodology and the outcomes.

4.2 The Laser Scanners

It was ideally desirable to have as wider spectral range of laser wavelengths as possible to cover the possible spectral response of the construction materials in the scans. In reality, only three scanners were available with different laser wavelengths, these were the FARO^{3D}120 (905nm, near IR), Leica HDS3000 (510nm, visible green), Figure 57 and the Riegl VZ-400 (1550nm, mid IR), Figure 58. The FARO and Leica belonged to the University and the Riegl was loaned from 3D Laser Mapping[4]. The Leica and the Riegl scanners use ToF, the FARO uses phase shift, for range measurement. The FARO and Leica scanners had built-in cameras. The Riegl scanner had an attached SLR camera. All three scanners recorded Cartesian coordinates, intensity and RGB values for each scan point, Riegl VZ400 with attached DSLR.



Figure 57 FARO 3D 120, left, FARO © and Leica HDS3000, right, Leica ©.

[4] 3D Laser Mapping (3DLM), Bingham, Notts



Figure 58 Riegl VZ400, Riegl ©.

The datasheets with detailed specification for each scanner are in Appendix C.

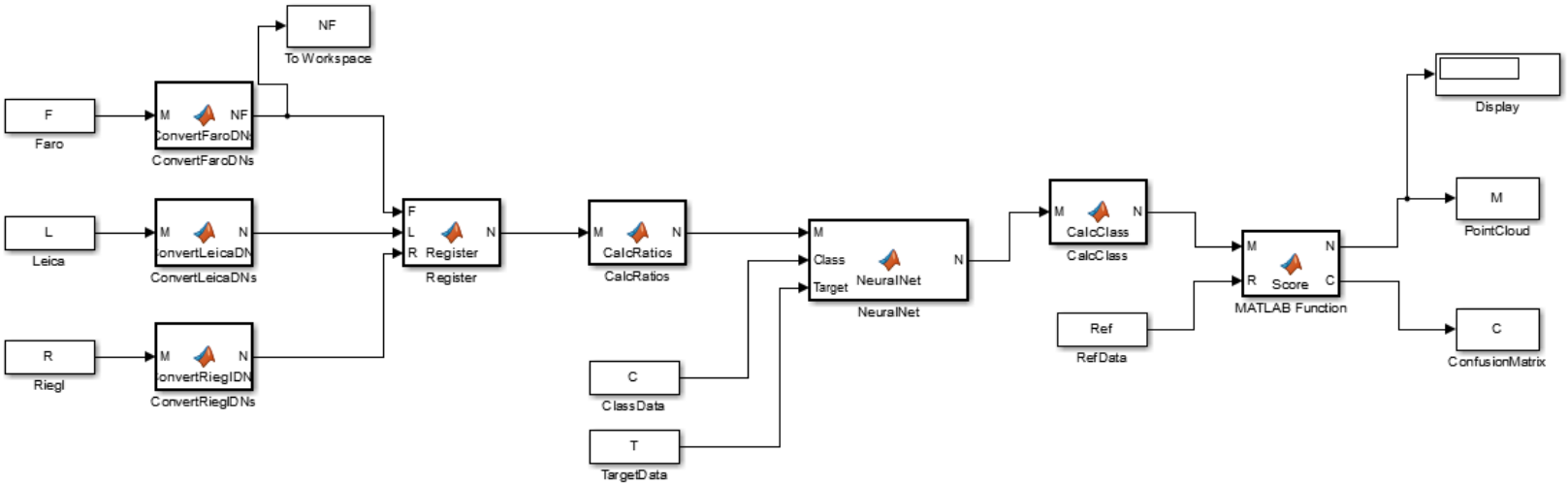


Figure 59 Workflow diagram of proposed method for materials classification. Based on a Simulink (Mathworks ©) model. This example shows the use of an Artificial Neural Network classifier; trials were also carried out using other classification methods

4.2.1 FARO 3D 120 Intensity Values

The manufacturer stated[5] that the FARO 3D 120 scanner was not designed as a reflected laser intensity measurement device. In addition, stated the method by which it is measured is as follows, the reflected laser light that is returned to the scanner goes through a pin hole at the rear of the optics and is transformed into an electrical current via a unknown type of photo-sensor. This current is amplified; a logarithmic A/D converter produces the digital output. The manufacturer does not calibrate the pin hole, amplifier, or converter, so the reflectance measurements on the same surface may differ from scanner to scanner. The values are stipulated in self-made units, (DN) which have a range of 0 to 2047 (2^{11}-1 or divided by 8. gives the range 0 to 255).

The scanner measures irradiance the reflected power received from a surface at the phot-sensor. This power is measured as Watts/m². The conversion between FARO units and Watts/m² is also scanner specific due to the lack of calibration. The conversion from power to intensity unit is non-linear. The maximum intensity measured by the scanner is 2047 units, an auto-gain control limits this in relation to a 99% Lambertian target to prevent overexpose within the scanner's measurement range. It is also ensured that a 2% Lambertian target yields at least a reflectance value of 300. A limiting dark scan point filter is used to eliminate very noisy data. The darker an object, the noisier the scan points. There is also a filter to remove points that have a range

[5] Email FARO Technologies UK, 2012

calculated beyond the ambiguity interval, in trials if this filter is not used a sequence of hemispheres of stray points are apparent in the point cloud.

4.2.2 Leica HDS3000 Intensity Values

The Leica HDS300 records the reflected laser intensity as a Digital number (DN) with a range from -1047 to +1047 ($\pm 2^{10}$).

4.2.3 Riegl VZ400 Intensity Values

The V-Line series of laser scanners were the first of Riegl scanners to provide an amplitude measurement (A) for every echo. This value is defined as the ratio of the actual detected optical amplitude (P_{echo}) versus a detection threshold (P_{DL})

$$A_{dB} = 10Log\left(\frac{P_{echo}}{P_{DL}}\right) \quad 39$$

The ratio is defined in decibels (dB), the range is 0dB to 50dB. The amplitude values can also be output, after processing, as reflectance; the relative amplitude to a reference target at the same range. Although useful this measure of reflectance does not make any correction for incidence angle.

4.3 Test Scan Sites

Two 360º horizontal by -30º/+60º vertical scans were made with each scanner of the two test sites on Jubilee campus at the University of Nottingham. The sites were chosen on campus and close to the Nottingham Geospatial Institute (NGI) for ease of deployment, security and ease of re-scanning if required. In addition, the Leica scanner

required mains power which was available from the nearby offices. The fist site was the campus gymnasium and the second a student accommodation block. The two buildings were also chosen because they were constructed of some common materials; this allowed validation of the method. Also the buildings were constructed mainly of brick, steel and wood and the area surrounding paved with similar materials; this reduced the difficulty of creating a reference model to validate the classification rate.

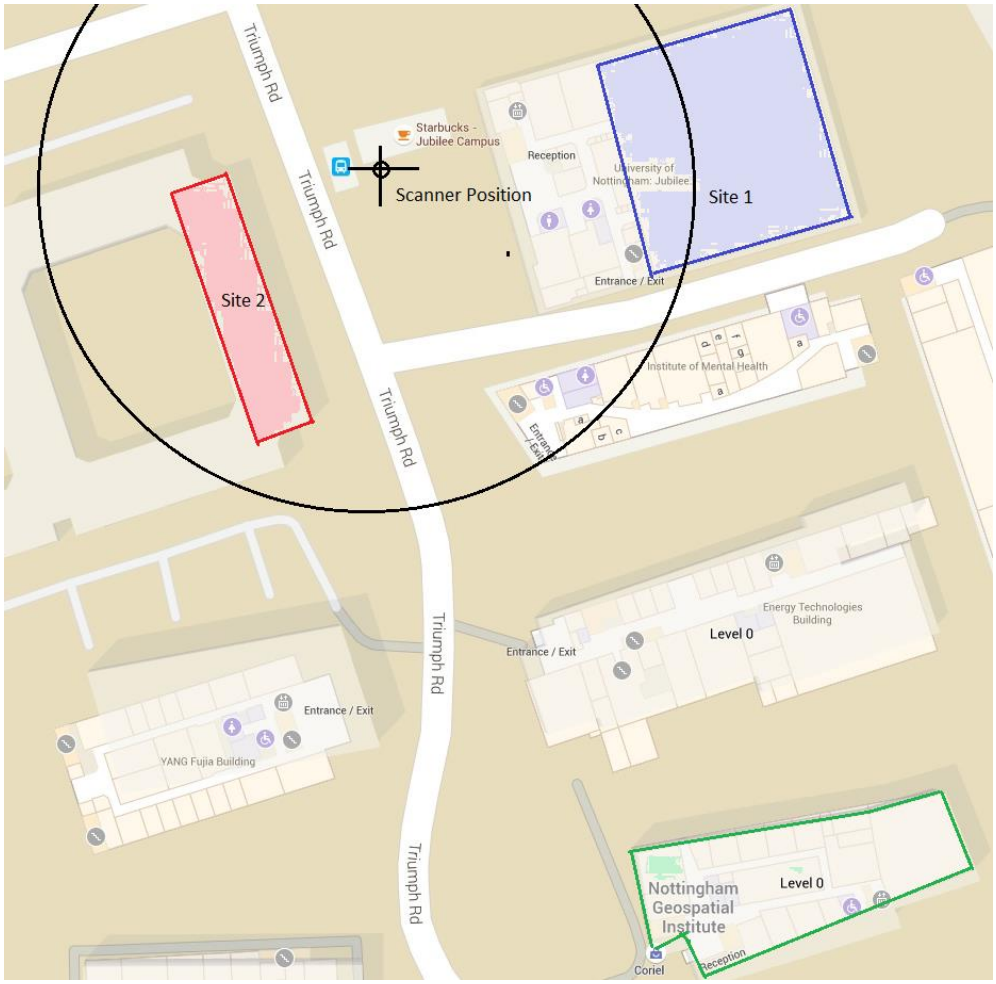


Figure 60 Position of scanners (black cross) and location of buildings for site 1 (blue) and 2 (red).

To ensure that laser beam origin was from the same 3D point each scanner was positioned with its optical centre at ‘the same’ 3D location. The importance of this alignment was to ensure the range and incidence angle to each scan point, from each scanner, was as close as possible within feasible alignment accuracy. The scanners were mounted on a tripod and tribrach, over a reference point, using the tribrach’s optical plummet. Using the offset from the base of the scanner to the optical centre a difference in height (dHt) to the top of the tribrach was calculated for each scanner (Table 4). The final measured alignment error was less than 5mm.

Table 4. Offset from base of scanner to optical centre, height from ground to top of tribrach (dHt).

Scanner	Offset (m)	dHt (m)
Faro	0.133	0.246
Leica	0.380	0
Riegl	0.232	0.147

The full FARO scanner point cloud, showing the scanner position, reference spheres and test site positions are show in Figure 61. The full scan is shown in Figure 61 site one is shown in Figure 62 and site two in Figure 63.

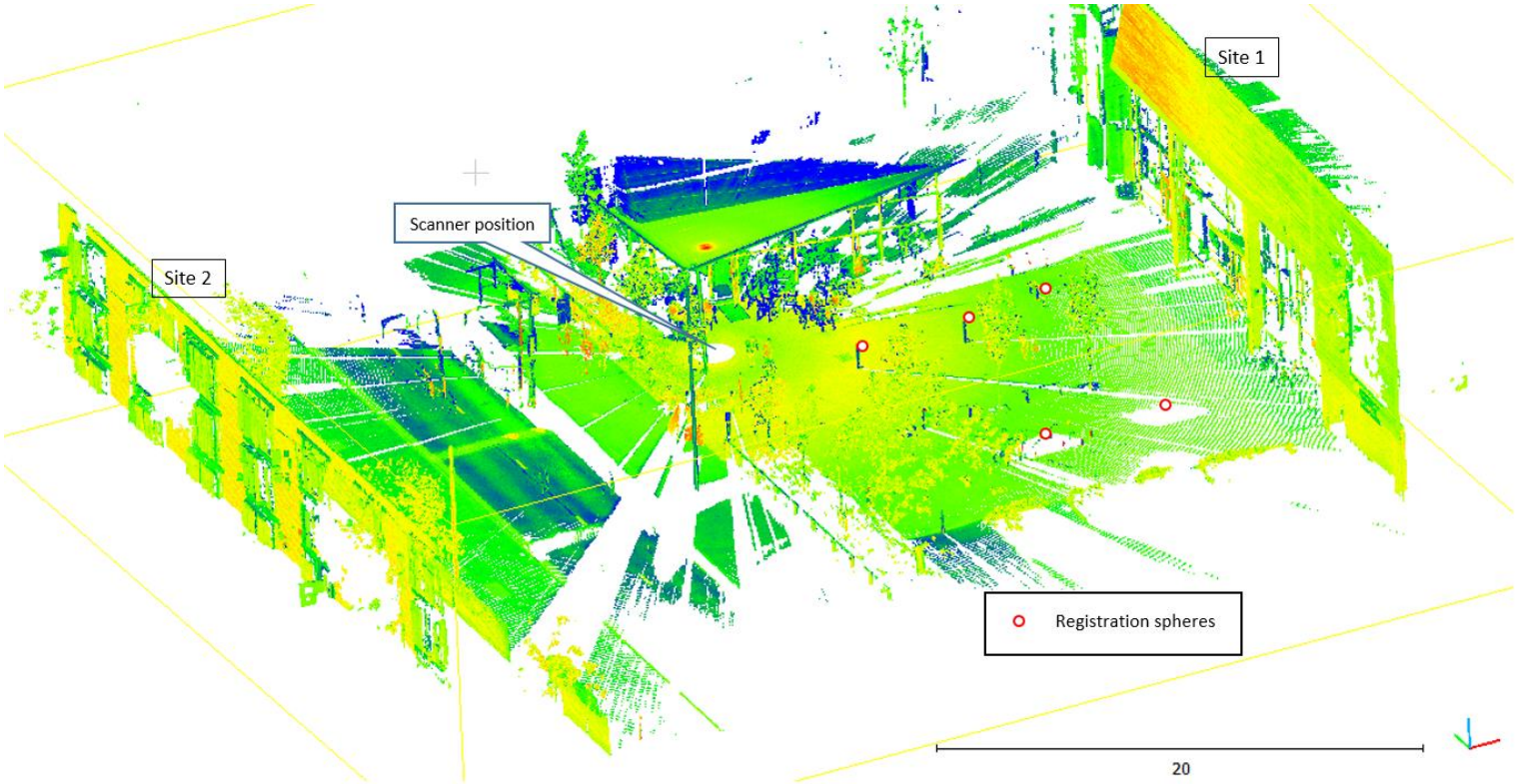


Figure 61 Point cloud of full FARO scan showing reference spheres and site positions. Both sites were scanned from the same position



Figure 62 Site 1 (Three of the five registration spheres are shown in green)



Figure 63 Site 2.

The training data for each classifier was randomly sampled from a separate area of the scan than the test data, Figure 64.

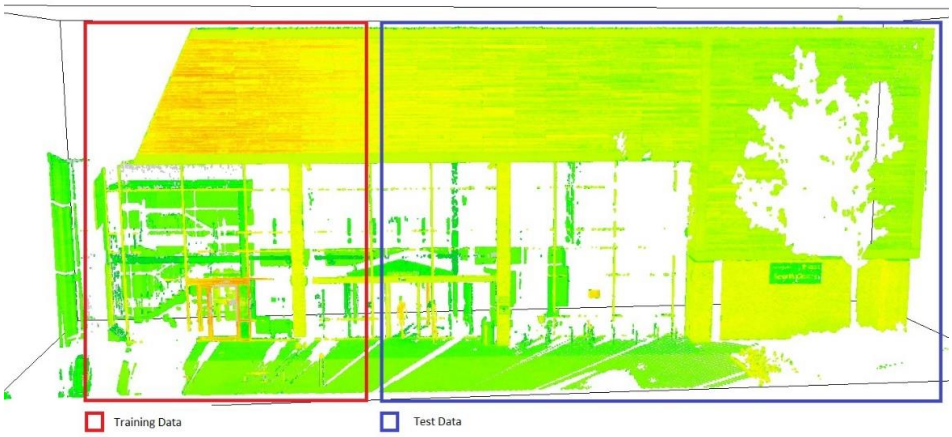


Figure 64 Training (red) and test (blue) data areas.

4.4 Scan Data Pre-processing

Initial processing of scan data was carried out using each individual scanner's proprietary software: FARO Scene, Leica Cyclone and Riegl RiScan. The Cartesian coordinates, intensity and RGB values were exported to file.

4.5 Intensity Ratios to Normalise for Incidence Angle and Range Variations

The laser incidence angle and range, in this study, produce similar problems as in the 'Great Plains' study, (Rouse et al. 1974). It could be argued that using laser scanning data that range and the incidence angle compensation could be directly calculated from the point cloud data. However, if the range error and point spacing are of a similar order, the calculated incidence angle is incorrect; an error of 45deg when the range error equals point spacing; intensity ratios were used in

this research to avoid this problem. Ratios of intensities (γ_{12}), between different laser wavelengths, were calculated for common points in two scans of the same scene.

$$\gamma_{12} = \frac{\mu_1 \frac{D_1^2}{4\pi R^4 \beta_1^2} \sigma_1 \cos\theta}{\mu_2 \frac{D_2^2}{4\pi R^4 \beta_2^2} \sigma_2 \cos\theta} \quad 40$$

The scanners optical centres were co-aligned so that the range and incidence angle at a common point was the same, reducing (γ_{12}) to:

$$\gamma_{12} = \frac{\mu_1 \frac{D_1^2}{\beta_1^2} \sigma_1}{\mu_2 \frac{D_2^2}{\beta_2^2} \sigma_2} \quad 41$$

The receiver aperture, beam width and backscatter cross-section are constants, (c_1, c_2), related to the two chosen scanners. The ratio of these constants is the same for all points and can be expressed as a single constant, (C_{12}). The calculated intensity ratio for each scan point therefore becomes dependent only on the surface reflectivity (spectral signature), related to the laser wavelengths (λ) of the scanners.

$$\gamma_{(\lambda_{12})} = \frac{\mu_{(\lambda_1)}}{\mu_{(\lambda_2)}} C_{12} \quad (42)$$

This ratio of intensities provides a measure of a materials reflectance, at the two different laser wavelengths, that is independent of range and incidence angle.

In order to achieve the goal of classifying materials using laser scanner intensity data the following factors were investigated:

1. Inter-scanner optical centre alignment.
2. Registration of scans from dissimilar scanners with dissimilar scan point patterns.
3. Registration accuracy.
4. Creation of multispectral point cloud from registered scans.
5. Range and incidence angle correction using intensity ratios.
6. Classification using an artificial neural network.

The intensity values of each scanner were normalised to have values within the range zero to one. This was achieved by scaling the data using the manufacturers specifications. Comparison of intensity values of a constant target with range showed that all three scanners attenuated the intensity values at close range; less than 6m. The attenuation was scanner specific; to avoid dissimilar objects having the same reflectance, the chosen test scan area ranges were greater than 6m. To test the intensity ratio concept, a material which had homogeneous surface reflectance/absorbance and a fine, near Lambertian, surface was required. The registration spheres provided a good test material providing a homogeneous reflectance and a variety of angles of incidence and ranges, in a single scan. The spheres are made of white coated polypropylene. A simple ratio of intensities μ at different wavelengths, λ_1 and λ_2, produces an infinite range of values, producing outliers which skew the distribution. To overcome this problem, Kriegler et al. (1969), in their research into detection of vegetation in satellite images, used Normalised Difference Vegetation Index (*NDVI)* which constrains the values to the range -1 to +1.

Crippen (1990), in his article ‘Calculating the vegetation index faster’, proposed a modified version of the NDVI which has values between 0 to 1, this output range is particularly suitable for visualisation using

proprietary software tools. The modified ratio is functionally and linearly equivalent to the *NDVI'*:

$$NDVI'_{(\lambda_{12})} = \frac{\mu_{(\lambda_1)}}{\left(\mu_{(\lambda_1)} + \mu_{(\lambda_2)}\right)} \quad 43$$

This function was used to normalise the laser intensity data for variation in incidence angle and range within the scans by creating ratios between the FARO and Leica, FARO and Riegl and Leica and Riegl scanner intensity values. These ratios were then used as the input to each classification method used in this research.

4.6 Registration

Each scanner had a different scan geometry, point density and start point. This meant that to create the intensity ratio data, intensities would have to be assigned to neighbouring rather than discrete points. The FARO scanner coordinate system was used as the reference, as the FARO scan data was the highest point density. A k-d-tree index was created to find the neighbouring points in the two other scanners' data and the intensity values were assigned to the FARO scanner's point data. A distance threshold (d^t) related to range (r), using a constant angular spacing (θ), was used to exclude neighbouring rather than nearest points.

$$d^t = r\theta \quad 44$$

The value of θ was set to the Leica (0.7 mrads) and Riegl (0.75 mrads) scanner's step angle.

In order to calculate intensity ratios, the scans required a common coordinate system. In order to register all three scanners point clouds to the same reference five reference spheres were positioned in the same place within the scan volume for the three separate scans. Once each scan was in a common coordinate system the intensity values of point within a chosen distance of each other could be used to calculate intensity ratios. Unlike a total station or a theodolite, direct determination of the coordinates of discrete points using a laser scanner is not usually possible, unless some points of different scans happen by chance to coincide; virtual discrete points common to each scan must be produced. A suitable object for deriving coordinates of an virtual discrete point is a sphere (Schultz 2007), absolutely defined in 3D by the coordinates of the centre point and its diameter. A sphere has a homogenous surface and is also invariant to viewing angle. The sphere centres were calculated by fitting a sphere to their scan points using least squares, by minimising *S*.

$$S = \sum ((x - x_c)^2 + (y - y_c)^2 + (z - z_c)^2 - r^2)^2 \quad 45$$

The residual sphere fitting error is shown in Table 5.

Table 5 Residual sphere fitting error.

Sphere #	Range (m)	Mean error (mm)	Std. Dev. (mm)
1	6.296	0.003	0.670
2	10.379	0.005	0.873
3	14.975	0.007	1.035
4	17.202	0.103	3.800

The error values were of the same order as the published range error of the scanner. The FARO scanner data was used to calculate the sphere centre positions, having the lowest published range error. Using the derived artificial sphere centre coordinates an adaption of registration method due to Arun et al. (1987) was used to convert the Riegl and Leica coordinates to the FARO coordinate system. There were five available reference points, the scanner position and the four virtual sphere centre positions. To reduce the effect of the residual error in the sphere centre positions, the range errors created by the high intensity values at low incidence angles were discarded. Registration was also attempted using an Iterative Closest Point (ICP) method (Besl and McKay 1992) but the dissimilar scan patterns of the three scanners often confounded the ICP algorithm. Image based registration methods were considered, (Tournas and Tsakiri 2009) and (Weinmann et al. 2011) but the variation in point density of the difference scanners made it difficult for these methods to find corresponding points in the reference scan image. The residual registration errors were calculated in using the relative distance between sphere centre positions after registration (Table 6).

Table 6 Residual registration errors

Method	Max error (m)	Min error (m)	Mean error (m)	Std. Dev. (m)
Rigid 3 point	0.025	<0.001	0.013	0.009
Rigid multi-point	0.016	0.002	0.008	0.005
ICP	0.013	0.002	0.008	0.005

The residual registration errors were attributed to the positioning of each scanner's optical centre and inherent range errors. The published range errors for each scanner are shown in Table 7; the error is dependent on target reflectivity.

Table 7 Published scanner range error.

Scanner	Range (m)	Range error ± (m)	Angular error (radians)
FARO 120	10	0.002	0.000010
Leica HDS3000	1-50	0.004	0.000060
Riegl VZ400	100	0.005	0.000009

4.6.1 Multi-scanner point cloud registration

The registration techniques discussed below refer to registering (aligning to a common reference frame) point clouds of a scene measured by the same scanner from different viewpoints. These methods are optimised for spatial accuracy; this research requires a method that provides both spatial and spectral precision. The spectral precision refers to the need to associate laser reflected intensity values from each of the three scanners point clouds in order to associate three intensity values to a single point. The challenge for this research was to register point clouds from different scanners; which had different point densities, scan patterns, range and angular precision. The existing methods were reviewed and tested, finally adapted to create a new method that provided both spatial and spectral precision.

4.6.2 Finding a Unique Common Point

Laser scanners, other than the latest integrated total station scanners, are unable to define a unique point; the user cannot decide which points are measured. Therefore, individual scans of the same scene will very rarely contain common points but only neighbouring points. In the past attempts to overcome this problem have depended on using geometrical primitives such as spheres or circles, various mathematical methods have then been applied to estimate a pseudo common point such as the sphere or circle centre. In this work only sphere were used due to their viewpoint invariance. They also were made of a very homogeneous material ‘Spectralon’ which could also provide spectral invariance.

4.6.3 Scanner and Sphere Alignment

The scans of the area of study were made on separate days; the Faro and Leica scans were within one day of each other and the Riegl scan a week later. The timing of the scans was dependent on the availability of the scanners. The possible effect of ambient light conditions was taken into consideration by choosing similar solar zenith angle and cloud conditions. The registration spheres were located in the same positions for all scans of the study area; in order to ensure repeatable accuracy physical markers were placed at the sphere positions. The position of each scanner was also physically marked; a periscopic tribrach was used to align the scanner axis. The optical centre of each scanner was positioned at same height above the marker. Positioning each scanner in this way ensured that the bearing and range to a common point from

each scanner would be the same; important to remove incidence angle and range variation effects on the measured reflected intensity values. The scanners were initially levelled using the tribrach and fine levelled using the scanners own electronic level. At the start of each scan an inbuilt inclinometer in each scanner measured the axis and angle error; this was used to calculate a rotation angle of each axis. This rotation angle was applied to correct each scan. The unusual arrangement of aligning scans made from the same datum point and levelled to the same local vertical, implied that to transform all scans into the same reference frame only required rotation around the Z axis. This would be very nearly true if the scans were made with the same instrument, making the assumption that the range and angle errors would be of the same order of magnitude and direction. The scans in this study were from three different instruments with significantly different error in range and angle measurement; the simple rotation method was modified to include a second stage ICP adjustment to compensate for the differing errors.

4.6.4 Calculating Registration Sphere Centres

Initial registration of the point clouds was carried out using a semi-rigid transformation method; rotation around the Z axis, followed by an ICP adjustment. To determine the rotation angle one or more common reference points were required; as reference spheres had been placed within the scan area, the calculate sphere centres provided this common reference. The registration spheres were extracted manually from each point cloud and the major outliers (>4 x residuals) were

removed from the data. Four methods for determining the sphere centre coordinates were assessed:

1. Least squares fit of a sphere using CloudCompare[6]; estimate sphere centre coordinates and radius.
2. Estimation of sphere centre coordinates and radius by solving linear system of normal equations. Code created in MatLab[7], solution of linear equations adapted from MatLab central code library[8]
3. Estimation of sphere centre coordinates with known radius by minimalizing function of a sphere. Code created in MatLab adapted from FileExchange[9].
4. ICP fit of artificial point cloud of sphere of known radius. A new method created by the author.

Each method is explained in more detail in the following sections.

4.6.5 Least squares fit of a sphere (CloudCompare)

Within the CloudCompare program tools there is a sphere fitting routine; this uses an unknown least squares method to achieve a best fit. In general least squares methods that fit a sphere are based on the assumption that (x_0,y_0,z_0) are the unknown centre coordinates, the unknown radius R can be defined as:

---

[6] CloudCompare V2 License: GNU GPL (General Public Licence)

[7] MatLab 2015b

[8] Levente Hunyadi ©2011, ©2014

[9] MatLab Central ©2015

$$R^2 = (x - x_0)^2 + (y - y_0)^2 + (z - z_0)^2 \quad 46$$

The value of R is the square of the Euclidean distance to each point. The aim is to minimise the sum of the squared distances between from the point cloud to points on the sphere given by the intersection of a straight line from the points to the centre of the sphere.

This can be expressed by a function S where:

$$S(x_0, y_0, z_0, R) = \sum \left(\sqrt{(x - x_0)^2 + (y - y_0)^2 + (z - z_0)^2} - R\right)^2 \quad 47$$

4.6.6 Least squares fit of a sphere (unknown radius)

In addition to the use of CloudCompare's least squares method a MatLab version was created, this gave complete control over the process rather than depending on effectively a black box solution. Additional features allowed the residual radius errors to be calculated and visualised by colour variation of the points in proportion with the error and direction of the error, Figure 65.

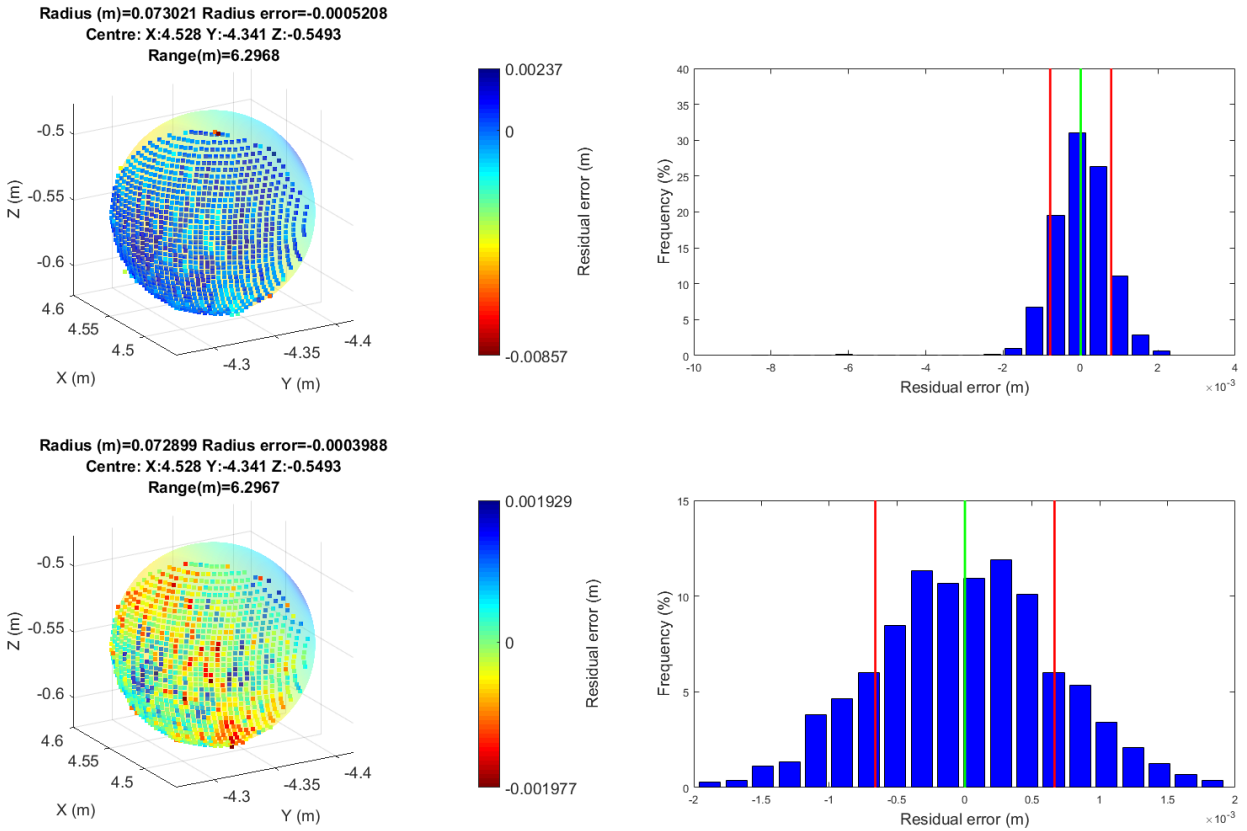


Figure 65 Residual sphere fit error, least squares method with radius unknown. Histogram shows mean [green], 1 std dev red]. Top shows initial fit and bottom shows fit with residuals >0.002m removed.

4.6.7 Minimalizing function of a sphere (known radius)

MatLab has a built-in function ‘fminsearch’ which finds the minimum of a scalar function using an initial estimate; often referred to as unconstrained nonlinear optimisation. It follows a method that uses the Nelder-Mead algorithm described in (Lagarias et al. 1998). An implementation of this function was used to minimise the function S2 where:

$$S2 = \sum((x-a)^2 + (y-b)^2 + (z-c)^2)^2 \quad (48)$$

4.6.8 Artificial sphere point cloud

In order to fit a sphere of the correct radius the following method was developed. An artificial sphere point cloud was created and registered with the spheres in each scanner’s point cloud using ICP. A sphere was then fitted to the artificial sphere point cloud to determine the coordinates of its centre, the centre point coordinates were then used to calculate the transform. This method initially proved to have very little success as the ICP method failed to achieve even a poor (<1cm) level of alignment. The full sphere model was cut to a hemi-sphere and the ICP algorithm reapplied; this produced a successful alignment. The artificial sphere was now at the position of the original registration sphere point cloud, a sphere was fitted to the artificial sphere point cloud and the centre coordinates were used to calculate the transformation matrix.

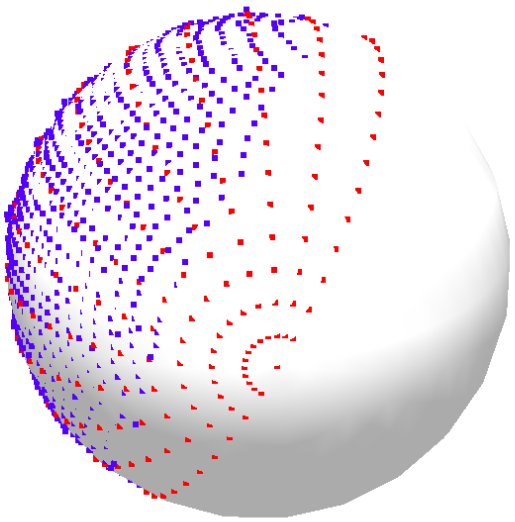


Figure 66 Artificial sphere point cloud [red] of defined radius (0.0725m) aligned to registration sphere point cloud [blue], then fitted with a sphere mesh [grey].

The rms error using this method was less than 3.85×10^{-7} and the radius error was 3.93×10^{-7} m. This method was applied to all of the registration spheres for each of the three scanners. This method was implemented in MatLab using the authors own code.

4.6.9 Error assessment of sphere centres

The determination of the sphere centres was dependent on two factors, scanner precision (range and bearing accuracy) and estimation of sphere radius (when known radius not used by technique). The first depends on the scanner and the second on the sphere fitting method employed. Assessment of the error in measuring the sphere centres was based on the methods used by Wunderlich et al. (2013). There were two main errors resulting from the process of determining the sphere centre, error between the known and estimated radius and spatial error. Spatial error was calculated for methods using known and

unknown radius. The sphere mean radius error R_k was defined as the sum of k squared radius errors r_e divided by k.

$$R_k = \frac{1}{k}\sqrt{\sum_{i=1}^{k} {r_e}^2} \qquad 49$$

The method of determining the centre of each sphere, for each individual scanner, varied the coordinates by less than 0.003m (Figure 67), the residuals have two components, range and bearing accuracy and sphere radius. The radius residual errors for each scanner are shown in Figure 68 (FARO), Figure 69 (Leica) and Figure 70 (Riegl).

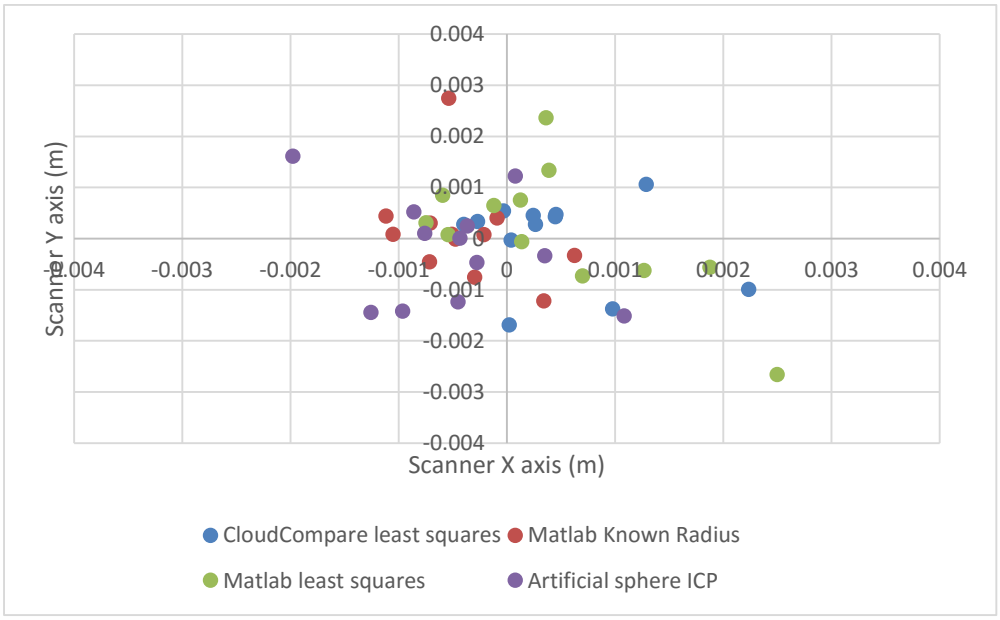


Figure 67 Residual error, in each scan, between each method of calculating sphere centres.

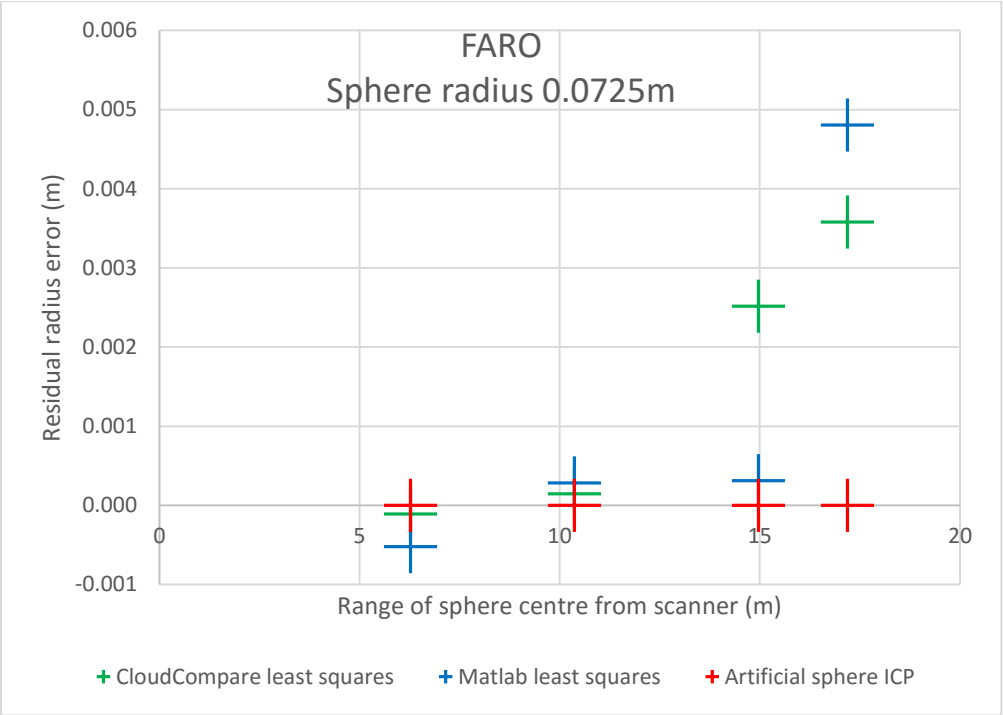


Figure 68 FARO scanner sphere radius residual error (m), where the method has estimated the radius. Artificial sphere method residuals <5 x 10^{-7}m.

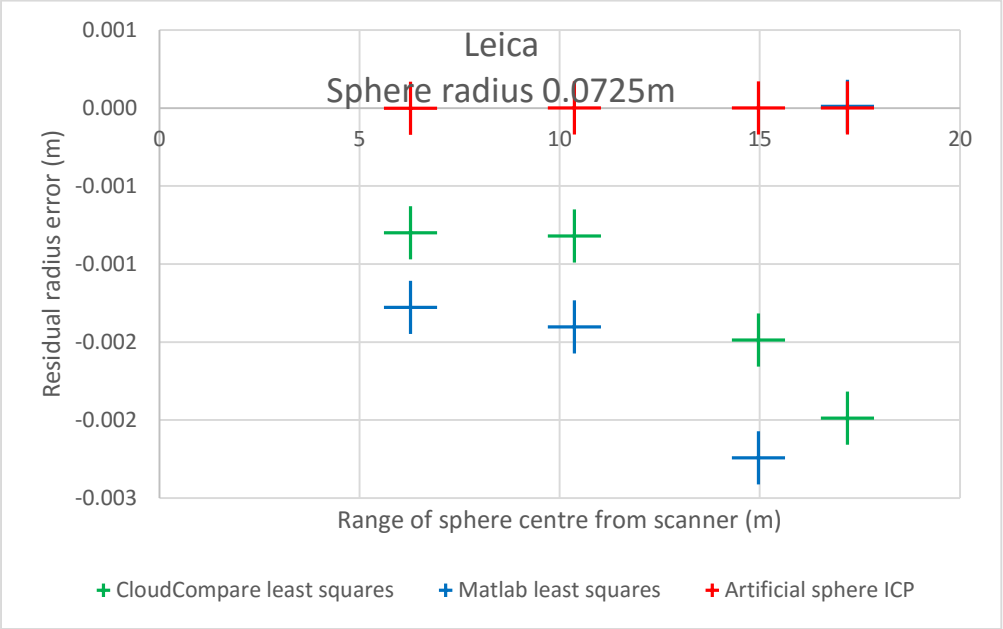


Figure 69 Leica scanner sphere radius residual error (m), where the method has estimated the radius. Artificial sphere method residuals <1 x 10^{-6}m.

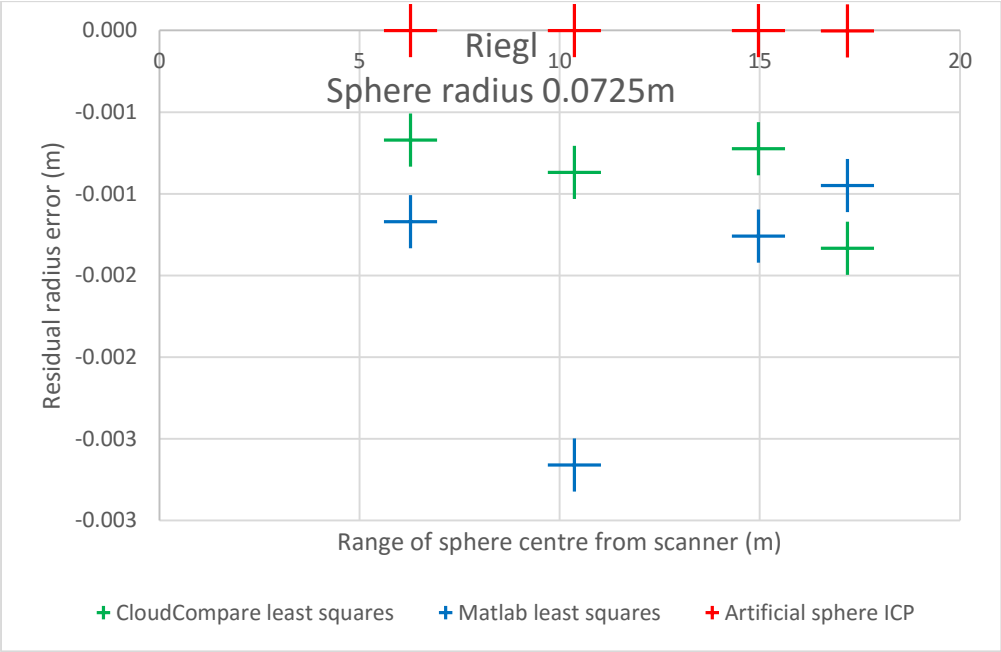


Figure 70 Riegl scanner sphere radius residual error (m), where the method has estimated the radius. Artificial sphere method residuals <2 x 10^{-6}m.

The artificial sphere ICP method of estimating the sphere radius had the smallest residuals for all scanners and the largest residual was 2 x 10^{-6}m. This method also had the smallest inter-sphere position errors; the results were used as input to inter-scan registration to create the multi-spectral point cloud.

4.6.10 Inter-scanner sphere position error

Having determined the variation in error between sphere centre calculations, the error between matching spheres from different scanners point clouds was necessary prior to registration. The spatial error between matching spheres from one scanner to another was determined by comparing the resulting position of the sphere centres. This error could be calculated as a bearing and range from the scanner or as Cartesian coordinates. Spatial error could be due to scanner or

sphere centre position error, the scanner position error would be evident as a XY translation error, whereas the sphere position error might involve translation and rotation. It is difficult, if not impossible, to decouple the scanner and sphere position errors. The spheres had to be removed and replaced between successive scans which introduced some error between scans. A summary of the sources and associated errors is shown in Table 8.

Table 8 Sphere position sources and associated errors (*estimated)

Error source	Bearing (radians)	Range/ distance (m)	Remarks
Sphere placement	<0.00048*	±0.003*	Bearing – nearest sphere, range - width of marker
Scanner placement	<0.00030*	±0.002*	Bearing – nearest sphere, range - width of registration nail
Scanner precision	0.000010	±0.002	FARO Focus[120]
	0.000060	±0.004	Leica HDS3000
	0.000009	±0.005	Riegl VZ400

The significance of the sphere position error in this work is related to the accuracy of the production of a multi-spectral point cloud; the errors ideally should be less than the point correlation between each scanners point cloud of the same scene. This ensures the most accurate assignment of triple intensity values to the reference point cloud. The point spacing and beam width for each scanner at various ranges is shown in Table 9. The table shows that at the scanners' maximum resolutions there is beam footprint overlap and the range and distance errors are of similar magnitude as the beam footprint. The scanners

quoted resolution are also of the same magnitude as the placement error. Due to the nature and source of the errors the overall effect may cancel or double the overall error for individual points within the cloud scene.

Table 9 Scanner laser beam diameter and point spacing with range at maximum resolution (min step angle).

Scanner	Range (m)	Beam Diameter (m)	Point spacing (m)	Points/Beam diameter
FARO	5	0.0040	0.0008	5
	10	0.0049	0.0016	3
	15	0.0059	0.0024	2.5
	20	0.0068	0.0031	2
Leica	5	0.0060	0.0012	5
	10	0.0060	0.0012	5
	15	0.0060	0.0012	5
	20	0.0060	0.0012	5
Riegl	5	0.0068	0.0002	34
	10	0.0085	0.0004	21
	15	0.0103	0.0006	17
	20	0.0120	0.0008	15

4.6.11 Registration Sphere Position Error Correction

Four registration spheres were used in each scan; these were placed in the same position for each scan and at a maximum range was set to ensure that there would be sufficient points (greater than 10) on all spheres. The spheres were placed in a pattern such that three were equally spaced and collinear and a fourth nearly at right angles to the centre of the line of spheres. The collinear arrangement was chosen so that range and bearing error could be assessed for each scanner; the

bearing from sphere one to two should be the same as from two to three. This arrangement would also indicate if inter-scanner optical centre miss-alignment, as this would show up as a constant error in the inter-sphere bearing and/or range. The collinear arrangement was considered acceptable as any transformation would not cause a rotation about the line as there was a further point and the scanners were levelled.

When using registration spheres with a single scanner the errors due to range and angle made by the scanner may be assumed to be similar for each scan. If different scanners are used, as in this research, then each scanner will have their own range and angle measurement errors. This will mean that the calculate sphere centres will have differing positional uncertainty; therefore, to improve the registration accuracy some form of correction must be made to the sphere centres. One scanner can be chosen as the reference; the other scanner sphere centre positions corrected to this reference.

If registration targets are used to calculate the rigid transform between two or more point clouds, there will be inherent errors in the absolute and relative position of each target between scans. The problem is to minimise this error; the similarity of this problem and that of traverse closure in surveying was used to develop a new method. A traditional traverse aims to measure the bearing and range between successive reference points, finishing by measuring back to the start point. Many methods of adjusting a traverse have been developed, the most notable being the compass, transit and least squares. The least squares

method was rejected as the method requires redundant measurements, which were not available for this problem (sphere alignment).

4.6.12 Pseudo traverse correction method

The error E can be expressed as the sum of the latitudes λ and the sum of the departures ϕ, (Bowditch 1807).

$$E_\lambda = \sum_{p_1}^{p_n} \lambda \ and \ E_\varphi = \sum_{p_1}^{p_n} \varphi \tag{50}$$

To close the traverse and minimise the error the error of closure E_C must be minimised.

$$E_c = \sqrt{\left(E_\lambda^2 + E_\varphi^2\right)} \tag{51}$$

The precision of the closure can be expressed as the ratio of the error to the length (L) of the traverse (perimeter).

$$Precision = \frac{E_c}{perimeter} \tag{52}$$

To reduce the overall error in the transform for registering two or more point clouds using targets the position of the targets in each scan must be adjusted.

4.6.13 Bowditch compass rule

The Bowditch (Bowditch 1807) or sometimes called the compass rule distributes the errors at each point made the assumption that angles and distances had the same error and the errors were random. A

correction (C) to the latitude and departure is made at each point (ab, bc …).

$$C_\lambda = -\frac{E_\lambda L_{ab}}{L} \; and \; C_\varphi = -\frac{E_\varphi L_{ab}}{L} \quad (53)$$

4.6.14 Transit Rule

The transit rule makes the assumption that the instrument has higher angular than range precision.

$$C_\lambda = -\frac{|\lambda| E_\lambda}{\sum|\lambda|} \; and \; C_\varphi = -\frac{|\varphi| E_\varphi}{\sum|\varphi|} \quad (54)$$

4.6.15 Pseudo traverse correction method selection

The main difference between the remaining two methods considered was the treatment of range and bearing error. Table 8 gives the manufacturer's published precision for the three instruments used in this study; Table 10 shows that the precision in angle measurement is always significantly better than range measurement for all three instruments. Therefore a traverse closure method that weights angle and range measurement error differently should be preferred; both methods were assessed and the results are shown in Figure 72 & Figure 73.

Table 10 Comparison of linear precision due to angle and range.

Scanner	Range (m)	Linear Precision (m)		Angle/Range (m)
		Angle	Range	
FARO	5	0.000050	0.002	40.00
	10	0.000100	0.002	20.00
	15	0.000150	0.002	13.33
	20	0.000200	0.002	10.00
Leica	5	0.000300	0.004	13.33
	10	0.000600	0.004	6.67
	15	0.000900	0.004	4.44
	20	0.001200	0.004	3.33
Riegl	5	0.000045	0.005	111.11
	10	0.000090	0.005	55.56
	15	0.000135	0.005	37.04
	20	0.000180	0.005	27.78

4.6.16 Registration using the corrected sphere centres

After minimising the sphere position errors using the adapted Bowditch method, the mean rotation angle was applied to initially align the Leica and Riegl point clouds to the FARO reference. The residual error point to point was calculated and then the alignment was refined using ICP (point to point). Again the residual error was recorded, and the mean rotation angle and ICP transformation matrix then applied to the full point clouds. The multi-spectral point cloud was then created from the aligned clouds.

4.6.17 Detection of angle and range error

Spheres surface were precision made so the curved lines drawn by the scanners on each sphere should be perfect major and minor circles, any deviation is an indication of ranging or angle error. As the angular precision of the scanners is very high, the main source of error was considered to be range.

4.6.18 Sphere position errors

The uncorrected residual error in sphere positions is shown in Figure 71, the corrected residuals using the Transit rule are shown in Figure 72 and the Bowditch method in Figure 73. It was concluded that spheres numbered 3 and 4 were moved from the datum positions in the Riegl and Faro scans. If the error was due to miss-position of the scanner all spheres for that scan would be shifted from the mean. The sphere positions were corrected using adapted versions of the Bowditch and Transit traverse closure methods; the Bowditch method produced the smaller residual errors.

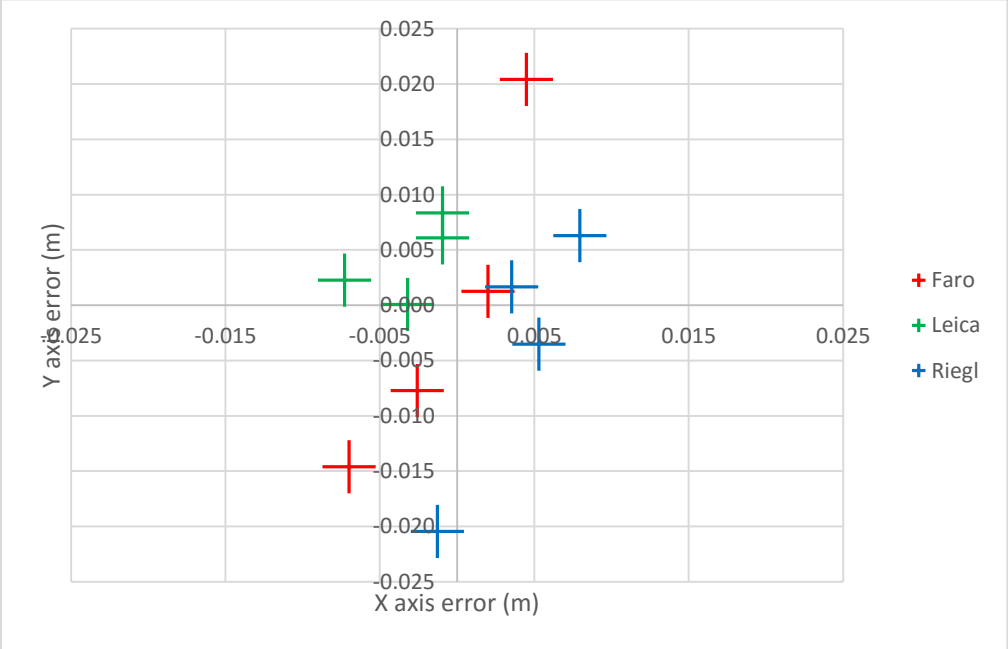


Figure 71 Residual sphere centre position errors (Uncorrected), Faro scanner reference system.

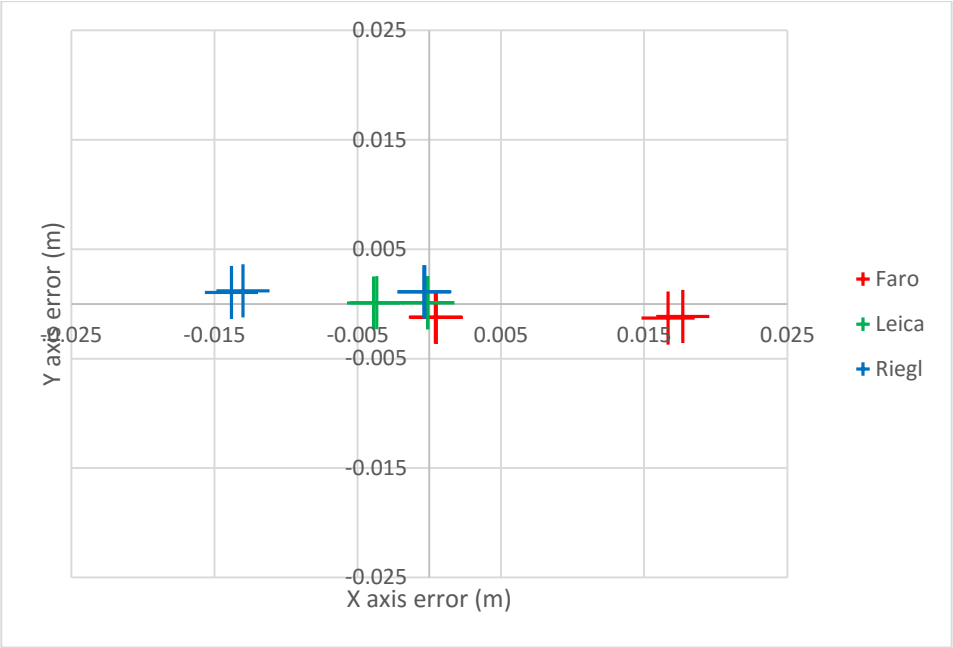


Figure 72 Residual sphere centre position errors (Transit rule correction), Faro scanner reference system.

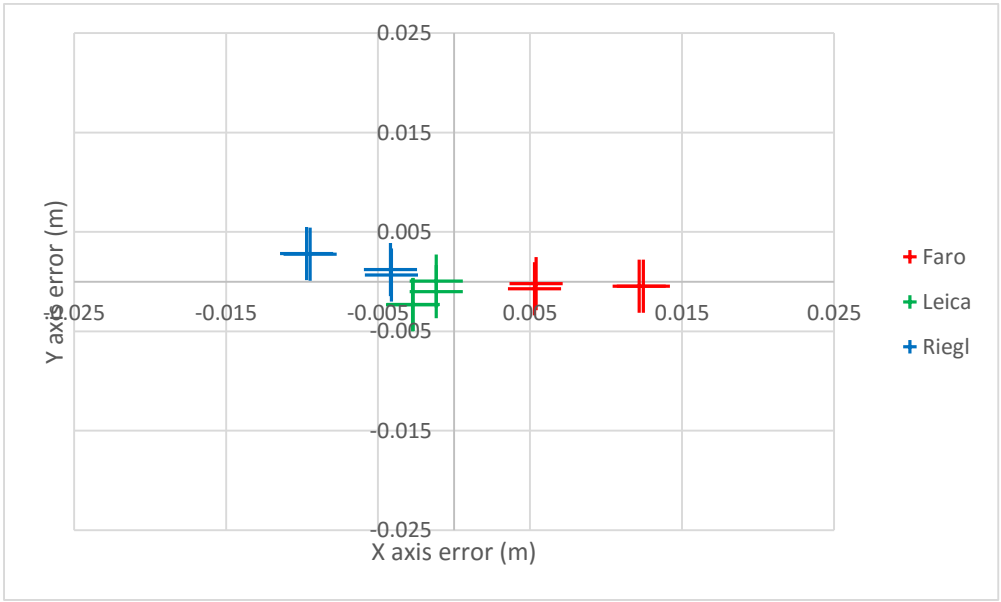


Figure 73 Residual sphere centre position errors (Bowditch correction), Faro scanner reference system.

4.7 Classifiers

There are many classification methods, including supervised, unsupervised, parametric and non-parametric (Tso and Mather 2009).

The maximum likelihood classifier may be suitable for thematic classification where the data is sourced from a single sensor (Lichti 2005). This research uses data from three dissimilar scanners, from multiple non-simultaneous scans; as such a classifier that was tolerant to sensor differences and changing atmospheric conditions was required. Brown et al. (2008) used an Artificial Neural Network (ANN) to map NDVI indices from the Advanced Very High Resolution Radiometer (AVHRR) to those from the Moderate Resolution Imaging Spectroradiometer (MODIS). Some artificial neural networks have been shown to classify data that are multi-mode or not linearly separable in the original spectral space (Szuster et al. 2011). A network designed with multiple layers and back propagation such as the Multi-Layer Perceptron (MLP) is capable of classifying non-linear datasets found in land cover and urban remotely sensed imagery. In light of the above several techniques were implemented as classifiers:

1. Feedforward backpropagation neural network.
2. Decision tree.
3. Discriminant.
4. Support Vector Machine (SVM).
5. K-Nearest neighbour.

Different configuration of each classifier and different combinations of the input dataset were tested. The neural network classifier has many factors to its configuration and therefore explained in more detail here the other classifiers have been discussed earlier.

4.7.1 Neural Network Classifier

The most common neural network that has been used in classification of remotely sensed data is the multi-layered perceptron (MLP), with feed forward back-propagation design. Artificial neural networks are based on biological neural networks, consisting of inter-connected neurons within a layer and between layers. The network typically has one input, one or more middle (hidden) and one output layer. The input to each neuron is a weighted sum of the outputs from the connected neurons; this is known as the transfer function. Each neuron processes the weighted sum using an activation function. The activation function is the biological neural network equivalent of the rate of action potential firing in the neuron. The most commonly used activation functions used in pattern recognition are log-sigmoid and tan-sigmoid functions (Mather 2004); both of these were used in this study. Sigmoid functions are thought to be the closest equivalent to biological neurons as, unlike a step function; they have a region of uncertainty. During training the weights are initially random values and after each cycle of calculation through the network the weights are adjusted so that the error between the calculated output and the required output value is minimised; this is the back-propagation element of the network. The cycle of calculation continues until the required error is achieved or the maximum number of cycles is reached. The network's memory is the final weight values; the network is tested by presenting unknown input values and using the store weights during the calculation. A set of inputs representing a trained class will produce the associated output to the class. A detailed

description of the training functions used with the proposed ANN are in Appendix D.

4.7.2 Artificial Neural Network Approach

Integration of the advantages in existing feature extraction and matching techniques and neural network classification techniques is proposed to create a more flexible and adaptive method. One proposal is to combine the rotation and scale invariance of the SIFT (Lowe 2004) algorithm with neural network stereo image disparity matching. The method would initially use stereo images from a point cloud in order to test existing image matching techniques; this step would be removed subsequently and the system would use raw point cloud data s input. A second hybrid proposal would use images of objects as training data but the recognition / matching phase would use point cloud data.

A difficulty in using a laser point cloud as input to a neural network is its 3D nature and consequent algorithmic and memory problems. If the point cloud could be reduced to 2D without any loss of fidelity these problems might be reduced and neural network methods used in 2D could be implemented. Wang & Hsiao (1999) extracted 3D information from stereo pairs of images using a BP network that was image independent; once trained on one pair of images it could be used to match any other pair. This ability was due to the use of feature differences; three features were used: intensity, variation and orientation. A limiting factor of their use of imagery was the variability of intensity values because of the variations in solar illumination; laser

scanner returns would not have this limitation as they are self-illuminated.

4.7.3 Design

An example of a feed-forward back-propagation network consisting of one input, one hidden and one output layer is shown in Figure 74. Only one and two hidden layer designs were used as larger number of hidden layers have been shown not to improve classification accuracy (Zhou and Yang 2004). The number of neurons in the input layer was set to the number of laser intensity ratios (three) for each point and the output layer was set to the number of trained classes (five). The number of neurons in the hidden layer was varied between five and fifteen. A bias was used to shift the activation function enabling customisation of input to output. The training algorithm was scaled conjugate gradient back-propagation, producing a fast gradient descent method (Møller 1993) which reduced the learning phase to an acceptable time when run on a standard PC.

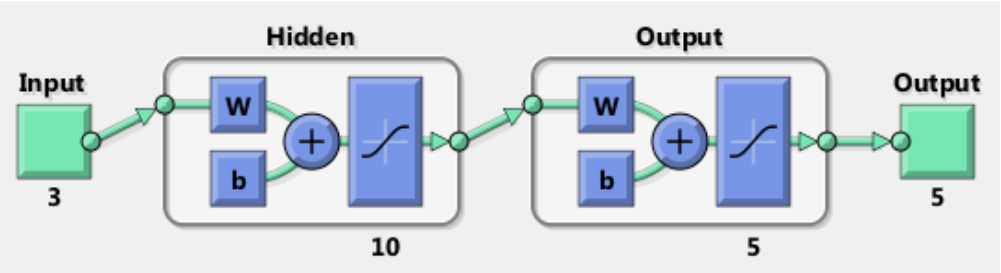


Figure 74 MATLAB Neural network design: w=weight, b=bias, activation function denoted by the rectangle and sum.

4.7.4 Data

The intensity values of a set of five classes of material, were extracted from the point cloud; these were wood, brick, steel, gravel and

pavement. These materials were chosen as they represented over 90% of the building's construction and provided a degree of variation in range and incidence angle, to test the capability of the chosen methodology. The neural network had inputs, representing the intensity ratios, a variable number of neurons in the hidden layer and five outputs, representing the five chosen classes of material. Training and test data sets were produced from co-registered multiple scan data. The training input data was created from random samples of each material class using *CloudCompare*© point cloud software. Training data was formatted into examples and targets for each class compatible with MatLab neural network application.

4.7.5 Training

A supervised network requires training; this is carried out by presenting the network with intensity ratio examples of each class. The network was trained with 500 examples of each of the five classes. The training data was chosen from an area of the scan that was not in the subsequent test data. This was important so that the training data would not influence the test results. However, the training data was less than 0.08% of the test data. Training was complete when no further improvement in the back-propagation error or the maximum number of iterations was reached. The training data was not used in the testing phase.

4.7.6 Testing

The network performance was evaluated using the 'ground truth' reference dataset of the complete test site. The network produced

output values, between zero and one, for each class; the higher the value the more certain the network was of the scan point belonged to that class. A class number and false colour value was then assigned to each scan point based on the ANN output to denote class membership. This classified point cloud was then scored against the reference point cloud and the results shown in a confusion matrix format.

4.8 Summary

To develop a method for classifying materials, using the spectral signature of the material, it was evident that the main influences on the quality of the results were: normalising reflected intensity for variations in range and incidence angle, alignment of each scanner, co-registration of the individual scanner point clouds and finding a suitable classifier that fitted the requirements of the data.

The variation in range and incidence angle was resolved by the use of ratios of the intensity ratios between each scanner and hence creating ratios of wavelengths. This solution was supported by the research by (Rouse et al. 1974) in their ‘Great Plains’ study into monitoring vegetation health by the creation of a new vegetation index they called NDVI. The accurate alignment of the instruments was achieved by knowledge of each scanners construction and dimensions so that their optical centres could be offset from a known reference. The registration of the three individual scanner point clouds was achieved by assessment of the reference sphere alignment using a variation of Bowditch traverse correction method and a semi-rigid transformation.

Rather than pick just one classification method several classifiers were implemented, including several configurations of each classifier. In addition to traditional classifiers a neural network classifier was also used. A common method of measuring the classifiers performance was used to enable ease of comparison of the results. The method drew aspects of methodology from many different disciplines, the method presented here was optimised for the task of material classification using laser scanner reflected intensity values.

The novel features of the presented methodology were:

1. Automated classification of construction materials, which could be used to populate a BIM database in parallel with the spatial data, by using multispectral laser intensity data.
2. The use of multiple terrestrial laser scanners, where each had a different laser wavelength, to produce a multispectral point cloud.
3. A novel reflected laser intensity normalisation approach which counteracted the variation in the recorded intensity values caused by incidence angle and range variation. This approach used intensity value ratios, at each point, using three different wavelengths.
4. An adaption of a traditional traverse closure method was developed; this method minimised the effect of the differences between each scanner's scan pattern, beam divergence and range precision, on the accuracy of the multispectral point cloud data.

5. Incorporation of texture as a classifier input to improve the delineation between classes, in order to improve tolerance to the natural variation in a material's spectral signature.

Chapter 5. Results

5.1 Introduction

The results are presented in three sections, the first shows validation of the intensity ratio principle using registration spheres to provide a variation of range and incidence angle and a homogeneous surface type. The second section presents the classification of site 1 and the third section, validation of the classification method. The final section presents the results from adding texture attribute to the classification process. This is followed by a summary of the results and discussion of the significant findings. The complete set of classification results are presented in Appendix A. A sub-set of results that are referenced in the discussion are also presented.

5.2 Intensity Ratio Validation

To test the validity of the intensity ratio theory, intensity ratios from each of the three different wavelength scanners where calculated from scan data of four registration spheres; Figure 75 shows intensity ratios at varying incidence angles and Figure 76 at varying ranges. The variation in the concentric patterns produced shows the deviation from constant ratio for each range or incidence angle change. As there were many points on each sphere the variation of the ratio of intensities appear almost circular, whereas the four spheres used for intensity ration variation with range appear as squares.

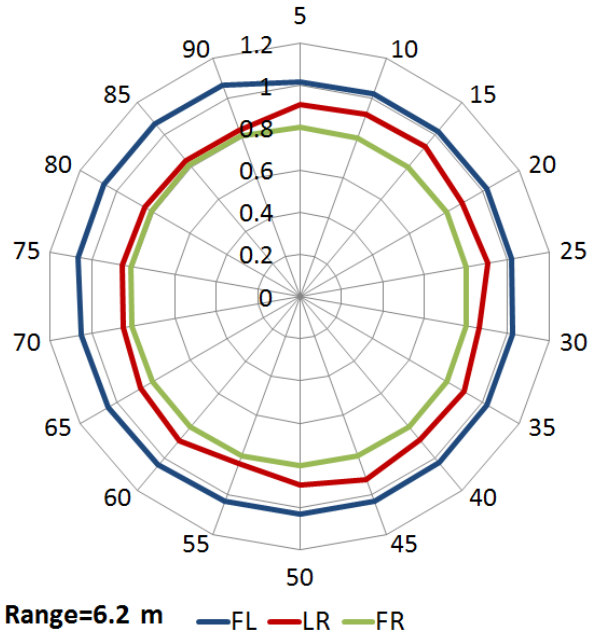


Figure 75 Sphere: Intensity ratios versus incidence angle (degs) @6.2 m: (FARO/Riegl [green], Leica/Riegl [red], FARO/Leica [blue]). Outer axis is incidence angle in degrees.

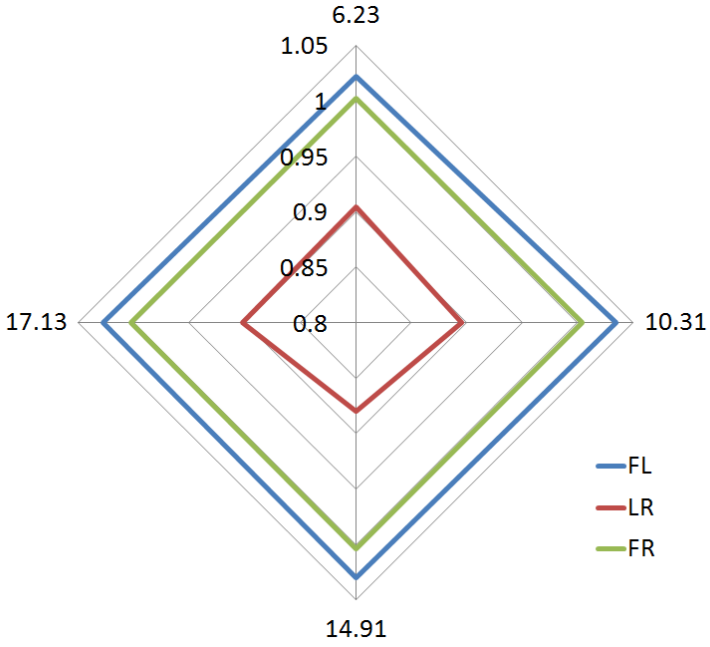


Figure 76 Sphere: Intensity ratios versus range (6.23m, 10.31m, 14.91m, 17.13m) FARO/Riegl [green], Leica/Riegl [red], FARO/Leica [blue]. Outer axis is range in metres.

To further show the result of using ratios of intensity to normalise the effects of changes in incidence angle, pairs of intensity values from

different wavelength scans were converted to ratios using the NDVI formula. The single wavelength result is shown in Figure 77 and the ratio of two different wavelengths is shown in Figure 78; this shows that the reflected intensity was normalised to constant value for a homogeneous material (FARO flexi sphere). The incidence angle variation was zero to eighty degrees. The registration sphere had a Lambertian reflective surface but the pillar it was mounted on was polished steel which was considered to be a specular reflector, the effect on the intensity ratio is shown in Figure 79.

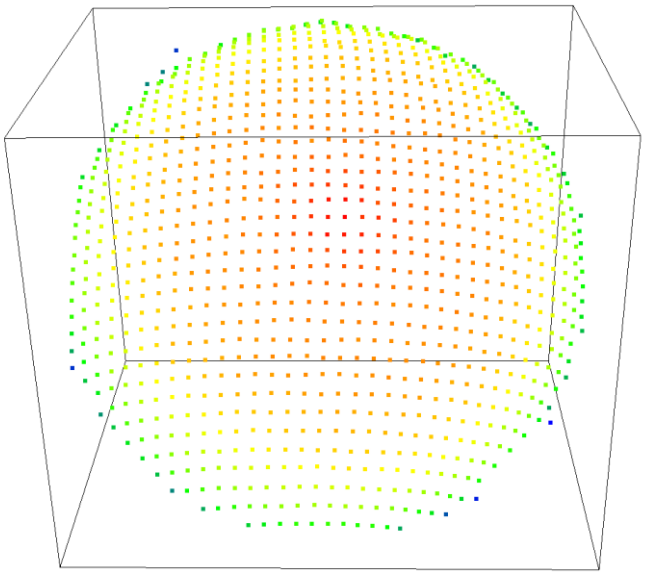


Figure 77 Variation of intensity across the surface of a registration sphere (FARO Flexi), single wavelength NIR, using the FARO scanner.

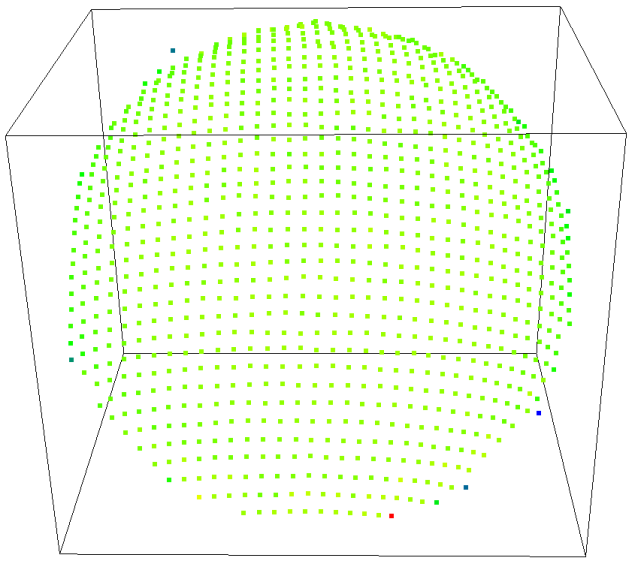


Figure 78 Constant intensity ratio variation across the surface of a registration sphere (FFARO Flexi), two wavelengths NIR and green, FARO and Leica scanners respectively.

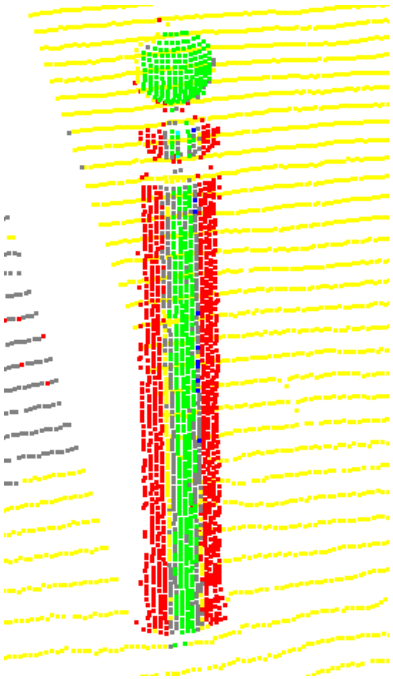


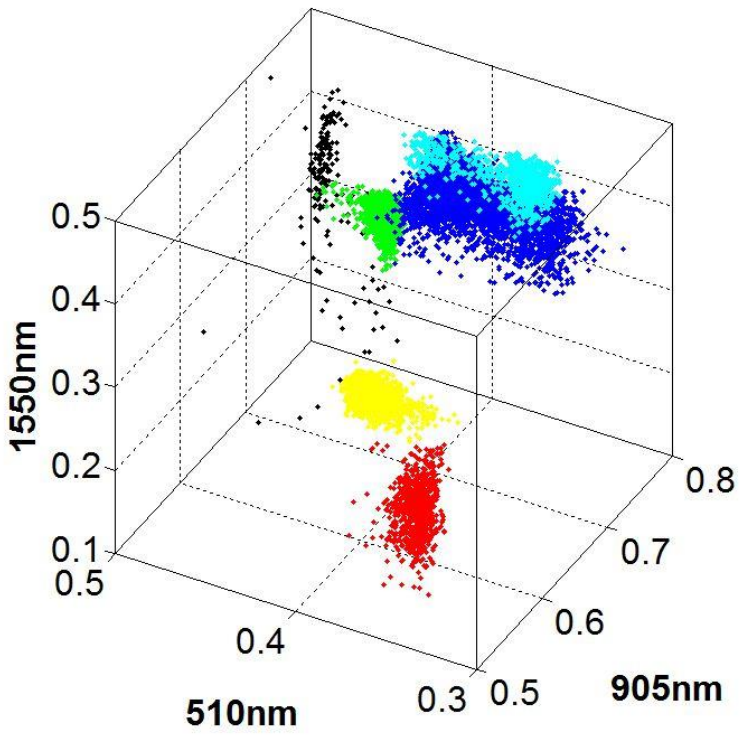
Figure 79 Ratios of intensity shown from a registration sphere and the mounting pillar. The pillar is polished steel, a specular reflector.

5.3 Class Separation

A plot of site 1 intensity ratio data representing each class is shown in

Figure 80. The plot shows that the classes were not linearly separable;

separation required a 2D or higher hyper plane. The some classifiers were able to use higher dimensional hyper planes to separate the data such as the ANN via the network's hidden layer. The results of classification of site 1 reflect the class clustering evident from the 3D view in Figure 80. This was especially so for classes one and two.



Class #	1	2	3	4	5	6
Description	Wood	Brick	Steel	Gravel	Pavement	Unclassified
False colour						

Figure 80 A plot of intensity ratios for each class at 1550nm, 905nm and 510nm wavelengths,

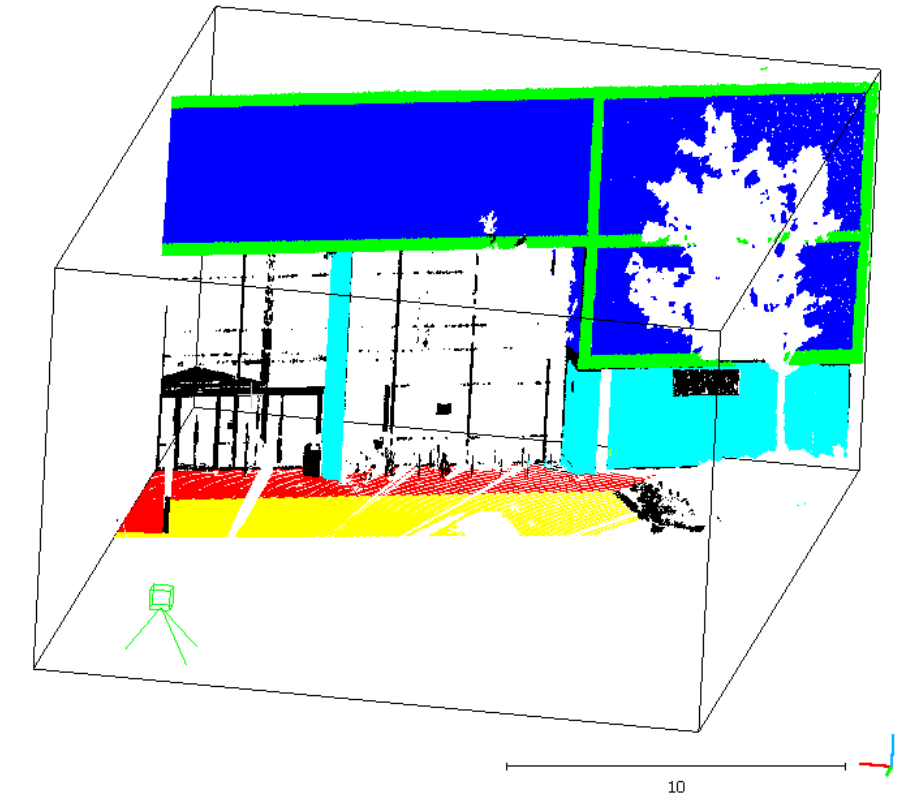
5.4 Site 1 Classification Results

The multispectral point cloud data was classified using a number of different classification techniques:

1. Decision tree.
2. Discriminant analysis.

3. Support Vector Machine (SVM).
4. K-nearest Neighbour (KNN).
5. Backpropagation Artificial Neural Network (ANN).

The classification learner application in MatLab was used for training except the neural network classifier which was developed using MatLab code for training and testing. The remaining classifiers were tested and scored using custom MatLab code. The created MatLab code is in Appendix B. The performance of each classification method was scored against a reference point cloud of known classes. The site 1 reference point cloud is shown in Figure 81.



Class #	1	2	3	4	5	6
Description	Wood	Brick	Steel	Gravel	Pavement	Unclassified
False colour						

Figure 81 Site 1 reference point cloud. The reference cloud was manually created within CloudCompare ©.

The choice of classes was also chosen to overlap materials in Site 2 point cloud, in order to further validate the usefulness of the technique.

5.4.1 Site 1 Classifier Results

The classification results for all classification methods except the ANN are shown in Table 11 and the ANN classifier results in Table 12. The complete set of detailed results are presented in Appendix A. These detailed results are for each classification method and for each trial are given in confusion matrix form for validation and test data and also as a false colour snapshot image of the 3D point cloud. The confusion matrices show the results as a percentage and include the False Negative Rate (FNR). Some detailed results are included in the next section to support the discussion.

Table 11 Classifier results for site 1.

Classifier				Classification rate (%)	
#	Type	Sub-Type	Ratios	Validation Data	Test Data
1	Decision tree	Complex	All	98.6	86.0
2	Discriminant	Linear	All	94.4	83.8
3	Discriminant	Quadratic	All	98.6	84.8
4	SVM	Linear	All	98.4	88.0
5	SVM	Quadratic	All	98.6	87.3
6	SVM	Gaussian	All	98.2	88.2
7	KNN	Medium	All	99.2	87.0
8	KNN	Subspace	All	99.0	85.4
9	KNN	Weighted	1,2	89.3	78.7
10	KNN	Weighted	1,3	89.8	77.1
11	KNN	Weighted	2,3	98.0	84.3
12	KNN	Weighted	All	98.2	87.0

Validation data was a sub-set of the training data that was separated from the data prior to training, the validation data was used after training to estimate the quality of the training before testing on the much larger test data. The training data and test data were from separate sections of the site and did not overlap. The test data is the complete site 1, point cloud.

Table 12 Summary of ANN classifier results for site 1.

				Hidden Layer		Classification rate (%)			
#	Transfer Function	Training Function	Ratios	No of layers	No of neurons	Validation data	Test data	Epochs	Score threshold
13	logsig	trainscg	All	1	10	99.5	87.2	51	0
14	logsig	traincgb	All	1	10	99.5	87.3	48	0
15	logsig	trainrp	All	1	10	98.9	86.9	73	0
16	logsig	trainrp	All	1	5	99.3	85.3	138	0
17	logsig	trainrp	All	1	15	98.7	86.6	53	0
18	logsig	trainrp	All	2	10,10	99.2	87.0	54	0
19	logsig	trainrp	2,3	1	10	97.6	88.9	37	0.9
20	logsig	trainrp	1,2	1	10	89.5	79.3	45	0.9
21	logsig	trainrp	1,3	1	10	89.7	74.7	65	0.9
22	logsig	trainrp	All	1	10	98.1	90.6	44	0.9
23	logsig	trainrp	1,3	1	10	89.7	78.1	66	0.5

The validation results were higher as the data was a sub-set of the training data and therefore a closer fit. Several backpropagation neural networks were trained and tested, different training and transfer functions and number of hidden neurons/layers were investigated. The log sigmoid (Figure 82) transfer function was used as this has a range 0-1 which matched the training data class format.

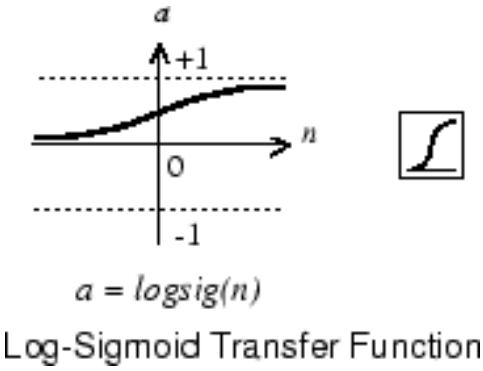


Figure 82 Log Sigmoid transfer function definition.

A summary of the ANN classifier results for site 1 are shown in Table 12 and confusion matrices and false colour images are listed below. The classification rate was measured against the same reference point cloud as the other classification methods above, Figure 81. A key to the training and transfer functions used with the ANN classifier are shown in Table 13 and Table 14.

Table 13 Training function and acronyms used in results table.

Training function	**Acronym**
BFGS Quasi-Newton	trainbfg
Conjugate Gradient with Powell/Beale Restarts	traincgb
Fletcher-Powell Conjugate Gradient	traincgf
Polak-Ribiére Conjugate Gradient	traincgp
Variable Learning Rate Backpropagation	traingdx
Levenberg-Marquardt	trainlm
One Step Secant	trainoss
Resilient Backpropagation	trainrp
Scaled Conjugate Gradient	trainscg

Table 14 Transfer functions and acronyms used in results table.

Transfer function	Acronym	Output
Log-Sigmoid	logsig	0 - 1
Tan-Sigmoid	tansig	-1 - +1
Linear	pureln	-inf - +inf
Radial Bias	radbas	-inf - +inf

5.4.2 Site 1 Classifier Results Analysis

The overall classification rate ranged between 74.7% to 90.6%, with a mean of 84.8% for the more traditional classifiers and 84.7% for the ANN classifier. The individual class classification rates varied from 74.8% to 100%. The classes with the highest classification rate were steel, gravel and pavement, whilst the wood and brick classes had significantly lower rates. Classifiers were tested with all three inputs and with combinations of two inputs; rates were higher with all three inputs

other than the combination of combination of ratios two and three. The class separation plot is repeated here in Figure 80 as this shows the distinct separation of the brick class into two clusters and the wood class spread across the same range of values; furthermore, the brick and wood class occupy the same region of space for a percentage of the clusters. The plot of the clusters shows how the classes are linearly separable in three dimensions; two linear classifiers were tested and performed much better than expected, failing only to separate the brick and wood classes, here the classification rate fell to 75.7% and 69.9% respectively for the Linear discriminant method

The test dataset included noise in the form of stray points due to scanner limitations, moving objects (people walking through the scan in progress) and reflections from glass. Some noise was also introduced by the process of combing the three scans caused by incorrect assignment of neighbouring scan points from different classes; a problem that might be reduced by iterating the classification process. The data set was not manually cleaned to remove the noise, where it was apparent, as it this would have overrated the viability of the method for realistic data sets.

Another factor that may have influenced the results was texture, the reflected intensity from a common surface might vary if the texture of the surface varies due to the varying normal angles to the micro structure of the material. However, surfaces with constant texture, such as the steel in this example should return similar reflections form any part of the surface. Absorption at certain wavelengths would also affect

the reflected intensity. The alignment and beam footprint difference between the three scanners also introduced variations in the intensity measurements; the magnitude of the effect would vary between textured and smooth surfaces. The beam footprint size acted similar to a mean filter and varied between the three scanners. A reason for this choice of test site was the range of material texture, as it was hoped to give some insight into the effect of texture. The texture size considered was not within the wavelengths of the lasers; this was considered earlier in the discussion on laser speckle. Some support for the preceding premise was evident in the consistently high classification rate of the steel class. The steel structure on this building was painted which gave it a smooth matt finish with very low texture variation. The high classification rate may also have been due to this being the only class where the surface was homogeneously one material; all the other classes were made up of one main material interspersed with several others. The classification rate varied dependent on the classifier. The results in any further study may be improved for these classes by treating the inter-material, for example mortar with brick, as an extra class.

In this section results are analysed by class. A summary of the classification rates for each class in each test is shown in Table 15.

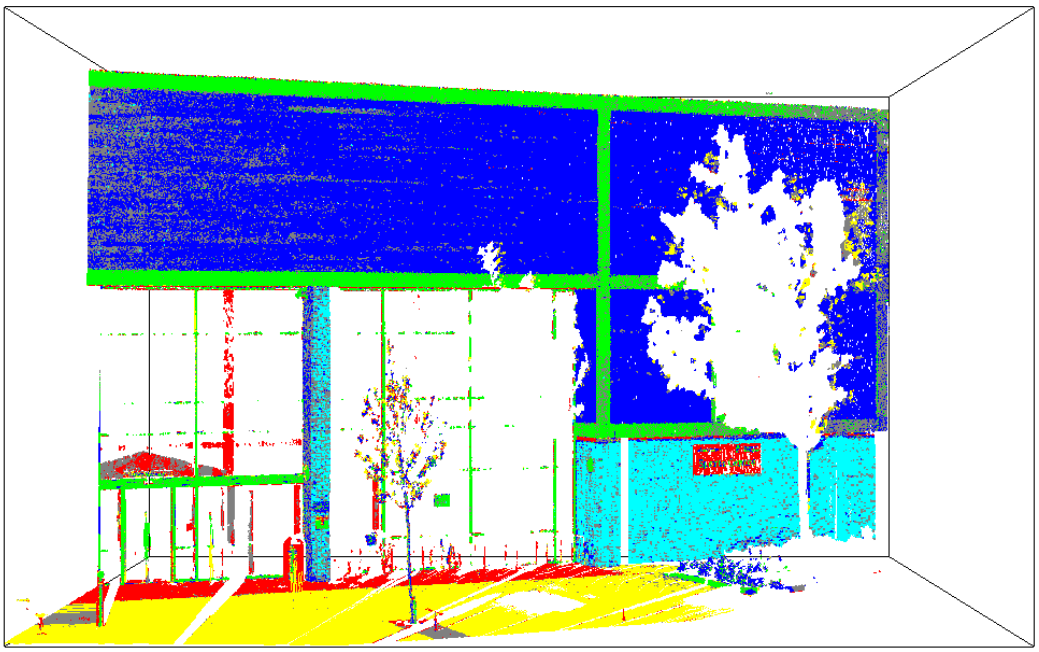
Table 15 summary of classification rate by class. Number of neurons in hidden layer (#), ANN score threshold (Thr).

				Class #	1	2	3	4	5			
				Class description	Wood	Brick	Steel	Gravel	Pavement			
#	Classifier		#	Ratios	Classification rate %					Thr	Mean	Rank
1	Decision tree	Complex		All	92.2	76.8	80.8	93.6	86.7	-	86.0	12
2	Discriminant	Linear		All	69.9	75.7	92.0	99.3	82.3	-	83.8	19
3	Discriminant	Quadratic		All	91.6	75.1	75.3	94.4	87.7	-	84.8	17
4	SVM	Linear		All	92.4	75.7	89.5	97.6	84.7	-	88.0	4
5	SVM	Quadratic		All	94.4	75.3	86.3	95.5	85.0	-	87.3	5
6	SVM	Gaussian		All	91.0	75.3	91.5	98.2	84.7	-	88.1	3
7	KNN	Medium		All	93.0	74.8	86.7	95.1	85.2	-	87.0	9
8	KNN	Subspace		All	87.4	75.9	79.4	98.4	86.0	-	85.4	13
9	KNN	Weighted		1,2	71.9	59.2	82.9	94.7	84.7	-	78.7	20
10	KNN	Weighted		1,3	71.8	76.0	52.6	98.6	86.8	-	77.2	22
11	KNN	Weighted		2,3	90.3	76.0	81.8	89.6	83.7	-	84.3	18
12	KNN	Weighted		All	92.5	76.1	85.7	95.0	85.6	-	87.0	8
13	ANN	trainscg	10	All	92.6	77.3	85.6	95.0	85.6	0	87.2	6
14	ANN	traincgb	10	All	90.0	76.2	85.4	98.9	84.0	0	86.9	10
15	ANN	trainrp	10	All	88.0	75.9	81.9	94.7	85.8	0	85.3	14
16	ANN	trainrp	5	All	90.3	76.1	85.9	95.2	85.3	0	86.6	11
17	ANN	trainrp	15	All	91.1	78.0	84.0	96.3	85.9	0	87.1	7
18	ANN	trainrp	10,10	All	90.2	76.0	82.8	93.2	83.0	0	85.0	15
19	ANN	trainrp	10	2,3	90.2	76.0	82.8	93.2	83.0	0.9	85.0	15
20	ANN	trainrp	10	1,2	79.7	70.2	97.4	100.0	100.0	0.9	89.5	2
21	ANN	trainrp	10	1,3	91.1	94.5	0.0	99.2	88.6	0.9	74.7	23
22	ANN	trainrp	10	All	97.0	81.2	88.2	99.2	87.3	0.9	90.6	1
23	ANN	trainrp	10	1,3	57.1	77.5	70.8	98.8	86.4	0.5	78.1	21
				Max	97.0	94.5	97.4	100.0	100.0			
				Mean	86.8	76.1	79.5	96.2	86.0			
				Min	57.1	59.2	0.0	89.6	82.3			

The highest scoring classes were gravel and pavement, the lowest brick, steel and wood in between. The worst classification rate was zero for the brick class with ANN classifier (21). The classification rate with the ANN classifier can be seen to be sensitive to the score threshold. The score threshold is a measure of the certainty of class membership, the scores range from 0-1, which equates to not in class to certainly in class.

5.4.3 Class 1 Wood

The highest score for class 1 wood was 97.0% this was an ANN classifier using all three ratios and with a score threshold of 0.9. A false colour image of the result is shown in Figure 83.



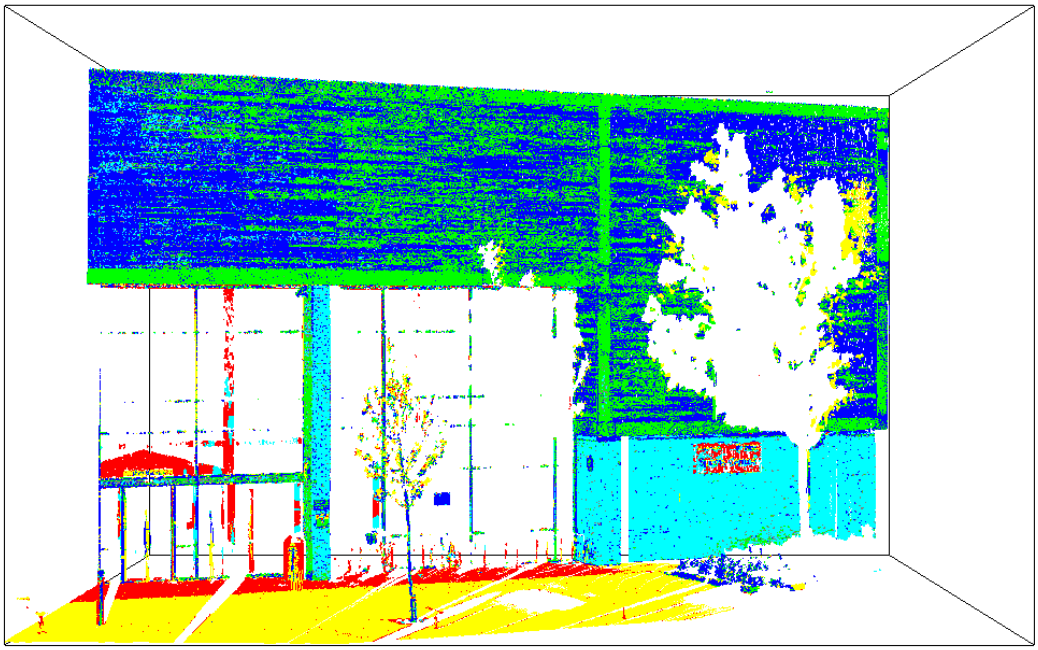
Class #	1	2	3	4	5	6
Description	Wood	Brick	Steel	Gravel	Pavement	Unclassified
False colour						

Figure 83 ANN classifier result as false colour image. Some areas of the scan are in shadow from vegetation.

The areas which were miss-classified or not classified were mainly in one area and showed a linear form consistent with the plank shape and gaps between the planks. It can be seen from the image that some of the brick was miss classified as wood, particularly on the near pillar. Vegetation, bottom right, and the tree trunk were also classified as wood. The lowest classification rate was 57.1% from an ANN classifier using only ratios one and three.

5.4.4 Class 2 Brick

The highest classification rate for class 2 brick was 94.5% using an ANN classifier and only ratios one and three, but this was at the expense of the other classes, Figure 84.



Class #	1	2	3	4	5	6
Description	Wood	Brick	Steel	Gravel	Pavement	Unclassified
False colour						

Figure 84 Classifier 21 classification rate as false colour.

5.4.5 Class 3 Steel

The highest classification rate for class 3 steel was 97.4% using classifier 20, ANN using ratios one and two. However the worst performance was 0%, classifier 21, ANN using ratios one and three. However, when the score threshold was set to 0.5 rather than the previous 0.9 improved to 70.8% with the same classifier (21). The

histogram of scores for this classifier shows the reason for this behaviour very clearly, Figure 85.

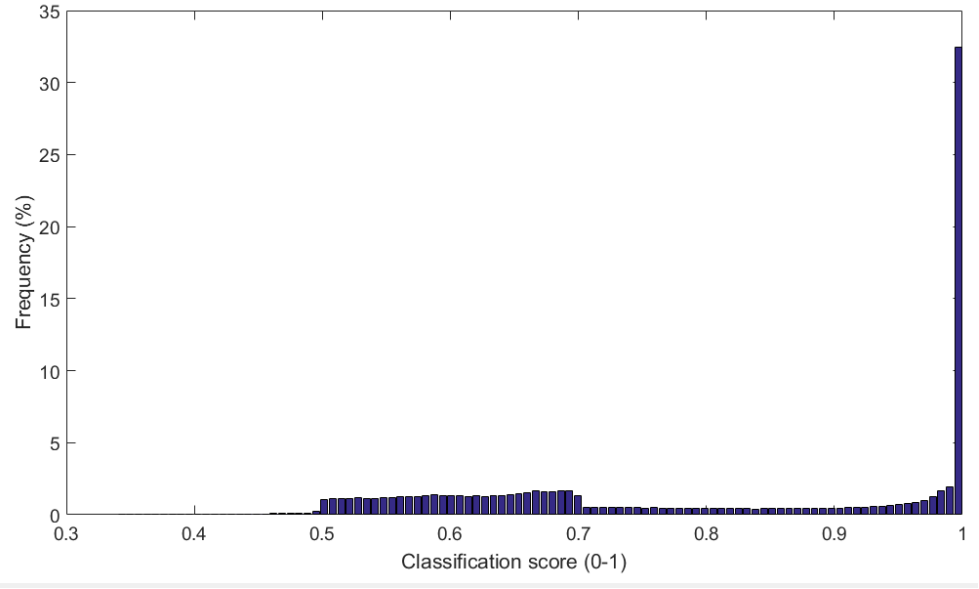


Figure 85 Histogram of ANN classifier scores for network 23, score threshold 0.5.

The range of scores between 0.5 and 0.7 were almost all relating to class 3, the ANN had low confidence but correctly classified the class.

5.4.6 Class 4 Gravel

This class was one of the two classes that scored 100% with an ANN classifier (20); this classifier was ranked second for overall performance across all classes. The lowest score was 89.6% with a KNN weighted classifier (11) using ratios two and three. The high scoring of this class with all classifiers, mean 96.2, was unexpected, as gravel it was thought to vary in colour and spacing; close inspection revealed that it was sealed with a resin and had been rolled level. It was thought that the resin layer was providing the consistency of ratio values over the whole surface.

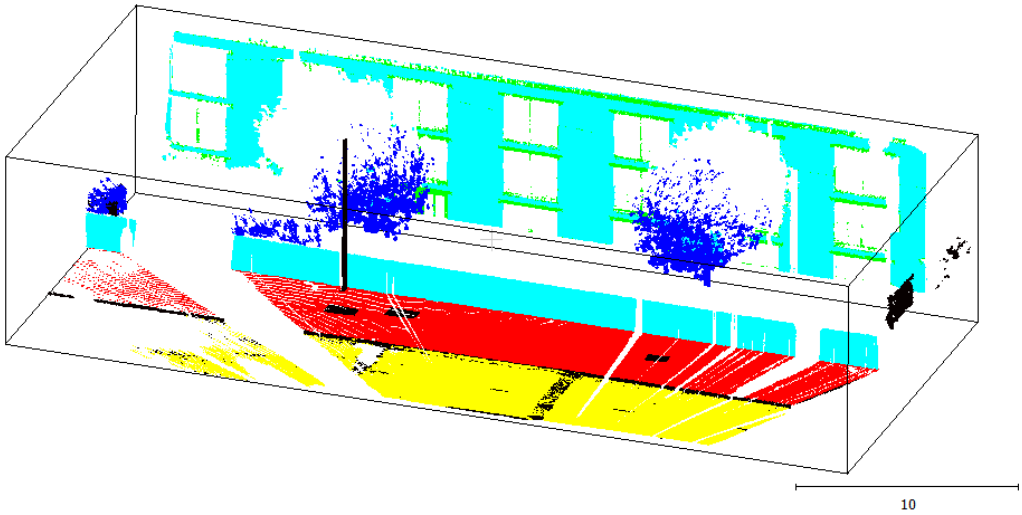
5.4.7 Class 5 Pavement

This class was the other class to score 100% with the same classifier as class 4. The lowest classification rate was 82.3%, linear discriminate (20). The number of points in this class was small and at a high angle of incidence to the laser beam, it was also a very low reflector in visible light.

5.5 Site 2 Classification Results

5.5.1 Introduction

To validate the material classification method several other sites were scanned which included many different building types constructed of many different materials to site 1; site 2 was chosen from these to independently validate the classification method as it contained some similar materials to site 1. Site 2 was scanned at the same time as site 1, as it was within the field of view of the scanners, but in the opposite direction and at a different range. The trial was performed using training data of similar but not identical materials; which included brick, steel and pavement classes. The training data was from site 1 for similar materials. Two additional classes were included in this trial, foliage and road surface, which was sufficiently different to the pavement class to warrant inclusion. The foliage class was not included in site 1 due to the time of year of the scan. As one scanner wavelength was green and another NIR it was thought that this would contribute to a high classification rate of these classes. The classification used the method that scored highest in site 1, an ANN classifier. The reference point cloud is shown in Figure 86, the ANN classified point cloud in Figure 87 and the classification accuracy in Table 16 ANN: classification rate, test data, per true class.



Class #	1	2	3	4	5	6
Description	Foliage	Brick	Steel	Road	Pavement	Unclassified
False colour						

Figure 86 Site 2 Reference Cloud.

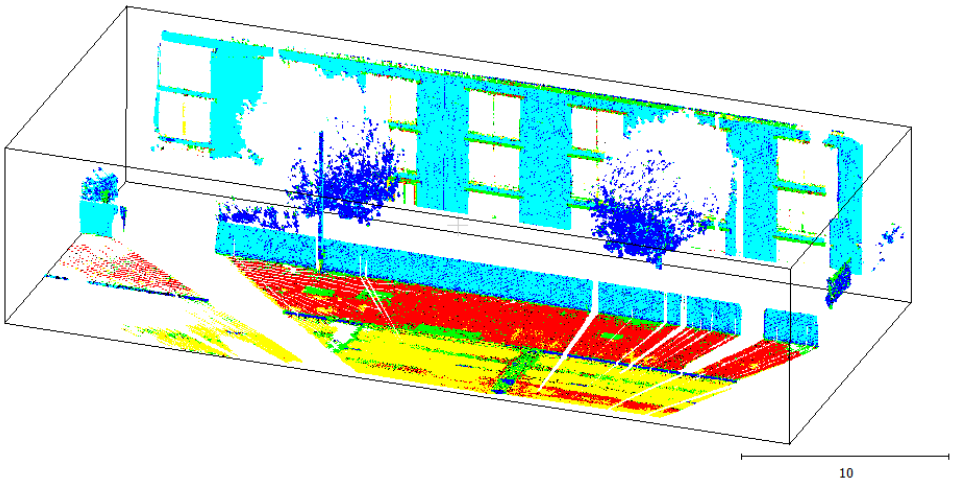


Figure 87 Site 2 ANN classified point cloud

Table 16 ANN: classification rate, test data, per true class.

	Per True Class						
True Class 1	86.7%	10.8%	2.4%	0.0%	0.0%	Foliage	13.3%
2	12.7%	86.8%	0.5%	0.0%	0.0%	Brick	13.2%
3	5.1%	0.0%	74.4%	10.3%	10.3%	Steel	25.6%
4	0.0%	0.0%	8.1%	76.8%	15.2%	Road	23.2%
5	1.0%	0.0%	11.2%	5.1%	82.7%	Pavement	17.3%
	1	2	3	4	5		FNR
	Predicted Class					Rate	81.5%

5.5.2 Site 2 Classification Results Discussion

The site 2 data was classified by an ANN classifier with the same parameters as classifier 22 in Table 12. The common classes with site 1 were brick, steel and pavement. The brick class performed better than in site 1, which may have been due to better separation from the closest class in site 1 which was wood, not present in this trial. The steel class performed worse than site 1 and this was thought to be due to the sharp internal angular corners which may have acted as retro reflectors, producing very high intensity returns not consistent with the rest of the surface. The pavement class classification rate was slightly down from site 1, this area had several depressions which had collected debris which may have presented intensity values too far from the trained values for this class. The ANN also classified the steel manhole covers

in the pavement as steel class, even though they were not in the training data set, these can be seen as square areas of green in Figure 87. Unfortunately, some road markings were also miss-classified as steel. The new classes of foliage and road had mixed results. The tree class classification rate was 86.7% and in Figure 87 a wooden fence on the right hand side and two bushes on the left were classified as foliage in addition to the trees. Unfortunately, the lamp post was also classified as foliage, an explanation may be that the particular paint on the lamp post was very reflective in the NIR, similar to the NIR response of vegetation.

5.6 Pseudo Texture

Additional trials were carried out which built on the concept proposed in Vickers (2013) where a measure of texture was detected in scans of concrete blocks; the texture granularity being well below the range resolution of the scanner. It was found that the variation in reflected Laser intensity had a pattern similar to the texture of the surface. The extra trials set out to test this theory with site 1 data. The data was re-configured such that each point in the point cloud contained its intensity ratio values and the intensity ratio values of the eight nearest neighbours, this resulted in 27 input predictors and 5 output classes for the classifier. The chosen classifier was the neural network design that scored highest in the previous trials, #22. The hidden layer size was varied between 10 and 30; the best result was obtained with 25 hidden layer neurons. The results of the trial are shown below in Table 17, Table 18, Figure 88 and Figure 89.

Table 17 Site 1ANN: classification rate, validation data, per true class. Pseudo texture trial.

Per True Class

True Class	1	2	3	4	5		
1	95.3%	3.5%	1.2%	0.0%	0.0%	Wood	4.7%
2	5.6%	94.4%	0.0%	0.0%	0.0%	Brick	5.6%
3	0.0%	0.0%	100.0%	0.0%	0.0%	Steel	0.0%
4	0.0%	0.0%	0.0%	100.0%	0.0%	Gravel	0.0%
5	0.0%	0.0%	0.0%	0.0%	100.0%	Pavement	0.0%
	1	**2**	**3**	**4**	**5**		FNR
	Predicted Class					**Rate**	**97.9%**

Table 18 Site 1ANN: classification rate, test data, per true class. Pseudo texture trial.

Per True Class

True Class	1	2	3	4	5		
1	93.9%	3.7%	1.6%	0.7%	0.0%	Wood	6.1%
2	8.7%	86.1%	4.5%	0.4%	0.2%	Brick	13.9%
3	4.6%	0.8%	92.1%	1.9%	0.7%	Steel	7.9%
4	3.2%	0.0%	1.4%	95.2%	0.2%	Gravel	4.8%
5	0.3%	0.1%	6.0%	10.3%	83.3%	Pavement	16.7%
	1	**2**	**3**	**4**	**5**		FNR
	Predicted Class					**Rate**	**90.1%**

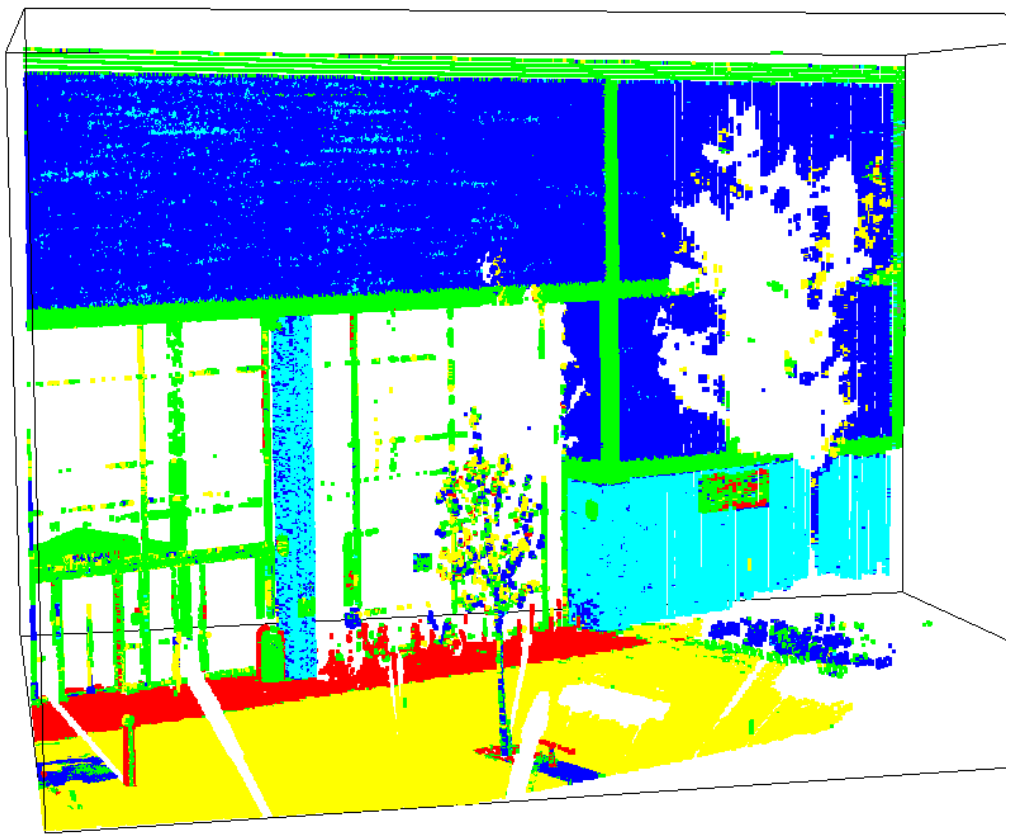


Figure 88 Site 1 ANN classified point cloud, pseudo texture trial

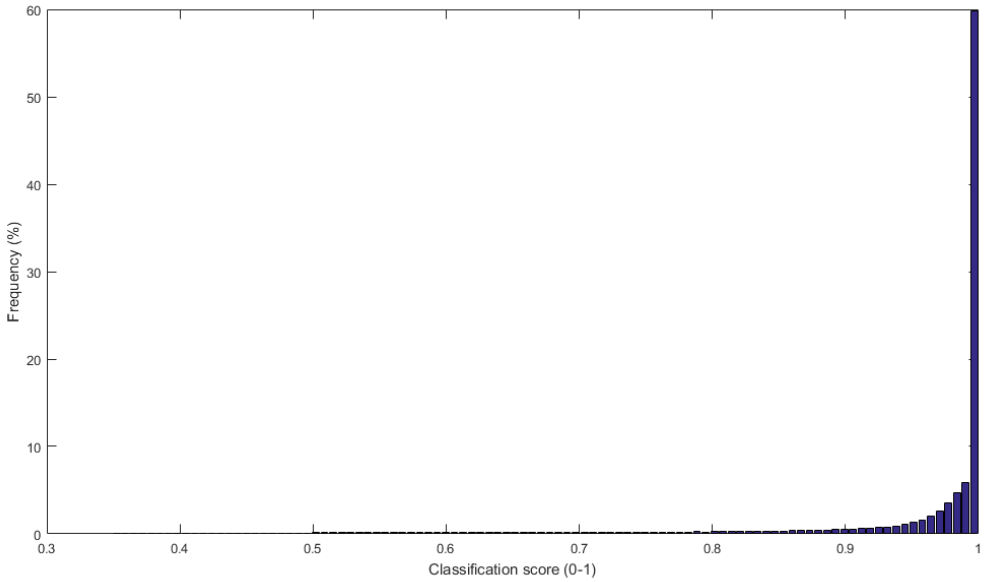


Figure 89 Site 1 ANN classified point cloud, score histogram, pseudo texture trial.

The results of the trial were comparable with the original site 1 trials returning a classification rate of 90.1% overall. There was an improvement in the separation of the wood and brick class but a reduction in the classification accuracy of the pavement class. In the original trials with concrete blocks by Vickers (2013) the scans were made at close range, 2m, at this range the point spacing would have been of a similar magnitude to the texture granularity. The lack of improvement over the original trials in these results may be due to the longer scan range and hence larger point spacing and also the beam diameter now all being greater than the texture density.

5.7 Summary

In chapter 5 the results and analysis for the methodology, defined in chapter 4, were presented and analysed. The first section presented validation of the intensity ratio method, followed by an assessment of class separation. The next section presented the main results for classification of the materials in test site 1; this included overall classification rates followed by individual class classification rates. Next results for the validation of the methodology were presented using test site 2. Finally, the results of the addition texture attribute test were presented. The complete set of results for all classifiers are presented in Appendix A.

The conclusions from analysis of the results is as follows:

1. The best classifier overall was the ANN, with a classification rate of 90.6%, however a SVM classifier ranked in third and fourth place.
2. ANN classifiers with more than one hidden layer did not perform any better than those with just one.
3. Reducing the number of intensity ratios did not significantly affect the classification rate other than with the ANN classifier.
4. During each of the three scans different objects moved through the scan space creating slightly differing point clouds. The moving objects introduced some error in the registration process.

5. The errors near boundaries between classes were in part caused by the registration of the dissimilar point clouds from the three scanners.
6. Some additional sources of error in the spatial and spectral accuracy of the point cloud data were varying atmospheric conditions slightly between scans and moisture. Moisture on a surface contributed to absorbent materials having some unrepresentative classifier training values, this has been noted in other work using intensity values (Voegtle and Wakaluk 2009).
7. The reference scan was manually created and had unavoidable errors near boundaries and areas of low point density, resulting in the incorrect class assignment.
8. Foliage had a more variable less homogeneous surface texture and spectral signature than man-made materials and expectation was that it would have a lower classification rate; this was not observed in the results. This may have been because one of the scanners had a near IR (NIR) wavelength and chlorophyll is highly reflective in the NIR, overriding the variability of the reflected intensity values at the other two wavelengths.
9. ANN classifiers can be over-trained reducing their ability to interpolate noisy or large variations of values; it was difficult to determine if this had affected any of the results. Detection of overtraining is easier to observe in the validation data at the completion of training.

10. Factors reducing the overall classification rate were attributed, in part, to scanner coaxial optical centre alignment and inter-scan registration error. Misalignment and poor registration would miss-associate points from the three scanners, reducing the effect of intensity ratio to normalise the values for incidence angle and range variation.
11. The three scanners had different point density and scan patterns; this resulted in a variation in the area covered by associated scan points. Higher accuracy of ratios of intensity were achieved in areas of high point density; resulting in related higher classification rates.

Chapter 6. Conclusions

6.1 Introduction

Over the period of this research BIM has progressed and been implemented in an increasing number of building and infrastructure projects, both government and private; these have included High Speed rail link two (Mace Ltd 2013), Royal Arsenal Woolwich (over station development blocks, 345 residential units across three towers, utilised for detailed planning through to construction) (GVA 2014), Manchester city library redevelopment (Royal Institute of Charted Surveyors 2015) and London residential development (PRP Architects LLP 2016). BIM is here to stay and that puts even more pressure on development of suitable processes and software, such those proposed in this research.

To investigate the assumption that materials would have related spectral signatures that could be used to classify them was tested by simulating a multi-spectral scanner using three terrestrial laser scanners. Scans were made of two sites, with similar and dissimilar materials to test if the theory held across more than one simple set of data. An ANN was chosen to classify the point cloud intensity data as they are able to separate non-linear data similar to that found in the two datasets in this study and interpolate in the presence of noise. Variation in range and incidence angle was compensated for by using ratios of reflected laser intensity. The registration problems, caused by the scanners having different resolutions and scan patterns, were mitigated by using registration spheres rather than other methods. The results of

this study show that an ANN classifier, using multi-spectral intensity ratios, was able to produce classification accuracies as high as 90.6% overall and 100% for certain materials within this dataset. The results were affected by registration errors, point density variations and optical centre alignment between scanners. Also varying nearest neighbour distances of each individual scanner beams produced a variation in intensity ratio accuracy.

This thesis has set out the research proposal in terms of aims and objectives; the prime aim to classify features in a laser point cloud. A literature review has revealed the progress of research in feature classification within laser scanning and the wider electromagnetic spectrum such as Radar. Other areas of remote sensing have methods that are transferrable to laser scanning; specifically, applicable was the previous work using neural networks to match stereo images.

Classification in remote sensing has used mainly photographic and multi-spectral data; the reflected radiation in these have been un-controlled although from a known source, the Sun. Laser point cloud data has the unique aspect of having direct control of the illumination of the scene; this factor was exploited within this research.

At the start of this research commercial multi/hyper spectral laser scanners were not in commercial existence, although some dual wavelength instruments existed for specific use in bathymetric surveys. The first commercial multi-spectral instrument was introduced at the European LiDAR mapping forum in Amsterdam on 8 Dec 2014 by Optech; an airborne sensor. There is great future potential use for multi-

spectral laser scanning in areas such as smart agriculture and classification of land use in areas without ambient light for much of the year.

6.2 Objective 1

A good starting point for developing a new method of classification using the multi-spectral signature of a material was to review the large extent of research in multi-spectral remote sensing, in particular remotely sensed imagery. This was then further expanded to search for past and current application of multi-spectral classification using laser scanner data. Many of the methods were found to be transferrable to

It was apparent that the main focus of classification of laser point clouds had been classification of spatial data rather than spectral and the review focussed on these works to look for cross-over to the spectral feature extraction tasks. The more traditional segmentation / algorithmic approaches to feature classification have assumed that all walls are vertical and large planar surfaces. Assumptions that roofs are non-vertical large planar surfaces, windows are small parts of walls (not true of a glass building). Windows seem to have been the biggest challenge as glass is transparent to laser light. After segmentation, rule-based methods have been employed to classify each plane or line set; complex buildings would require very large rule sets. AI languages such as Prolog or Lisp might have been more suitable than the languages that have been used in current algorithmic approaches to feature classification. Classification methods covering a wide variety of

disciplines were reviewed to search for methods that would be suitable for material classification using spectral data.

The literature review has shown that there is very limited research into material classification in laser point cloud data; fortunately, there has been significant research using imagery from which this research was able to adapt or extend the original concepts and methods.

6.3 Objective 2

The objective of this chapter was to investigate the influences on laser scanning intensity values including the potential benefit of multi-spectral scanners to material classification. Laser scanning and the added advantage of measuring both spatial and spectral quantities simultaneously was considered a major advantage of laser scanning versus imagery. The basics of laser scanner technology were reviewed, including methods of range measurement, intensity correction and anomalous effects created in laser point clouds. As this research proposed the use of multiple scanners it was important to review registration methods to combine the resultant point clouds. The geometry of a laser point cloud leads to an assumption that a rigid or semi-rigid method would be appropriate. Scanner characteristics which depend on the detector type were reviewed. The increase in intensity with range below 5m for the FARO 120 and the Leica HDS3000 scanners was unexpected and influenced the selection of test data for this research. Laser light is coherent which introduces an extra characteristic to that of non-coherent light, the speckle pattern created

by constructive and destructive interference should possibly be taken into account when measuring the reflected intensity from a surface. It may also hold a key to measuring texture that is below the precision of laser scanners. In order to make use of the scanners intensity data an understanding of each individual scanners method of recording the values was documented.

Laser point cloud data has a unique aspect in that the light source is controlled and known, unlike photographic images, but it still has the limitation requiring the normalisation for varying range and incidence angle. If the intensity values are normalised for range and angle of incidence, only the reflecting surface remains as a variable; this was a key aspect developing an approach which can normalise the intensity values to enable classification building materials in real world environments. Point clouds cannot be simply indexed like image data as they are not arranged in rows and columns but a set of points spaced dependent on the geometry of the object scanned; in order not to lose the raw resolution nearest neighbour indexing must be used to relate the position of one point with another. Texture was also considered and its influence on reflected intensity variation across a surface.

In future research it might be possible to use lasers with different transmission frequencies, super-continuum laser, to further enhance material classification techniques. This would be analogous to hyper-spectral classification techniques using photographic imagery. As the

intention of this research was to employ multiple laser scanners, registering point cloud data was reviewed.

6.4 Objective 3

To develop a method for classifying materials using the spectral signature of the material it was evident that the main problems to be solved were: normalising intensity for range and incidence angle, accurate alignment of each scanner to place each of their optical centres in the same point in space, subsequent accurate co-registration of the individual scanner point cloud and finding a suitable classifier that fitted the requirements of the data.

The variation in range and incidence angle was resolved by the use of ratios of the intensity ratios between each scanner and hence creating ratios of wavelengths. The accurate alignment of the instruments was achieved by knowledge of each scanners construction and dimensions so that their optical centres could be offset from a known reference. The registration of the three individual scanner point clouds was achieved by assessment of the reference sphere alignment using a variation of Bowditch traverse correction method and a semi-rigid transformation. Rather than pick just one classification method several classifiers were used in the trials, including several configurations of each classifier. A common method of measuring the classifiers performance was used to enable ease of comparison of the results.

The method drew aspects of methodology from many different disciplines, the method presented here was optimised for the task of material classification using laser scanner reflected intensity values.

6.5 Objective 3 &4

The best classifier overall was an ANN with a classification rate of 90.6%. ANN classifiers with more than one hidden layer did not perform any better than those with one. Reducing the number of ratios used did not significantly affect the classification rate other than with an ANN classifier.

During each of the three scans different objects moved through the scan space creating slightly differing point clouds. The moving objects introduced error in the registration process. The errors near boundaries between classes were in part caused by the registration of dissimilar point clouds. Atmospheric conditions varied slightly between scans. Moisture across a surface contributed to absorbent materials having some unrepresentative classifier training values, this has been noted in other work using intensity (Voegtle and Wakaluk 2009). The reference scan was manually created and has errors near boundaries due to resolution possible when assigning class membership. Natural materials had less consistent surface texture and reflectivity than man-made and therefore should have had higher classification accuracy.

Factors reducing the overall classification accuracy may have been due to scanner coaxial optical centre alignment and inter-scan registration error. Misalignment and poor registration would introduce errors in

range and incidence angle and hence the intensity ratio would not cancel these correctly. The three scanners could not be set to exactly the same resolution; this created a spread of nearest neighbour distances. Therefore, areas of the scan with low nearest neighbour distances produced higher accuracy ratios of intensity. Very bright or dark reflectors introduced inconsistent intensity values caused by the scanner receiver gain controls. For very bright returns this effect was seen in the sphere data where the point nearest to zero incidence angles was significantly higher, due to being non Lambertian, than that of its nearest neighbours and this caused range errors. The natural interpolation of an ANN classifier and mean filtering helped to reduce the influence of variability on the results. Other areas of misclassification may be due to the reflecting material area being smaller than the laser footprint, the surface illuminated is homogeneous and larger than the backscatter cross-section, would not hold true.

The additional trials to test a concept to detect texture and add this as an attribute to the classification input data was carried out and in part the results were successful, but with further trials at a higher point density the classification rate would be expected to improve. Including texture as an additional attribute alongside the intensity ratios is a new method developed in this research. Further research, in this area, could possibly include the geometry of the surface as well as texture and intensity data.

6.6 Comparison with Current Research

This section compares these research findings with current and ongoing research by other groups. The comparison is of method and the significance of the results and observations.

A similar setup of TLS to this research was used by Hartzell et al. (2014) to classify a rock outcrop; they placed three TLS side-by-side, a Riegl VZ400, Leica HDS3000 and a Zoller+Frohlich 5003. In this configuration the optical paths were not coincident therefore there would have been some variation in incidence angle and range between scanners. The Leica and Riegl scanners were the same choice as this research, only the Zoller+Frohlich differed with a wavelength in the visible red. The variation of reflected intensity due to range was compensated for by first deriving calibration values using a Spectralon[10] panel placed at intervals from 5m to 70m. The rock outcrop sample that was chosen was nearly perpendicular to the TLS and at a range that there would have been only small variation in incidence angle; they did not correct the reflected intensity values for incidence angle. The assumption that these results confirmed earlier assumptions by (Franceschi et al. 2009) that when texture of a surface is of the same magnitude as the laser spot size, incidence angle did not cause any variance in the reflected laser intensity values, may have been due to the very small variation in incidence angle of the rock outcrop.

[10] Labsphere ©2013

An investigation of the potential of using spatial an spectral information from multispectral LiDAR by Gong et al. (2015) used a laser scanner developed by Wuhan university which operated on four wavelengths. They used a SVM to classify seven classes of objects: wall, ceramic, *Cactaceae* (Cactus), carton, plastic foam and dead and healthy leaves. As a method of compensating for range variation, range to the object was include as input to the classifier. The results showed an overall classification rates as high as 88.7%. Discrimination between dead and healthy vegetation was high, it was thought this was due two of the chosen wavelengths being those normally chosen for NDVI calculation.

One of the small number of Multispectral airborne laser scanners now in commercial production is the Optec Titan (three wavelengths) and the Leica Hawk Eye (two wavelengths), Bakula (2015) investigate the possibility of generating colour composite ortho-images of laser intensity and using this for classification tasks. The choice of wavelengths was optimised for bathymetric survey. This research does not report any quantitative classification results but qualitatively shows great promise for land use classification. The same instrument was used by Wichmann et al. (2015) to produce pseudo NDVI, using the IR and green laser channels, to classify seven classes which included a mixture of man-made and natural materials.

6.7 Main Research Findings

Several research outcomes have been produced during the period of study, including:

1. The developed multispectral classification of laser scanner point cloud data method could potentially speed up the production of materials databases in BIM. The results show that high classification rates can be achieved.
2. Incidence angle and range variation have a significant effect on the reflected laser intensity. The developed method of using ratios of associated scan points, of different wavelengths, can significantly reduce this effect and provide normalised data to a classifier.
3. Alignment of the optical paths when using multiple scanners to create multispectral point cloud data is significant in the accuracy of defining each point's spectral signature. Alignment error introduces a variation in incidence angle and range; thus introducing error in the intensity values of each scanner.
4. Using k-nearest neighbour method for associating scan points from different scanners should be adopted as the similarity of the scan patterns and density cannot be assumed to be identical.
5. Where the materials, may vary due to weathering or age, the choice of classifier must be capable of interpolation and tolerant to outliers; these are attributes of human vision and usefully neural networks.
6. Finding a common point in scans from different scans or different scanners of the same scene requires very high point density to ensure that there is beam footprint overlap.

6.8 Research Contributions

The main contribution was a new construction material classification method, using multispectral laser scanner reflected intensity data. During the research a number of additional contributions were produced:

1. The use of ratios of laser intensity values to normalise the effects of variation of incidence angle and range of the surface of the building material.
2. An adaption of a traditional traverse closure method, similar to Bowditch's method, was developed to ensure the differences between each scanner's scan pattern, beam divergence and precision were minimised.
3. The interpolation characteristic of some classifiers, especially neural networks, can allow the classification method to be successfully transferred to other buildings with similar construction materials.
4. Incorporation of texture as a classifier input provides improved delineation between classes improving tolerance to the natural variation in materials.

6.9 Suggestions for Research

The areas for future development and improvements in this research are summarised as:

1. A common optical path, within one instrument, for the three laser wavelengths was not possible within the scope of this research.

However, a common optical path would provide a higher level of alignment of all wavelengths at each scan point, improving the accuracy and precision of the results. A purpose built multi-spectral might include this in its design. Current commercial multispectral scanners have separate sensors for each wavelength and do no share a common optical path.

2. The accuracy of the classification input data was reliant on the scan points from each scanner being as close together as possible. This was in part dependent on the accuracy of the co-registration of the scans. Therefore, it is recommended that one of the new generation of total station / scanners is used so a distinct set of registration points can be chosen in each scan.
3. The use of areas of neighbouring scan points to detect texture in a material's surface and use this as an additional classifier input had limited success partly because of the relative size of the laser beam footprint to the texture. A laser scanner with a footprint similar or smaller than the material's texture or using an existing scanner at close range should be used to improve results when including texture as a classification attribute.
4. Ratios of wavelengths were used to normalise laser intensity values to take into account variations in incidence angle and range. It was discussed earlier that point density varies directly with range and also with incidence angle, due to the geometric nature of the scan pattern; using these attributes as additional

inputs to a classifier might add additional accuracy to the intensity value normalisation process.

5. The main BIM environment will probably be infrastructure and construction; by their nature thy contain materials that can have extremes of variation in temperature. This variation in temperature can cause a temperature gradient with height which acts as a prism and bends the laser light on its journey from scanner to target and back. This effect causes range and position errors in the point cloud, using a guide laser concurrently with the scanner might reduce these errors.

References

Abed, F.., 2012. *Calibration of Full-Waveform Airborne Laser Scanning Data for 3D Object Segmentation*. Newcastle.

Abellan, A., Oppikofer, T., Jaboyedoff, M., Rosser, N.J., Lim, M. & Lato, M.J., 2014. Terrestrial Laser Scanning of Rock Slope Instabilities. *Earth Surface Processes and Landforms*, 39(1), pp.80–97. (doi:10.1002/esp.3493) .

Abmayr, T., Härtl, F., Reinköster, M. & Fröhlich, C., 2005. Terrestrial Laser Scanning – Applications In Cultural Heritage Conservation And Civil Engineering. In *ISPRS WG V/4 £D-Arch*. pp. 1–8.

Ahmadizadeh, S., Yousefi, M. & Saghafi, M., 2014. Land Use Change Detection Using Remote Sensing and Artificial Neural Network : Application to Birjand , Iran. , 4(4), pp.276–288.

Ahokas, E., Kaasalainen, S., Hyyppä, J. & Suomalainen, J., 2006. Calibration of the Optech ALTM 3100 Laser Scanner Intensity Data Using Brightness Targets. *International Archives of Photgrammetry Remote Sensing*, 36(1A), pp.T03–T11. http://www.isprs.org/proceedings/XXXVI/part1/Papers/T03-11.pdf.

Akram, M.N., 2011. Sinusoidal Rotating Grating for Speckle Reduction in Laser Projectors: Feasibility Study. *Optical Engineering*, 50(8), p.083202. (doi:10.1117/1.3613937) http://opticalengineering.spiedigitallibrary.org/article.aspx?doi=10.1117/1.3613937.

Alba, M., Roncoroni, F. & Scaioni, M., 2009. Application of TLS for Change Detection in Rock Faces. In F. Bretar, M. Pierrot-Deseillgny, & G. Vosselman, eds. *Laser scanning 2009, IAPRS*. Paris, France, pp. 99–104.

Aleksander, I., 1966. Self Adaptive Logic Circuits. *Electronic Letters*, 2(8), pp.321–322.

Aleksander, I., Thomas, W.V. & Bowden, P.A., 1984. WISARD·a Radical Step Forward in Image Recognition. *Sensor Review*, 4(3), pp.120–124. (doi:10.1108/eb007637) http://www.emeraldinsight.com/10.1108/eb007637.

Allen, P., 2007. *3D Photography: Point Based Rigid Registration*, http://scholar.google.com/scholar?hl=en&btnG=Search&q=intitle:3D+Photography+:+Point+Based+Rigid+Registration#9.

Antonarakis, a. S., Richards, K.S. & Brasington, J., 2008. Object-Based Land Cover Classification Using Airborne LiDAR. *Remote Sensing of Environment*, 112(6), pp.2988–2998. (doi:10.1016/j.rse.2008.02.004) http://linkinghub.elsevier.com/retrieve/pii/S0034425708000667.

Arun, K.S., Huang, T.S. & Blostein, S.D., 1987. Least Squares Fitting of

Two 3D Point Sets. *IEEE transactions on Pattern Analysis and Machine Intelligence*, PAMI-9(5), pp.698–700.

Atkinson, P.M. & Tatnall, A.R.L., 1997. Introduction Neural Networks in Remote Sensing. *International Journal of Remote Sensing*, 18(4), pp.699–709. (doi:10.1080/014311697218700) http://dx.doi.org/10.1080/014311697218700\nhttp://www.tandfonline.com.www.sndl1.arn.dz/doi/abs/10.1080/014311697218700.

Awrangjeb, M., Zhang, C. & Fraser, C.S., 2013. Automatic Extraction of Building Roofs Using LiDAR Data and Multispectral Imagery. *ISPRS Journal of Photogrammetry and Remote Sensing*, 83, pp.1–18. (doi:10.1016/j.isprsjprs.2013.05.006) http://linkinghub.elsevier.com/retrieve/pii/S0924271613001342.

Azhar, S., Khalfan, M. & Maqsood, T., 2012. Building Information Modelling (BIM): Now and beyond. *Australasian Journal of Construction Economics and Building*, 12(4), pp.15–28. (doi:10.5130/ajceb.v12i4.3032) http://epress.lib.uts.edu.au/journals/index.php/AJCEB/article/view/3032.

Bakula, K., 2015. Multispectral Airborne Laser Scanning - a New Trend in the Development of Lidar Technology. *Archiwum Fotogrametrii, Kartografii i Teledetekcji*, 27, pp.25–44. (doi:10.14681/afkit.2015.002) .

Baligh Jahromi, A., Zoej, M.J.V., Mohammadzadeh, A. & Sadeghian, S., 2011. A Novel Filtering Algorithm for Bare-Earth Extraction from Airborne Laser Scanning Data Using an Artificial Neural Network. *IEEE Journal of Selected Topics in Applied Earth Observations and Remote Sensing*, 4(4), pp.836–843. (doi:10.1109/jstars.2011.2132793) http://dx.doi.org/10.1109/JSTARS.2011.2132793.

Ball, G.H. & Hall, D.J., 1965. ISODATA, a Novel Method of Data Analysis and Pattern Classification. *Analysis*, (AD699616), pp.1–79. http://oai.dtic.mil/oai/oai?verb=getRecord&metadataPrefix=html&identifier=AD0699616.

Ballard, D.H. & Brown, C.M., 1982. *Computer Vision* P. Hall, ed., Prentice Hall. http://homepages.inf.ed.ac.uk/rbf/BOOKS/BANDB/bandb.htm.

Ban, Y. & Wu, Q., 2005. RADARSAT SAR Data for Landuse/Land-Cover Classification in the Rural-Urban Fringe of the Greater Toronto Area. *Proceedings of 8th AGILE Conference on Geographic Information Science*, (2000), pp.26–28.

Bandos, T. & Bruzzone, L., 2009. Classification of Hyperspectral Images with Regularized Linear Discriminant Analysis. *IEEE Transactions on Geoscience and Remote Sensing*, 47(3), pp.862–873. http://ieeexplore.ieee.org/xpls/abs_all.jsp?arnumber=4786582.

Beard, N., 1990. Harnessing Neural Networks. *Electronics World and Wireless World*, pp.1047–1–52.

Becerik-gerber, B., Asce, A.M. & Kensek, K., 2010. Building Information Modeling in Architecture , Engineering , and Construction : Emerging Research Directions and Trends. *Journal of Professional Issues in Engineering Education and Practice*, (July), pp.139–147. (doi:10.1061/ASCEEI.1943-5541.0000023) .

Bekkari, A., El, M., Idbraim, S. & Ducrot, D., 2013. SVM Classification of Urban High-Resolution Imagery Using Composite Kernels and Contour Information. *International Journal of Advanced Computer Science and Applicacations*, 4(7), pp.126–141.

Bellekens, B., Spruyt, V., Berkvens, R., Penne, R. & Weyn, M., 2015. A Benchmark Survey of Rigid 3D Point Cloud Registration Algorithms. , 8(1), pp.118–127.

Bellekens, B., Spruyt, V. & Weyn, M., 2014. A Survey of Rigid 3D Pointcloud Registration Algorithms. In *AMBIENT 2014, The Fourth International Conference on Ambient Computing, Applications, Services and Technologies*. pp. 8–13.

Benvenuto, N. & Piazza, F., 1992. The Backpropagation Algorithm. *IEEE Transactions on Signal Processing*, 40(4), pp.967–969. (doi:10.1109/78.127967) .

Berg, J. & Gerhard, F., 1998. United States Patent. , pp.1–11.

Besl, P.J. & McKay, H.D., 1992. A Method for Registration of 3-D Shapes. *IEEE Transactions on Pattern Analysis and Machine Intelligence*, 14(2), pp.239–256. (doi:10.1109/34.121791) http://ieeexplore.ieee.org/lpdocs/epic03/wrapper.htm?arnumber=121791.

BIM Industry Working Group (BIWG), 2011. Strategy Paper for the Government Construction Client Group From the BIM Industry Working Group. *Department of Business, Innovation and Skills, URN 11*, (March), pp.1– 107.

Biosca, J.M. & Lerma, J.L., 2008. Unsupervised Robust Planar Segmentation of Terrestrial Laser Scanner Point Clouds Based on Fuzzy Clustering Methods. *ISPRS Journal of Photogrammetry and Remote Sensing*, 63(1), pp.84–98. (doi:10.1016/j.isprsjprs.2007.07.010) http://dx.doi.org/10.1016/j.isprsjprs.2007.07.010.

Bischof, H., Schneider, W. & Pinz, A.J., 1992. Multispectral Classification of Landsat-Images Using Neural Networks. *IEEE Transactions on Geoscience and Remote Sensing*, 30(3), pp.482–490.

Bowditch, N., 1807. Compass Traverse Adjustment. *The Analyst*.

Brown, M.E., Lary, D.J., Vrieling, A., Stathakis, D. & Mussa, H., 2008.

Neural Networks as a Tool for Constructing Continuous NDVI Time Series from AVHRR and MODIS. *International Journal of Remote Sensing*, 29, pp.7141–7158. (doi:10.1080/01431160802238435) .

Buján, S., González-Ferreiro, E., Reyes-Bueno, F., Barreiro-Fernández, L., Crecente, R. & Miranda, D., 2012. Land Use Classification from Lidar Data and Ortho-Images in a Rural Area. *The Photogrammetric Record*, 27(140), pp.401–422. (doi:10.1111/j.1477-9730.2012.00698.x) http://doi.wiley.com/10.1111/j.1477-9730.2012.00698.x.

Butters, J. & Leendertz, J., 1971. A Double Exposure Technique for Speckle Pattern Interferometry. *Journal of Physica E: Scientific Instruments*, 4, pp.277–279.

Cabinet Office, H., 2012. *Government Construction Strategy Implementation Report*, http://www.bimtaskgroup.org/reports/.

Castelluccio, M., Poggi, G., Sansone, C. & Verdoliva, L., 2015. Land Use Classification in Remote Sensing Images by Convolutional Neural Networks. , pp.1–11. http://arxiv.org/abs/1508.00092.

Chao, C.-F. & Horng, M.-H., 2015. The Construction of Support Vector Machine Classifier Using the Firefly Algorithm. *Computational Intelligence and Neuroscience*, 2015, pp.1–8. (doi:10.1155/2015/212719) .

Chauve, A., Mallet, C., Bretar, F., Durrieu, S., Pierrot-Deseillgny, M. & Puech, W., 2007. Processing Full Waveform LiDAR Data: Modelling Raw Signals. *International Archives of Photgrammetry Remote Sensing and Spacial Information Sciences*, 36 (Part 3, pp.102–107.

Chen, K.S., Yen, S.K. & Tsay, D.W., 1997. Neural Classification of SPOT Imagery through Integration of Intensity and Fractal Information. *International Journal of Remote Sensing*, 18(4), pp.763–783. (doi:10.1080/014311697218746) http://www.tandfonline.com/doi/abs/10.1080/014311697218746.

Chen, Y., Räikkönen, E., Kaasalainen, S., Suomalainen, J., Hakala, T., Hyyppä, J., et al., 2010. Two-Channel Hyperspectral LiDAR with a Supercontinuum Laser Source. *Sensors*, 10(7), pp.7057–7066. (doi:10.3390/s100707057) http://www.mdpi.com/1424-8220/10/7/7057/.

Chengyi, W. & Zhongming, Z., 2006. Automatic Building Extraction from LiDAR Point Data in Urban Areas. In *Geoinformatics 2006: Remotely Sensed Data and Information, October 28, 2006 - October 29, 2006*. Wuhan, China: SPIE, p. NSFC–Natural Science Foundation of China; CASM–Chi. (doi:10.1117/12.712940) http://dx.doi.org/10.1117/12.712940.

Cho, J.M.C.J.M., 2000. Chromosome Classification Using Backpropagation Neural Networks. *IEEE Engineering in Medicine*

and Biology Magazine, 19(1), pp.28–33. (doi:10.1109/51.816241) http://www.ncbi.nlm.nih.gov/pubmed/10659427.

Clark, J. & Robson, S., 2004. Accuracy of Measurements Made with a Cyrax 2500 Laser Scanner against Surfaces of Known Colour. *Survey Review - Commonwealth Association of Surveying and Land Economy*, 37 (294), pp.626–712. (doi:10.1179/003962604791482261) http://discovery.ucl.ac.uk/75921/.

Conghe Song & Woodcock, C.E., 2003. Monitoring Forest Succession with Multitemporal Landsat Images: Factors of Uncertainty. *IEEE Transactions on Geoscience and Remote Sensing*, 41(11), pp.2557–2567. (doi:10.1109/TGRS.2003.818367) http://ieeexplore.ieee.org/lpdocs/epic03/wrapper.htm?arnumber=1245242.

Crippen, R.E., 1990. Calculating the Vegetation Index Faster. *Remote Sensing of Environment*, 34, pp.71–73.

Daniels, J., Ha, L.K., Ochotta, T. & Silva, C.T., 2007. Robust Smooth Feature Extraction from Point Clouds. *IEEE International Conference on Shape Modeling and Applications 2007 (SMI '07)*. (doi:10.1109/SMI.2007.32) .

Dold, C. & Brenner, C., 2006. Registration of Terrestrial Laser Scanning Data Using Planar Patches and Image Data. *IAPRS*, 36(Part 5), pp.78–83. http://citeseerx.ist.psu.edu/viewdoc/download?doi=10.1.1.66.1760&rep=rep1&type=pdf.

Ducic, V., Hollaus, M., Ullrich, A., Wagner, W. & Melzer, T., 2006. 3D Vegetation Mapping and Classification Using Full-Waveform Laser Scanning. In *Workshop on 3 D Remote Sensing in Forestry, EARSeL/ISPRS*. Vienna, pp. 211–217.

Duncan, D. & Kirkpatrick, S., 2008. Algorithms for Simulation of Speckle (Laser and Otherwise). *SPIE*, 685505-685. (doi:10.1117/12.760518) http://proceedings.spiedigitallibrary.org/proceeding.aspx?articleid=818742.

Edelman, S., Intrator, N. & Poggio, T., 1997. *Complex Cells and Object Recognition*, Unpublised manuscript. http://cogprints.org/561/.

Erbek, F.S., Özkan, C. & Taberner, M., 2004. Comparison of Maximum Likelihood Classification Method with Supervised Artificial Neural Network Algorithms for Land Use Activities. *International Journal of Remote Sensing*, 25(9), pp.1733–1748. (doi:10.1080/0143116031000150077) http://www.tandfonline.com/doi/abs/10.1080/01431160310001500077.

Evans, H.F.J., 1996. *Neural Network Approach to the Classification of*

Urban Images. University of Nottingham.

Fischler, M. a & Bolles, R.C., 1981. Random Sample Consensus: A Paradigm for Model Fitting with Applications to Image Analysis and Automated Cartography. *Communications of the ACM*, 24, pp.381–395. (doi:10.1145/358669.358692) .

Fisher, R.A., 1936. THE USE OF MULTIPLE MEASUREMENTS IN TAXONOMIC PROBLEMS. *Annals of Eugenics*, 7(2), pp.179–188. (doi:10.1111/j.1469-1809.1936.tb02137.x) http://doi.wiley.com/10.1111/j.1469-1809.1936.tb02137.x.

Flight International, 1982. Ferranti Lasers Used in Falklands. *Flight International*, p.1551.

Foody, G.M. & Arora, M.K., 1997. An Evaluation of Some Factors Affecting the Accuracy of Classification by an Artificial Neural Network. *International Journal of Remote Sensing*, 18(4), pp.799–810. (doi:10.1080/014311697218764) http://www.tandfonline.com/doi/abs/10.1080/014311697218764.

Franceschi, M., Teza, G., Preto, N., Pesci, A., Galgaro, A. & Girardi, S., 2009. Discrimination between Marls and Limestones Using Intensity Data from Terrestrial Laser Scanner. *ISPRS Journal of Photogrammetry and Remote Sensing*, 64(6), pp.522–528.

Gong, W., Sun, J., Shi, S., Yang, J., Du, L., Zhu, B., et al., 2015. Investigating the Potential of Using the Spatial and Spectral Information of Multispectral LiDAR for Object Classification. *Sensors*, 15(9), pp.21989–22002. (doi:10.3390/s150921989) http://www.mdpi.com/1424-8220/15/9/21989/.

Gonzalez, R.C. & Woods, R.E., 1992. *Digital Image Processing* R. Gonzalez & R. Woods, eds., Addison-Wesley. (doi:10.2307/3719519) http://www.amazon.com/Digital-Image-Processing-William-Pratt/dp/0471857661.

Green, B.F., 1952. The Orthogonal Approximation of An Oblique Staructre in Factor Analysis. *Psychometrika*, 17(4), pp.429–440. (doi:10.1007/BF02288918) .

Gross, H. & Thoennessen, U., 2006. Extraction of Lines from Laser Point Clouds. *Symposium of ISPRS Commission III Photogrammetric Computer Vision*, 36, pp.86–91. http://www.isprs.org/proceedings/XXXVI/part3/singlepapers/O_05.pdf.

Grussenmeyer, P., Landes, T., Voegtle, T. & Ringle, K., 2008. Comparison Methods of Terrestrial Laser Scanning, Photogrammetry and Tachometry Data for Recording of Cultural Heritage Buildings. In *The International Archives of the Photogrammetry, Remote Sensing and Spatial Information Sciences.* Beijing 2008, pp. 213–218.

Guan, H., Ji, Z., Zhong, L., Li, J. & Ren, Q., 2013. Partially Supervised

Hierarchical Classification for Urban Features from Lidar Data with Aerial Imagery. *International Journal of Remote Sensing*, 34, pp.190–210. (doi:10.1080/01431161.2012.712228) .

Guarnieri, A., Vettore, A., Pirotti, F. & Marani, M., 2009. Filtering of TLS Point Clouds for the Generation of DTM in Salt-Marsh Areas. In F. Bretar, M. Pierrot-Deseillgny, & G. Vosselman, eds. *Laser scanning, IAPRS*. Paris, France, pp. 293–298.

Gumhold, S., Wang, X. & MacLeod, R., 2001. *Feature Extraction from Point Clouds*, Sandia National Laboratories. www.cs.utah.edu/~sgumhold/Finals/fe_preprint.pdf.

Guo, B., Huang, X., Zhang, F. & Sohn, G., 2015. Classification of Airborne Laser Scanning Data Using JointBoost. *ISPRS Journal of Photogrammetry and Remote Sensing*, 100, pp.71–83. (doi:10.1016/j.isprsjprs.2014.04.015) http://dx.doi.org/10.1016/j.isprsjprs.2014.04.015.

GVA, 2014. *Crossrail Development Pipeline Study*, London. www.gva.co.uk.

Haboudane, D., Miller, J.., Pattey, E., Zarco-Tejada, P.. & Strachan, I.., 2004. Hyperspectral Vegetation Indices and Novel Algorithms for Predicting Green LAI of Crop Canopies: Modeling and Validation in the Context of Precision Agriculture. *Remote Sensing of Environment*, 90(3), pp.337–352. (doi:10.1016/j.rse.2003.12.013) http://linkinghub.elsevier.com/retrieve/pii/S0034425704000264.

Hakala, T., Suomalainen, J., Kaasalainen, S. & Chen, Y., 2012. Full Waveform Hyperspectral LiDAR for Terrestrial Laser Scanning. *Optics Express*, 20(7), pp.7119–27. (doi:10.1364/OE.20.007119) http://www.ncbi.nlm.nih.gov/pubmed/22453394.

Haralick, R., Shanmugan, K. & Dinstein, I., 1973. Textural Features for Image Classification. *IEEE Transactions on Systems, Man and Cybernetics*, 3(6), pp.610–621. (doi:10.1109/TSMC.1973.4309314) http://dceanalysis.bigr.nl/Haralick73-Textural features for image classification.pdf.

Hartzell, P., Glennie, C., Biber, K. & Khan, S., 2014. Application of Multispectral LiDAR to Automated Virtual Outcrop Geology. *ISPRS Journal of Photogrammetry and Remote Sensing*, 88, pp.147–155. (doi:10.1016/j.isprsjprs.2013.12.004) http://linkinghub.elsevier.com/retrieve/pii/S0924271613002967.

Hebb, D., 1949. *Organisation of Behaviour*, New York, NY, United States: John Wiley and Sons.

Hill, D., 1994. Voxel Similarity Measures for Automated Image Registration. *Visualization in …*, 2359.

HM Government Cabinet Office, 2011. *Government Construction Strategy. Building Information Modelling* C. Office, ed., London: HMG.

Höfle, B., 2007. Glacier Surface Segmentation Using Airborne Laser Scanning Point Cloud and Intensity Data. *IAPRS*, XXXVI, pp.195–200.

Hofle, B. & Pfeifer, N., 2007. Correction of Laser Scanning Intensity Data: Data and Model-Driven Approaches. *ISPRS Journal of Photogrammetry and Remote Sensing*, 62(6), pp.415–433. (doi:10.1016/j.isprsjprs.2007.05.008) http://linkinghub.elsevier.com/retrieve/pii/S0924271607000603.

Hug, C. & Wehr, A., 1997. Detecting and Identifying Topographic Objects in Imaging Laser Altimeter Data. In *3D Reconstruction and Modeling of Topographic Objects*. Stuttgart: IAPRS, pp. 19–26.

Hunt, E.., 1962. *Concept Learning: An Information Processsssing Problem*, New York, NY, United States: Wiley.

Iyer, S. V & Mohan, B.K., 2002. Urban Landuse Monitoring Using Neural Network Classification. In *IEEE International Geoscience and Remote Sensing Symposium 24th Canadian Symposium on Remote Sensing*. IEEE, Piscataway, NJ, USA, pp. 2959–2961. http://ieeexplore.ieee.org/stamp/stamp.jsp?tp=&arnumber=1026836.

Julesz, B., 1971. *Foundations of Cyclopean Perception*, University of Chicago Press. (doi:10.1080/716099300) http://www.amazon.com/Foundations-Cyclopean-Perception-Bela-Julesz/dp/0226415279.

Jutzi, B. & Gross, H., 2009. Normalization of LIDAR Intensity Data Based on Range and Surface Incidence Angle. In *Proceedings of ISPRS, Laserscanning 2009 workshop*. pp. 213–218. http://www.isprs.org/proceedings/xxxviii/3-w8/papers/213_laserscanning09.pdf.

Kaasalainen, S., Anssi, K., Antero, K. & Harri, K., 2009. Radiometric Calibration of Terrestrial Laser Scanners with External Reference Targets. *Remote Sensing.*, 1, pp.144–158. (doi:doi:10.3390/rs1030144) .

Kaasalainen, S., Jaakkola, A., Mikko, K., Anssi, K. & Kukko, A., 2011. Analysis of Incidence Angle and Distance Effects on Terrestrial Laser Scanner Intensity: Search for Correction Methods. *Remote Sensing*, 3, pp.2207–2221.

Kaasalainen, S. & Kukko, A., 2009. Brightness Measurements and Calibration with Airborne and Terrestrial Laser Scanners. *IEEE TRANSACTIONS ON GEOSCIENCE AND REMOTE SENSING*, 47(2), pp.588–598. http://ieeexplore.ieee.org/xpls/abs_all.jsp?arnumber=4432711.

Kaasalainen, S., Pyysalo, U., Krooks, A., Vain, A., Kukko, A., Hyyppä, J., et al., 2011. Absolute Radiometric Calibration of ALS Intensity Data: Effects on Accuracy and Target Classification. *Sensors*, 11,

pp.10586–10602. (doi:10.3390/s111110586) http://www.pubmedcentral.nih.gov/articlerender.fcgi?artid=3274302&tool=pmcentrez&rendertype=abstract.

Kavzoglu, T. & Mather, P.M., 2003. The Use of Backpropagating Artificial Neural Networks in Land Cover Classification. *International Journal of Remote Sensing*, 24(23), pp.4907–4938. (doi:10.1080/0143116031000114851) http://www.tandfonline.com/doi/abs/10.1080/01431160310001148511.

Kennaugh, E.M., 1981. K-Pulse Concept. *IEEE Transactions on Antennas and Propagation*, AP-29(2), pp.327–331.

Kirchner, N., Taha, T., Liu, D.K. & Paul, G., 2007. Simultaneous Material Type Classification and Mapping Data Acquisition Using a Laser Range Finder. In *The Eighth International Conference on Intelligent Technologies*. Sidney, Australia, pp. 12–14.

Kohonen, T., 1984. *Self-Organisation and Associative Memory*, Berlin, Germany: Springer Verlag.

Kohonen, T., 1989. *Self-Organising and Associative Memory*, Springer-Verlag.

Kriegler, F.J., Malila, W.A., Nalepka, R.F. & Richardson, W., 1969. Preprocessing Transformations and Their Effects on Multispectral Recognition. In *Proceedings of the Sixth International Symposium on Remote Sensing of Environment*. pp. 97–131.

Lagarias, J., Reeds, J., Margaret, H. & Wright, P.E., 1998. Convergence Properties of the Nelder–mead Simplex Method in Low Dimensions ∗ . *Journal of Optimization*, 9(1), pp.112–117. (doi:10.1137/S1052623496303470) .

Lambert, J.H., 1760. *Photometria Sive de Mensura et Gradibus Luminis, Colorum et Umbrae*, Augsburg: Augustae Vindelicorum: Vidvae Eberhardi Klett.

LeCun, Y., Boser, B., Denker, J.S., Henderson, D., Howard, R.E., Hubbard, W., et al., 1989. Backpropagation Applied to Handwritten Zip Code Recognition. *Neural Computation*, 1(4), pp.541–551. (doi:10.1162/neco.1989.1.4.541) http://www.mitpressjournals.org/doi/abs/10.1162/neco.1989.1.4.541.

Lee, S., Wolberg, G. & Shin, S.Y., 1997. Scattered Data Interpolation with Multilevel B-Splines. *IEEE Transactions on Visualization and Computer Graphics*, 3(3), pp.228–244. (doi:10.1109/2945.620490) .

Lemmens, M., 2011. BIM. *GIM International*, p.11.

Lende, R., Csernai, L.P. & Kamp, D., 1994. Classification of Genetic Sequences with Backpropagation. *International Journal of Neural*

Systems, 5(3), pp.159–163.

Li, H., Liping, D., Huang, X. & Li, D., 2008. Laser Intensity Used in Classification of Lidar Point Cloud Data. In *2008 IEEE International Geoscience and Remote Sensing Symposium - Proceedings, July 6, 2008 - July 11, 2008*. Boston, MA, United states: Institute of Electrical and Electronics Engineers Inc., pp. II1140–II1143. (doi:10.1109/igarss.2008.4779201) http://dx.doi.org/10.1109/IGARSS.2008.4779201.

Liang, X., Kukko, A., Kaartinen, H., Hyyppä, J., Yu, X., Jaakkola, A., et al., 2013. Possibilities of a Personal Laser Scanning System for Forest Mapping and Ecosystem Services. *Sensors (Basel, Switzerland)*, 14(1), pp.1228–48. (doi:10.3390/s140101228) http://www.pubmedcentral.nih.gov/articlerender.fcgi?artid=3926612&tool=pmcentrez&rendertype=abstract.

Lichti, D.D., 2005. Spectral Filtering and Classification of Terrestrial Laser Scanner Point Clouds. *The Photogrammetric Record*, 20(111), pp.218–240. (doi:10.1111/j.1477-9730.2005.00321.x) http://dx.doi.org/10.1111/j.1477-9730.2005.00321.x.

Lin, B., Sakai, K., Tamaki, T., Raytchev, B., Kaneda, K. & Ichii, K., 2013. Semi-Rigid Registration of 3D Points. *Journal of Signal and Information Processing*, 04(03), pp.25–29. (doi:10.4236/jsip.2013.43B005) http://www.scirp.org/journal/PaperDownload.aspx?DOI=10.4236/jsip.2013.43B005.

Lindenbergh, R., Pfeifer, N. & Rabbani, T., 2005. Accuracy Analysis of the Leica HDS3000 and Feasibility of Tunnel Deformation Monitoring. In *ISPRS WG III/3, III/4, V/3 Workshop "Laser scanning 2005."* Enschede, the Netherlands: ISPRS, pp. 24–29.

Liu, C., Wu, H. & Zhang, Y., 2011. Extraction of Urban 3D Features from Lidar Data Fused with Aerial Images Using an Improved Mean Shift Algorithm. *Survey Review*, 43(322), pp.402–414. (doi:10.1179/003962611X13055561708821) http://www.maneyonline.com/doi/abs/10.1179/003962611X13055561708821.

Loncharich, R.J., Brooks, B.R. & Pastor, R.W., 1992. Langevin Dynamics of Peptides: The Frictional Dependence of Isomerization Rates ofN-Acetylalanyl-N?-Methylamide. *Biopolymers*, 32(5), pp.523–535. (doi:10.1002/bip.360320508) http://doi.wiley.com/10.1002/bip.360320508.

Low, K., 2004. Linear Least-Squares Optimization for Point-to-Plane ICP Surface Registration. *Chapel Hill, University of North Carolina*, (February), pp.2–4. https://www.iscs.nus.edu.sg/~lowkl/publications/lowk_point-to-plane_icp_techrep.pdf.

Lowe, D.G., 2004. Distinctive Image Features from Scale-Invariant

Keypoints. *International Journal of Computer Vision*, 60(2), pp.91–110. (doi:10.1023/B:VISI.0000029664.99615.94) http://www.springerlink.com/openurl.asp?id=doi:10.1023/B:VISI.00000029664.99615.94.

Lucieer, V.L., 2008. Object- oriented Classification of Sidescan Sonar Data for Mapping Benthic Marine Habitats. *International Journal of Remote Sensing*, 29(3), pp.905–921. (doi:10.1080/01431160701311309) http://www.tandfonline.com/doi/abs/10.1080/01431160701311309.

Lunga, D. & Ersoy, O., 2011. *Spherical Nearest Neighbor Classification: Application to Hyperspectral Data*, http://link.springer.com/chapter/10.1007/978-3-642-23199-5_13.

Mace Ltd, 2013. *HS2 Supply Chain BIM Upskilling Study*, London.

MacQueen, J.B., 1967. Some Methods for Classification and Analysis of Multivariate Observations. *5th Berkeley Symposium on Mathematical Statistics and Probability 1967*, 1(233), pp.281–297. (doi:citeulike-article-id:6083430) http://projecteuclid.org/euclid.bsmsp/1200512992.

Mahalingam, N. & Kumar, D., 1997. Neural Networks for Signal Processing Applications: ECG Classification. *Australasian physical engineering sciences in medicine supported by the Australasian College of Physical Scientists in Medicine and the Australasian Association of Physical Sciences in Medicine*, 20(3), pp.147–151. http://www.ncbi.nlm.nih.gov/pubmed/9409015.

Mallet, C., Soergel, U. & Bretar, F., 2008. Analysis of Full Waveform LiDAR Data for an Accurate Classification of Urban Areas. *International Archives of Photgrammetry Remote Sensing and Spacial Information Sciences*, 37(Part 3A, pp.85–92.

Marquardt, D.W., 1963. An Algorithm for Least-Squares Estimation of Nonlinear Parameters. *Journal of the Society for Industrial and Applied Mathematics*, 11(2), pp.431–441. (doi:10.1137/0111030) http://epubs.siam.org/doi/abs/10.1137/0111030.

Marr, D. & Poggio, T., 1976. Cooperative Computation of Stereo Disparity. *Science*, 194(4262), pp.283–287. (doi:10.1126/science.968482) http://www.ncbi.nlm.nih.gov/pubmed/968482.

Mather, P., 2004. *Computer Processing of Remotely Sensed Images* Third., Chichester, UK: Wiley.

McCulloch, W. & Pitts, W., 1943. A Logical Calculus of the Ideas Immanent in Nervous Activity. *Bulletin of Mathematical Biophysics*, 5, pp.115–133.

Miettinen, R. & Paavola, S., 2014. Beyond the BIM Utopia: Approaches to the Development and Implementation of Building Information Modeling. *Automation in Construction*, 43, pp.84–91.

(doi:10.1016/j.autcon.2014.03.009) http://dx.doi.org/10.1016/j.autcon.2014.03.009.

Mills, J. & Barber, D., 2004. Geomatics Techniques for Structural Surveying. *Journal of Surveying Engineering*, 130(2), pp.56–64. (doi:10.1061/(ASCE)0733-9453(2004)130:2(56)) .

Minsky, M.L. & Papert, S., 1969. *Perceptrons: An Introduction to Computational Geometry* M. L. Minsky & S. Papert, eds., MIT Press. (doi:10.1109/T-C.1969.222718) http://cdsweb.cern.ch/record/114106.

Mole, L. & Araujo, A., 2010. Growing Self-Organizing Surface Map: Learning a Surface Topology from a Point Cloud. In *Self Organizing Maps - Applications and Novel Algorithm Design*. Croatia: InTech, pp. 689–729. http://www.ncbi.nlm.nih.gov/pubmed/19842987.

Møller, M., 1993. A Scaled Conjugate Gradient Algorithm for Fast Supervised Learning. *Neural networks*, 6, pp.525–533. http://www.sciencedirect.com/science/article/pii/S0893608005800565.

Monserrat, O. & Crosetto, M., 2008. Deformation Measurement Using Terrestrial Laser Scanning Data and Least Squares 3D Surface Matching. *ISPRS Journal of Photogrammetry and Remote Sensing*, 63(1), pp.142–154. (doi:10.1016/j.isprsjprs.2007.07.008) http://linkinghub.elsevier.com/retrieve/pii/S0924271607000810.

Nitzan, D., Brain, A. & Duda, R., 1977. The Measurement and Use of Registered Reflectance and Range Data in Scene Analysis. *IEEE*, 65(2), pp.206–220. http://ieeexplore.ieee.org/stamp/stamp.jsp?tp=&arnumber=1454727.

Nurunnabi, A., West, G. & Belton, D., 2015. Robust Methods for Feature Extraction from Mobile Laser Scanning 3D Point Clouds Mobile Laser Scanning & Point Cloud Data. , pp.10–12.

Ogundana, O.O., Coggrave, C.R., Burguete, R.L. & Huntley, J.M., 2007. Fast Hough Transform for Automated Detection of Spheres in Three-Dimensional Point Clouds. *Optical Engineering*, 46(5), p.051002. (doi:10.1117/1.2739011) http://link.aip.org/link/OPEGAR/v46/i5/p051002/s1&Agg=doi.

Pal, M. & Mather, P., 2002. A Comparison of Decision Tree and Backpropagation Neural Network Classifiers for Land Use Classification. *Neural Networks*, 00(C), pp.503–505.

Paola, J.D. & Schowengerdt R. A., 1995. A Review and Analysis of Backpropagation Neural Networks for Classification of Remotely-Sensed Multi-Spectral Imagery. *International Journal of Remote Sensing*, 16(16), pp.3033–3058. (doi:10.1080/01431169508954607)

http://www.tandfonline.com/doi/abs/10.1080/01431169508954607.

Paola, J.D. & Schowengerdt, R.A., 1995. A Detailed Comparison of Backpropagation Neural Network and Maximum-Likelihood Classifiers for Urban Land Use Classification. *IEEE Transactions on Geoscience and Remote Sensing*, 33(4), pp.981–996. (doi:10.1109/36.406684) http://ieeexplore.ieee.org/lpdocs/epic03/wrapper.htm?arnumber=406684.

Parker, D., 1982. Learning Logic (Invention Rep. 581-641, File 1).

Pesci, A. & Teza, G., 2008. Terrestrial Laser Scanner and Retro-Reflective Targets: An Experiment for Anomalous Effects Investigation. *International Journal of Remote Sensing*, 29(19), pp.5749–5765. (doi:10.1080/01431160802108489) http://www.informaworld.com/openurl?genre=article&doi=10.1080/01431160802108489&magic=crossref.

Pfeifer, N., Dorninger, P., Haring, A. & Fan, H., 2007. Investigating Terrestrial Laser Scanning Intensity Data: Quality and Functional Relations. In *Proc. of VIII conference on Optical 3D measurement tech*. pp. 328–337.

Pfennigbauer, M. & Ullrich, A., 2011. Multi-Wavelength Airborne Laser Scanning Wavelength Considerations. In *International LiDAR Mapping Forum*. New Orleans, pp. 1–10.

Pooja, a. P., Jayanth, J. & Koliwad, S., 2011. Classification of RS Data Using Decision Tree Approach. *International Journal of Computer Applications*, 23(3), pp.7–11.

Pozo, S. Del, Rodr??guez-Gonz??lvez, P., Hern??ndez-L??pez, D. & Felipe-Garc??a, B., 2014. Vicarious Radiometric Calibration of a Multispectral Camera on Board an Unmanned Aerial System. *Remote Sensing*, 6(3), pp.1918–1937. (doi:10.3390/rs6031918) .

PRP Architects LLP, 2016. Technical Delivery and BIM. http://www.prp-co.uk/services/technical-delivery-bim/.

Pu, S. & Vosselman, G., 2006. Automatic Extraction of Building Features from Terrestrial Laser Scanning. In *International Archives of Photogrammetry Remote Sensing and Spatial Information Sciences*. ISPRS, pp. 25–27. http://www.isprs.org/proceedings/XXXVI/part5/paper/1219_Dresden06.pdf.

Pu, S. & Vosselman, G., 2007. Extracting Windows from Terrestrial Laser Scanning. In *IAPRS Workshop on Laser scanning 2007 and SilviLaser 2007*. Espoo, Finland: ISPRS.

Pu, S. & Vosselman, G., 2010. Knowledge Based Building Facade Reconstruction from Laser Point Clouds and Images. *Geodesy*, (75), p.133. http://library.wur.nl/WebQuery/clc/1932258\nwww.ncg.knaw.nl.

Pu, S. & Vosselman, G., 2009. Knowledge Based Reconstruction of Building Models from Terrestrial Laser Scanning Data. *ISPRS Journal of Photogrammetry and Remote Sensing*, 64(6), pp.575–584. (doi:10.1016/j.isprsjprs.2009.04.001) http://dx.doi.org/10.1016/j.isprsjprs.2009.04.001.

Puttonen, E., Suomalainen, J., Hakala, T., Räikkönen, E., Kaartinen, H., Kaasalainen, S., et al., 2010. Tree Species Classification from Fused Active Hyperspectral Reflectance and LIDAR Measurements. *Forest Ecology and Management*, 260(10), pp.1843–1852. (doi:10.1016/j.foreco.2010.08.031) http://linkinghub.elsevier.com/retrieve/pii/S0378112710004901.

Remondino, F. & El-Hakim, S., 2006. Image Based 3D Modelling A Review. *The Photogrammetric Record*, 21(115), pp.269–291.

Roberts, L.G., 1961. *Machine Perception of Three Dimensional Solids*. Massachusetts Institue of Technology.

Roli, F., Serpico, S.B. & Bruzzone, L., 1996. Classification of Multisensor Remote-Sensing Images by MultipleStructured Neural Networks. *Proceedings of 13th International Conference on Pattern Recognition*, 4. (doi:10.1109/ICPR.1996.547257) .

Rosenblatt, F., 1957. *The Perceptron: A Perceiving and Recognizing Automaton (Technical Report 85-460-1)*, http://scholar.google.com/scholar?hl=en&btnG=Search&q=intitle:The+perceptron?a+perceiving+and+recognizing+automaton+(Technical+Report+85-460-1)#0.

Rottensteiner, F., Trinder, J., Clode, S. & Kubik, K., 2005. Using the Dempster-Shafer Method for the Fusion of LIDAR Data and Multi-Spectral Images for Building Detection. *Information Fusion*, 6(4), pp.283–300. (doi:10.1016/j.inffus.2004.06.004) .

Rouse, J.W., Haas, R.H., Schell, J.A. & Deering, D.W., 1974. Monitoring Vegetation Systems in the Great Plains with ERTS. In *NASA Goddard Space Flight Center 3d ERTS-1 Symposium*. pp. 309–317.

Royal Institute of Charted Surveyors, 2015. Manchester Town Hall Complex and BIM: Reaping the Benefits. http://www.rics.org/uk/footer/bim-solutions/manchester-town-hall-complex/manchester-town-hall-complex---part-3/.

Rueckert, D., Sonoda, L.I., Hayes, C., Hill, D.L., Leach, M.O. & Hawkes, D.J., 1999. Nonrigid Registration Using Free-Form Deformations: Application to Breast MR Images. *IEEE Transactions on Medical Imaging*, 18(8), pp.712–21. (doi:10.1109/42.796284) http://www.ncbi.nlm.nih.gov/pubmed/10534053.

Rumelhart, D.E. & McClelland, J.L., 1986. *Parallel Distributed Processing* M. I. T. Press, ed., MIT Press.

Runne, H., Niemeier, W. & Kern, F., 2001. Application of Laser

Scanners to Determine the Geometry of Buildings. In *Optical 3-D Measurement Techniques*. Vienna, pp. 41–48. http://www.xdesy.de/paper/runne_niemeier_kern_optical3d_2001.PDF.

Rusu, R.B., 2010. Semantic 3D Object Maps for Everyday Manipulation in Human Living Environments. *KI - Künstliche Intelligenz*, 24(4), pp.345–348. (doi:10.1007/s13218-010-0059-6) http://link.springer.com/10.1007/s13218-010-0059-6.

Rutzinger, M., Elberink, S.O., Pu, S. & Vosselman, G., 2009. Automatic Extraction of Vertical Walls from Mobile and Airborne Laser Scanning Data. *GeoInformation Science*, XXXVIII(3/W8), pp.7–11. http://www.itc.nl/personal/vosselman/papers/rutzinger2009.paris.pdf.

Rutzinger, M., Höfle, B., Hollaus, M. & Pfeifer, N., 2008. Object-Based Point Cloud Analysis of Full-Waveform Airborne Laser Scanning Data for Urban Vegetation Classification. *Sensors (Peterboroug*, 8(8), pp.4505–4528. (doi:10.3390/s8084505) http://www.mdpi.com/1424-8220/8/8/4505/.

Ryding, J., Williams, E., Smith, M. & Eichhorn, M., 2015. Assessing Handheld Mobile Laser Scanners for Forest Surveys. *Remote Sensing*, 7(1), pp.1095–1111. (doi:10.3390/rs70101095) http://www.mdpi.com/2072-4292/7/1/1095/.

S. Lemeš, N.Z.-U., 2009. Study of Ambient Light Influence on Laser 3D Scanning. In *7th International Conference on Induxtrial Tools and Material Processing Technologies*. pp. 327–330.

Schmitt, A. & Vögtle, T., 2009. An Advanced Approach for Automatic Extraction of Planar Surfacees and Their Topology from Point Clouds. *Photogrammetrie Fernerkundung Geoinformation PFG*, 1, pp.43 – 52.

Schönemann, P.H., 1966. A Generalized Solution of the Orthogonal Procrustes Problem. *Psychometrika*, 31(1), pp.1–10. (doi:10.1007/BF02289451) http://link.springer.com/10.1007/BF02289451.

Schultz, T., 2007. *Calibration of a Terrestrial Laser Scanner for Engineering Geodesy*. Technical University of Berlin. http://www.igp-data.ethz.ch/berichte/Blaue_Berichte_PDF/96.pdf.

Segal, a, Haehnel, D. & Thrun, S., 2009. Generalized-ICP. *Robotics: Science and Systems*. (doi:10.1.1.149.3870) .

Serpico, S.B., Bruzzone, L. & Roli, F., 1996. An Experimental Comparison of Neural and Statistical Non-Parametric Algorithms for Supervised Classification of Remote-Sensing Images. *Pattern Recognition Letters*, 17(13), pp.1331–1341. (doi:10.1016/S0167-8655(96)00090-6) http://www.sciencedirect.com/science/article/pii/S01678655960009

06.

Shaker, A. & Nagwa, E.-A., 2012. Land Cover Information Extraction Using LIDAR Data. *International Archives of the Photogrammetry, Remote Sensing and Spatial Information Sciences*, Volume XXX, pp.167–182. http://www.int-arch-photogramm-remote-sens-spatial-inf-sci.net/XXXIX-B7/167/2012/isprsarchives-XXXIX-B7-167-2012.pdf.

Shan, J. & Toth, C.K., 2009. *Topographic Laser Ranging And Scanning*, Raton: CRC Press/Taylor & Francis Group.

Shijiana, Z., Yunlanb, G., Xinwud, Z. & Tiedingb, L., 2008. Robust Algorithm for Fitting Sphere to 3D Point Clouds in Terrestrial Laser Scanning. *The International Archives of the Photogrammetry, Remote Sensing and Spatial Information Sciences*, XXXVII(B5), pp.519–522. http://www.isprs.org/proceedings/XXXVII/congress/5_pdf/90.pdf.

Shupe, S.M. & Marsh, S.E., 2004. Cover- and Density-Based Vegetation Classifications of the Sonoran Desert Using Landsat TM and ERS-1 SAR Imagery. *Remote Sensing of Environment*, 93(1-2), pp.131–149. (doi:10.1016/j.rse.2004.07.002) http://linkinghub.elsevier.com/retrieve/pii/S0034425704002093.

Sobel, I., 1978. Neighbourhood Coding of Binary Images for Fast Contour Following and General Array Binary Processing. *Computer Graphics and Image Processing*, 8, pp.127–135.

Song, J., Han, S., Yu, K. & Kim, Y., 2002. Assessing the Possibility of Land-Cover Classification Using Lidar Intensity Data. *International Archives of Photogrammetry, Remote Sensing and Spatial Information Sciences*, 34, pp.259–262.

Sotoodeh, S., 2006. Outlier Detection in Laser Scanner Point Clouds. *International Archives of Photogrammetry Remote Sensing and Spatial Information Sciences XXXVI5 297e302*, XXXVI(Jain), pp.297–302. http://citeseerx.ist.psu.edu/viewdoc/download?doi=10.1.1.113.2043&rep=rep1&type=pdf.

Soudarissanane, S., Lindenbergh, R., Menenti, M. & Teunissen, P., 2009. Incidence Angle Influence on the Quality of Terrestrial Laser Scanning Points. *Proc in the 3DNordOst BerlinGermany*, also avail, pp.183 – 188. http://repository.tudelft.nl/assets/uuid:b739bd05-c5bc-4ffa-aedb-318726f15e34/Incidence_angle_20091.pdf.

Statnikov, A., Aliferis, C.F., Hardin, D.P. & Guyon, I., 2011. *A Gentle Introduction to Support Vector Machines in Biomedicine*, Singapore: World Scientific. (doi:10.1142/7922) http://www.worldscientific.com/worldscibooks/10.1142/7922.

Studholme, C., Hill, D.L. & Hawkes, D.J., 1996. Automated 3-D Registration of MR and CT Images of the Head. *Medical image*

analysis, 1(2), pp.163–75. (doi:10.5244/C.9.3) http://www.ncbi.nlm.nih.gov/pubmed/9873927.

Suomalainen, J., Hakala, T., Kaartinen, H., Räikkönen, E. & Kaasalainen, S., 2011. Demonstration of a Virtual Active Hyperspectral LiDAR in Automated Point Cloud Classification. *ISPRS Journal of Photogrammetry and Remote Sensing*, 66(5), pp.637–641. (doi:10.1016/j.isprsjprs.2011.04.002) http://linkinghub.elsevier.com/retrieve/pii/S0924271611000529.

Szuster, B.W., Chen, Q. & Borger, M., 2011. A Comparison of Classification Techniques to Support Land Cover and Land Use Analysis in Tropical Coastal Zones. *Applied Geography*, 31(2), pp.525–532. (doi:10.1016/j.apgeog.2010.11.007) http://linkinghub.elsevier.com/retrieve/pii/S0143622810001530.

Toth, C., Laky, S., Zaletnyik, P., Grejner-Brzezinska, D. & Ayer, A., 2010. Compressing and Classifying LiDAR Waveform Data.

Tournas, E. & Tsakiri, M., 2009. Automatic 3D Point Cloud Registration for Cultural Heritage Documentation. *Laser scanning 2009, IAPRS*, XXXVIII, pp.189–194.

Tsin, Y. & Kanade, T., 2004. A Correlation-Based Approach to Robust Point Set Registration. *Proc. of ECCV*, 0, pp.558–569. (doi:10.1007/978-3-540-24672-5_44) .

Tso, B. & Mather, P.M., 2009. *Classification Methods for Remotely Sensed Data*, Abingdon, UK: Taylor & Francis. (doi:10.4324/9780203303566) http://www.tandfebooks.com/action/showBook?doi=10.4324/9780203303566.

Turhan-Sayan, G., Inan, S., Ince, T. & Leblebicioglu, K., 1998. Applications of Artificial Neural Networks and Genetic Algorithms to Electromagnetic Target Classification. *RTO SCI Symposium on "The Application of Information Technologies (Computer Science) to Mission Systems."*

Turhan-Sayan, G., Leblebicioglu, K. & Ince, T., 1999. Electromagnetic Target Classification Using Time-Frequency Analysis and Neural Networks. *Microwave and Optical Technology Letters*, 21(1), pp.63–69. (doi:10.1002/(sici)1098-2760(19990405)21:1<63::aid-mop18>3.0.co;2-3) http://dx.doi.org/10.1002/(SICI)1098-2760(19990405)21:1<63::AID-MOP18>3.0.CO;2-3.

Tymkow, P. & Borkowski, A., 2002. Airborne Laser Scanning Data and Photographs. In *The International Archives of the Photogrammetry, Remote Sensing and Spacial Information Sciences*. Beijing, China, pp. 185–190.

Varga, K., Szabó, S., Szabó, G., Dévai, G. & Tóthmérész, B., 2014. Improved Land Cover Mapping Using Aerial Photographs and Satellite Images. *Open Geosciences*, 7(1), pp.15–26.

(doi:10.1515/geo-2015-0002) http://www.degruyter.com/view/j/geo.2015.7.issue-1/geo-2015-0002/geo-2015-0002.xml.

Vickers, D., 2013. *The Detection of Fire Damaged Concrete Using Laser Scanning*. University of Nottingham.

Voegtle, T. & Wakaluk, S., 2009. Effects on the Measurements of the Terrestrial Laser Scanner HDS 6000 (Leica) Caused by Different Object Materials. In *IAPRS, Vol. XXXVIII Part 3/W8*. Paris, France, pp. 68–74.

Volk, R., Stengel, J. & Schultmann, F., 2014. Automation in Construction Building Information Modeling (BIM) for Existing Buildings — Literature Review and Future Needs. , 38, pp.109–127. (doi:10.1016/j.autcon.2013.10.023.Abstract) .

Vosselman, G., Gorte, B., Sithole, G. & Rabbani, T., 2004. Recognising Structure in Laser Scanner Point Clouds. *Information Sciences*, 46, pp.1–6. (doi:10.1002/bip.360320508) http://citeseerx.ist.psu.edu/viewdoc/download?doi=10.1.1.118.6228&rep=rep1&type=pdf.

Vosselman, G. & Maas, H.-G., 2010. *Airborne and Terrestrial Laser Scanning*, CRC Press. http://www.amazon.com/dp/1439827982.

Wagner, W., Hyyppä, J., Ullrich, A., Lehner, H., Briese, C. & Kaasalainen, S., 2008. Radiometric Calibration of Full-Waveform Small-Footprint Airborne Laser Scanners. *The International Archives of Photogrammetry, Remote Sensing and Spatial Information Sciences*, XXXVII(B1), pp.163–168.

Wagner, W., Ullrich, A., Ducic, V., Melzer, T. & Studnicka, N., 2006. Gaussian Decomposition and Calibration of a Novel Small-Footprint Full-Waveform Digitising Airborne Laser Scanner. *ISPRS Journal of Photogrammetry and Remote Sensing*, 60(2), pp.100–112. (doi:10.1016/j.isprsjprs.2005.12.001) http://dx.doi.org/10.1016/j.isprsjprs.2005.12.001.

Wahl, R. & Klein, R., 2006. Shape Detection in Point Clouds † Shape Detection in Point Clouds. *Group*. cg.cs.uni-bonn.de/docs/publications/2006/cg-2006-2.pdf.

Wang, J.H. & Hsiao, C., 1999. On Disparity Matching in Stereo Vision via a Neural Network Framework. *Proc Natl Sci Counc ROC A*, 23(5), pp.665–678. http://citeseerx.ist.psu.edu/viewdoc/download?doi=10.1.1.105.9067&rep=rep1&type=pdf.

Wang, J.-H. & Hsiao, C.-P., 1997. Representation-Burden Conservation Network Applied to Learning VQ (NPL270). *Neural Processing Letters*, 5(3), pp.209–217.

Wang, Y., Hao, W., Ning, X., Zhao, M., Zhang, J., Shi, Z., et al., 2013. Automatic Segmentation of Urban Point Clouds Based on the

Gaussian Map. *The Photogrammetric Record*, 28(144), pp.342–361. (doi:10.1111/phor.12041) http://doi.wiley.com/10.1111/phor.12041.

Wani, M.A. & Arabnia, H.R., 2003. Parallel Edge-Region-Based Segmentation Algorithm Targeted at Reconfigurable MultiRing Network. *The Journal of Supercomputing*, 25(1), pp.43–62.

Wehr, A. & Lohr, U., 1999. Airborne Laser Scanning—an Introduction and Overview. *ISPRS Journal of Photogrammetry and Remote Sensing*, 54(2-3), pp.68–82. (doi:10.1016/S0924-2716(99)00011-8) http://linkinghub.elsevier.com/retrieve/pii/S0924271699000118.

Wehr, A. & Lohr, U., 1990. Reflectivity of a Diffuse Target. *ISPRS J. Photogrammetry and Remote Sensing*, 54, p.68.

Weinmann, M., Weinmann, M., Hinz, S. & Jutzi, B., 2011. Fast and Automatic Image-Based Registration of TLS Data. *ISPRS Journal of Photogrammetry and Remote Sensing*, 66(6 SUPPL.), pp.S62–S70. (doi:10.1016/j.isprsjprs.2011.09.010) http://dx.doi.org/10.1016/j.isprsjprs.2011.09.010.

Welde, K., 2010. *Master of Science in Electronics Investigation of Methods for Speckle Contrast Reduction*. Norwgian University of Science and technology.

Werbos, P.J., 1974. *Beyond Regression: New Tools for Prediction and Analysis in the Behavioral Sciences*. Harvard University. http://www.citeulike.org/group/1938/article/1055600.

Were:, scanner project, Gaulton, R., Danson, F.M., Ramirez, F.A. & Gunawan, O., 2013. The Potential of Dual-Wavelength Laser Scanning for Estimating Vegetation Moisture Content. *Remote Sensing of Environment*, 132, pp.32–39.

Westoby, M.J., Brasington, J., Glasser, N.F., Hambrey, M.J. & Reynolds, J.M., 2012. “Structure- from- Motion” Photogrammetry: A Low- Cost, Effective Tool for Geoscience Applications. *Geomorphology*, 179, pp.300–314. (doi:10.1016/j.geomorph.2012.08.021) .

Wichmann, V., Bremer, M., Lindenberger, J., Rutzinger, M., Georges, C. & Petrini-Monteferri, F., 2015. Evaluating the Potential of Multispectral Airborne Lidar for Topographic Mapping and Land Cover Classification. *ISPRS Annals of Photogrammetry, Remote Sensing and Spatial Information Sciences*, II-3/W5(2012), pp.113–119. (doi:10.5194/isprsannals-II-3-W5-113-2015) http://www.isprs-ann-photogramm-remote-sens-spatial-inf-sci.net/II-3-W5/113/2015/.

Wujanz, D. & Daniel, W., 2009. Intensity Calibration Method for 3D Laser Scanners. *Journal of the New Zealand Institute of Surveyors*, 299(299), pp.7–12. http://www.geodesy.tu-berlin.de/fileadmin/fg261/Publikationen/NZ_Surveyor_Journal_09_

Wujanz.pdf.

Wunderlich, P.T., Wasmeier, P., Ohlmann-lauber, J., Schäfer, T. & Reidl, F., 2013. *Objective Specifications of Terrestrial Laserscanners – A Contribution of the Geodetic Laboratory at the Technische Universität München*,

Xu, H., Li, T. & Wu, F., 2012. Knowledge-Based Classification Method for Urban Area Objects Feature Extraction Based on LIDAR Points. In *4th International Conference on Measuring Technology and Mechatronics Automation, ICMTMA 2012, January 6, 2012 - January 7, 2012*. Sanya, China: Trans Tech Publications, pp. 1157–1162. (doi:10.4028/www.scientific.net/AMM.128-129.1157) http://dx.doi.org/10.4028/www.scientific.net/AMM.128-129.1157.

Yan, W.Y., Shaker, A. & El-Ashmawy, N., 2015. Urban Land Cover Classification Using Airborne LiDAR Data: A Review. *Remote Sensing of Environment*, 158, pp.295–310. (doi:10.1016/j.rse.2014.11.001) http://dx.doi.org/10.1016/j.rse.2014.11.001.

Yang, S., Ho, C. & Chen, Y., 2010. Neural Network Based Stereo Matching Algorithm Utilizing Vertical Disparity. *Update*, pp.1149–1154. (doi:10.1109/IECON.2010.5675532) .

Yuan, Y.W. & Zeng, X.H., 2004. Adaptive 3D Mesh Reconstruction from Dense Unorganized Weighted Points Using Neural Network. In *Third International Conference on Machine Leaning and Cybernetics*. Shanghai,: IEEE, pp. 3238–3242. http://ieeexplore.ieee.org/xpls/abs_all.jsp?arnumber=1378594.

Zhang, S., Wootton, J. & Chisholm, A., 2005. Geometric Feature Extraction from Point Clouds Obtained by Laser Scanning. In *Workshop on Laser Applications in Europe*. Dresden, Germany: SPIE, p. SPIE Europe; EPIC–European Photonics Industry Cons. (doi:10.1117/12.660387) http://dx.doi.org/10.1117/12.660387.

Zhang, Z., 1995. Parameter Estimation Techniques: A Tutorial with Application to Conic Fitting.

Zhou, L. & Yang, X., 2004. Use of Neural Networks for Land Cover Classification from Remotely Sensed Imagery. *The International Archives of Photogrammetry, Remote Sensing and Spatial Information Sciences*, XXXVII(Part B7), pp.575–578.

Appendix A Classification Results

A summary of the classification results are shown in Table 11 and Table 20. The summaries are followed by the detailed results in the form of confusion matrix and false colour images representing predicted class.

Table 19 Classifier results for site 1. Validation data was an unused sub-set of the complete dataset.

Classifier				Classification rate (%)	
#	Type	Sub-Type	Ratios	Validation Data	Test Data
1	Decision tree	Complex	All	98.6	86.0
2	Discriminant	Linear	All	94.4	83.8
3	Discriminant	Quadratic	All	98.6	84.8
4	SVM	Linear	All	98.4	88.0
5	SVM	Quadratic	All	98.6	87.3
6	SVM	Gaussian	All	98.2	88.2
7	KNN	Medium	All	99.2	87.0
8	KNN	Subspace	All	99.0	85.4
9	KNN	Weighted	1,2	89.3	78.7
10	KNN	Weighted	1,3	89.8	77.1
11	KNN	Weighted	2,3	98.0	84.3
12	KNN	Weighted	All	98.2	87.0

Table 20 ANN classifier results for site 1. Validation data was an unused sub-set of the complete dataset.

				Hidden Layer		Classification rate (%)			
#	Transfer Function	Training Function	Ratios	No of layers	No of neurons	Validation data	Test data	Epochs	Score threshold
13	logsig	trainscg	All	1	10	99.5	87.2	51	0
14	logsig	traincgb	All	1	10	99.5	87.3	48	0
15	logsig	trainrp	All	1	10	98.9	86.9	73	0
16	logsig	trainrp	All	1	5	99.3	85.3	138	0
17	logsig	trainrp	All	1	15	98.7	86.6	53	0
18	logsig	trainrp	All	2	10,10	99.2	87.0	54	0
19	logsig	trainrp	2,3	1	10	97.6	85.1	37	0.9
20	logsig	trainrp	1,2	1	10	89.5	79.3	45	0.9
21	logsig	trainrp	1,3	1	10	89.7	74.7	65	0.9
22	logsig	trainrp	All	1	10	98.1	90.6	44	0.9
23	logsig	trainrp	1,3	1	10	89.7	78.1	66	0.5

1 Complex Decision Tree

Table 21 Complex decision tree: classification rate, site 1 test data

Per True Class								FNR
True Class	1	92.2%	4.1%	1.4%	0.1%	2.1%	Wood	7.8%
	2	17.9%	76.8%	4.1%	0.5%	0.7%	Brick	23.2%
	3	15.1%	0.5%	80.8%	1.5%	2.0%	Steel	19.2%
	4	0.0%	0.0%	0.1%	93.6%	6.3%	Gravel	6.4%
	5	1.5%	0.0%	0.3%	11.5%	86.7%	Pavement	13.3%
		1	2	3	4	5	Accuracy	86.0%
		Predicted Class						

Per Predicted Class							
True Class	1	91.7%	15.9%	7.1%	0.4%	26.1%	Wood
	2	5.0%	83.7%	5.8%	0.5%	2.5%	Brick
	3	3.2%	0.4%	87.0%	1.2%	5.3%	Steel
	4	0.0%	0.0%	0.1%	96.0%	21.1%	Gravel
	5	0.1%	0.0%	0.1%	1.8%	44.9%	Pavement
Reliability	80.7%	1	2	3	4	5	
	FDR	8.3%	16.3%	13.0%	4.0%	55.1%	
		Predicted Class					

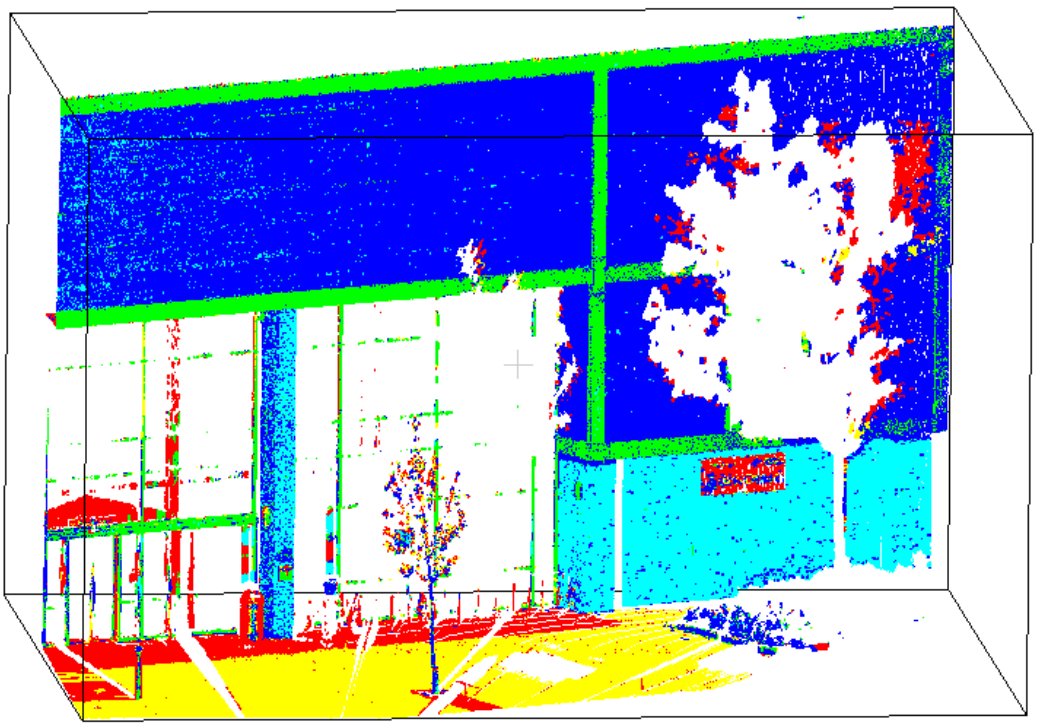


Figure 90 Complex decision tree: classification rate created as a false colour point cloud.

2 Linear Discriminant

Table 22 Linear Discriminant: classification rate, site 1 test data.

		Per True Class						FNR
True Class	1	69.9%	16.5%	11.5%	1.9%	0.3%	Wood	30.1%
	2	12.5%	75.7%	9.6%	1.5%	0.8%	Brick	24.3%
	3	3.3%	0.2%	92.0%	2.5%	2.0%	Steel	8.0%
	4	0.0%	0.0%	0.1%	99.3%	0.7%	Gravel	0.7%
	5	0.2%	0.0%	0.4%	17.0%	82.3%	Pavement	17.7%
		1	2	3	4	5	Accuracy	83.8%
		Predicted Class						

		Per Predicted Class					
True Class	1	94.3%	43.5%	34.0%	6.3%	6.2%	Wood
	2	4.8%	56.4%	8.0%	1.4%	4.8%	Brick
	3	1.0%	0.1%	57.9%	1.7%	9.5%	Steel
	4	0.0%	0.0%	0.0%	88.3%	3.9%	Gravel
	5	0.0%	0.0%	0.1%	2.4%	75.7%	Pavement
Reliability	74.5%	1	2	3	4	5	
	FDR	5.7%	43.6%	42.1%	11.7%	24.3%	
		Predicted Class					

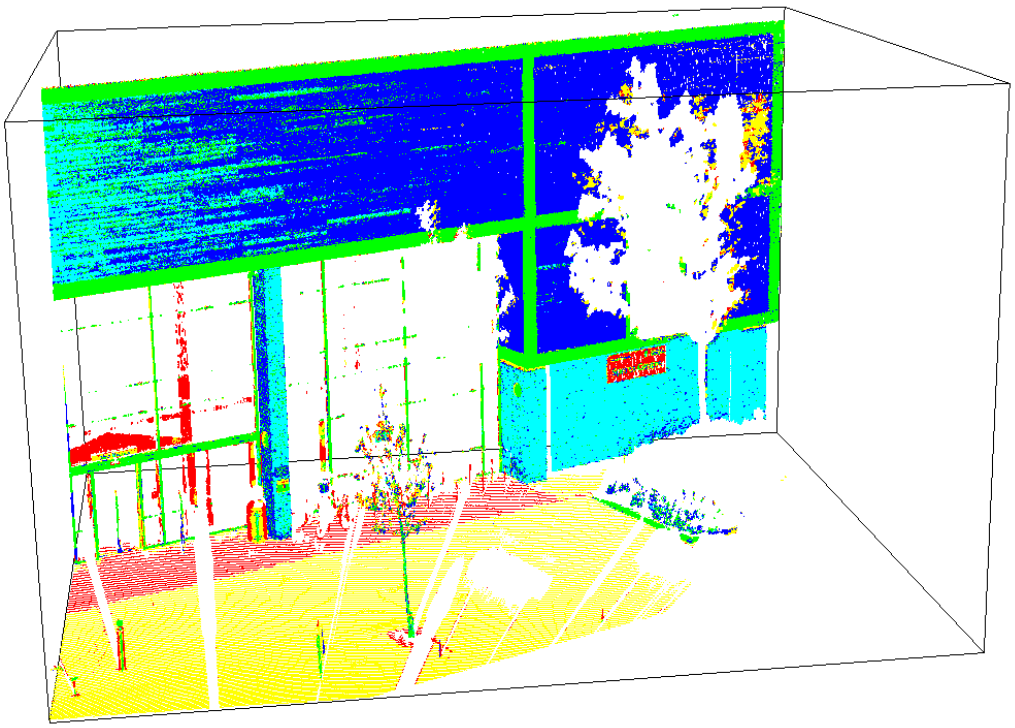


Figure 91 Linear Discriminant: classification rate created as a false colour point cloud.

3 Quadratic Discriminant

Table 23 Quadratic Discriminant: classification rate, site 1test data.

		Per True Class						FNR
True Class	1	91.6%	5.4%	1.4%	0.0%	1.6%	Wood	8.4%
	2	19.8%	75.1%	3.5%	0.3%	1.4%	Brick	24.9%
	3	21.1%	0.3%	75.3%	0.6%	2.7%	Steel	24.7%
	4	0.1%	0.0%	0.0%	94.4%	5.4%	Gravel	5.6%
	5	1.0%	0.0%	0.1%	11.2%	87.7%	Pavement	12.3%
		1	2	3	4	5	Accuracy	84.8%
		Predicted Class						

		Per Predicted Class					
True Class	1	90.0%	20.2%	7.5%	0.1%	20.9%	Wood
	2	5.5%	79.5%	5.4%	0.3%	5.0%	Brick
	3	4.4%	0.3%	87.1%	0.5%	7.4%	Steel
	4	0.0%	0.0%	0.0%	97.3%	19.1%	Gravel
	5	0.0%	0.0%	0.0%	1.8%	47.7%	Pavement
Reliability	80.3%	1	2	3	4	5	
	FDR	10.0%	20.5%	12.9%	2.7%	52.3%	
		Predicted Class					

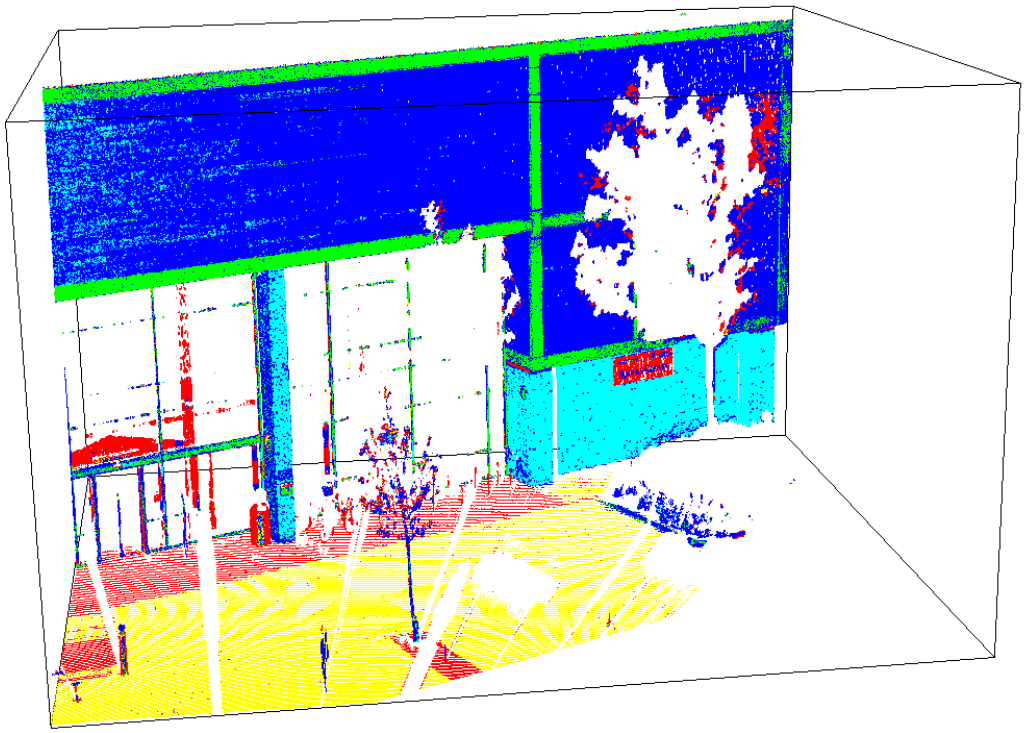


Figure 92 Quadratic Discriminant: classification rate created as a false colour point cloud.

4 Linear SVM

Table 24 Linear SVM: classification rate, site 1 test data.

		Per True Class						FNR
True Class	1	92.4%	3.7%	2.1%	1.7%	0.2%	Wood	7.6%
	2	17.0%	75.7%	5.5%	0.6%	1.1%	Brick	24.3%
	3	6.5%	0.2%	89.5%	1.6%	2.3%	Steel	10.5%
	4	0.0%	0.0%	0.1%	97.6%	2.3%	Gravel	2.4%
	5	0.4%	0.0%	0.5%	14.4%	84.7%	Pavement	15.3%
		1	2	3	4	5	Accuracy	88.0%
		Predicted Class						

		Per Predicted Class					
True Class	1	93.7%	14.7%	9.3%	5.8%	3.0%	Wood
	2	4.9%	85.2%	6.9%	0.6%	6.2%	Brick
	3	1.4%	0.1%	83.6%	1.2%	9.5%	Steel
	4	0.0%	0.0%	0.1%	90.4%	12.1%	Gravel
	5	0.0%	0.0%	0.1%	2.1%	69.2%	Pavement
Reliability	84.4%	1	2	3	4	5	
	FDR	6.3%	14.8%	16.4%	9.6%	30.8%	
		Predicted Class					

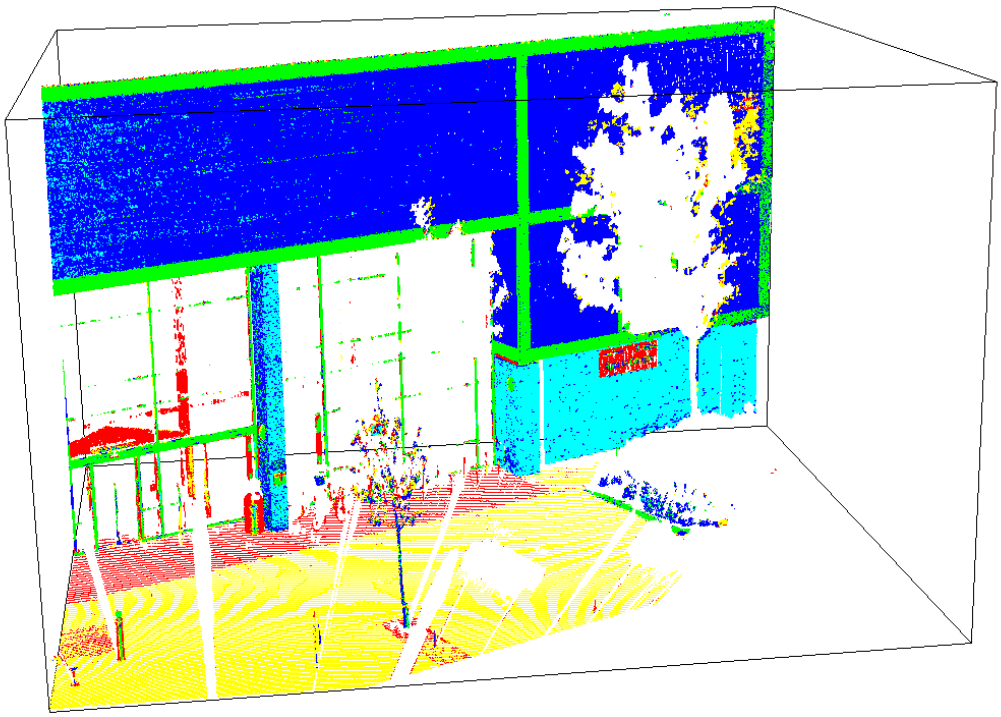


Figure 93 Linear SVM: classification rate created as a false colour point cloud.

5 Quadratic SVM

Table 25 Quadratic SVM: classification rate, site 1 test data.

		Per True Class						FNR
True Class	1	94.4%	2.2%	1.7%	0.8%	0.8%	Wood	5.6%
	2	17.9%	75.3%	5.1%	0.6%	1.1%	Brick	24.7%
	3	9.8%	0.1%	86.3%	1.5%	2.3%	Steel	13.7%
	4	0.1%	0.0%	0.1%	95.5%	4.3%	Gravel	4.5%
	5	0.5%	0.0%	0.4%	14.1%	85.0%	Pavement	15.0%
		1	2	3	4	5	Accuracy	87.3%
		Predicted Class						

		Per Predicted Class					
True Class	1	92.9%	9.5%	8.0%	3.0%	12.8%	Wood
	2	5.0%	90.3%	6.7%	0.6%	4.9%	Brick
	3	2.0%	0.1%	85.1%	1.1%	7.7%	Steel
	4	0.0%	0.0%	0.1%	93.2%	18.3%	Gravel
	5	0.0%	0.0%	0.1%	2.1%	56.2%	Pavement
Reliability	83.6%	1	2	3	4	5	
	FDR	7.1%	9.7%	14.9%	6.8%	43.8%	
		Predicted Class					

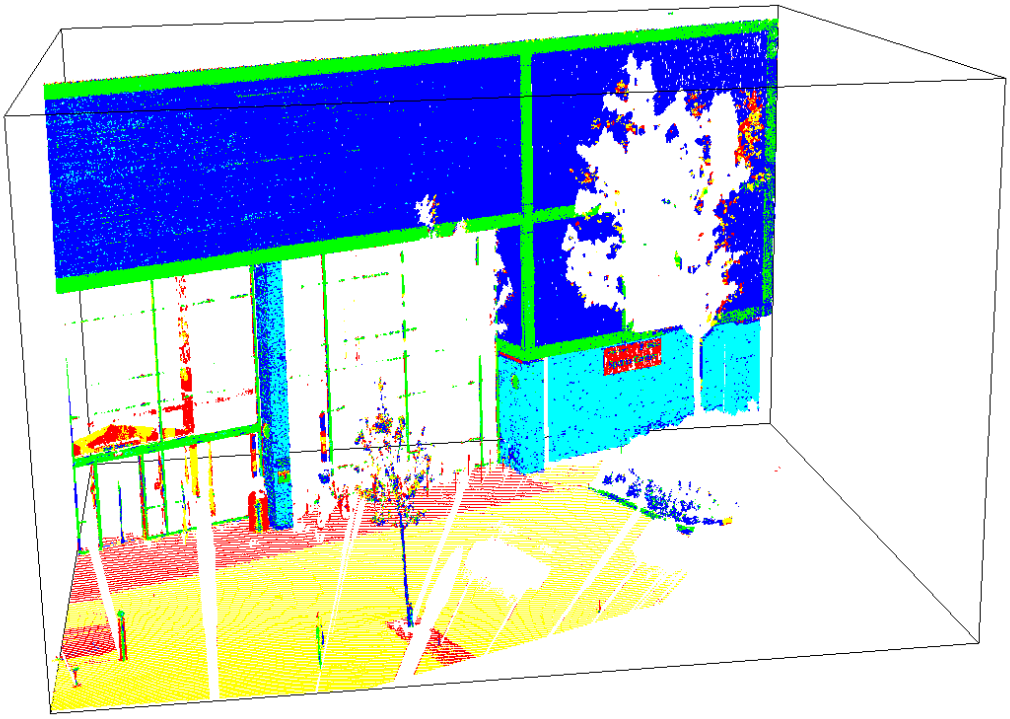


Figure 94 Quadratic SVM: classification rate created as a false colour point cloud.

6 Gaussian SVM

Table 26 Gaussian SVM: classification rate, site 1 test data.

		Per True Class						FNR
True Class	1	91.0%	4.4%	3.0%	1.4%	0.2%	Wood	9.0%
	2	16.8%	75.3%	6.2%	0.7%	1.0%	Brick	24.7%
	3	4.1%	0.2%	91.5%	2.0%	2.2%	Steel	8.5%
	4	0.1%	0.0%	0.1%	98.2%	1.7%	Gravel	1.8%
	5	0.4%	0.0%	0.4%	14.4%	84.7%	Pavement	15.3%
		1	2	3	4	5	Accuracy	88.2%
		Predicted Class						

		Per Predicted Class					
True Class	1	94.2%	17.2%	12.3%	4.9%	3.3%	Wood
	2	4.9%	82.7%	7.2%	0.7%	5.9%	Brick
	3	0.9%	0.1%	80.4%	1.5%	9.4%	Steel
	4	0.0%	0.0%	0.1%	90.8%	9.1%	Gravel
	5	0.0%	0.0%	0.1%	2.1%	72.3%	Pavement
Reliability	84.1%	1	2	3	4	5	
	FDR	5.8%	17.3%	19.6%	9.2%	27.7%	
		Predicted Class					

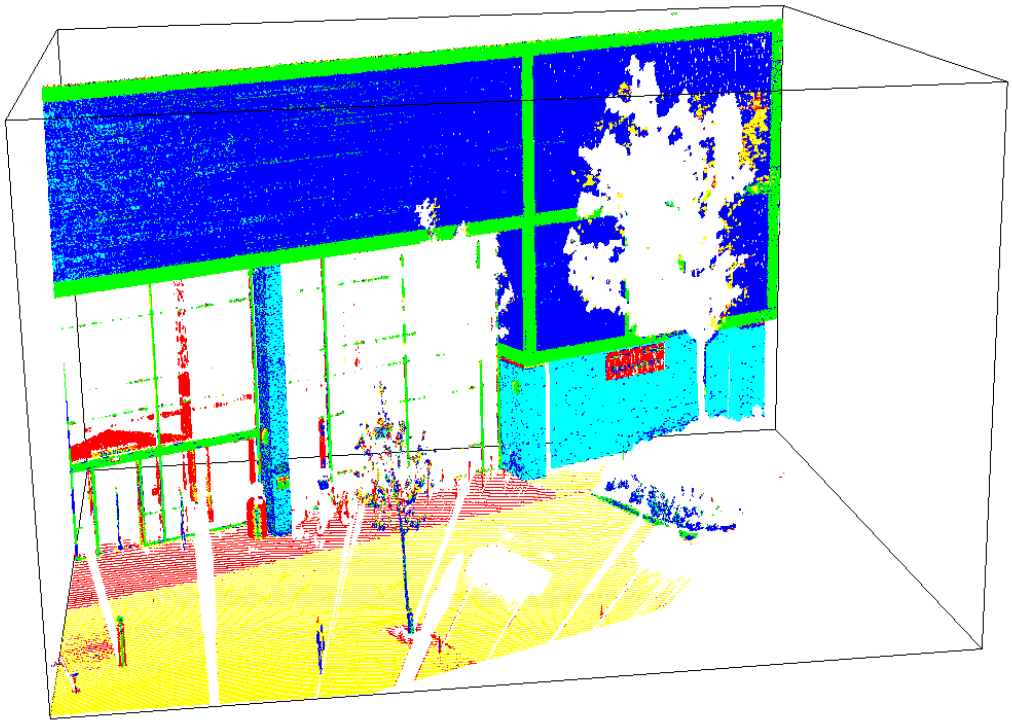


Figure 95 Gaussian SVM: classification rate created as a false colour point cloud.

7 KNN

Table 27 KNN: classification rate, site 1 test data.

Per True Class								FNR
True Class	1	93.0%	3.6%	2.0%	0.5%	0.9%	Wood	7.0%
	2	18.0%	74.8%	5.3%	0.8%	1.1%	Brick	25.2%
	3	8.9%	0.2%	86.7%	2.2%	2.0%	Steel	13.3%
	4	0.2%	0.0%	0.0%	95.1%	4.7%	Gravel	4.9%
	5	0.4%	0.0%	0.4%	14.0%	85.2%	Pavement	14.8%
		1	2	3	4	5	Accuracy	87.0%
		Predicted Class						

Per Predicted Class							
True Class	1	93.0%	14.5%	9.2%	1.8%	13.5%	Wood
	2	5.1%	85.3%	6.8%	0.8%	4.9%	Brick
	3	1.9%	0.2%	83.9%	1.7%	6.7%	Steel
	4	0.0%	0.0%	0.1%	93.5%	19.5%	Gravel
	5	0.0%	0.0%	0.1%	2.1%	55.4%	Pavement
Reliability	82.2%	1	2	3	4	5	
	FDR	7.0%	14.7%	16.1%	6.5%	44.6%	
		Predicted Class					

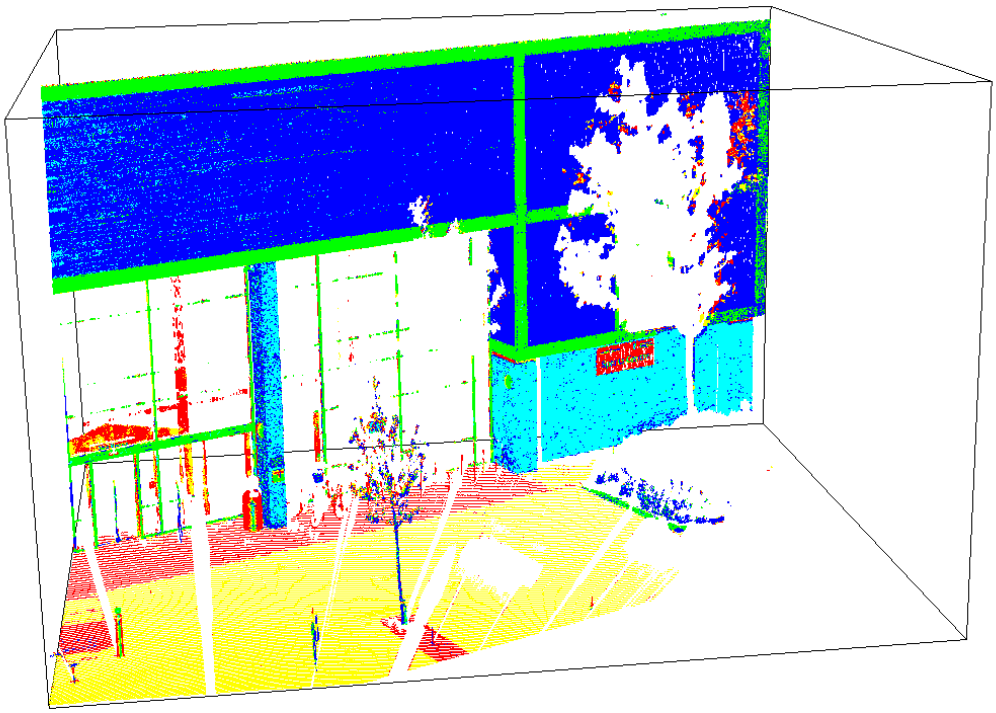


Figure 96 KNN: classification rate created as a false colour point cloud.

8 Sub-space KNN

Table 28 Sub-space KNN: classification rate, site 1 test data.

		Per True Class						FNR
True Class	1	87.4%	4.1%	6.5%	1.5%	0.5%	Wood	12.6%
	2	17.0%	75.9%	5.3%	0.6%	1.1%	Brick	24.1%
	3	16.2%	0.4%	79.4%	1.2%	2.7%	Steel	20.6%
	4	0.0%	0.0%	0.0%	98.4%	1.5%	Gravel	1.6%
	5	0.9%	0.0%	0.2%	12.8%	86.0%	Pavement	14.0%
		1	2	3	4	5	Accuracy	85.4%
		Predicted Class						

		Per Predicted Class					
True Class	1	91.3%	16.1%	26.0%	5.0%	9.9%	Wood
	2	5.0%	83.6%	6.1%	0.6%	5.7%	Brick
	3	3.6%	0.4%	67.8%	0.9%	10.6%	Steel
	4	0.0%	0.0%	0.0%	91.7%	7.5%	Gravel
	5	0.0%	0.0%	0.0%	1.9%	66.3%	Pavement
Reliability	80.1%	1	2	3	4	5	
	FDR	8.7%	16.4%	32.2%	8.3%	33.7%	
		Predicted Class					

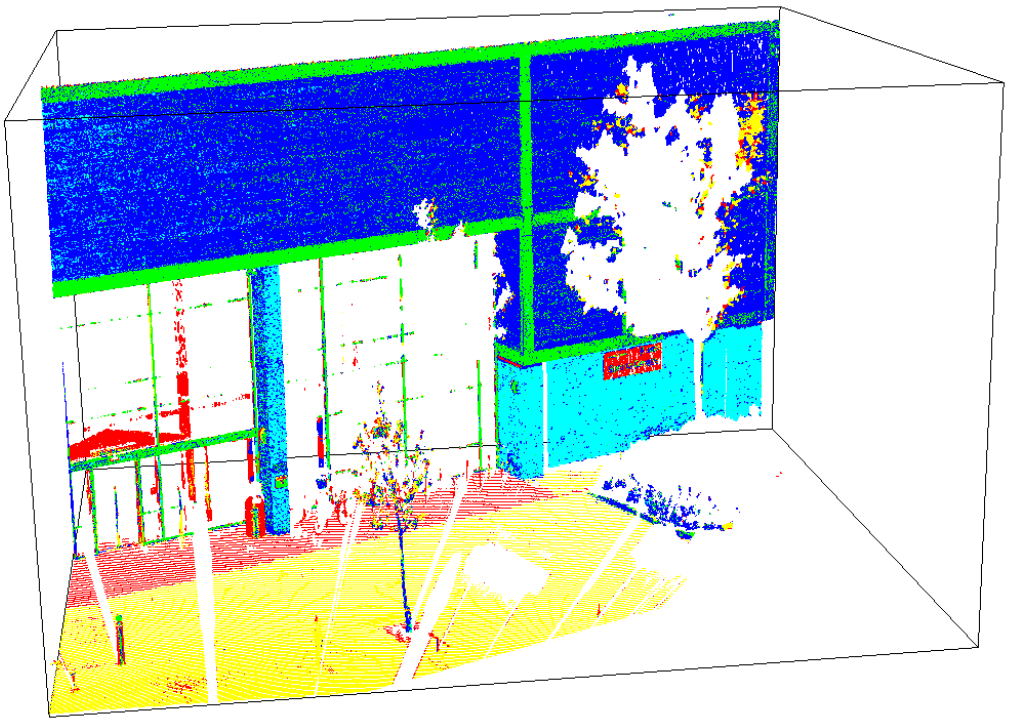


Figure 97 Sub-space KNN: classification rate created as a false colour point cloud.

9 Weighted KNN FARO, Ratios 1 & 2

Table 29 Weighted KNN: classification rate, site 1 test data.

		Per True Class						FNR
True Class	1	71.9%	26.2%	1.3%	0.4%	0.2%	Wood	28.1%
	2	33.6%	59.2%	4.8%	1.1%	1.3%	Brick	40.8%
	3	9.5%	3.1%	82.9%	2.2%	2.3%	Steel	17.1%
	4	4.2%	0.0%	0.2%	94.7%	0.9%	Gravel	5.3%
	5	0.4%	0.0%	0.3%	14.7%	84.7%	Pavement	15.3%
		1	2	3	4	5	Accuracy	78.7%
		Predicted Class						

		Per Predicted Class					
True Class	1	85.0%	60.1%	6.3%	1.3%	4.3%	Wood
	2	11.2%	38.4%	6.7%	1.1%	7.6%	Brick
	3	2.4%	1.5%	86.7%	1.7%	9.9%	Steel
	4	1.4%	0.0%	0.2%	93.6%	4.9%	Gravel
	5	0.0%	0.0%	0.1%	2.2%	73.2%	Pavement
Reliability	75.4%	1	2	3	4	5	
	FDR	15.0%	61.6%	13.3%	6.4%	26.8%	
		Predicted Class					

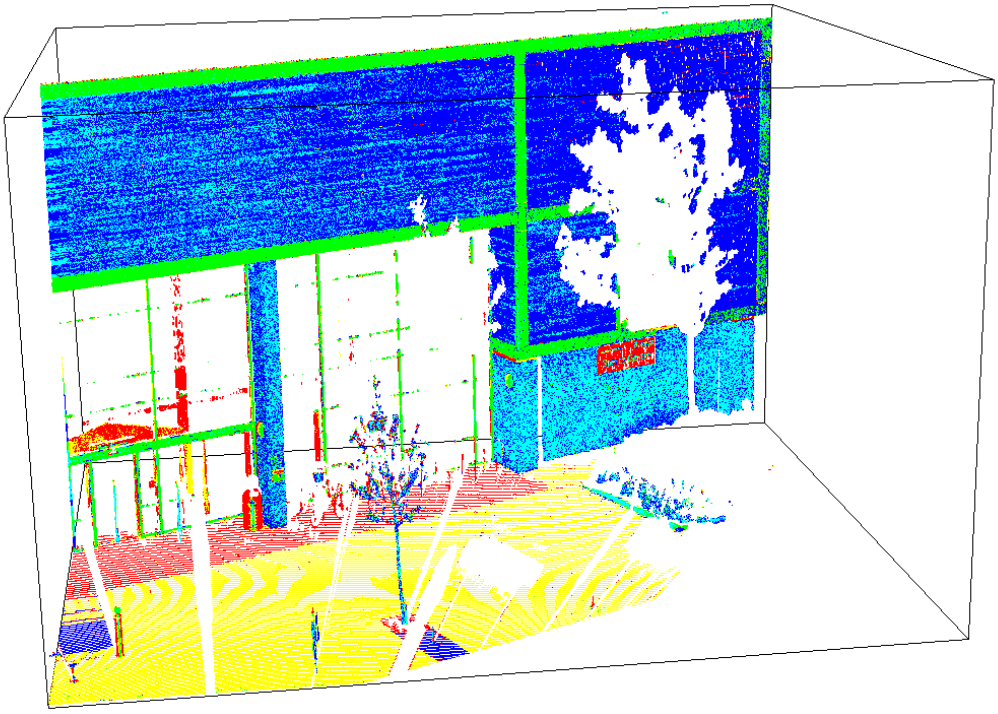


Figure 98 Weighted KNN: classification rate created as a false colour point cloud.

10 Weighted KNN, Ratios 1 & 3

Table 30 Weighted KNN: classification rate, test data, per true class, ratios 1 & 3.

Per True Class								FNR
True Class	1	71.8%	3.6%	22.6%	1.8%	0.2%	Wood	28.2%
	2	13.9%	76.0%	8.3%	0.6%	1.2%	Brick	24.0%
	3	42.8%	0.6%	52.6%	1.4%	2.6%	Steel	47.4%
	4	0.1%	0.0%	0.0%	98.6%	1.3%	Gravel	1.4%
	5	0.8%	0.0%	0.1%	12.3%	86.8%	Pavement	13.2%
		1	2	3	4	5	Accuracy	77.1%
		Predicted Class						

Per Predicted Class							
True Class	1	84.6%	14.1%	62.6%	6.2%	3.2%	Wood
	2	4.6%	85.4%	6.5%	0.6%	6.4%	Brick
	3	10.7%	0.5%	30.9%	1.0%	11.1%	Steel
	4	0.0%	0.0%	0.0%	90.4%	7.2%	Gravel
	5	0.0%	0.0%	0.0%	1.8%	72.1%	Pavement
Reliability	72.7%	1	2	3	4	5	
	FDR	15.4%	14.6%	69.1%	9.6%	27.9%	
		Predicted Class					

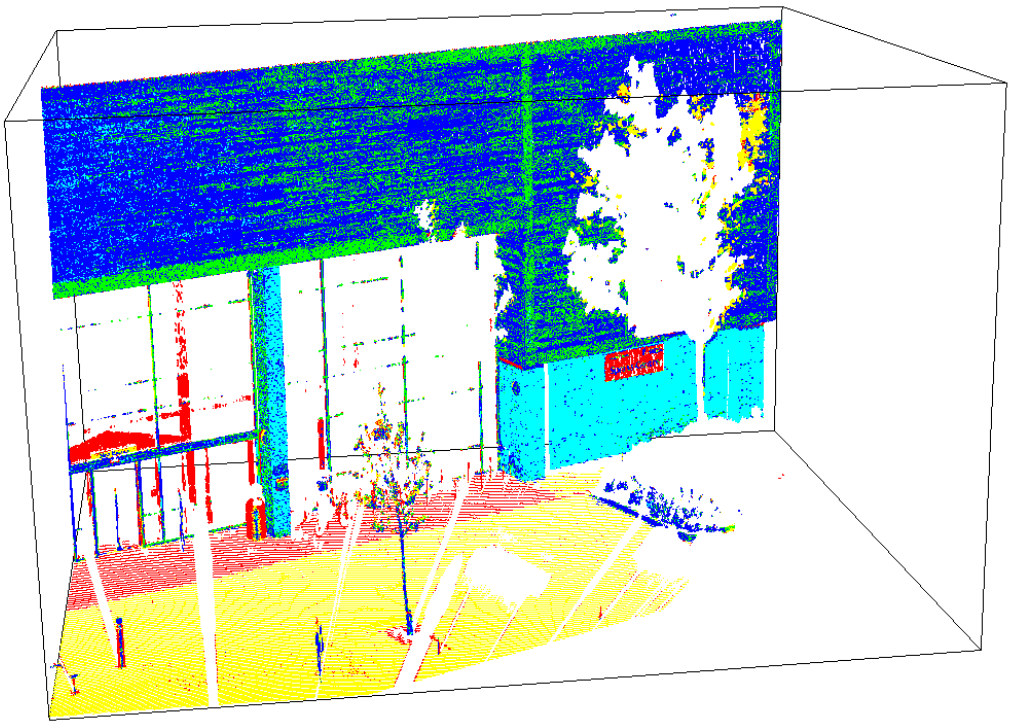


Figure 99 Weighted KNN: classification rate created as a false colour point cloud, ratios 1 & 3.

11 Weighted KNN, Ratios 2 & 3

Table 31 Weighted KNN: classification rate, test data, per true class, ratios 2 & 3.

Per True Class								FNR
True Class	1	90.3%	3.9%	3.8%	0.1%	1.9%	Wood	9.7%
	2	17.4%	76.0%	5.5%	0.5%	0.7%	Brick	24.0%
	3	14.3%	0.4%	81.8%	1.8%	1.7%	Steel	18.2%
	4	0.0%	0.0%	0.1%	89.6%	10.3%	Gravel	10.4%
	5	1.3%	0.0%	0.4%	14.6%	83.7%	Pavement	16.3%
		1	2	3	4	5	Accuracy	84.3%
		Predicted Class						

Per Predicted Class							
True Class	1	91.9%	15.2%	16.8%	0.3%	21.6%	Wood
	2	5.0%	84.5%	6.8%	0.5%	2.3%	Brick
	3	3.1%	0.3%	76.3%	1.5%	4.2%	Steel
	4	0.0%	0.0%	0.1%	95.3%	31.9%	Gravel
	5	0.1%	0.0%	0.1%	2.4%	40.1%	Pavement
Reliability	77.6%	1	2	3	4	5	
	FDR	8.1%	15.5%	23.7%	4.7%	59.9%	
		Predicted Class					

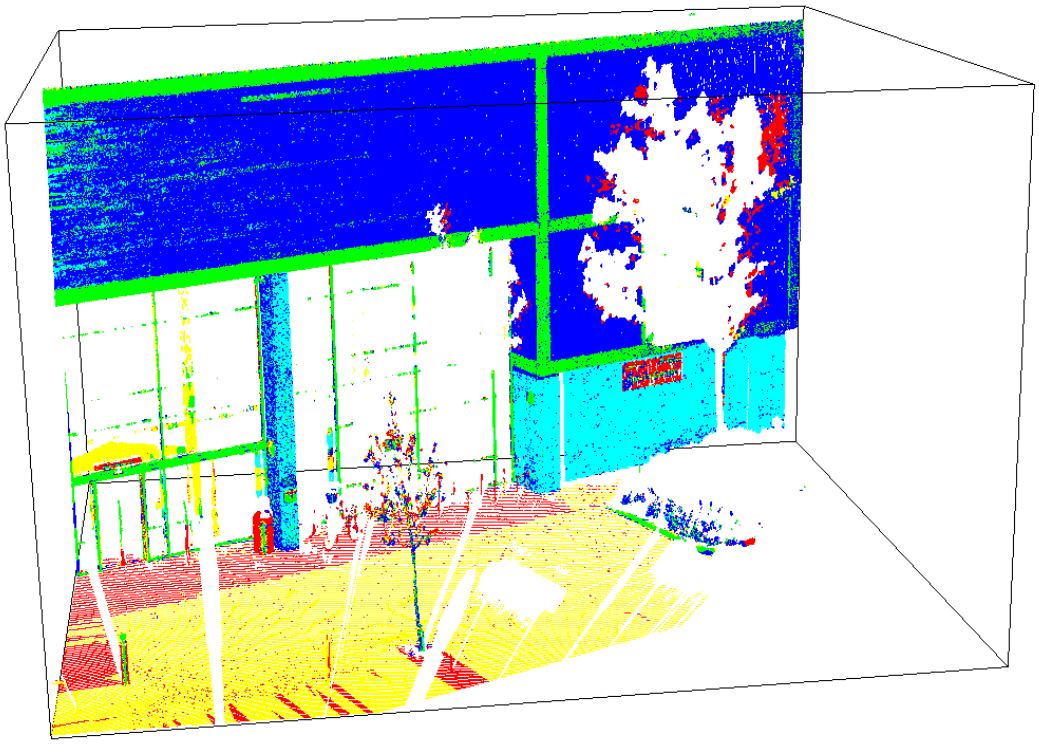


Figure 100 Weighted KNN: classification rate created as a false colour point cloud, ratios 2 & 3.

12 Weighted KNN – All ratios

Table 32 Weighted KNN: classification rate, test data, per true class.

Per True Class								FNR
True Class	1	92.5%	4.2%	1.9%	0.5%	0.9%	Wood	7.5%
	2	16.8%	76.1%	5.2%	0.8%	1.2%	Brick	23.9%
	3	9.8%	0.2%	85.7%	2.1%	2.1%	Steel	14.3%
	4	0.2%	0.0%	0.0%	95.0%	4.8%	Gravel	5.0%
	5	0.4%	0.0%	0.4%	13.5%	85.6%	Pavement	14.4%
		1	2	3	4	5	Accuracy	87.0%
		Predicted Class						

Per Predicted Class							
True Class	1	93.1%	16.3%	8.9%	1.8%	13.4%	Wood
	2	4.8%	83.6%	6.8%	0.8%	5.0%	Brick
	3	2.1%	0.2%	84.1%	1.7%	6.8%	Steel
	4	0.0%	0.0%	0.1%	93.6%	19.7%	Gravel
	5	0.0%	0.0%	0.1%	2.1%	55.1%	Pavement
Reliability	81.9%	1	2	3	4	5	
	FDR	6.9%	16.4%	15.9%	6.4%	44.9%	
		Predicted Class					

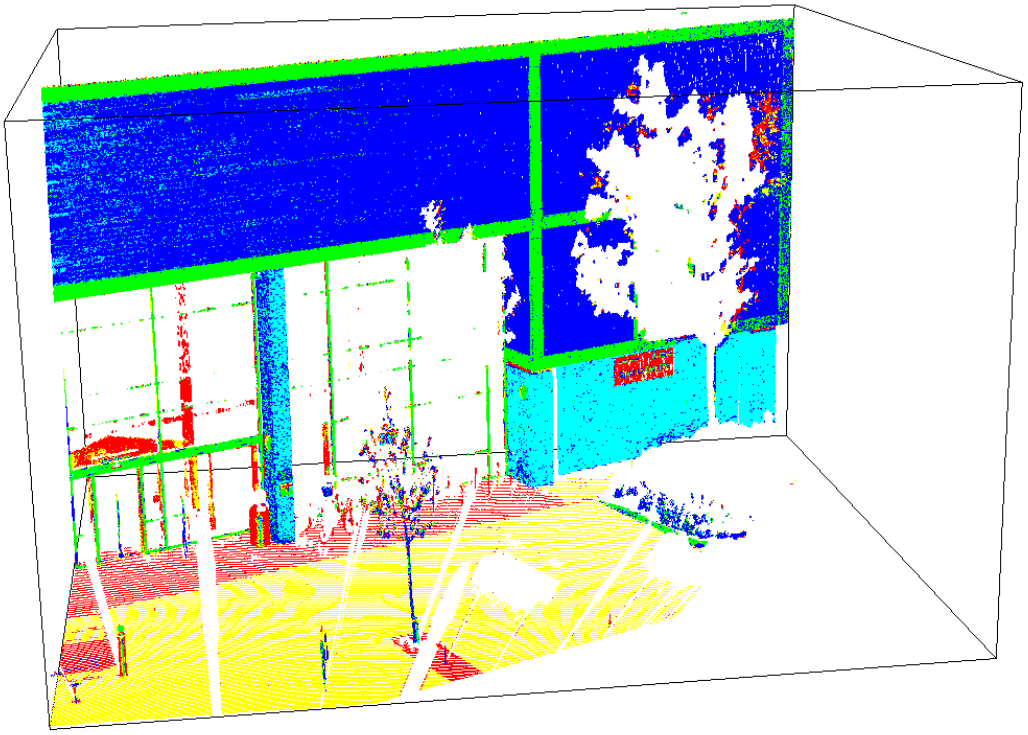


Figure 101 Weighted KNN: classification rate created as a false colour point cloud,

ANN Classifier Results

A summary of the ANN classifier results is shown in Table 33. The individual network configuration results are presented after the summary.

Table 33 ANN classifier results

				Hidden Layer		Classification rate (%)			
#	Transfer Function	Training Function	Ratios	No of layers	No of neurons	Validation data	Test data	Epochs	Score threshold
13	logsig	trainscg	All	1	10	99.5	87.2	51	0
14	logsig	traincgb	All	1	10	99.5	87.3	48	0
15	logsig	trainrp	All	1	10	98.9	86.9	73	0
16	logsig	trainrp	All	1	5	99.3	85.3	138	0
17	logsig	trainrp	All	1	15	98.7	86.6	53	0
18	logsig	trainrp	All	2	10,10	99.2	87.0	54	0
19	logsig	trainrp	2,3	1	10	97.6	85.1	37	0.9
20	logsig	trainrp	1,2	1	10	89.5	79.3	45	0.9
21	logsig	trainrp	1,3	1	10	89.7	74.7	65	0.9
22	logsig	trainrp	All	1	10	98.1	90.6	44	0.9
23	logsig	trainrp	1,3	1	10	89.7	78.1	66	0.5

Table 34 Summary of classification rate by class. Number of neurons in hidden layer (#), ANN score threshold (Thr).

				Class #	1	2	3	4	5			
				Class description	Wood	Brick	Steel	Gravel Pavement				
#	Classifier		#	Ratios	Classification rate %					Thr	Mean	Rank
1	Decision tree	Complex		All	92.2	76.8	80.8	93.6	86.7	-	86.0	12
2	Discriminant	Linear		All	69.9	75.7	92.0	99.3	82.3	-	83.8	18
3	Discriminant	Quadratic		All	91.6	75.1	75.3	94.4	87.7	-	84.8	16
4	SVM	Linear		All	92.4	75.7	89.5	97.6	84.7	-	88.0	3
5	SVM	Quadratic		All	94.4	75.3	86.3	95.5	85.0	-	87.3	5
6	SVM	Gaussian		All	91.0	75.3	91.5	98.2	84.7	-	88.1	2
7	KNN	Medium		All	93.0	74.8	86.7	95.1	85.2	-	87.0	9
8	KNN	Subspace		All	87.4	75.9	79.4	98.4	86.0	-	85.4	13
9	KNN	Weighted		1,2	71.9	59.2	82.9	94.7	84.7	-	78.7	20
10	KNN	Weighted		1,3	71.8	76.0	52.6	98.6	86.8	-	77.2	22
11	KNN	Weighted		2,3	90.3	76.0	81.8	89.6	83.7	-	84.3	17
12	KNN	Weighted		All	92.5	76.1	85.7	95.0	85.6	-	87.0	8
13	ANN	trainscg	10	All	92.6	77.3	85.6	95.0	85.6	0	87.2	6
14	ANN	traincgb	10	All	94.0	76.3	85.9	96.2	84.2	0	87.3	4
15	ANN	trainrp	10	All	90.0	76.2	85.4	98.9	84.0	0	86.9	10
16	ANN	trainrp	5	All	88.0	75.9	81.9	94.7	85.8	0	85.3	14
17	ANN	trainrp	15	All	90.3	76.1	85.9	95.2	85.3	0	86.6	11
18	ANN	trainrp	10,10	All	91.1	78.0	84.0	96.3	85.9	0	87.1	7
19	ANN	trainrp	10	2,3	90.2	76.0	82.8	93.2	83.0	0.9	85.0	15
20	ANN	trainrp	10	1,2	85.2	40.5	88.7	96.4	85.8	0.9	79.3	19
21	ANN	trainrp	10	1,3	91.1	94.5	0.0	99.2	88.6	0.9	74.7	23
22	ANN	trainrp	10	All	97.0	81.2	88.2	99.2	87.3	0.9	90.6	1
23	ANN	trainrp	10	1,3	57.1	77.5	70.8	98.8	86.4	0.5	78.1	21
				Max	97.0	94.5	92.0	99.3	88.6			
				Mean	87.2	74.8	79.3	96.2	85.4			
				Min	57.1	40.5	0.0	89.6	82.3			

Table 35 Training function and acronyms used in results table.

Training function	**Acronym**
BFGS Quasi-Newton	trainbfg
Conjugate Gradient with Powell/Beale Restarts	traincgb
Fletcher-Powell Conjugate Gradient	traincgf
Polak-Ribiére Conjugate Gradient	traincgp
Variable Learning Rate Backpropagation	traingdx
Levenberg-Marquardt	trainlm
One Step Secant	trainoss
Resilient Backpropagation	trainrp
Scaled Conjugate Gradient	trainscg

Table 36 Transfer functions and acronyms used in results table.

Transfer function	Acronym	Output
Log-Sigmoid	logsig	0 - 1
Tan-Sigmoid	tansig	-1 - +1
Linear	pureln	-inf - +inf
Radial Bias	radbas	-inf - +inf

13 Scaled Conjugate Gradient

Table 37 Artificial Neural Network classification rate, Scaled Conjugate Gradient, site 1 test data.

		Per True Class						FNR
True Class	1	92.6%	3.9%	1.9%	1.1%	0.5%	Wood	7.4%
	2	16.4%	77.3%	4.8%	0.6%	0.9%	Brick	22.7%
	3	10.1%	0.6%	85.6%	1.6%	2.1%	Steel	14.4%
	4	0.9%	0.0%	0.1%	95.0%	4.0%	Gravel	5.0%
	5	1.7%	0.1%	0.4%	12.2%	85.6%	Pavement	14.4%
		1	2	3	4	5	Accuracy	87.2%
		Predicted Class						

		Per Predicted Class					
True Class	1	92.9%	15.0%	9.0%	3.8%	9.0%	Wood
	2	4.7%	84.5%	6.3%	0.6%	4.3%	Brick
	3	2.1%	0.5%	84.5%	1.3%	7.5%	Steel
	4	0.3%	0.0%	0.1%	92.5%	18.2%	Gravel
	5	0.1%	0.0%	0.1%	1.8%	60.9%	Pavement
Reliability	83.1%	1	2	3	4	5	
	FDR	7.1%	15.5%	15.5%	7.5%	39.1%	
		Predicted Class					

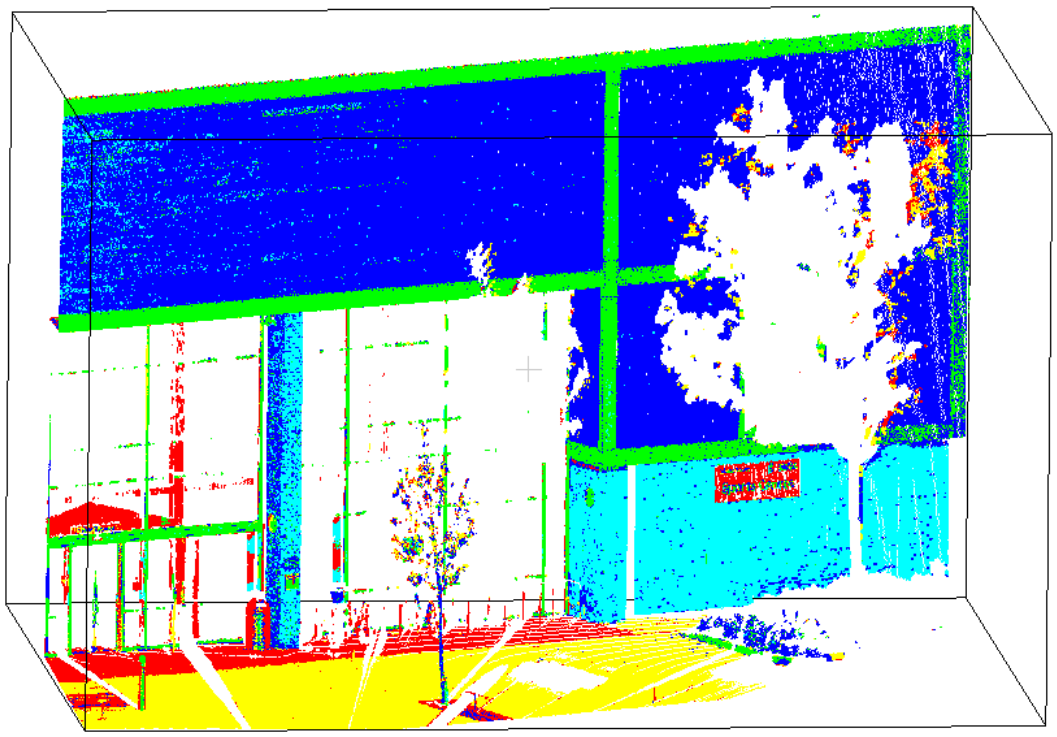


Figure 102 (Network #13) Network classification rate, false colour point cloud.

14 Conjugate Gradient Powell/Beale Restarts

Table 38 Artificial Neural Network classification rate, Conjugate Gradient Powell/Beale Restarts, site 1 test data.

		Per True Class						FNR
True Class	1	94.0%	3.4%	2.0%	0.6%	0.1%	Wood	6.0%
	2	17.2%	76.3%	4.7%	0.8%	1.0%	Brick	23.7%
	3	9.4%	0.3%	85.9%	2.1%	2.2%	Steel	14.1%
	4	3.0%	0.0%	0.0%	96.2%	0.8%	Gravel	3.8%
	5	0.8%	0.0%	0.4%	14.6%	84.2%	Pavement	15.8%
		1	2	3	4	5	Accuracy	87.3%
		Predicted Class						

		Per Predicted Class					
True Class	1	92.4%	13.4%	9.2%	2.0%	2.7%	Wood
	2	4.8%	86.3%	6.1%	0.8%	6.3%	Brick
	3	2.0%	0.2%	84.6%	1.6%	10.1%	Steel
	4	0.8%	0.0%	0.0%	93.3%	4.7%	Gravel
	5	0.0%	0.0%	0.1%	2.2%	76.2%	Pavement
Reliability	86.6%	1	2	3	4	5	
	FDR	7.6%	13.7%	15.4%	6.7%	23.8%	
		Predicted Class					

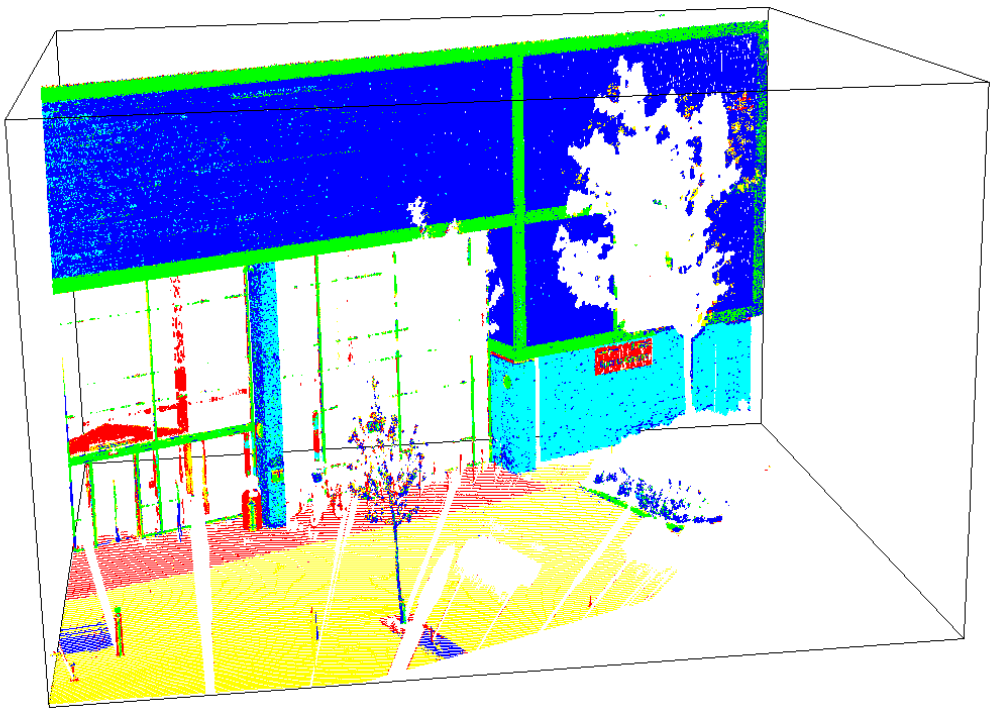


Figure 103 (Network #14) Network classification rate, false colour point cloud.

15 Resilient backpropagation, 10 hidden layer neurons

Table 39 Artificial Neural Network classification rate, Resilient backpropagation, 10 hidden layer neurons , site 1 test data.

		Per True Class						FNR
True Class	1	90.0%	4.4%	2.7%	2.6%	0.3%	Wood	10.0%
	2	16.5%	76.2%	5.4%	1.0%	0.9%	Brick	23.8%
	3	9.8%	0.5%	85.4%	2.2%	2.0%	Steel	14.6%
	4	0.1%	0.0%	0.1%	98.9%	0.9%	Gravel	1.1%
	5	0.7%	0.1%	0.5%	14.7%	84.0%	Pavement	16.0%
		1	2	3	4	5	Accuracy	86.9%
		Predicted Class						

		Per Predicted Class					
True Class	1	93.0%	17.0%	11.9%	8.5%	5.6%	Wood
	2	4.8%	82.6%	6.8%	0.9%	5.5%	Brick
	3	2.2%	0.4%	81.1%	1.5%	9.1%	Steel
	4	0.0%	0.0%	0.1%	87.1%	5.1%	Gravel
	5	0.0%	0.0%	0.1%	2.0%	74.7%	Pavement
Reliability	83.7%	1	2	3	4	5	
	FDR	7.0%	17.4%	18.9%	12.9%	25.3%	
		Predicted Class					

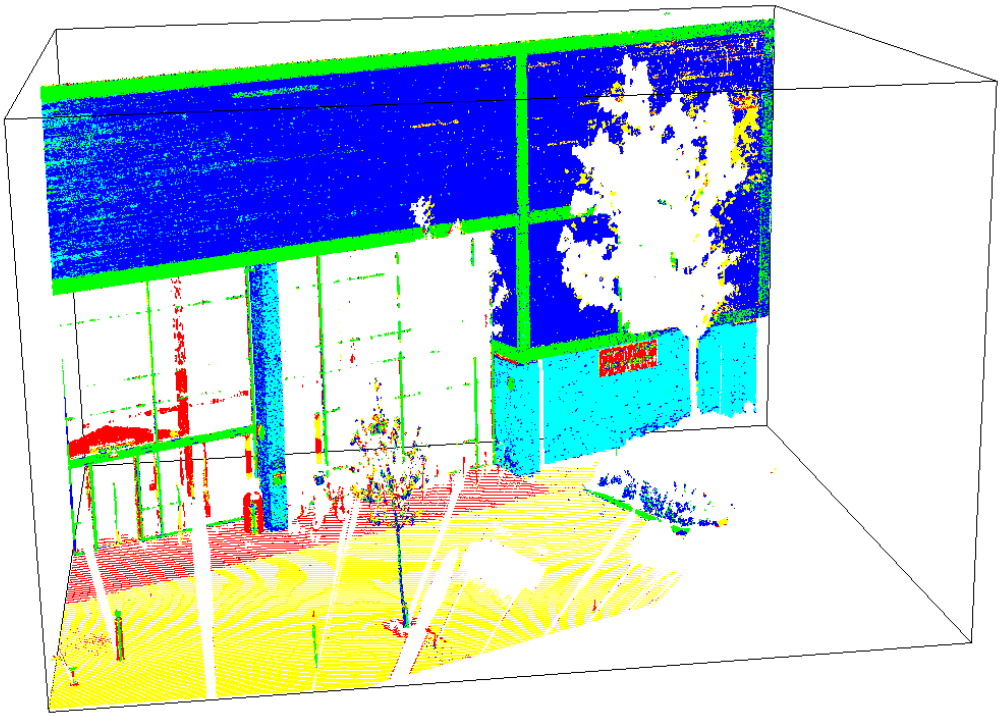


Figure 104 (Network #15) Network classification rate, false colour point cloud.

16 Resilient backpropagation, 5 hidden layer neurons

Table 40 Artificial Neural Network classification rate, Resilient backpropagation, 5 hidden layer neurons, site 1 test data.

		Per True Class						FNR
True Class	1	88.0%	8.6%	2.1%	1.1%	0.2%	Wood	12.0%
	2	17.5%	75.9%	3.7%	1.6%	1.3%	Brick	24.1%
	3	12.9%	0.2%	81.9%	2.9%	2.1%	Steel	18.1%
	4	4.4%	0.0%	0.0%	94.7%	0.9%	Gravel	5.3%
	5	1.7%	0.0%	0.2%	12.3%	85.8%	Pavement	14.2%
		1	2	3	4	5	Accuracy	85.3%
		Predicted Class						

		Per Predicted Class					
True Class	1	90.8%	28.7%	10.2%	3.8%	3.9%	Wood
	2	5.1%	71.2%	5.1%	1.6%	7.3%	Brick
	3	2.8%	0.1%	84.6%	2.1%	9.4%	Steel
	4	1.2%	0.0%	0.0%	90.6%	4.8%	Gravel
	5	0.1%	0.0%	0.0%	1.8%	74.6%	Pavement
Reliability	82.4%	1	2	3	4	5	
	FDR	9.2%	28.8%	15.4%	9.4%	25.4%	
		Predicted Class					

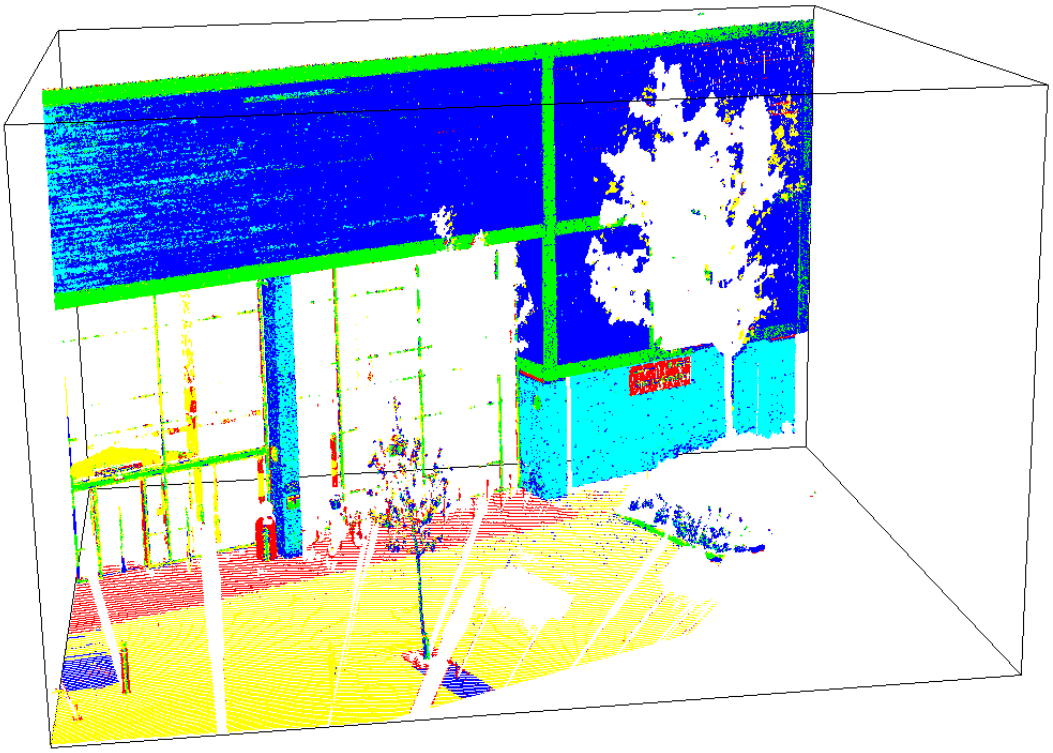


Figure 105 (Network #16) Network classification rate, false colour point cloud.

17 Resilient backpropagation, 15 hidden layer neurons

Table 41 Artificial Neural Network classification rate, Resilient backpropagation, 15 hidden layer neurons, site 1 test data.

		Per True Class						FNR
True Class	1	90.3%	5.6%	1.9%	1.6%	0.6%	Wood	9.7%
	2	16.9%	76.1%	5.1%	0.6%	1.3%	Brick	23.9%
	3	9.5%	0.2%	85.9%	1.9%	2.4%	Steel	14.1%
	4	0.2%	0.0%	0.1%	95.2%	4.6%	Gravel	4.8%
	5	0.5%	0.0%	0.4%	13.8%	85.3%	Pavement	14.7%
		1	2	3	4	5	Accuracy	86.6%
		Predicted Class						

		Per Predicted Class					
True Class	1	92.9%	20.5%	8.8%	5.7%	9.1%	Wood
	2	4.9%	79.3%	6.7%	0.6%	5.8%	Brick
	3	2.1%	0.2%	84.3%	1.4%	8.2%	Steel
	4	0.0%	0.0%	0.1%	90.3%	19.8%	Gravel
	5	0.0%	0.0%	0.1%	2.0%	57.1%	Pavement
Reliability	80.8%	1	2	3	4	5	
	FDR	7.1%	20.7%	15.7%	9.7%	42.9%	
		Predicted Class					

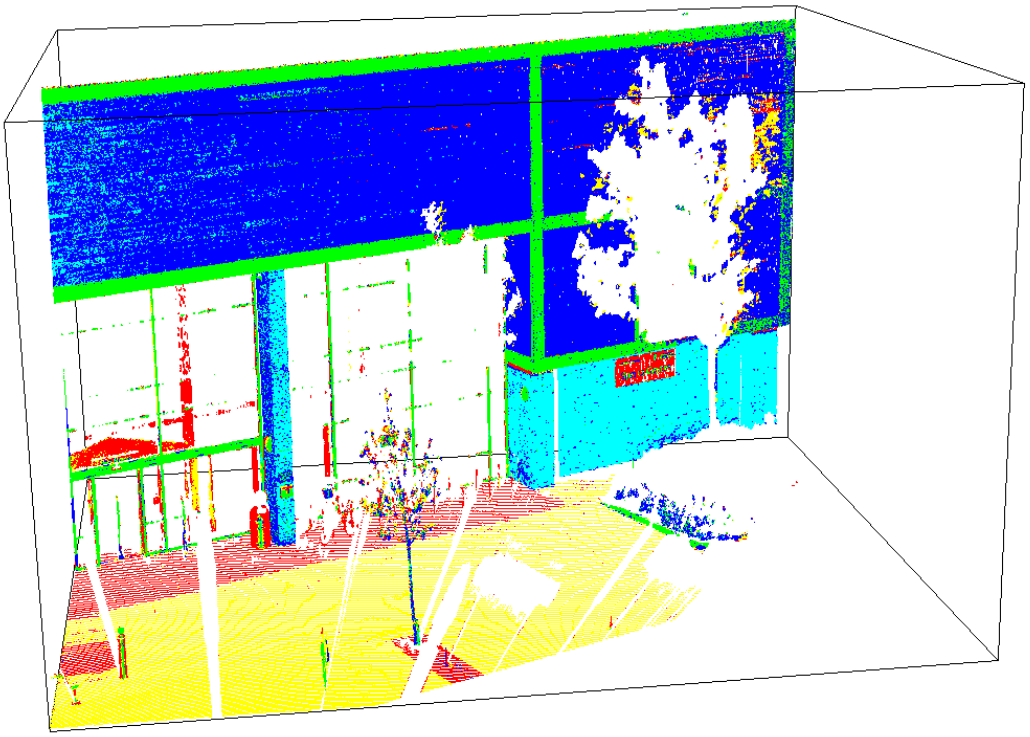


Figure 106 (Network #17) Network classification rate, false colour point cloud.

18 Resilient backpropagation, 2 hidden layers,10 neurons per hidden layer

Table 42 Artificial Neural Network classification rate, Resilient backpropagation, 2 hidden layers,10 neurons per hidden layer, site 1 test data.

		Per True Class						FNR
True Class	1	91.1%	4.1%	2.0%	1.7%	1.2%	Wood	8.9%
	2	15.1%	78.0%	4.5%	0.9%	1.6%	Brick	22.0%
	3	10.6%	0.5%	84.0%	2.0%	2.9%	Steel	16.0%
	4	0.0%	0.0%	0.1%	96.3%	3.6%	Gravel	3.7%
	5	0.3%	0.0%	0.4%	13.4%	85.9%	Pavement	14.1%
		1	2	3	4	5	Accuracy	87.0%
		Predicted Class						

		Per Predicted Class					
True Class	1	93.3%	15.6%	9.4%	5.8%	17.0%	Wood
	2	4.4%	84.0%	6.0%	0.8%	6.6%	Brick
	3	2.3%	0.4%	84.4%	1.5%	9.1%	Steel
	4	0.0%	0.0%	0.1%	89.9%	14.4%	Gravel
	5	0.0%	0.0%	0.1%	1.9%	52.9%	Pavement
Reliability	80.9%	1	2	3	4	5	
	FDR	6.7%	16.0%	15.6%	10.1%	47.1%	
		Predicted Class					

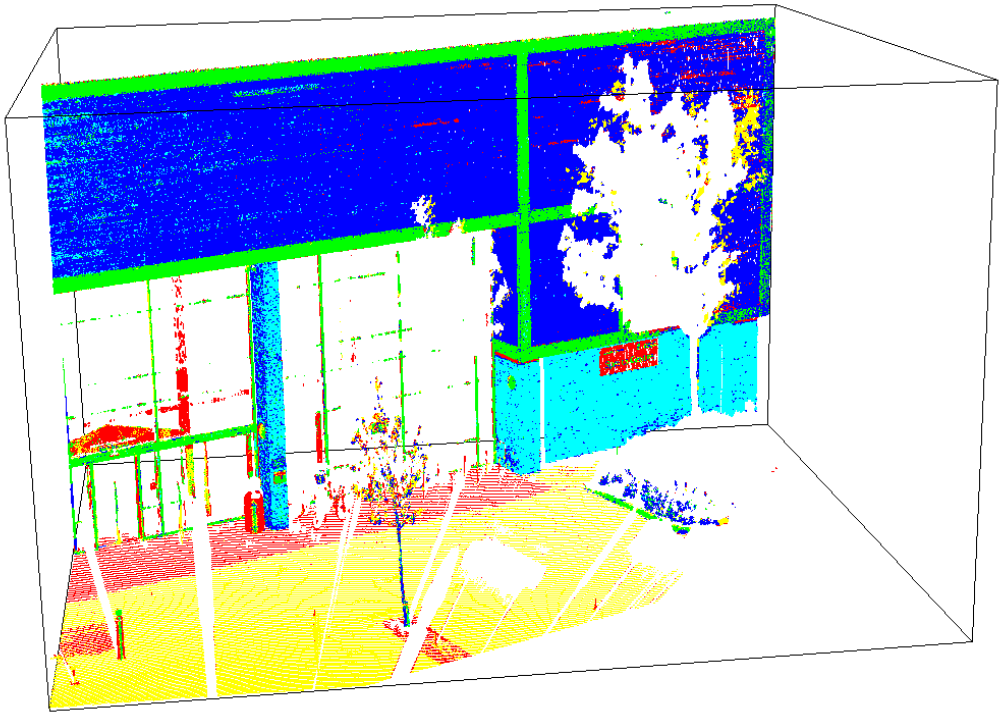


Figure 107 (Network #18) Network classification rate, false colour point cloud.

19 Resilient backpropagation, 1 hidden layers,10 neurons per hidden layer, Ratios 2 & 3

Table 43 Artificial Neural Network classification rate, Resilient backpropagation, 1 hidden layers,10 neurons per hidden layer, Ratios 2 & 3, site 1 test data.

		Per True Class						FNR
True Class	1	90.2%	3.6%	3.9%	0.1%	2.2%	Wood	9.8%
	2	17.2%	76.0%	5.4%	0.6%	0.8%	Brick	24.0%
	3	13.3%	0.2%	82.8%	1.9%	1.8%	Steel	17.2%
	4	0.0%	0.0%	0.1%	93.2%	6.7%	Gravel	6.8%
	5	0.9%	0.0%	0.3%	15.6%	83.0%	Pavement	17.0%
		1	2	3	4	5	Accuracy	85.1%
		Predicted Class						

		Per Predicted Class					
True Class	1	92.1%	14.4%	16.8%	0.3%	27.1%	Wood
	2	5.0%	85.4%	6.6%	0.6%	2.8%	Brick
	3	2.9%	0.2%	76.5%	1.5%	4.6%	Steel
	4	0.0%	0.0%	0.1%	95.1%	22.4%	Gravel
	5	0.0%	0.0%	0.1%	2.5%	43.1%	Pavement
Reliability	78.4%	1	2	3	4	5	
	FDR	7.9%	14.6%	23.5%	4.9%	56.9%	
		Predicted Class					

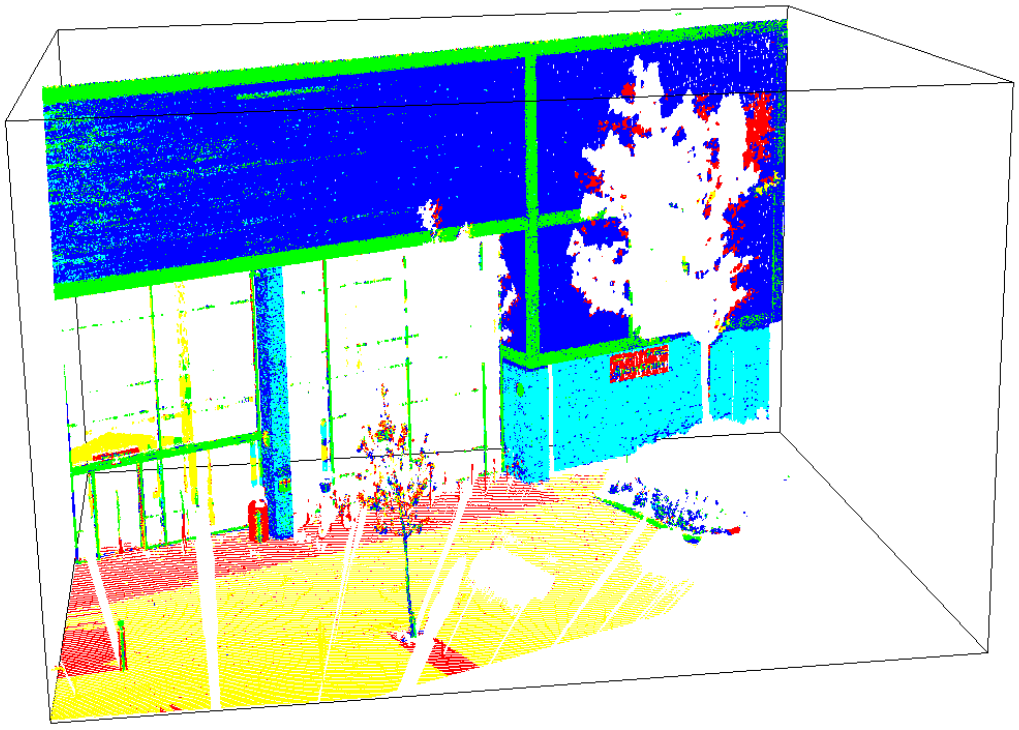


Figure 108 (Network #19) Network classification rate, false colour point cloud

20 Resilient backpropagation, 1 hidden layers,10 neurons per hidden layer, Ratios 1 & 2

Table 44 Artificial Neural Network classification rate, Resilient backpropagation, 1 hidden layers,10 neurons per hidden layer, Ratios 1 & 2, site 1 test data.

		Per True Class						FNR
True Class	1	85.2%	8.2%	2.7%	0.3%	3.6%	Wood	14.8%
	2	26.8%	40.5%	21.6%	3.7%	7.3%	Brick	59.5%
	3	6.9%	0.1%	88.7%	1.2%	3.1%	Steel	11.3%
	4	0.7%	0.0%	0.0%	96.4%	2.9%	Gravel	3.6%
	5	0.2%	0.0%	0.2%	13.8%	85.8%	Pavement	14.2%
		1	2	3	4	5	Accuracy	79.3%
		Predicted Class						

		Per Predicted Class					
True Class	1	91.5%	58.5%	5.2%	0.5%	19.8%	Wood
	2	4.1%	41.1%	5.9%	0.7%	5.6%	Brick
	3	3.8%	0.4%	88.8%	0.8%	8.6%	Steel
	4	0.6%	0.0%	0.1%	95.9%	11.7%	Gravel
	5	0.0%	0.0%	0.0%	2.2%	54.2%	Pavement
Reliability	74.3%	1	2	3	4	5	
	FDR	8.5%	58.9%	11.2%	4.1%	45.8%	
		Predicted Class					

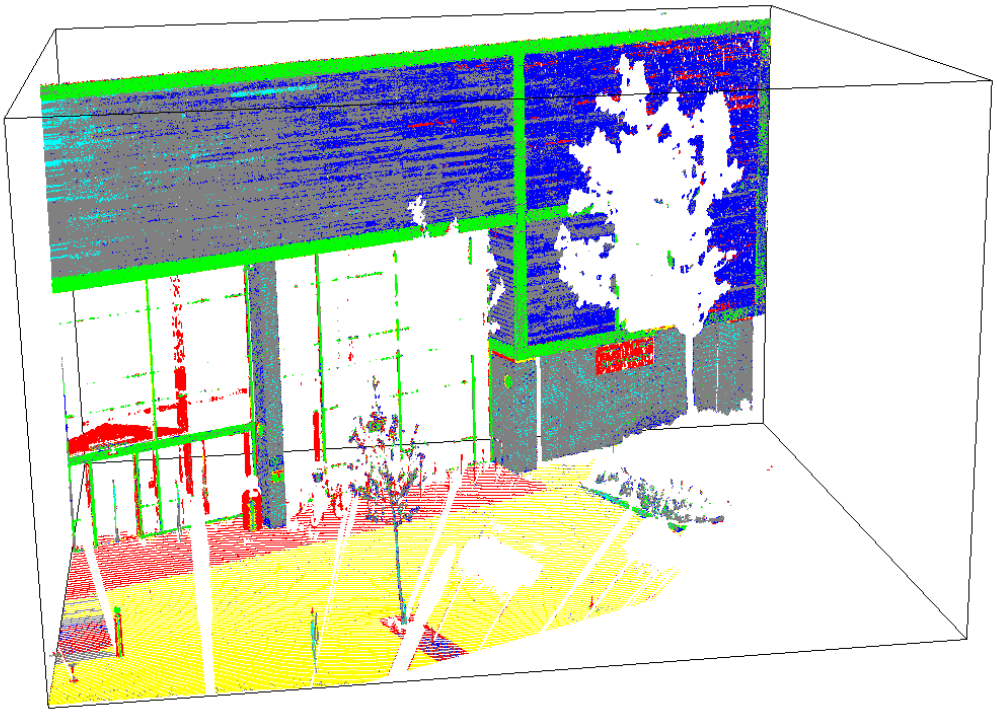


Figure 109 (Network #20) Network classification rate, false colour point cloud

21 Resilient backpropagation, 1 hidden layers,10 neurons per hidden layer, Ratios 1 & 3

Table 45 Artificial Neural Network classification rate, Resilient backpropagation, 1 hidden layers,10 neurons per hidden layer, Ratios 1 & 3, site 1 test data.

		Per True Class						FNR
True Class	1	91.1%	2.7%	0.0%	5.9%	0.3%	Wood	8.9%
	2	3.0%	94.5%	0.0%	0.7%	1.8%	Brick	5.5%
	3	61.0%	1.0%	0.0%	12.8%	25.2%	Steel	100.0%
	4	0.0%	0.0%	0.0%	99.2%	0.8%	Gravel	0.8%
	5	0.5%	0.0%	0.0%	10.9%	88.6%	Pavement	11.4%
		1	2	3	4	5	Accuracy	74.7%
		Predicted Class						

		Per Predicted Class					
True Class	1	93.1%	4.0%	#DIV/0!	6.3%	2.2%	Wood
	2	2.0%	95.8%	#DIV/0!	0.5%	7.8%	Brick
	3	4.7%	0.1%	#DIV/0!	1.0%	12.2%	Steel
	4	0.0%	0.0%	#DIV/0!	90.7%	4.2%	Gravel
	5	0.1%	0.0%	#DIV/0!	1.5%	73.5%	Pavement
Reliability	#DIV/0!	1	2	3	4	5	
	FDR	6.9%	4.2%	#DIV/0!	9.3%	26.5%	
		Predicted Class					

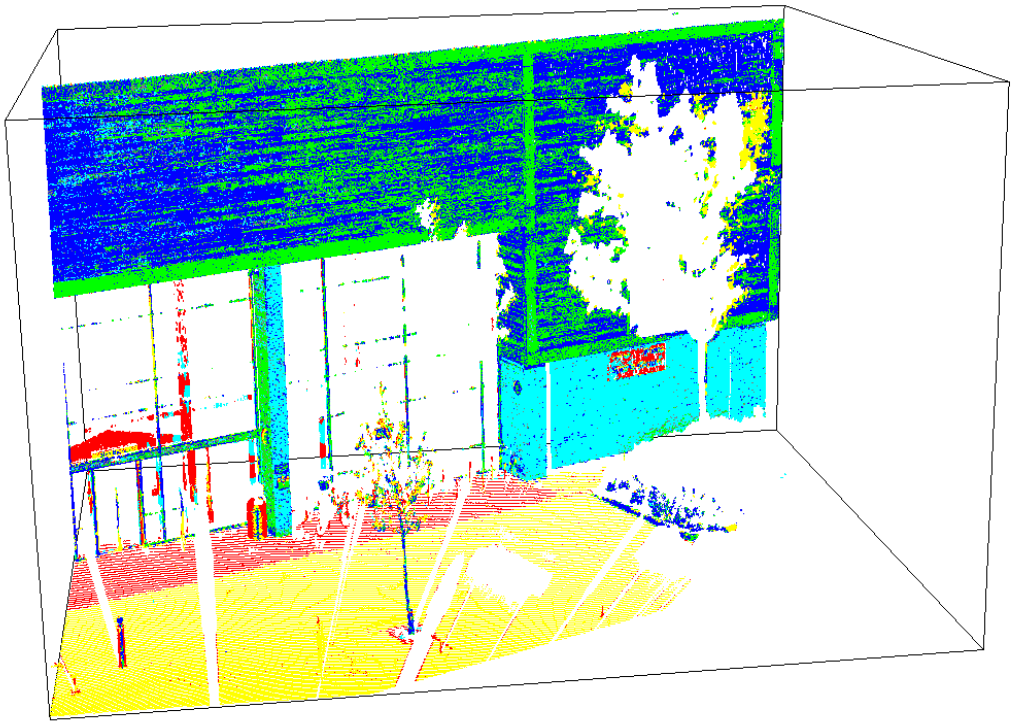


Figure 110 (Network #21) Network classification rate, false colour point cloud

22 Resilient backpropagation, 1 hidden layers,10 neurons per hidden layer, Ratios All

Table 46 Artificial Neural Network, Resilient backpropagation, 1 hidden layers,10 neurons per hidden layer, Ratios all, site 1 test data.

Per True Class								FNR
True Class	1	97.0%	0.3%	1.3%	0.9%	0.2%	Wood	2.8%
	2	11.8%	81.2%	4.3%	0.6%	1.5%	Brick	18.2%
	3	7.0%	0.0%	88.2%	1.8%	2.9%	Steel	11.7%
	4	0.0%	0.0%	0.0%	99.2%	0.8%	Gravel	0.8%
	5	0.5%	0.0%	0.3%	11.9%	87.3%	Pavement	12.6%
		1	2	3	4	5	Accuracy	90.6%
		Predicted Class						

Per Predicted Class							
True Class	1	95.6%	1.4%	6.4%	2.9%	3.7%	Wood
	2	3.0%	98.6%	5.2%	0.5%	7.1%	Brick
	3	1.4%	0.0%	88.2%	1.2%	10.9%	Steel
	4	0.0%	0.0%	0.1%	93.7%	4.2%	Gravel
	5	0.0%	0.0%	0.1%	1.8%	74.1%	Pavement
Reliability	90.0%	1	2	3	4	5	
	FDR	4.4%	1.4%	11.8%	6.3%	25.9%	
		Predicted Class					

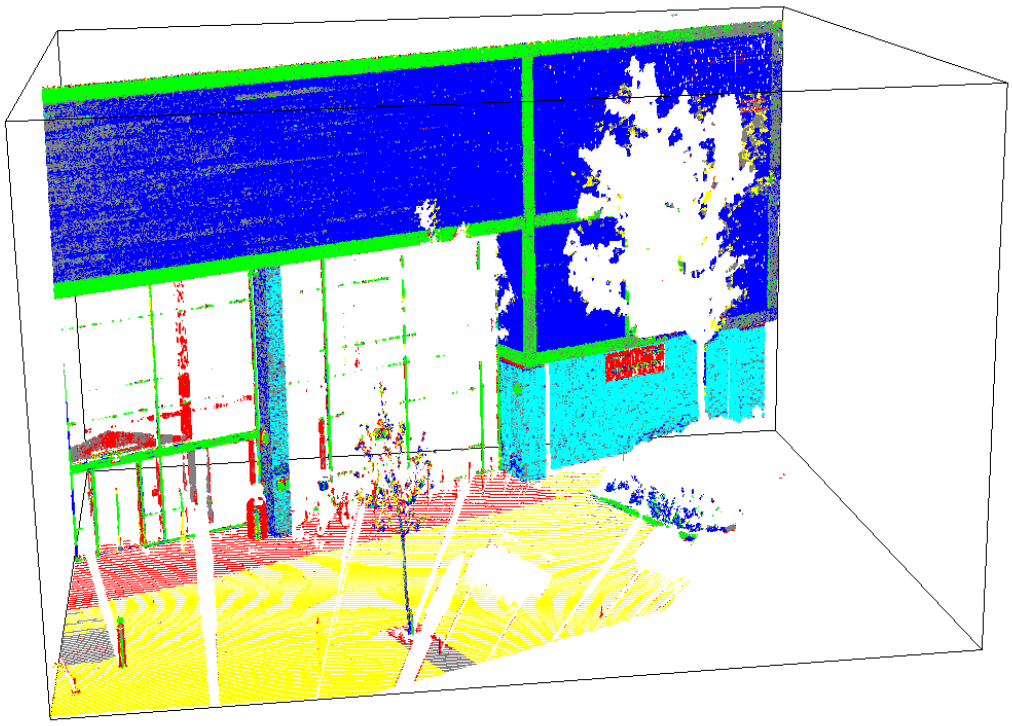


Figure 111 (Network #22) Network classification rate, false colour point cloud

23 Resilient backpropagation, 1 hidden layers,10 neurons per hidden layer, Ratios 1 & 3, threshold 0.5

Table 47 Artificial Neural Network classification rate, Resilient backpropagation, 1 hidden layers,10 neurons per hidden layer, Ratios 1 & 3, threshold 0.5, site 1 test data.

		Per True Class						FNR
True Class	1	57.1%	6.6%	34.1%	2.2%	0.0%	Wood	42.9%
	2	12.6%	77.5%	8.1%	0.7%	1.1%	Brick	22.5%
	3	24.0%	1.0%	70.8%	1.8%	2.5%	Steel	29.2%
	4	0.0%	0.2%	0.0%	98.8%	1.0%	Gravel	1.2%
	5	0.4%	1.7%	0.1%	11.5%	86.4%	Pavement	13.6%
		1	2	3	4	5	Accuracy	78.1%
		Predicted Class						

		Per Predicted Class					
True Class	1	86.9%	23.1%	66.4%	7.3%	1.0%	Wood
	2	5.3%	75.8%	4.4%	0.6%	6.2%	Brick
	3	7.7%	0.7%	29.2%	1.2%	11.2%	Steel
	4	0.0%	0.2%	0.0%	89.2%	5.5%	Gravel
	5	0.0%	0.2%	0.0%	1.6%	76.1%	Pavement
Reliability	71.5%	1	2	3	4	5	
	FDR	13.1%	24.2%	70.8%	10.8%	23.9%	
		Predicted Class					

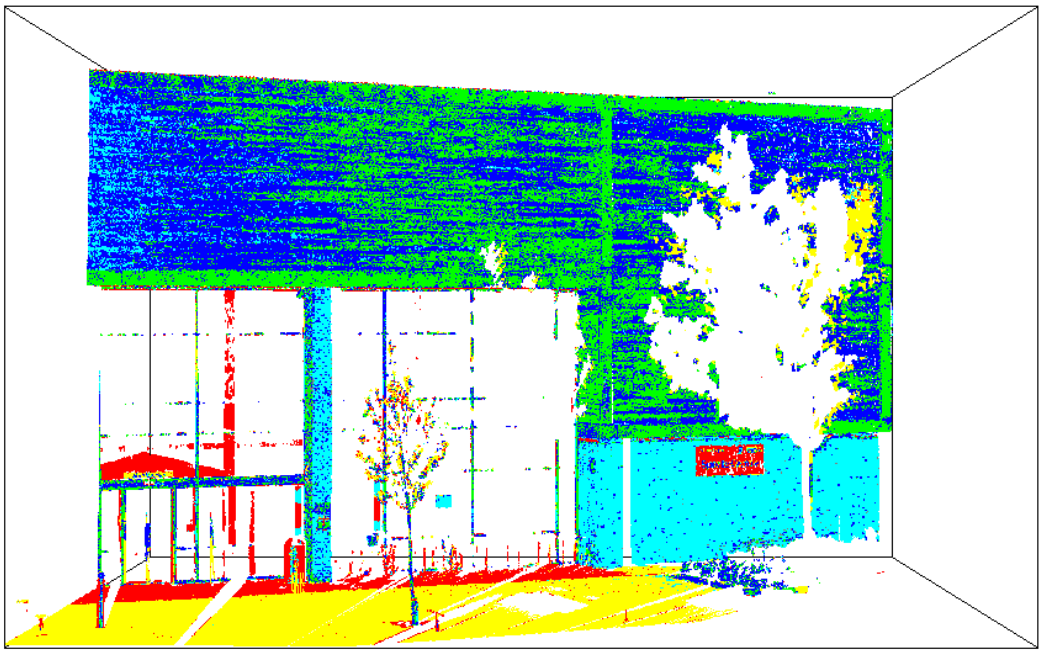


Figure 112 (Network #23) Network classification rate, false colour point cloud

Appendix B MATLAB Programs

The following MatLab programs were written during the research to implement algorithms in the multi-spectral classification process. Minor sub functions are not shown for brevity.

Create multi-spectral point cloud

```
function KNN
%Create file of nearest neighbours from 3 input files
%Define a reference cloud, then store the intensity values in
three columns

strpath='E:Scans\';
strdlm=' ';
strtitle='Open Reference Cloud';
strdlm=' ';
[ strfilename,strpath,R1,nrows,ncols,a ] =
ImportCloud(strpath,strdlm,strtitle);
if a==1
    return;
end
n1=nrows;
strtitle='Open Cloud 1';
strdlm=' ';
[ strfilename,strpath,R2,nrows,ncols,a ] =
ImportCloud(strpath,strdlm,strtitle);
if a==1
    return;
end
strtitle='Open Cloud 2';
strdlm=' ';
[ strfilename,strpath,R3,nrows,ncols,a ] =
ImportCloud(strpath,strdlm,strtitle);
if a==1
    return;
end

%output array: xyzr1r2r3
[r,c]=size(R1);
B=zeros(r,6);
B(:,1:4)=R1(:,1:4);

%get index of nearest neighbours between R1 & R2
display('KNN 1-2');
[IDX,D1]=knnsearch(R2(:,1:3),R1(:,1:3),'K',3);
for k=1:1:n1
    B(k,5)=R2(IDX(k,1),4);
end

%get index of nearest neighbours between R1 & R3
display('KNN 1-3');
[IDX,D2]=knnsearch(R3(:,1:3),R1(:,1:3),'K',3);
for k=1:1:n1
```

```
    B(k,6)=R3(IDX(k,1),4);
end

%write to file
[strfilename,a ] = ExportCloud(strpath,strdlm,B);
```

Classify multi-spectral point cloud

```
%Script to execute classifier routines
%define number of columns in test data and predicted data
pcol=7;
rcol=7;

%run clssifier with trained model
[predictedData,class]=testClassifer(trainedClassifier,testData)
;
%Calculate confusion matrix
[C,outputData]=ConfusionMatrix(referenceData,rcol,predictedData
,pcol);
%Create point cloud of predicted data using set colours for
each predicted
%class
[rgbData]=ClassesAddRGB(outputData,pcol);


function
[predictedData,class]=testClassifer(trainedClassifier,testData)
%extract test data columns
T=testData(:,4:6);
%use trained classifier to predict classes in test data
class = trainedClassifier.predictFcn(T);

%convert testData to array
testDataA=table2array(testData);
%combin test data with esults
[rows,cols]=size(testDataA);
predictedData=zeros(rows,cols+1);
predictedData(:,1:cols)=testDataA(:,1:cols);
predictedData(:,cols+1)=class;

%write to file
% strpath='D:';
% strdlm=' ';
% [ strfilename,a ] =
ExportCloud(strpath,strdlm,predictedData);
% close 'all';
end


function
[C,outputData]=ConfusionMatrix(referenceData,rcol,predictedData
,pcol)
%calulate confusion matrix
%referenceData x,y,z,r,g,b,class
%predictedData x,y,z,s1,s2,s3,class
%g1 is reference (known classes)
%g2 is predicted
```

```
%IDX to ensure correct correlation of position
[IDX,D]=knnsearch(predictedData(:,1:3),referenceData(:,1:3),'K'
,3);
g2=predictedData(IDX(:,1),pcol);
g1=referenceData(:,rcol);
[C,order] = confusionmat(g1,g2);
%xlswrite('output',C);
% plotconfusion(g2,g1);

%add ref class to predictedData
[rows,cols]=size(predictedData);
outputData=zeros(rows,cols+1);
outputData(:,1:cols)=predictedData(IDX(:,1),1:cols);
outputData(:,cols+1)=g1;
%xyzs1,s2,s3,refclass,predictedclass
end


function [rgbData]=ClassesAddRGB(outputData,pcol)
%xyz,s1,s2,s3,ref class,predicted class

%colors
C=[0,0,255;...      %1  Blue
   0,255,255;...    %2  Cyan
   0,255,0;...      %3  Green
   255,255,0;...    %4  Yellow
   255,0,0;...      %5  Red
   128,128,128;...  %6  Grey
   0,0,0;...        %7  Black
   255,255,255];... %8 White

[rows,cols]=size(outputData);
rgbData=zeros(rows,cols+3);
rgbData(:,1:cols)=outputData(:,1:cols);

%add rgb
%no class is black
rgbData(:,9:11)=C(outputData(:,pcol),:);

%export
%xlswrite('rgbData.xlsx',rgbData);
dlmwrite('rgbData.xyz',rgbData,' ');
end
```

Classify multi-spectral point cloud using ANN classifier

```
%Script to execute neural classifier functions
%define hidden layer size
hiddenLayerSize=[10];
%define number of columns
pcol=7;
rcol=7;
%Define score threshold
t=0.5;
%define training function
% trainFcn='trainscg';
% trainFcn='traincgb';
trainFcn='trainrp';
%define performance function
performFcn='crossentropy';

%Train network and then test to produce predicted data
[predictedData]=neuralClassifier(trainingData,tgtData,testData,
hiddenLayerSize,trainFcn,performFcn,t);
%Calculate confusion matrix
[C,outputData]=ConfusionMatrix(referenceData,rcol,predictedData
,pcol);
%creat predicted data point cloud each class with a set colour
[rgbData]=ClassesAddRGB(outputData,pcol);

function
[predictedData]=neuralClassifier(trainingData,tgtData,testData,
hiddenLayerSize,trainFcn,performFcn,t)
%Selection of scanners
%Faro=1
%Leica=2
%Riegl=3

% testDataA=table2array(testData(1:end,:));
testDataA=testData;
inputs=trainingData(:,[1 3])';%change number to scanners
required
targets=tgtData';
%extract spectral data from testdata xyzsi,s2,s3
test=testDataA(:,[4 6])';%Faro=4, Leia=5, Riegl=6

% Create a Pattern Recognition Network
net = patternnet(hiddenLayerSize,trainFcn,performFcn);
%net=feedforwardnet(hiddenLayerSize,'trainscg');

[r,c]=size(hiddenLayerSize);
% net.layers{1}.transferFcn = 'tansig';
net.layers{1:c}.transferFcn = 'logsig';


% Setup Division of Data for Training, Validation, Testing
net.divideParam.trainRatio = 70/100;
net.divideParam.valRatio = 15/100;
net.divideParam.testRatio = 15/100;

% Train the Network
[net,tr] = train(net,inputs,targets);
```

```
% Test the Network
outputs = net(inputs);
errors = gsubtract(targets,outputs);
performance = perform(net,targets,outputs);

% View the Network
view(net);

%Test, thi has a score from 0-1 for each class
testOutputs=net(test);

%determine class from scores
[score,class]=max(testOutputs);

%threshold the results
[n,m]=size(class);
%t=0.98;
for k=1:1:m
   if score(k)<=t
       class(k)=6;
   end
end

%put in column format
class=class';
[rows,cols]=size(testDataA);
predictedData=zeros(rows,cols+1);
predictedData(:,1:cols)=testDataA(:,1:cols);
predictedData(:,cols+1)=class;
score=score';

%histogram of scoring
numOfBins = 100;
[histFreq, histXout] = hist(score, numOfBins);
figure;
bar(histXout, histFreq/sum(histFreq)*100);
xlabel('Classification score (0-1)');
ylabel('Frequency (%)');

end
```

Appendix C Scanner Specifications

The following figures shown an image of the scanners and their associated manufacturers specification sheet.

FARO 3D 120



Performance Specifications

Ranging unit

Unambiguity interval:	153.49m (503.58ft)
Range Focus^{3D} 120[1]:	0,6m - 120m indoor or outdoor with low ambient light and normal incidence to a 90% reflective surface
Range Focus^{3D} 20:	0,6m - 20m at normal incidence on >10% matte reflective surface
Measurement speed (Pts/Sec):	122,000 / 244,000 / 488,000 / 976,000
Ranging error[2]:	±2mm at 10m and 25m, each at 90% and 10% reflectivity

Ranging noise[3]	@10m	@10m - noise compressed[4]	@25m	@25m - noise compressed[4]
@ 90% refl.	0.6mm	0.3mm	0.95mm	0.5mm
@ 10% refl.	1.2mm	0.6mm	2.20mm	1.1mm

Colour unit

Resolution:	Up to 70 megapixel colour
Dynamic colour feature:	Automatic adaption of brightness

Deflection unit

Field of view (vertical/horizontal):	300° / 360°
Step size (vertical/horizontal):	0,009° (40,960 3D-Pixel on 360°) / 0,009° (40,960 3D-Pixel on 360°)
Max. vertical scan speed:	5,820rpm or 97Hz

Laser (Optical transmitter)

Laser power (cw Ø):	20mW (Laser class 3R)
Wavelength:	905nm
Beam divergence:	Typical 0.19mrad (0.011°)
Beam diameter at exit:	Typical 3.0mm, circular

Data handling and control

Data storage:	SD, SDHC™, SDXC™; 32GB card included
Scanner control:	Via touchscreen display and WiFi
New Wifi(WLAN) access:	Remote control, Scan Visualisation and download are possible on mobile devices with Flash[5]

Multi-Sensor

Dual axis compensator:	levels each scan: Accuracy 0,015°; Range ± 5°
Height sensor:	via an electronic barometer the height relative to a fixed point can be detected and added to a scan.
Compass:	the electronic compass gives the scan an orientation. A calibration feature is included.

Leica HDS3000 Specifications



General	
Instrument type	Pulsed, high-speed laser scanner, with survey-grade accuracy, range, and field-of-view
User interface	Notebook or Tablet PC
Scanner drive	Servo motor
Camera	Integrated high-resolution digital camera
System Performance	
Accuracy of single measurement	
Position*	6 mm
Distance*	4 mm
Angle (horizontal/vertical)	60 microradians/60 microradians, one sigma
Modeled surface precision/noise**	2 mm, one sigma
Target acquisition**	2 mm std. deviation
Data integrity monitoring	Periodic self-check during operation and start-up
Laser Scanning System	
Type	Pulsed; proprietary microchip
Color	Green
Laser Class	3R (IEC 60825-1)
Range	300 m @ 90%; 134 m @ 18% albedo
Scan rate	Up to 4,000 points/sec, maximum instantaneous rate Average: dependent on specific scan density and field-of-view
Scan resolution	
Spot size	From 0 - 50 m : 4 mm (FWHH - based); 6mm (Gaussian - based)
Selectability	Independently, fully selectable vertical and horizontal point-to-point measurement spacing†
Point spacing	Fully selectable horizontal and vertical; 1.2 mm minimum spacing, through full range†
Maximum sample density	1.2 mm†
Scan row (horizontal)	20,000 points/row, maximum†
Scan column (vertical)	5,000 points/column, maximum†
Field-of-view (per scan)	
Horizontal	360° (maximum)†
Vertical	270° (maximum)†
Aiming/Sighting	Optical sighting using QuickScan™ button
Scanning Optics	Single mirror, panoramic, front and upper window design Environmentally protected by housing and two glass shields

Riegl VZ400 Specifications



Technical Data *RIEGL* VZ®-400

Laser Product Classification

Class 1 Laser Product according to IEC60825-1:2007

The following clause applies for instruments delivered into the United States: Complies with 21 CFR 1040.10 and 1040.11 except for deviations pursuant to Laser Notice No. 50, dated June 24, 2007.



Range Performance [1]

	Long Range Mode	High Speed Mode
Laser Pulse Repetition Rate PRR (peak) [2]	100 kHz	300 kHz
Effective Measurement Rate (meas./sec) [2]	42 000	122 000
Max. Measurement Range [3]		
natural targets ρ ≥ 90 %	600 m	350 m
natural targets ρ ≥ 20 %	280 m	160 m
Max. Number of Targets per Pulse	practically unlimited [4]	
Accuracy [5] [7]	5 mm	
Precision [6] [7]	3 mm	
Minimum Range	1.5 m	
Laser Wavelength	near infrared	
Laser Beam Divergence [8]	0.35 mrad	

1) With online waveform processing.
2) Rounded values.
3) Typical values for average conditions. Maximum range is specified for flat targets with size in excess of the laser beam diameter, perpendicular angle of incidence, and for atmospheric visibility of 23 km. In bright sunlight, the max. range is shorter than under overcast sky.
4) Details on request.
5) Accuracy is the degree of conformity of a measured quantity to its actual (true) value.
6) Precision, also called reproducibility or repeatability, is the degree to which further measurements show the same result.
7) One sigma @ 100 m range under *RIEGL* test conditions.
8) Measured at the 1/e² points. 0.35 mrad corresponds to an increase of 35 mm of beam diameter per 100 m distance.

Scanner Performance

	Vertical (Line) Scan	*Horizontal (Frame) Scan*
Scan Angle Range	total 100° (+60° / -40°)	max. 360°
Scanning Mechanism	rotating multi-facet mirror	rotating head
Scan Speed	3 lines/sec to 120 lines/sec	0°/sec to 60°/sec [10]
Angular Step Width Δ ϑ (vertical), Δ φ (horizontal)	0.0024° ≤ Δ ϑ ≤ 0.288° [9] between consecutive laser shots	0.0024° ≤ Δ φ ≤ 0.5° [9] between consecutive scan lines
Angle Measurement Resolution	better 0.0005° (1.8 arcsec)	better 0.0005° (1.8 arcsec)
Inclination Sensors	integrated, for vertical scanner setup position, details see page 2	
GPS Receiver	integrated, L1, with antenna	
Compass	optional, for vertical scanner setup position, details see page 2	
Internal Sync Timer	integrated, for real-time synchronized time stamping of scan data	
Scan Sync (optional)	scanner rotation synchronization	

9) Selectable.
10) Frame scan can be disabled, providing 2D scanner operation.

General Technical Data

Power Supply Input Voltage	11 - 32 V DC
Power Consumption	typ. 65 W (max. 80 W)
External Power Supply	up to three independent external power sources can be connected for uninterrupted operation
Main Dimensions	Ø 180 x 308 mm (diameter x length)
Weight	approx. 9.6 kg
Humidity	max. 80 % non condensing @ +31°C
Protection Class	IP64, dust- and splash-proof
Temperature Range	
Storage	-10°C up to +50°C
Operation	0°C up to +40°C: standard operation
Low Temperature Operation [11]	-20°C: continuous scanning operation if instrument is powered on while internal temperature is at or above 0°C and still air -40°C: scanning operation for about 20 minutes if instrument is powered on while internal temperature is at or above 15°C and still air

11) Insulating the scanner with appropriate material will enable operation at even lower temperatures.

Appendix D Neural Network Definitions

The following neural network definitions are courtesy of Mathworks © 2015.

Conjugate Gradient Algorithms

The basic backpropagation algorithm adjusts the weights in the steepest descent direction (negative of the gradient). This is the direction in which the performance function is decreasing most rapidly. It turns out that, although the function decreases most rapidly along the negative of the gradient, this does not necessarily produce the fastest convergence. In the conjugate gradient algorithms, a search is performed along conjugate directions, which produces generally faster convergence than steepest descent directions. In this section, we present four different variations of conjugate gradient algorithms.

In most of the training algorithms that we discussed up to this point, a learning rate is used to determine the length of the weight update (step size). In most of the conjugate gradient algorithms, the step size is adjusted at each iteration. A search is made along the conjugate gradient direction to determine the step size, which minimizes the performance function along that line. There are five different search functions included in the toolbox, and these are discussed at the end of this section. Any of these search functions can be used interchangeably with a variety of the training functions described in the remainder of this chapter. Some search functions are best suited to certain training functions, although the optimum choice can vary according to the

specific application. An appropriate default search function is assigned to each training function, but this can be modified by the user.

Powell-Beale Restarts (traincgb)

For all conjugate gradient algorithms, the search direction will be periodically reset to the negative of the gradient. The standard reset point occurs when the number of iterations is equal to the number of network parameters (weights and biases), but there are other reset methods that can improve the efficiency of training. One such reset method was proposed by Powell, based on an earlier version proposed by Beale. For this technique we will restart if there is very little orthogonality left between the current gradient and the previous gradient. This is tested with the following inequality.

$$\left|\mathbf{g}_{k-1}^{T}\mathbf{g}_{k}\right| \geq 0.2\left\|\mathbf{g}_{k}\right\|^{2}$$

If this condition is satisfied, the search direction is reset to the negative of the gradient.

In the following code, we recreate our previous network and train it using the Powell-Beale version of the conjugate gradient algorithm

Scaled Conjugate Gradient (trainscg)

Each of the conjugate gradient algorithms that we have discussed so far requires a line search at each iteration. This line search is computationally expensive, since it requires that the network response to all training inputs be computed several times for each search. The

scaled conjugate gradient algorithm (SCG), developed by Moller, and was designed to avoid the time-consuming line search.

The trainscg routine may require more iterations to converge than the other conjugate gradient algorithms, but the number of computations in each iteration is significantly reduced because no line search is performed.

Resilient Backpropagation

Multilayer networks typically use sigmoid transfer functions in the hidden layers. These functions are often called "squashing" functions, because they compress an infinite input range into a finite output range. Sigmoid functions are characterized by the fact that their slopes must approach zero as the input gets large. This causes a problem when you use steepest descent to train a multilayer network with sigmoid functions, because the gradient can have a very small magnitude and, therefore, cause small changes in the weights and biases, even though the weights and biases are far from their optimal values.

The purpose of the resilient backpropagation (Rprop) training algorithm is to eliminate these harmful effects of the magnitudes of the partial derivatives. Only the sign of the derivative can determine the direction of the weight update; the magnitude of the derivative has no effect on the weight update. The size of the weight change is determined by a separate update value. The update value for each weight and bias is increased by a factor whenever the derivative of the performance function with respect to that weight has the same sign for two

successive iterations. The update value is decreased by a factor whenever the derivative with respect to that weight changes sign from the previous iteration. If the derivative is zero, the update value remains the same. Whenever the weights are oscillating, the weight change is reduced. If the weight continues to change in the same direction for several iterations, the magnitude of the weight change increases.